THE QUINTUPLET CLUSTER

A young massive cluster study based on proper motion membership

DISSERTATION

zur

Erlangung des Doktorgrades (Dr. rer. nat.)

der

Mathematisch-Naturwissenschaftlichen Fakultät

der

Rheinischen Friedrich-Wilhelms-Universität Bonn

vorgelegt von

Benjamin Hußmann

aus

Amberg

Bonn 2013

Angefertigt mit Genehmigung der Mathematisch-Naturwissenschaftlichen Fakultät der Rheinischen Friedrich-Wilhelms-Universität Bonn

1. Gutachter:	Dr. Andrea Stolte
2. Gutachter:	Prof. Dr. Norbert Langer
Tag der Promotion:	14. Januar 2014
Erscheinungsjahr:	2014

Abstract

Young massive clusters define the high mass range of current clustered star formation and are frequently found in starburst and interacting galaxies. As – with the exception of the nearest galaxies within the local group – extragalactic clusters can not be resolved into individual stars, the few young massive clusters in the Milky Way and the Magellanic Clouds might serve as templates for unresolved young massive clusters in more distant galaxies. Due to their high masses, these clusters sample the full range of stellar masses. In combination with the small or negligible spreads in age or metallicity of their stellar populations, this makes these object unique laboratories to study stellar evolution, especially in the high mass range. Furthermore, they allow to probe the initial mass function, which describes the distribution of masses of a stellar population at its birth, in its entirety.

The Quintuplet cluster is one of three known young massive clusters residing in the central molecular zone and is located at a projected distance of 30 pc from the Galactic centre. Because of the rather extreme conditions in this region, a potential dependence of the outcome of the star formation process on the environmental conditions under which the star formation event takes place might leave its imprint in the stellar mass function. As the Quintuplet cluster is lacking a dense core and shows a somewhat dispersed appearance, it is crucial to effectively distinguish between cluster stars and the rich population of stars from the Galactic field along the line of sight to the Galactic centre in order to measure its present-day mass function.

In this thesis, a clean sample of cluster stars is derived based on the common bulk proper motion of the cluster with respect to the Galactic field and a subsequent colour selection. The diffraction limited resolution of multi-epoch near-infrared imaging observations obtained at the ESO Very Large Telescope with adaptive optics correction provided by the NAOS-CONICA instrument allowed to determine individual stellar proper motions even at the Galactic centre distance of 8 kpc. The required colour information was provided by additional near-infrared data from the Very Large Telescope and the WFC3 camera onboard the Hubble Space Telescope. The knowledge of both, the individual proper motions and stellar colours, was found to be essential in order to derive the cleanest possible cluster sample. The clean cluster sample allowed to derive the present-day mass function of the Quintuplet cluster for the first time in the approximate mass range from $4 < m < 40\,M_{\odot}$ and out to a distance of 2.1 pc from the cluster centre. While the mass function in the central part of the cluster ($r < 0.5$ pc) is found to be top-heavy, i.e. overabundant in high mass stars compared to the standard initial mass function, its slope steepens towards larger radii and is consistent with the standard initial mass function in the outermost covered annulus ($1.2 < r < 2.1$ pc). The observed outward steepening of the mass function is indicative of mass segregation which is a common finding in young massive clusters. The determined mass function is discussed and compared to the findings in other young massive clusters with special regard to the Arches cluster which is also located in the Central Molecular Zone. The extrapolated total present-day mass of the cluster is found to be on the order of $2 \times 10^4\,M_{\odot}$. Based on their position in the $J_s - K_s$, $K_s - L'$ colour-colour diagram, a fraction of 2.5 ± 0.8% of proper motion members ($K_s < 17.5$ mag) were found to show an excess in the near-infrared. The excess sources cover the mass range from 2 to 10 $M_{\odot}$. This excess fraction is compared to the fraction of circumstellar discs in young clusters from the literature and, as the survival of primordial circumstellar discs around intermediate mass stars to the age of the Quintuplet cluster is surprising, alternative origins of the

near-infrared excess are discussed.

Future work based on the presented study might involve the inference of the initial mass function and other initial properties of the Quintuplet cluster by numerical models, customized to the observed properties of the cluster. The nature of the detected excess sources as potential circumstellar discs could be supported or disproved by the presence or absence of rotation signatures in near-infrared spectra covering the wavelength range of first overtone CO bandhead emission.

Contents

1 Introduction

This thesis presents the results of a study of the Quintuplet cluster, a young massive star cluster at a projected distance of 30 pc from the Galactic centre, with the focus on the derivation of the present-day mass function of this cluster. Multi-epoch high precision imaging data obtained at near-infrared wavelengths with adaptive optics correction allowed to discern cluster stars from the rich field star population along the line of sight based on the common motion of the cluster members with respect to the Galactic field. After a refinement of the proper motion membership sample by rejecting stars with colours strongly deviating from the cluster main sequence, the present-day mass function of the cluster could be determined from an unbiased cluster sample in the mass range of $4 < m \lesssim 40\,M_{\odot}$.

The outline of the thesis is as follows: in this chapter an introduction to the stellar mass function (Sect. 1.1) and to young massive clusters in the Milky Way is given (Sect. 1.2). Due to the location of the Quintuplet cluster in the Galactic centre region, the conditions in this environment as well as the three known young massive clusters in this region (including the Quintuplet cluster) are described in some detail (Sect. 1.3). Chapter 2 introduces the NAOS-CONICA instrument at the Very Large Telescope and the reduction of the obtained datasets which form the basis of this thesis. The present-day mass function of the Quintuplet cluster in its inner ($r \lesssim 0.5$ pc) and outer parts ($0.6 < r < 2.1$ pc) is derived based on a clean sample of cluster members in Chapters 3 and 4, respectively. Chapter 3 was previously published in Astronomy & Astrophysics: 'The present-day mass function of the Quintuplet cluster based on proper motion membership' (Hußmann, B., Stolte, A., Brandner, W., Gennaro, M., & Liermann, A. 2012, A&A, 540, A57). In order to avoid repetitions, the abstract, the introduction, the description of the datasets and the data reduction as well as the summary are omitted, as the contents of these parts are stated in more detail in this chapter, in Chapter 2, in Sect. 4.1 and in the summary of this thesis. In Chapter 5, stars with near-infrared excess within the proper motion membership sample are identified and the possible origins of this excess are discussed. A summary of the main results and a short outlook conclude this thesis (Chapter 6).

1.1 Stellar mass function

The stellar mass function describes the mass spectrum of a stellar population, i.e. the number of stars within a certain mass range. A common and convenient representation of the mass function is in the form of a broken power-law

$$dN/dm \propto m^{\alpha}, \qquad m_1 < m < m_2\,, \tag{1.1}$$

where the power-law index α is often referred to as the slope of the mass function and m_1 and m_2 define the mass range in which the mass function slope is valid. The mass of a star is the essential property which – apart from its metallicity and potential close companions – defines its further evolutionary path. Hence, the mass function of a stellar population at its birth, the so-called initial mass function (IMF), has a pronounced impact on its further dynamical evolution as well as the stellar evolution of its members. As it determines the ratio of high to low mass stars, it influences the chemical enrichment of the interstellar medium by the stellar population and the observed properties such as, e.g., the mass-to-light ratio of a stellar cluster. The IMF is also, besides the star formation history, the essential

ingredient for stellar population models used to constrain the physical properties of unresolved stellar populations in external galaxies. As the IMF is the outcome of the star formation process, its measured shape is an important property to be explained and reproduced by star formation theories.

The IMF was first derived by Salpeter (1955) for stars in the solar neighbourhood who found a slope of $\alpha = -2.35$ in the mass range from 0.4 to 10 $M_\odot$. During the last 50 years, the IMF has been extensively studied in various environments such as the solar neighbourhood and the Galactic field, young star forming regions, open and globular clusters as well as other galaxies (see e.g. reviews by Scalo 1986; Kroupa 2002; Chabrier 2003; Bastian et al. 2010; Kroupa et al. 2013). Although most star formation theories predict a systematic variation of the IMF as a function of the conditions under which the star formation event occurs, i.e. a preferred formation of high mass stars in a low metallicity or high temperature environment (Kroupa et al. 2013, and references therein), the IMF is found to be seemingly universal and strong evidence for a systematic variation with the conditions of star formation is lacking (Bastian et al. 2010). In the stellar mass regime ($m > 0.07\,M_\odot$) the so-called canonical IMF for single stars can be represented by a two-part power-law (cf. Eq. (55) in Kroupa et al. 2013):

$$dN/dm \propto \begin{cases} m^{-1.3\pm0.3} & , 0.07 < m \leq 0.5\,M_\odot \\ m^{-2.3\pm0.36} & , 0.5 < m \leq 150\,M_\odot \end{cases} . \tag{1.2}$$

As the large distance to the Quintuplet cluster of 8 kpc prevents the determination of the mass function down to subsolar masses, a mass function slope of $\alpha = -2.3$ is referred to as the standard or canonical slope in this thesis. Due to its similar value, the IMF slope derived by Salpeter (1955, $\alpha = -2.35$) is also often used as the standard slope in the literature. A mass function which is flatter than the canonical IMF for $m > 0.5\,M_\odot$, i.e. the mass function slope α is larger (less negative) than the canonical slope, is termed as top-heavy, as it is composed of a proportionally larger fraction of high mass stars.

As systematic variations of the IMF are expected and might help to constrain and improve current theories of star formation, the quest for deviations from the standard IMF has been one of the most active fields of research on young stellar populations over the past two decades. Only recently it was claimed that for extreme star forming events with very high star formation densities ($\gtrsim 0.1\,M_\odot\,\mathrm{yr}^{-1}\mathrm{pc}^{-3}$), which occur during the formation of initially dense globular clusters or ultra-compact dwarf galaxies, there exists a dependence of the IMF slope for $m > 1\,M_\odot$ on the metallicity and the cloud density, with higher densities and low metallicities leading to a flatter slope of the IMF (Dabringhausen et al. 2012; Marks et al. 2012; Kroupa et al. 2013).

Unfortunately, the IMF cannot be directly measured. For a composite stellar population such as the Galactic field, the loss of higher mass stars which evolved from the main sequence and are no longer detectable has to be corrected by accounting for the star formation history of the population. Furthermore, the study has to be limited to some defined volume requiring a distance estimate for each star. The derivation of the IMF of a star cluster offers the advantage that all stars have similar ages, metallicities and are located at the same distance. Yet, even in young star clusters the mass spectrum differs from the IMF, as due to dynamical interactions the cluster may lose stars even before the formation of stars in the forming cluster is terminated (see Sect. 4.2 in Kroupa et al. 2013, and references therein). This unavoidable deviation of the observable present-day mass function (PDMF) of a star cluster from its IMF depends on its age and is due to the stellar and dynamical evolution of its population. The higher mass range of the PDMF of a cluster is first altered by the effects of stellar evolution, i.e. by the mass losses of evolved stars and high mass stars ending their lives as visible stars. High mass stars might also be dynamically ejected due to close encounters especially in the dense core of young clusters (Pflamm-Altenburg & Kroupa 2006; Fujii & Zwart 2011; Banerjee et al.

2012a). Stars are also lost at all stages due to evaporation, i.e. the loss of stars from the high velocity tail of the Maxwell-Boltzmann distribution of speed which are fast enough to leave the gravitational potential of the cluster. Because of dynamical mass segregation, this evaporation affects mostly the low mass part of the mass function (Baumgardt & Makino 2003). For a cluster orbiting the Galactic centre at small Galactocentric radii ($r_{\rm GC} \lesssim 100\,{\rm pc}$), tidal losses in the strong gravitational potential of the Galactic centre can be significant and even lead to its rapid dissolution within a few tens of Myr (Kim et al. 2000; Portegies Zwart et al. 2002). Hence, the inference of the IMF of a cluster from its measured PDMF requires its detailed numerical modelling in order to correct for dynamical stellar losses.

As mentioned above, the canonical mass function slope of $\alpha = -2.3$ refers to the single star IMF. Therefore, for a valid comparison of the measured mass function slope with the canonical IMF star counts have in principle to be corrected also for unresolved companions. This requires knowledge of the multiplicity fraction which depends on the mass of the primary as well as the mass ratio (see Bastian et al. 2010, and references therein). Due to the location of the Quintuplet cluster near the Galactic centre, it is not possible to resolve multiple systems in the cluster into single stars and the measured PDMF is in fact a system PDMF. Fortunately, for the relevant mass range above $1\,M_{\odot}$ the difference between the slope of a system mass function and the respective single star mass function is expected to be $\lesssim 0.1$ dex and hence on the same order as the typical uncertainty of the measured mass function slope (Weidner et al. 2009). The PDMFs derived for the Quintuplet cluster and presented in this thesis needed therefore not to be corrected for the effects of stellar multiplicity.

1.2 Young massive clusters in the Milky Way

Young massive clusters are defined by their large masses ($M_{\rm cl} \gtrsim 10^4\,M_{\odot}$) which cover the high mass range of the young cluster mass function, their relative youth (age: $< 20\,{\rm Myr}$[1]) and their high density which distinguishes them from massive associations. As discovered by Pfalzner (2009), the young massive clusters in the Milky Way follow a defined age sequence in the cluster density vs. radius diagram (termed 'starburst clusters' in their Fig. 2) which is distinct from a second sequence occupied by massive associations ($M_{\rm cl} > 10^3\,M_{\odot}$, termed 'leaky clusters'). In this diagram, young massive clusters (age: $< 10\,{\rm Myr}$) cover a density range of $10^2 - 10^6\,M_{\odot}\,{\rm pc}^{-3}$ and have radii $\lesssim 3\,{\rm pc}$, while even the youngest and most compact massive associations have densities $< 10^2\,M_{\odot}\,{\rm pc}^{-3}$ and radii $> 3\,{\rm pc}$. Young massive clusters are found in great number in other galaxies, i.e. in the interaction zones of starburst galaxies such as NGC 1569 or the Antennae Galaxies (Whitmore et al. 2010). In the Milky Way, which is currently not in a very active phase of star formation, only about a dozen of these objects are detected and well-studied (see e.g. Table 2 in Portegies Zwart et al. 2010). However, as these clusters are located close to the Galactic plane (see Fig. 2 in Portegies Zwart et al. 2010), this might be an observational bias due to the high stellar densities and high extinction caused by molecular clouds encountered for line of sights in the Galactic plane. In fact, follow-up observations of cluster candidates detected in infrared surveys (e.g. Dutra & Bica 2001; Ivanov et al. 2002; Mercer et al. 2005) revealed several potential young massive clusters such as [DBS2003] 179 or Mercer 81 (Borissova et al. 2008; Davies et al. 2012).

With a few exceptions for the nearest galaxies within the local group, e.g. R136 in the Large Magellanic Cloud, extragalactic young massive clusters can not be resolved into individual stars and

[1]The age limit was chosen with regard to the known young massive clusters in the Milky Way and ensures that evolved high mass stars ($m \gtrsim 15 M_{\odot}$) are still present in the cluster, but also older age limits are used in the literature (e.g. 100 Myr in Portegies Zwart et al. 2010).

their properties have to be inferred from integrated spectroscopic and imaging observations and stellar population models. In contrast, the stellar population of the young massive clusters in the Milky Way located at distances of 'only' few kiloparsecs from the Sun can in some cases be analysed even down to subsolar masses (e.g. for h and χ Persei at a distance of 2.8 kpc, Currie et al. 2010). Hence, the study of Galactic young massive clusters and their mass function may contribute to a better understanding of the extragalactic, unresolved clusters.

Besides this possibility to serve as templates for extragalactic starburst clusters, young massive clusters in the Milky Way and the Magellanic clouds are ideal cases to study large populations of stars which have formed from the same molecular cloud with a uniform metallicity and little or no age spread (Kudryavtseva et al. 2012). The stellar mass function in these clusters is well populated even at high stellar masses and can in principle be studied over the entire stellar mass range. However, the large distances, crowding and the difficulty to distinguish cluster stars from field stars constrain the lower observable mass limit, while the presence of the highest mass stars requires young cluster ages of $\lesssim 4$ Myr. The large number of high mass stars in different evolutionary stages including Wolf-Rayet (WR) stars of different subtypes, luminous blue variables (LBVs), and yellow and red supergiants (RSGs), make these clusters excellent targets to study the evolution of the most massive stars and set constraints on the respective theoretical models. Furthermore, by comparing the maximum stellar mass observed in a young massive cluster with the predicted number of stars at even higher masses based on the observed properties and the presumed IMF of the cluster, the hypothesis of a fundamental stellar mass limit can be addressed (e.g. Weidner & Kroupa 2004; Figer 2005; Oey & Clarke 2005; Crowther et al. 2010). The observed correlation of the maximum mass of a star within a cluster with its total mass (Weidner & Kroupa 2006) and the fact that most if not all isolated OB stars are runaway stars (de Wit et al. 2005; Schilbach & Röser 2008; Gvaramadze & Bomans 2008; Pflamm-Altenburg & Kroupa 2010) indicate that the formation of massive stars is closely connected to the formation of massive clusters or associations. Smoothed particle hydrodynamic simulations show that the formation of massive clusters and of massive stars proceeds simultaneously, with the most massive stars being formed in the most bound clusters (Smith et al. 2009). The masses of the cores from which the massive stars form are similar to the average core mass, but due to their location close to the potential well of the protocluster gas from large radii is channelled onto these protostars during global infall enhancing their accretion rates. According to this scenario, the mass to form a massive star is not originating from an especially massive core, but is gathered during the formation of the massive star and the surrounding cluster (Smith et al. 2009). The formation of massive stars in the core of the forming cluster in this competitive accretion scenario (see also Bonnell et al. 2004; Bonnell & Bate 2006) further proposes that clusters form primordially mass segregated.

Young massive clusters in itself provide an extreme environment for star formation and the subsequent cluster evolution due to their high density, the radiation field produced by the numerous massive stars, and the onset of supernovae after the first few Myr. Due to photoevaporation by the intense UV field and the strong winds of the massive stars, the natal molecular cloud of the cluster is quickly dispersed. Depending on whether massive stars form prior or subsequent to the low mass stars, this removal of the available gas reservoir for accretion might affect the formation of low mass stars. The conditions in young massive clusters, i.e. the large number of massive stars and the high stellar densities, may even enable the occurrence of stellar mergers between massive stars. In an attempt to explain the presence of very massive stars in R136 (Crowther et al. 2010), i.e. of stars exceeding the stellar mass limit of 150 $M_\odot$ proposed by Weidner & Kroupa (2004), Banerjee et al. (2012b) demonstrated that these stars might have formed by stellar mergers of massive binaries in the cluster core, whose eccentricity is increased or which harden by close encounters.

The locations of the Milky Way young massive clusters allow to probe the potential effects of

different Galactic environments on the outcome of star formation. Most of the known young massive clusters reside in the spiral arms, e.g. NGC 3603 (Sung & Bessell 2004; Stolte et al. 2004, 2006; Harayama et al. 2008; Pang et al. 2013) and Westerlund 2 (Ascenso et al. 2007; Carraro et al. 2013) in the Carina spiral arm and Westerlund 1 in the Scutum-Crux spiral arm (Clark et al. 2005; Brandner et al. 2008; Gennaro et al. 2011; Lim et al. 2013). The three red supergiant clusters RSGC1, RSGC2, and RSGC3 are located close to where the Scutum-Crux arm meets the Galactic bulge (Figer et al. 2006; Davies et al. 2007; Clark et al. 2009; Alexander et al. 2009). A fourth potential young massive cluster containing eight RSGs, Alicante 8, is found in the same area in the sky, but its distance has not yet been measured such that its location in this part of the Galaxy is not certain (Negueruela et al. 2010). Due to their relative closeness within a few hundred parsecs and similar ages between ~ 10 and 20 Myr it is suggested that the red supergiant clusters originate from the same large-scale starburst event. As their location is close to the northern tip of the Long Bar, this might correspond to the enhanced star formation observed along the stellar bars of other galaxies (Alexander et al. 2009, and references therein). Interestingly, the candidate young massive cluster Mercer 81 seems to be located at a similar position, but at the opposite side of the Galactic centre near the southern tip of the Bar (Davies et al. 2012). A third Galactic environment harbouring young massive clusters is the Galactic centre region. This environment and the three young massive clusters located in this region including the Quintuplet cluster, are introduced in more detail in the following section.

1.3 Young massive clusters in the Galactic centre region

1.3.1 Star formation in the Galactic centre

Star formation in the Galactic centre region, i.e. within the Central Molecular Zone (CMZ, $r_{\rm GC} \lesssim 200$ pc), proceeds under rather extreme conditions compared to other star forming regions in the Milky Way (Morris & Serabyn 1996). The CMZ harbours about 10% of the molecular gas in our Galaxy and is distinguished by the high gas densities ($n \gtrsim 10^4 {\rm cm}^{-3}$) and temperatures (50 – 100 K) encountered in this environment (Morris & Serabyn 1996, and references therein; Ao et al. 2013). As the Jeans mass, i.e. the mass required for a molecular cloud to become gravitationally unstable, increases with temperature ($\propto T^{3/2}$), it is suggested that the formation of higher mass stars might be favoured in the Galactic centre region (Morris 1993; Klessen et al. 2007). The internal velocity dispersion of molecular clouds in the CMZ is elevated compared to the Milky Way spiral arms and due to the strong Galactic centre tidal field high densities are required for clouds to be stable (Morris & Serabyn 1996; Shetty et al. 2012). Furthermore, strong magnetic fields with a large-scale amplitude of about $\sim 100\,\mu$G permeate the Galactic centre region (Crocker et al. 2010). In contrast to this, the nonthermal filaments with lengths $\gtrsim 30$ pc running perpendicular to the Galactic plane require an amplitude of the magnetic field of the order of mG (Yusef-Zadeh & Morris 1987). The high kinetic gas temperatures of 50 – 100 K seem not to be correlated with the temperature of the dust (~ 20 K, e.g. Lis et al. 2001). The external heating of the molecular gas required to explain this discrepancy could be provided by turbulence or cosmic rays (Yusef-Zadeh et al. 2007; Ao et al. 2013). Yusef-Zadeh et al. (2007) suggested that the increased ionization fraction as a consequence of the enhanced flux of cosmic rays in the CMZ (Oka et al. 2005; van der Tak et al. 2006; Yusef-Zadeh et al. 2013) might lead to a decreased star formation efficiency by hindering the ambipolar diffusion and hence the collapse of cloud cores.

In spite of these potential impairments, the Galactic centre region is a site of ongoing star formation. Besides three young massive clusters (Young Nuclear Cluster, Arches and Quintuplet cluster), the CMZ contains the giant molecular cloud Sgr B2 which is one of the most active star forming

regions in the Milky Way and numerous young stellar objects (YSOs). The star formation rate within the last 1 Myr in the CMZ was estimated based on the number of YSOs to be in range of 0.07 to 0.14 $M_\odot$/yr (Yusef-Zadeh et al. 2009; An et al. 2011). A similar star formation rate of 0.08 $M_\odot$/yr was obtained by Immer et al. (2012) based on the number of young sources (ages $<$ 1 Myr) in the CMZ contained in the ISOGAL survey. These results imply that currently about one-tenth of the total star formation in the Milky Way (1.2 $M_\odot$/yr, Lee et al. 2012) proceeds in the CMZ. However, in proportion to the amount of dense gas and dust concentrated in the CMZ, the number of YSOs and other tracers of current star formation appears to be lower in the Galactic centre environment than in the rest of the Galaxy. Beuther et al. (2012) determined the number of cold dust clumps in the ATLASGAL survey as a function of the Galactic longitude and found a pronounced peak in the direction of the Galactic centre, while the number of YSOs showed no corresponding peak. This result was confirmed by Longmore et al. (2013a) who compared the amount of dense gas as probed by NH_3 and 500 μm emission with the number of methanol and water masers as tracers of recent star formation. Longmore et al. (2013a) also compared the measured star formation rate in the CMZ with the predictions of the scaling relations for the star formation rate as a function of the gas surface density or the gas mass which apply in nearby galaxies as well as in Galactic molecular clouds. They found that the scaling relations by Lada et al. (2012) and Krumholz et al. (2012) overpredict the star formation rate in the CMZ by one order of magnitude given the amount of available dense gas. As a possible reason for the seemingly impaired star formation in the Galactic centre region, the authors suggested that the larger internal cloud velocity dispersion in the CMZ might counteract gravitational collapse. In summary, while the Galactic centre region is an active site of star formation, there are indications that the extreme conditions in this region have an impact on the efficiency of star formation. Whether this also affects the outcome of the star formation process, i.e. the IMF, is still the subject of ongoing research including the study presented in this thesis.

The formation of young massive clusters in the CMZ may be linked to the same mechanism which is thought to be responsible for the concentration of molecular gas in the Galactic centre region, i.e. the formation of the CMZ (Morris & Serabyn 1996; Kim et al. 2011). The movement of gas in the potential of the Galactic bar proceeds mostly on two families of closed orbits (Morris & Serabyn 1996; Ferrière et al. 2007, and references therein). The x1 orbits are located outside of the inner Lindblad resonance of the bar and are elongated and aligned parallel to the bar. The x2 orbits inside the inner Lindblad resonance are aligned perpendicular to the major axis of the bar and typically less elongated. Due to energy dissipation, gas may gradually drift along different x1 orbits towards the Galactic centre. As the innermost stable x1 orbits are self-intersecting and also intersect with the outermost x2 orbits, clouds initially moving along x1 orbits may lose energy and angular momentum due to shocks and cloud collisions and settle onto x2 orbits. Kim et al. (2011) showed with their hydrodynamical simulations of gas moving in a Galactic bar potential, that gas originally orbiting on x1 orbits undergoes shocks at the tip of the bar and moves inwards along dust lanes. Close to the transition from x1 to x2 orbits, the gas settles into a ring of dense clouds which has a striking resemblance to the CMZ. While the '180 pc molecular ring' in the CMZ was suggested to represent the innermost stable x1-orbit (Binney et al. 1991), the twisted, elliptical ring of molecular clouds ('100 pc ring') described by Molinari et al. (2011) may mark the outermost stable x2 orbit. Notably, the star forming regions Sgr B2 and C are located close to the tips of the ellipse where x1 and x2 orbits are expected to intersect (Molinari et al. 2011). A possible formation scenario for young massive clusters in the CMZ involves the collision of a massive molecular cloud on an x1 orbit with a second cloud on an x2 orbit (Hasegawa et al. 1994; Rodriguez-Fernandez et al. 2006; Stolte et al. 2008). Due to the shock compression, the initially stable cloud could collapse and fragment into stars to form a massive clusters

(cf. Sect. 1.3.3). An alternative scenario was proposed by Longmore et al. (2013b) based on the detection of four potential progenitor clouds for young massive clusters within the 100 pc ring. In this scenario, massive molecular clouds moving within the 100 pc ring along an x2 orbit are compressed after pericentre passage close to Sgr A*. As the clouds are found to be close to virial equilibrium (Longmore et al. 2012, 2013b), this compression of the cloud might be sufficient to induce gravitational collapse. Longmore et al. (2013b) point out that the four detected progenitor clouds between Sgr A* and Sgr B2, i.e. after their pericentre passage, show gradually more signs of star formation in agreement with this model.

1.3.2 Young Nuclear Cluster

The Young Nuclear Cluster (Krabbe et al. 1991, 1995; see also Genzel et al. 2010 for a review) is one of the three young massive clusters found in the Galactic centre environment. Because its stellar population is surrounding and orbiting Sgr A*, i.e. the supermassive black hole (SMBH) in the Galactic centre ($M_{\mathrm{SMBH}} = 4.3 \pm 0.5 \times 10^6\,M_\odot$, Gillessen et al. 2009), the kinematic properties and also the conditions for star formation for this cluster differ considerably from other young clusters. Within a radius of ~ 0.5 pc from Sgr A*, three dynamically distinct groups of young stars can be distinguished (cf. Lu et al. 2013). Within $r = 1''$ $(0.04\,\mathrm{pc})$[2], main sequence B stars constituting the so called S-star cluster move on highly eccentric and isotropic orbits around Sgr A*. At a projected distance of $0.8'' < r < 12''$, about 50% of the detected WR and O stars belong to a clockwise rotating coherent structure which forms either a strongly warped disc or a system of streamers (Paumard et al. 2006; Lu et al. 2009; Bartko et al. 2009). A further 20% of the young stars seem to belong to a second, less well-defined counterclockwise rotating disc which has an inclination angle relative to the first disc of $\sim 100^\circ$ and is supposed to be in a dissolving state (Paumard et al. 2006; Bartko et al. 2009). All of the early-type stars within $0.8'' < r < 12''$, including the stars which are not part of the discs, are consistent with constituting one stellar population (Paumard et al. 2006).

The presence of a young massive cluster located around Sgr A* is surprising. In addition to the extreme star formation conditions in the Galactic centre region, the strong tidal shearing in the immediate vicinity of the Galactic centre imposes severe constraints for the gravitational collapse of molecular clouds. There are two main scenarios for the origin of the young stars outside the S-star cluster (see Sect. VI in Genzel et al. 2010, for a detailed overview of the different star formation scenarios). In the infalling cluster scenario, a massive cluster forms a few parsecs outside the Galactic centre and, due to dynamical friction, spirals into the central parsec to form a disc of stars orbiting the SMBH (Gerhard 2001; Kim & Morris 2003). In order to reach the central parsec before being completely disrupted and within the lifetime of its massive stars, the cluster has to be more massive and concentrated ($M_{\mathrm{cl}} > 10^5\,M_\odot$, $\rho_{\mathrm{core}} > 10^8\,M_\odot\,\mathrm{pc}^{-3}$) than observed for any other cluster in the Galaxy. In simulations, the presence of an intermediate mass black hole was found to stabilise the cluster core against disruption and to lower the density required for the cluster to enter the central parsec by about two orders of magnitude (Kim et al. 2004; Gürkan & Rasio 2005). For the currently favoured in-situ formation scenario, the stellar disc(s) are formed from either a single massive, high-density cloud falling into the Galactic centre which subsequently settles into a disc and fragments into stars (Nayakshin et al. 2007; Bonnell & Rice 2008), or by a cloud-cloud collision in the central parsec (Hobbs & Nayakshin 2009).

The age of the stellar population in the Young Nuclear Cluster was determined by Paumard et al. (2006) from the number ratios of WR and O stars and the location of OB supergiants in the Hertzsprung-

[2]Throughout this thesis the Galactic centre distance of 8 kpc (Ghez et al. 2008) is applied for all three young massive clusters in the Galactic centre region to convert distances stated in arcseconds into parsecs.

Russel diagram (HRD) to be 6 ± 2 Myr. A recent study by Lu et al. (2013) favours a slightly younger age with a best value of 3.9 Myr and a 95% confidence interval spanning from 2.5 to 5.8 Myr. The mass function of the Young Nuclear Cluster was found to be top-heavy which is qualitatively consistent with the theoretical predictions for an in-situ formation scenario (Nayakshin et al. 2007; Bonnell & Rice 2008; Hobbs & Nayakshin 2009) and is also consistent with the expectation that the conditions in the Galactic centre environment favour the formation of high mass stars. By modelling their K-band luminosity function ($K < 17$ mag, $m \gtrsim 5\,M_\odot$) with population synthesis models, Bartko et al. (2010) inferred an extremely top-heavy mass function with a slope of $\alpha = -0.45 \pm 0.3$ within $0.8'' < r < 12''$. At larger radii ($r > 12''$), i.e. outside of the discs, the mass function of early-type stars has a slope of $\alpha = -2.15 \pm 0.3$ which is consistent with the slope of an Salpeter IMF ($\alpha = -2.35$). In contrast to this result and based on the sample of stars in the Young Nuclear Cluster by Do et al. (2013), Lu et al. (2013) derived for the stellar population inside of $r < 12''$ a mass function slope of $\alpha = -1.7 \pm 0.2$ ($m > 10\,M_\odot$) which is still top-heavy but significantly steeper than the value found by Bartko et al. (2010). They ascribe the discrepancy of their results to the findings of Bartko et al. (2010) to the different approaches of the applied completeness corrections and the different areas probed by the respective samples which stretch preferentially parallel (Lu et al. 2013) or vertical (Bartko et al. 2010) to the clockwise rotating stellar disc. In spite of this discrepancy, the top-heaviness of the mass function observed for the Young Nuclear Cluster still provides the best evidence found in the Milky Way for a dependence of the outcome of the star formation process, i.e. the IMF, from the conditions in the star forming cloud.

1.3.3 Arches cluster

The Arches cluster (Nagata et al. 1995; Cotera et al. 1996; Serabyn et al. 1998; Figer et al. 1999a) is located at a projected distance of about 26 pc from the Galactic centre in the vicinity of the thermal arched filaments (Yusef-Zadeh et al. 1984). Due to its compactness which at least in its inner parts ($r < 0.4$ pc) renders the distinction between the cluster population and the field less critical, it is so far the best-studied cluster in the CMZ. Because of its similar location and its age the Arches cluster is sometimes considered in the literature as being the younger 'brother' of the Quintuplet cluster (Figer et al. 1999b). The cluster contains 15 WN stars within $r < 0.5$ pc, a further three WN stars within $0.5 < r < 2$ pc (van der Hucht 2006[3], and references therein; Mauerhan et al. 2010a) and an approximate number of 160 O stars (Figer et al. 1999a; Figer 2004). From the lack of WC stars, the presence of WNL stars and model fits to the K-band spectra of five evolved, massive stars, a cluster age of 2.5 ± 0.5 Myr was determined (Figer et al. 2002; Najarro et al. 2004). Apart from NGC 3603 (age: 1 – 2 Myr), the Arches cluster has hence the youngest stellar population among the known young massive clusters in our Galaxy which offers the opportunity to study the earlier stages of high mass stellar evolution. Early studies of the cluster population yielded a very flat (top-heavy) mass function in the cluster core ($r < 0.2$ pc) with a slope α of about -1.3 (Figer et al. 1999a; Stolte et al. 2005). More recent determinations of the mass function which account for the individual stellar extinctions derived steeper, yet still top-heavy mass function slopes. Using initial stellar masses ($m > 10\,M_\odot$), Espinoza et al. (2009) and Habibi et al. (2013) derived mass function slopes of $\alpha = -1.9 \pm 0.2$ and $\alpha = -1.6 \pm 0.2$ in the core of the Arches cluster ($r < 0.2$ pc), respectively. At larger distances to the cluster centre, the mass function slope steepens to $\alpha = -2.3$ ($0.2 < r < 0.4$ pc) which is consistent with the canonical IMF slope, and steepens further to -3.2 at larger radii (Habibi et al. 2013). According to customised numerical models of the cluster by Harfst et al. (2010), the flat mass function slope

[3]The stated position of WR102b listed in Table 1 from van der Hucht (2006) as being associated with the Arches cluster is ~24 pc apart from the cluster near Sgr A* and is hence disregarded.

in the core and the outward steepening can be explained by the internal dynamical evolution, i.e. mass segregation, within the presumed cluster age of 2.5 Myr. A top-heaviness of the IMF is hence not required to produce the observed top-heavy mass function in the cluster core. The assessment whether the elevated cloud temperatures in the Galactic centre region still leave an imprint on the IMF in the form of a truncation at the low mass end, requires to determine the mass function down to lower masses than is currently possible. The total cluster mass of the Arches cluster is about $2 \times 10^4\,M_\odot$ (Espinoza et al. 2009; Clarkson et al. 2012; Habibi et al. 2013) and hence on same order as the masses of NGC 3603 (Harayama et al. 2008; Pang et al. 2013) and the Quintuplet cluster (see Sect. 4.4.2), but lower than the mass estimates for Westerlund 1 ($0.5 - 1 \times 10^5\,M_\odot$, Gennaro et al. 2011; Lim et al. 2013). With a central density of $2.0 \pm 0.4 \times 10^5\,M_\odot\,\mathrm{pc}^{-3}$ (Espinoza et al. 2009), the Arches cluster is the densest young massive cluster in our Galaxy.

The bulk motion of the Arches cluster with respect to stars in the Galactic field was first determined by Stolte et al. (2008) from the difference between the mean proper motions of cluster members and field stars. Their value of the bulk proper motion of 212 ± 29 km/s is somewhat higher, yet consistent within the errors with the value derived by Clarkson et al. (2012) of 172 ± 15 km/s. The latter value was inferred from the separation of the centroids of a two-component fit to the two-dimensional distribution of proper motions. By combining their bulk motion with the radial velocity of the cluster of 95 ± 8 km/s from Figer et al. (2002), Stolte et al. (2008) determined a three-dimensional space motion of the cluster of 232 ± 30 km/s. The high orbital velocity of the cluster excludes circular orbits in the azimuthally symmetric potential of the Galactic centre and is also inconsistent with the motion of molecular clouds on closed x1 or x2 orbits (Stolte et al. 2008). Hence, the scenario proposed by Longmore et al. (2013b) for the formation of young massive clusters from massive molecular clouds in the 100 pc ring (Molinari et al. 2011) seems not to apply to the Arches cluster. A possible formation scenario of the Arches includes the collision of a cloud on an x1 orbit with a cloud on the outermost x2 orbit with a subsequent starburst being triggered by the shock compression. A complication for this scenario is the fact, that the mass and density of the cloud on the x1 orbit required in order that the cluster inherits its high velocity are higher than currently observed for these clouds. Based on the present orbital motion and position on the plane of the sky of the cluster, Stolte et al. (2008) calculated its orbit for various line of sight distances of the cluster to the Galactic centre in order to determine the position of the Arches cluster at its birth about 2.5 Myr ago. They found that if the cluster is presently located within a Galactocentric radius of $r_{\mathrm{GC}} = 200$ pc, its initial location and radial velocity are consistent with the scenario that a x1-x2 cloud collision triggered the star formation in its progenitor cloud(s). Whether a similar scenario might also be necessary to explain the formation of the Quintuplet cluster with an estimated three-dimensional space motion of 164 ± 17 km/s (Sect. 4.2.3.3), significantly smaller than observed for the Arches cluster, or not is currently not clear.

1.3.4 Quintuplet cluster

The Quintuplet cluster ($\alpha = 17^{\mathrm{h}}46^{\mathrm{m}}15^{\mathrm{s}}$, $\delta = -28^\circ 49' 41''$, J2000) is located only $3'40''$ below the Galactic plane as defined by the galactic coordinate system, at a projected distance of about 30 pc from the Galactic centre assuming a Galactic centre distance of 8 kpc (Ghez et al. 2008). It is thought to be the ionizing source for two H II regions in its immediate vicinity, the 'Sickle' (G0.18-0.04) to the north and the 'Pistol' nebula (G0.15-0.05) located within the cluster (Yusef-Zadeh & Morris 1987; Lang et al. 1997; Figer et al. 1998, 1999). The Quintuplet cluster was detected first as a single bright source in surveys of the Galactic centre region at near- and mid-infrared wavelengths (Allen et al. 1977; Becklin & Neugebauer 1978) which was successively resolved into several components (Kobayashi et al. 1983; Glass et al. 1987; Okuda et al. 1987). Based on imaging data at higher res-

olution, the eponymous quintuplet of five, bright near-infrared sources was first described by Nagata et al. (1990) and Okuda et al. (1990). That this quintuplet resides within the Galactic centre region was inferred from the polarisation of the five sources which is similar to those found for the Young Nuclear Cluster in the centre of the Milky Way and the optical depth of the silicate absorption in their spectral energy distributions (Okuda et al. 1990). Because of their small relative separations (< 0.6 pc), their featureless spectra, and cool spectral energy distributions (SEDs), these sources were suggested to form a cluster of massive protostars (Okuda et al. 1990; Glass et al. 1990; Nagata et al. 1990). Although further bright stars were found in the Quintuplet cluster in the same year (Nagata et al. 1990; Glass et al. 1990), it was not established that these stars together with the quintuplet constitute a young, massive cluster until narrow-band and spectroscopic observations revealed their high masses and young ages (Moneti et al. 1994; Figer et al. 1995; Cotera et al. 1996; Figer et al. 1996). The 15 stars observed and designated by number by Glass et al. (1990) (Q1 – Q15, the 'Q'-label was first used in Figer et al. 1995) are indicated in Fig. 1.1, where the quintuplet is formed by the stars Q1 – Q4 and Q9. The first derivation of the properties of the Quintuplet cluster such as the cluster age (see below), mass and density was carried out by Figer et al. (1999b) based on a sample of 34 stars with spectral classifications. Adopting the Salpeter IMF slope, they extrapolated the total measured mass in stars of $\sim 10^3\,M_\odot$ down to $1\,M_\odot$ and determined a total cluster mass of $6.3 \times 10^3\,M_\odot$ which placed the cluster among the most massive open clusters in our Galaxy. In combination with the average distance of stars to the cluster centre of 1 pc, they estimated a cluster density of $10^{2.4}\,M_\odot\,\mathrm{pc}^{-3}$ and $10^{3.2}\,M_\odot\,\mathrm{pc}^{-3}$ using the measured and the extrapolated total cluster mass, respectively. The density of the Quintuplet cluster is hence by more than two orders of magnitude below the density of the Arches cluster of $\rho = 10^{4.9}\,M_\odot\,\mathrm{pc}^{-3}$ within 0.4 pc, adopting the cluster mass of $M_\mathrm{cl} = 2 \times 10^4\,M_\odot$ from Espinoza et al. (2009). It should be noted that in a subsequent paper based on better resolved HST NICMOS photometry (Figer et al. 1999a), the lower limit of the measured mass within 1 pc of the Quintuplet cluster was increased to $6.3 \times 10^3\,M_\odot$ ($m > 10\,M_\odot$) which is the same value as its previously extrapolated total mass. The fact that the Arches cluster is decidedly more compact than the Quintuplet cluster does still hold despite this increase of the measured mass in the Quintuplet cluster. The estimated ionizing flux from the high mass stars is sufficient to ionize the 'Sickle' H II region which provides further evidence for the location of the cluster in the Galactic centre region (Figer et al. 1999b). Liermann et al. (2009) covered a significant portion of the Quintuplet cluster ($36'' \times 36'' \mathrel{\hat{=}} 1.4 \times 1.4\,\mathrm{pc}^2$ at 8 kpc) with K-band spectroscopic observations using the integral field spectrograph SINFONI-SPIFFI installed at the Very Large Telescope. Their spectral catalogue, termed LHO catalogue throughout this thesis, contains 98 early-type stars and has a completeness limit of about $K = 13$ mag.

To this day, a total of 92 OB stars, 21 WR stars (within $r < 2.5$ pc), and 2 LBVs have been spectroscopically identified in the cluster (Figer et al. 1999b; Homeier et al. 2003; Liermann et al. 2009, 2010; Mauerhan et al. 2010a). The ratio of the number of WC to the number of WN stars in the Quintuplet cluster is N_WC:N_WN = 14:7 compared to 0:17 in the Arches cluster (Liermann et al. 2012). As WC stars are thought to represent a later evolutionary stage than WN stars, this signifies the older age of the Quintuplet cluster. The nature of the five stars forming the prominent quintuplet was enigmatic for a long time due to their cool SEDs, their large luminosities typical for supergiants and the lack of intrinsic absorption or emission lines in their near- or mid-infrared spectra (Moneti et al. 2001, and references therein). The diffraction limited images obtained by Tuthill et al. (2006) using rapid-exposure speckle interferometry resolved these four sources into 'pinwheel nebulae' which are characteristic for colliding-wind binaries consisting of a WC and a OB star. The orbital motion of the two stars causes the dust produced in the bow shock between the two stellar winds to be wrapped around into a spiral. The five quintuplet sources could be spectroscopically identified by Liermann et al. (2009) as late-type WC stars (WC8 or WC9) with dust emission. The spectra for Q2 and Q3

showed additional features of OB stars which is consistent with the expected high mass companion of the WC star in these systems. The two LBVs in the Quintuplet cluster are the so-called Pistol star (Figer et al. 1995; Figer et al. 1998) located to the south and qF362 (Figer et al. 1999b; Geballe et al. 2000) north-east of the cluster centre (see guide stars of Fields 2 and 4 in Fig. 1.1). The signature of spherical shell expansion, the line of sight velocity, as well as the foreground extinction of the Pistol nebula suggest that the nebula was formed by a massive ejection of stellar material from the Pistol star within the last 10^4 yr (Figer et al. 1995; Figer et al. 1999). The largest contribution of the flux ionizing the nebula originates not from the Pistol star itself, but from other massive stars in the Quintuplet cluster which explains why the nebula is brightest in Paschen-α emission in the direction towards the cluster centre. Due to its high gas to dust ratio ($M_{\rm gas}/M_{\rm dust} \approx 2800$, Figer et al. 1999), the additional extinction caused by the nebula and its impact on the photometry of cluster stars located in its line of sight at near-infrared wavelengths are expected to be small. A third LBV (LBV G0.120-0.048) was detected at a projected distance of 7 pc (2′.8) south-west of the cluster (Mauerhan et al. 2010b). Due to this relative closeness, the authors suggest that this LBV might have formed in the same star formation event as the cluster, either outside or close to its centre from which it would have been ejected by a dynamical interaction.

The metallicity of the two LBVs in the cluster was determined by Najarro et al. (2009) from a quantitative analysis of high resolution near-infrared spectra. They found a solar iron abundance and twice a solar abundance of α-elements. Based on the nitrogen surface abundances of WN stars, the metallicity in the Arches cluster was determined to be solar (Najarro et al. 2004) or slightly super-solar ($Z = 1.3 - 1.4\,Z_\odot$, Martins et al. 2008). With the same method, the metallicity in the Young Nuclear Cluster was estimated to range between solar and twice solar metallicity (Martins et al. 2007). As these metallicity studies for the Arches and the Young Nuclear Cluster rely on the nitrogen surface abundance of WN stars, it is assumed that the abundance of other metals can be inferred from the nitrogen abundances (Martins et al. 2008). Using high resolution *H*- and *K*-band spectra of a sample of nine cool, luminous stars with projected distances of < 2.5 pc from the Galactic centre and of Q7 in the Quintuplet cluster, Cunha et al. (2007) derived slightly enhanced solar iron abundances ([Fe/H] = 0.14) and also an enhancement of α-elements. Davies et al. (2009) confirmed their results for IRS 7 and Q7, but noted that the observed enhanced abundances of iron and α-elements are consistent with solar values if the depletion of hydrogen at the surface due to stellar evolution is taken into account. Hence, solar metallicities are assumed for stars in the Quintuplet cluster for the comparison with stellar evolution models and isochrones throughout this thesis (see Sect. 3.6).

The age of the Quintuplet cluster was first determined by Figer et al. (1999b) by comparing the position of six, early B supergiants in the HRD with theoretical isochrones based on the Geneva stellar evolution models at twice the solar metallicity (Meynet et al. 1994). The best cluster age from this comparison and from the age range required for the simultaneous presence of WC stars, O supergiants and one RSG in the cluster, was found to be 4 ± 1 Myr, assuming that the cluster population is coeval. Liermann et al. (2012) found that the positions of the 85 OB stars contained in their *K*-band spectral catalogue of the Quintuplet cluster (Liermann et al. 2009) in the HRD are well represented by Geneva (Lejeune & Schaerer 2001) and Padova isochrones (Girardi et al. 2002) in the age range from 3 to 5 Myr. From the number ratios of WR and O stars and of WC and WN stars, and from the predictions of population synthesis models, Liermann et al. (2012) obtained a consistent result for the cluster age of 3.5 ± 0.5 Myr. The ages inferred for three WN stars in the range from 2.1 to 3.6 Myr are a bit lower than the age of the best fitting isochrone for the OB stars of 4 Myr (Liermann et al. 2010). Such a difference between the ages determined from OB stars or WN stars was also observed for the Arches cluster (Martins et al. 2008). Recently, by modelling the high mass end of the observed mass function of the Quintuplet cluster and by accounting for stellar wind mass losses and mass transfer in close

binary systems, Schneider et al. (2013) derived an age of 4.8 ± 1.1 Myr, which is more consistent with the age derived from the population of OB stars. According to the authors, the younger ages inferred for the WN stars can be explained by rejuvenation of these stars by mass transfer processes. For this thesis, an age of 4 ± 1 Myr was adopted for the Quintuplet cluster, which covers the approximate age range deduced from the position of the OB stars in the HRD, the predictions of the population synthesis models, and the modelling of the mass function.

The spectral catalogue of the Quintuplet cluster by Liermann et al. (2009) (LHO catalogue) contains in total 62 evolved stars of spectral types KM. For most of these stars cluster membership can be readily dismissed due to their low masses ($m < 9\,M_\odot$) and hence old ages (> 30 Myr) according to their position in the HRD (Liermann et al. 2012). Even for the two brightest late-type supergiants in their sample (Q7 and Q15 in Fig. 1.1), the masses inferred from stellar evolution models with and without rotation are $\leq 15\,M_\odot$ which implies an age of ≥ 15 Myr. The membership of these stars to the cluster would require that the star formation occurred during a prolonged period of ~ 10 Myr or that several bursts of star formation happened in this cluster. Such a prolonged or repeated star formation activity seems to be unlikely, as providing that also higher mass stars would have formed at the same time as the observed RSGs their UV radiation and stellar winds would have expelled any remaining cloud material within about 3 Myr. Furthermore, the age spreads of the young massive clusters NGC 3603 and Westerlund 1 were determined by Kudryavtseva et al. (2012) and found to be small with 0.1 and 0.4 Myr, respectively. Assuming a coeval cluster population also for the Quintuplet cluster, i.e. that all cluster stars formed during the same burst of star formation, all stars with spectral types KM are consequently regarded as field stars (cf. Sect. 3.5).

A reliable determination of the extent, the mass function and the total mass of the Quintuplet cluster requires to study its stellar population over a large mass range. Due to the rich field population along line of sights to the Galactic centre region, in combination with the rather dispersed configuration of the cluster compared to for example the Arches cluster, the identification of cluster stars with low and intermediate masses ($m < 10\,M_\odot$), or of cluster stars residing in its outer parts is complicated. Hence, for a study of the full stellar population of the Quintuplet cluster, an effective mean to disentangle the cluster from the field population is needed. While high and intermediate mass stars belonging to the cluster can be readily identified based on their early spectral types, such cluster samples are limited to higher mass stars. Due to the large distance to the cluster, comparatively long integration times are necessary to obtain spectra suited for spectral classification which puts an additional restriction to spectroscopic samples of the cluster population. For example, the completeness limit of the LHO catalogue at $K = 13$ mag corresponds to a stellar mass of about $10\,M_\odot$ assuming an age of 4 Myr for this cluster (Liermann et al. 2012). As the stellar population in the Galactic centre region is highly variable, it is also very difficult to find a control field which may accurately represent the population of field stars in the science field and would hence be suited for a statistical removal of field stars from the colour-magnitude diagram (CMD) of the cluster. Another possibility to establish cluster membership is the identification of cluster stars based on their common motion with respect to the field. This approach, which requires multiple epochs of high resolution imaging data of the cluster in order to measure the proper motion of individual stars, is applied in this thesis.

The difficulty to retrieve a representative sample of cluster stars was the main reason why the PDMF of the Quintuplet cluster could only be determined recently (Hußmann et al. 2012; Liermann et al. 2012[4]). The derivation of the PDMF in the central region (Chapter 3) as well as in the outer

[4]Liermann et al. (2012) determined the mass function slope from their spectroscopic sample of OB stars in the mass range from $10 < m_{\rm init} < 78\,M_\odot$. Their results were published in the same issue of Astronomy & Astrophysics as the results presented in Hußmann et al. (2012) (Chapter 3).

parts (Chapter 4) of the Quintuplet cluster was the main purpose of the study presented in this thesis. The knowledge of the mass function of this Galactic centre cluster is an important milestone in order to address the question whether the mode of star formation in young massive clusters or in the Galactic centre region is different than in less extreme star forming environments such as the solar neighbourhood. Furthermore, the slope of the PDMF is necessary for a detailed numerical modelling of the cluster's dynamical evolution required to infer the IMF of the Quintuplet cluster, to determine its current dynamical state, and to assess its further evolution and survival in the strong tidal field of the Galactic centre.

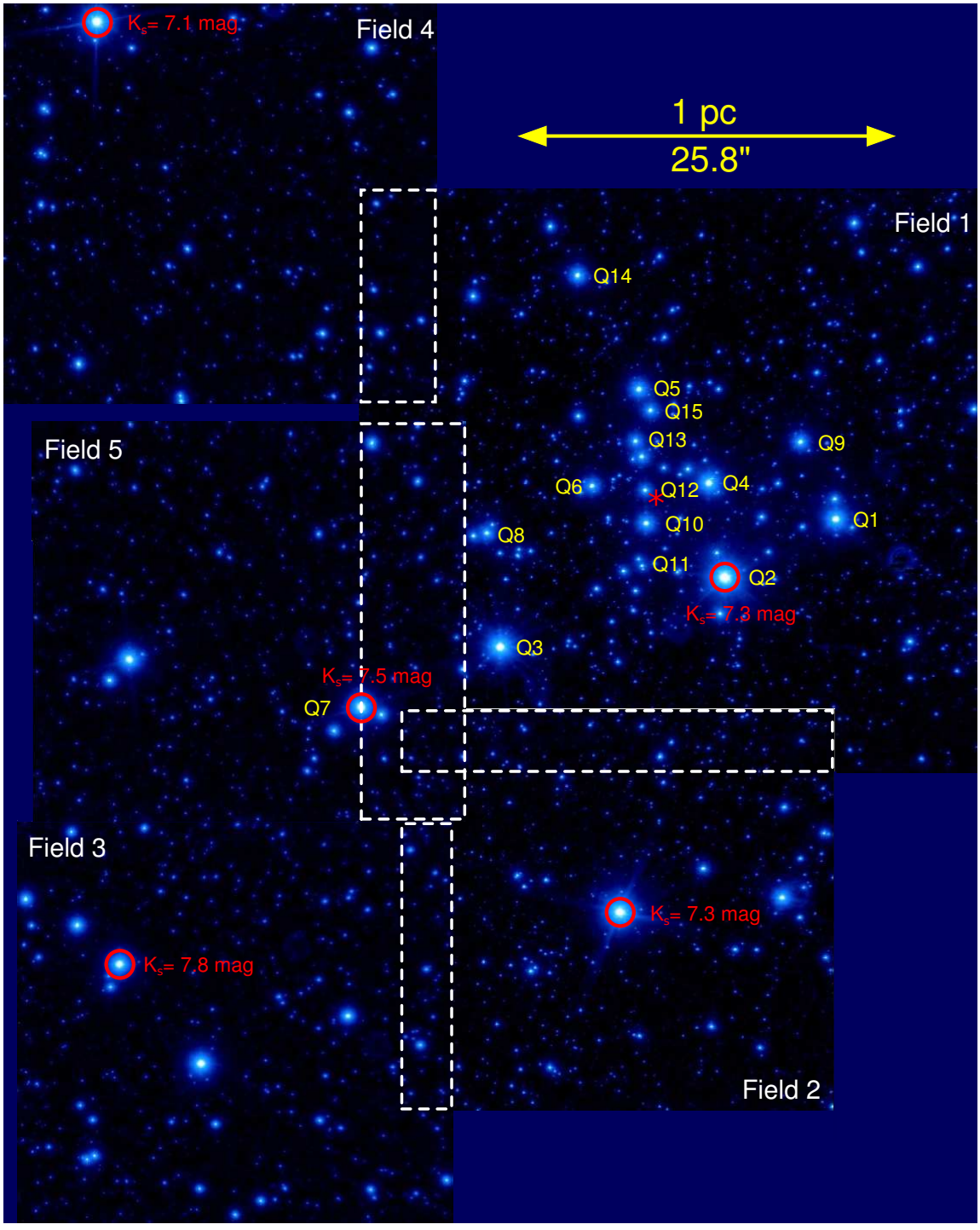

Figure 1.1: K_s-band image of the Quintuplet cluster as covered by the VLT/NACO observations presented in this thesis (north is up, and east is to the left). Field 1 covers the central part of the Quintuplet cluster (cf. Chapter 3), while the Fields 2 to 5 probe its outer regions (cf. Chapter 4). The red circles indicate the natural guide stars used to provide AO correction with the NAOS instrument. The guide star of Field 2 is the so called Pistol star. The stars Q1 – Q15 (yellow) are the 15 sources reported in Glass et al. (1990). Apparently, Q11 is comprised of two to three bright sources, which were not resolved at that time. The dashed rectangles mark the overlap regions of different fields. The red asterisk indicates the cluster centre (see Sect. 4.2.2.3).

2 Reduction of NAOS-CONICA datasets

Due to its location in the Galactic centre region, which is obscured at optical wavelengths by molecular clouds along the light of sight, a detailed study of the stellar population of the Quintuplet cluster requires high resolution, near-infrared data. The high spatial resolution achieved with the NAOS-CONICA instrument providing adaptive optics correction for the Utility Telescope 4 at the Very Large Telescope[1] is sufficient to resolve even the pre-main sequence population of the cluster and to measure individual stellar proper motions in order to distinguish cluster members from field stars using multi-epoch imaging data. As the data obtained with NAOS-CONICA form the basis of this thesis, the instrument and the performed data reduction are described in this chapter in some detail.

2.1 NAOS-CONICA

The NAOS-CONICA instrument (NACO), mounted at the Utility Telescope 4 (UT4, 'YEPUN') of the Very Large Telescope (VLT) on Cerro Paranal in Chile, is designed to obtain adaptive optics (AO) corrected observations at near-infrared wavelengths ($1-5\,\mu$m, Lenzen et al. 2003; Rousset et al. 2003; Ageorges et al. 2007). As only near-infrared broadband imaging observations obtained with VLT/NACO are used for this thesis, other available observation modes, such as polarimetry or long slit spectroscopy, are not considered in the following.

AO correction is provided by the Nasmyth Adaptive Optics System (NAOS) which either uses a natural guide star or a laser guide star in combination with a natural guide star. This second option was not applied for any of the used NACO datasets and is hence not discussed further. The distance of the natural guide stars to the science target may be as large as 55″, but as the size of the isoplanatic angle is typically much smaller ($\sim 20''$ at $2\,\mu$m, Ageorges et al. 2007), such large distances are not recommend for achieving a significant AO correction. For the NACO data used in this thesis, the maximum distance to the natural guide star was in the range of 20″ to 35″ depending on the respective field (see Fig. 1.1)[2]. The beamsplitter (or dichroic), which splits the incoming light from the telescope into a beam leading to the wavefront sensor and another to the camera, is selected with respect to the brightness of the available natural guide star and the filter (cf. Table 2 in Ageorges et al. 2007). Due to the bright guide stars in the Quintuplet cluster, the dichroic N20C80, which reflects 20% of the incoming light onto the wavefront sensor while 80% are transmitted to the camera, could be applied for the H- and K_s-band observations of the cluster (Chapters 3 and 4)[3]. For observations at longer wavelengths (Chapter 5), i.e. with the L'- or M'-broadband filters, the JHK dichroic is always used which allows to divert 90% of the light in the wavelength range from 0.80–2.5 μm to the wavefront

[1] This thesis is based on observations made with the ESO VLT telescope at the La Silla Paranal Observatory. The various programme IDs are stated in the text.

[2] The impairments of the astrometric and photometric accuracy introduced by the large maximal guide star distances of 35″ for Fields 1 and 4 are discussed in Sects. 3.4.2 and 4.3.1.2, respectively.

[3] One K_s-band dataset (Field 2, observed at 2011-09-19, cf. Table 4.1) was obtained using the visual dichroic and the visual wavefront sensor. This setting was applied as for observations of the outer parts of the Arches cluster requested in the same proposal the available guide stars were not sufficiently bright in the K_s-band. The quality of this dataset was not affected by this setting.

sensor while 90% of the light at longer wavelengths (2.8–5.5 μm) are sent to the camera. The N20C80 as well as the JHK dichroic are both used in combination with the near-infrared wavefront sensor which is a Shack-Hartmann sensor. The distortion of the wavefront by atmospheric turbulence is measured in real-time and the shape of the deformable mirror is adjusted by 185 actuators to produce a flat wavefront (Ageorges et al. 2007).

The second beam from the dichroic enters the Coudé Near Infrared Camera (CONICA) which is a high resolution imager and spectrograph. CONICA allows to choose from seven camera settings, designed for different wavelength ranges, field of views (FOVs) and observing modes (Table 5 in Ageorges et al. 2007). All observations of the Quintuplet cluster in H- or K_s-band were obtained with the S27 camera which covers a FOV of $27.8'' \times 27.8''$. The L27 camera, applied for the observations in L', has the same FOV. The current detector, a Santa Barbara Research Center InSb Aladdin 3 array, contains 1024×1024 pixels[4] and in combination with the S27 or the L27 camera yields a pixel scale of $0.02715''\text{pixel}^{-1}$ or $0.02719''\text{pixel}^{-1}$, respectively. The original detector, Aladdin 2, was replaced in May 2004 and had a slightly different pixel scale of $0.02710''\text{pixel}^{-1}$ for the S27 camera. The detector can be read out in three different modes which are suited for different amounts of thermal background and influence the readout noise of the detector (see Sect. 4.7.3 in Ageorges et al. 2007). The detector mode, i.e. the bias voltage applied to the detector array, determines the full well depth and hence the linearity and the saturation limit of the detector (see Table 2.1). The detector readout mode and the detector mode cannot be chosen freely and independently, but are preassigned according to the setup and wavelength range of the observations. Due to the high thermal background for the observations in L', the uncorrelated (Uncorr) readout-mode, where the array is reset and read only once, in combination with the HighWellDepth detector mode had to be applied (Table 15 in Ageorges et al. 2007). The Fowler sampling readout mode (FowlerNsamp), available for observations in the H- or K_s-band and used with the detector mode HighSensitivity, offers the lowest readout-noise and lowest number of hot pixels, but the full well depth is only half the value as for the alternative double read-reset-read (Double_RdRstRd) readout mode. In order to study the whole population of the Quintuplet cluster, including the bright members with $K_s < 10$ mag as well as faint sources with $K_s \sim 19$ mag, a large dynamic range and a large full well depth are required. Hence, for the H- or K_s-band observations the Double_RdRstRd readout mode was selected, for which the array is read, reset and read again (Ageorges et al. 2007). The applied settings used for the NACO observations presented in this thesis are summarized in Table 2.1. By default, a number, i.e. NDIT, of individual Detector Integration Times (DITs) are averaged by the Infrared Array Control Electronics (IRACE) of the CONICA imager into a single layer frame before it is transferred to the disc. For some of the datasets obtained in 2011 or later (see Sects. 4.1.1.1 and 5.1.1), the cube mode was applied, for which each individual DIT is stored into a single layer of a data cube (Girard et al. 2011). This allows to choose only those single DIT frames from the data cube for the image combination which offer the best AO correction.

2.2 Reduction pipeline

In order to reduce all NACO datasets in a consistent and reproducible fashion adopted to the NACO data and the special need of combining high astrometric accuracy and photometric depth, a custom made reduction pipeline was developed in the framework of the Emmy-Noether group. The pipeline is written in PyRAF[5], which is a powerful scripting language for IRAF (Tody 1986, 1993) and is

[4] Actually, the detector array contains 1026×1024 pixels, but the first two rows contain no useable data.

[5] PyRAF and STSDAS are products of the Space Telescope Science Institute, which is operated by AURA for NASA.

Table 2.1: Instrument settings of the NACO observations presented in this thesis (cf. Ageorges et al. 2007).

Filters[a]	Dichroic[b]	Camera	Readout mode	Detector mode	Linearity limit[c]	
					Aladdin 2 (10^3 ADU)	Aladdin 3 (10^3 ADU)
H, K_s	N20C80[d]	S27	Double_RdRstRd	HighDynamic	3.6	12.0
L'	JHK	L27	Uncorr	HighWellDepth	–	12.0

Notes. [(a)] See Table 6 in Ageorges et al. (2007) for the central wavelengths and the FWHM of the applied broadband filters. [(b)] The stated dichroics are used in combination with the near-infrared wavefront sensor. [(c)] For the H- and K_s-band observations the linearity limit was set to $4/5$ of the full well depth (see Table 3.1 in Hartung 2003 for the Aladdin 2 and Table 15 in Ageorges et al. 2007 for the Aladdin 3 detector). The factor of $4/5$ was inferred from Table 3.1 in Hartung 2003 and corresponds to a deviation from the linearity by roughly 3% for the appropriate reverse bias voltage of 0.2 V. The approximate linearity limit in the L'-band was inferred from the data as stars clearly saturate below the full well depth stated in Table 15 in Ageorges et al. (2007). [(d)] As the only exception, Field 2 (see Fig. 1.1) was observed in the K_s-band in 2011 with the visual dichroic and the visual wavefront sensor.

based on the programming language Python. The pipeline calls a series of self-written IDL routines which frequently involve routines from the IDL Astronomy User's Library (Landsman 1993) as well as PyRAF tasks and encompasses the basic data reduction and the combination of a set of dithered images into one final image.

Four major steps in the reduction of the images can be discerned: 1.) The generation of the calibration frames, i.e. the master dark, the flat field and the sky image. 2.) The basic data reduction of each science frame by applying the calibration frames. 3.) The creation of individual masks to cover electronic and optical ghosts and the assessment of the quality of each image. 4.) The combination of the dithered images of a dataset.

2.2.1 Generation of the calibration frames

The output files from this first step in the data reduction pipeline are the master dark, the flat field, the bad pixel masks for the master dark and the flat field, and the sky image. The generation of the master dark and the flat field from a set of dark exposures and twilight flat fields closely follows the recipe of the ESO NACO pipeline (Marco et al. 2007).

2.2.1.1 Dark

In order to determine the dark current and the zero level offset of the detector usually three dark frames, which are exposures without any illumination, are obtained per observation night at the ESO VLT for each employed combination of the DIT, readout mode and camera (Marco et al. 2007). The data reduction pipeline combines the dark frames belonging to a certain dataset to one master dark by a median combination. After excluding extreme outliers in each dark frame with a preliminary $3\,\sigma$-cut, the median and standard deviation σ for each individual dark frame are determined and pixels deviating by more than $3\,\sigma$ from the median are flagged as bad pixels. The bad pixels of each dark frame are then combined to a bad pixel mask for the master dark. If a hot bad pixel appears only in one dark frame it is assumed to have been caused by a cosmic ray hit. The value of the master dark at that position is determined as the mean of the remaining two good measurements and the respective pixel is not flagged as bad in the bad pixel mask.

2.2.1.2 Flat field

The effects of the non-uniform illumination of the detector and variations of the pixel-to-pixel sensitivity are corrected by the application of a flat field. For the derivation of a flat field, twilight flats and lamp flats are obtained on a regular basis for the NACO instrument (Amico et al. 2008, and earlier issues). Twilight flats are exposures of the cloud-free sky usually taken one hour before sunset as a series of 10 – 20 frames. Due to the amount of time needed for a series of twilight flats (15 – 60 min) and the short available time slot, twilight flats with all supported optical and detector setups cannot be observed daily. Instead, the different setups are cycled through on consecutive days within one or two weeks. Lamp flats are obtained with a halogen lamp internal to the CONICA camera and can therefore be taken during daytime for every instrumental setup used during the previous night. As they do not include any effects introduced by the light passing through the telescope optics and the AO system, and as the NACO flats are very stable, appropriate twilight flats obtained within a few days from the respective science data were preferred for the generation of the flat fields.

After the exclusion of twilight flats whose median flux is above the linearity limit of the used detector (Aladdin 2 or Aladdin 3) and readout mode (see Table 2.1), a master dark with the same DIT, camera and detector setting as the twilight flats is subtracted from each twilight flat. To measure the response of each pixel in dependence of the illumination, the count value at each pixel position is fitted by a straight line as a function of the median flux in each twilight flat using the standard deviation of the flux as measurement errors. The fit is iterated once after excluding those values in the stack of count values for each pixel differing by more than 3σ from the respective preliminary fit, with σ being the standard deviation of the count values scattering around the linear fit. The fitted slopes at each pixel position constitute the flat field. To conserve the flux in the science frame before and after the application of the flat field, the flat field was normalized by dividing it by its mean. Pixels deviating by more than 0.2 (Aladdin 2) or 0.1 (Aladdin 3) from the normalized mean value of 1.0 are conservatively assumed to be unreliable and stored in a bad pixel mask. As flat fields for the Aladdin 3 detector are flatter and have less structure than for the older Aladdin 2 detector, the criterion for the new detector could be chosen more strictly to better represent visible dust grains in the bad pixel mask of the flat field.

2.2.1.3 Sky

The sky is derived from a set of frames which consists either of the science frames to be reduced or sky frames specially observed subsequent to the science frames with the same telescope and detector settings[6]. As it is not possible to select star-free sky fields in the Galactic centre region due to the high stellar density, in general all available sky and science frames were used to derive the sky for the respective dataset in order to avoid stellar residua.

Usually the contribution of the detector bias and dark current is removed from the flat fielded science frames by subtraction of the sky, which in that case is derived from unreduced sky frames. As in a latter step the derived sky is scaled to the background levels of the science frames (see Sect. 2.2.2), which would alter the dark hidden in the sky, this approach is not employed by the pipeline. Instead the sky frames are reduced by subtraction of the appropriate dark and subsequent division by the flat field. In a later step of the data reduction the dark is subtracted from the science frame as well. Before the combination of the reduced sky frames to the final sky the sky frames may be scaled to a common background level. The final sky was derived using the PyRAF/IRAF task *imcombine* by determining

[6] In the following, all frames used to derived the sky are called sky frames for simplicity, whether they are designated sky frames or science frames.

at each position the median of the second to fifth faintest pixel which resulted in skies least affected by residual stellar light.

2.2.2 Basic data reduction

Each science frame is reduced by subtracting the master dark and dividing by the flat field. Subsequently the derived sky is subtracted, scaled to the background level of the respective science frame to account for slow variations in the overall brightness of the sky during the observation block. To estimate the linearity limit of each image, the detector linearity limit (Table 2.1) was corrected by subtracting the average dark and sky levels. The average dark level was determined as the median value in the dark, while the average sky level is the sum of the mean and the standard deviation of the sky after applying an iterative $3\,\sigma$-clipping to the sky. The estimated linearity limit of each image is written into an individual output file. The position of a preferably isolated, bright reference star common to all science frames is inferred from the cumulative offset header keyword and the known position in the first science frame and also stored in an output file. The reference star is later used to determine the Strehl ratio and the full width at half maximum (FWHM) in the respective image (Sect. 2.2.4.2)

Pixels affected by cosmic ray hits are identified with the IRAF task *cosmicrays* and stored in a bad pixel mask. The bad pixel mask for the dark and the flat field are combined with an optional constant mask containing known bad detector areas. Finally, this combined bad pixel mask, common to all frames, is then combined with the individual bad pixel mask to cover the cosmic rays in each image.

2.2.3 50 Hz noise correction

NACO data is sporadically affected by the so called 50 Hz noise causing a pattern of horizontal stripes (see Sect. 5.1 in Lundin et al. 2007). It is induced by the fans in the front end electronics of the IRACE[7], which preprocesses the data before it is transferred to the workstation (Ageorges et al. 2007). As the noise is the beat of two 50 Hz signals, the position and intensity of the stripes vary in space and time and therefore have to be corrected for each affected frame individually. For this purpose, a correction routine from the ECLIPSE pipeline (Devillard 2001) for the Infrared Spectrometer and Array Camera (ISAAC) was implemented into the data reduction pipeline and the parameters of the routine were adapted to the NACO data. The correction routine first determines the median brightness in each row of a frame. The 40 darkest and 420 brightest pixels in each row with 1024 pixels are excluded previously, so that the median is not affected by bad pixels or stellar flux. The median value of each row is stored in a one-dimensional array which is smoothed with a median filter of half-width 40 pixels. The smoothed median array represents the diffuse image background without stars and without the 50 Hz noise. By subtracting the smoothed median array from the original median value of each row, the contribution of the 50 Hz noise to the median value of each row is hence retrieved. The one-dimensional array containing the value of the 50 Hz noise in each row is subsequently subtracted from each column of the frame resulting in a corrected frame.

Dark frames affected by the 50 Hz noise are corrected before they are combined to the master dark. The 50 Hz noise correction is not applied to twilight flat fields because the high count levels of these frames prevent the potentially present noise pattern to be visible due to its comparatively low amplitude. Due to the change in intensity and position of the stripes in subsequent twilight frames the noise introduces only an additional scatter to the count values of each pixel being fitted as function of the median brightness of the twilight flat (see Sect. 2.2.1.2). The impact of the 50 Hz noise on

[7] http://www.eso.org/observing/dfo/quality/NACO/ServiceMode/naco_noise.html

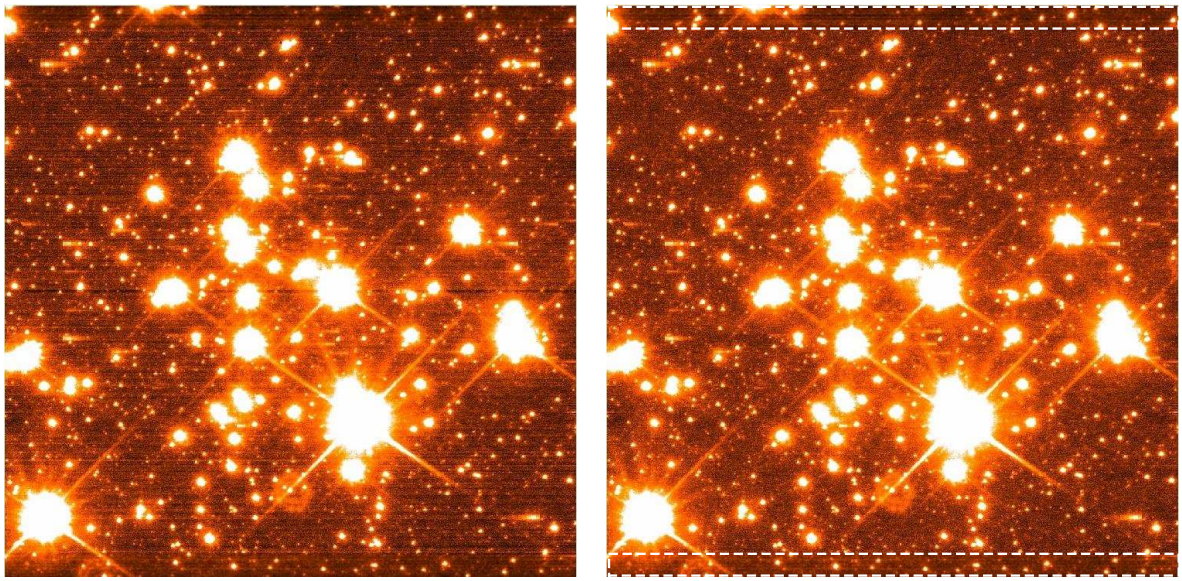

Figure 2.1: *Left panel*: NACO K_s-band science frame affected by the 50 Hz noise after the basic data reduction. *Right panel*: The same image, but after application of the 50 Hz noise correction routine. Image areas, which due to the half-width of the median filter (see Sect. 2.2.3) can not be corrected, are marked by the white, dashed boxes and are not included in the final combined image. A bright optical ghost, visible as a set of concentric rings, is located below and to the left of the brightest star. The large number of bright stars in this view of the cluster centre create the pronounced pattern of electronic ghosts (see Sect. 2.2.4.1).

the derived flat field is hence most likely negligible. Furthermore, the NACO flat fields as well as unreduced sky and science frames exhibit a grid pattern due to the rows and columns alternating in brightness in steps of one pixel which is effectively removed by the application of the flat field. As the correction routine can not distinguish between the 50 Hz noise and this genuine detector pattern, it would thus distort the final flat field and prevent the correct removal of the grid pattern by the flat field during basic data reduction. Hence the 50 Hz noise correction routine cannot be applied to the twilight flats, but as the noise is not visible in the twilight flats due to their high flux levels, this is not necessary, anyway. If the sky frames are affected by 50 Hz noise, the correction routine is applied after dark subtraction and flat fielding but before the generation of the final sky. The science frames are corrected for the 50 Hz noise after the basic data reduction. As the 40 upper- and lowermost rows cannot be corrected due to the half-width of the median filter, the uncorrected rows are covered by a constant mask which is combined with the individual bad pixel masks for each image during the basic data reduction step (see Sect. 2.2.2). Figure 2.1 gives an example of a reduced science frame obtained in 2008 in the K_s-band before and after the application of the 50 Hz correction routine.

2.2.4 Preparative steps before the image combination

2.2.4.1 Ghost masks

The presence of bright sources in a science frame leads to visible electronic and optical ghosts (see Sect. 4.7.1 Ageorges et al. 2007). The positions of the electronic ghosts are determined by the positions of the inducing stars. A bright star at the pixel position (x, y) generates three ghosts located at $(x, 1024 - y)$, $(1024 - x, 1024 - y)$ and $(1024 - x, y)$. As the position of bright sources on the detector changes for the dithered frames of a dataset, the pattern of electronic ghosts, i.e. their position on

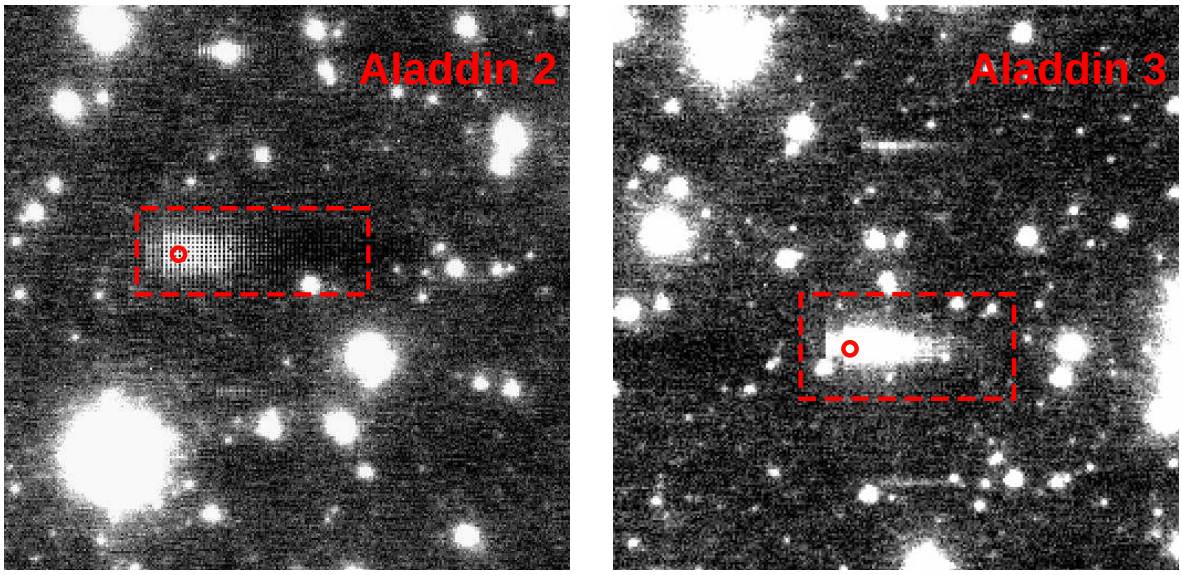

Figure 2.2: Electronic ghost induced by the same star in a science frame obtained in 2003 with the Aladdin 2 (*left panel*) or in 2008 with the Aladdin 3 detector (installed in May 2004, *right panel*). The red, dashed boxes indicate the size of the respective ghost masks and the theoretical position of the ghost is marked by the red circle.

the detector as well as their position relative to the inducing sources, changes, too. Therefore, an individual mask covering the electronic ghosts has to be created for each frame of the dataset. The size of an electronic ghost depends on the brightness of the star and on the detector (Aladdin 2 or Aladdin 3, see Fig. 2.2). The routine for creating a ghost mask for each science frame first determines stellar positions and fluxes in the respective image with the *starfinder* algorithm (Diolaiti et al. 2000, see also Sect. 3.2.1). For a number of bright stars, to be set after a visual inspection of the reduced science frames, the position of the electronic ghosts in the ghost mask is covered by a rectangular box, the size of which is scaled by the flux of the inducing source and the detector.

Optical ghosts emerge as a set of concentric rings and have a constant radius of roughly 40 pixels or 1.1″ for the S27 camera (see Figs. 2.1 and 2.3). Apparently they are caused by the brightest stars in the image ($K_s \lesssim 9.2$ mag, $H \lesssim 10.5$ mag) and are roughly located at the pixel position $(x+445, y+45)$ from the respective star at (x, y). A possible origin of these ghosts is the defocused projection of a reflection of the stellar light by an optical element onto the detector. As the positions of the few optical ghosts are fixed relative to the observed star field, a correction of the optical ghosts in the course of image combination is not possible (see Sect. 2.2.5). Hence, no masks to cover these ghosts are created.

2.2.4.2 Strehl ratio and FWHM measurement

In order to assess the image quality in a dataset and thus be able to exclude images with inferior AO performance or deteriorated seeing conditions, the Strehl ratio and the FWHM of the reference star are measured in all images. The position of the reference star is read from the appropriate output file created in the basic reduction step (Sect. 2.2.2). The FWHM of the star is determined by a two-dimensional Gaussian fit. To determine the Strehl ratio, i.e. the ratio of the normalized, measured peak flux of the point spread function (PSF) and the normalized, theoretical PSF peak flux of the diffraction limited PSF, the peak flux of the fit is normalized by the total flux within an aperture with a radius

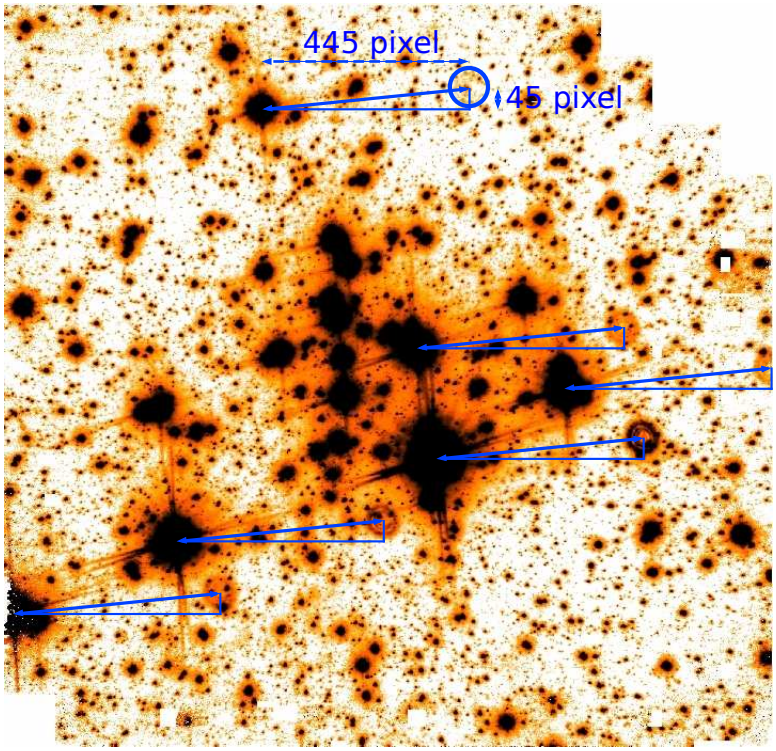

Figure 2.3: Optical ghosts in the K_s-band image of Field 1 from 2003 (S27 camera, DIT = 20.0 s). The optical ghosts appear at about 445 pixels to the right and 45 pixels above the position of the inducing star and have an approximate radius of 40 pixels (indicated in blue).

of 10 FWHM centred at the star. The theoretical, diffraction limited PSF generated by the light of a point source passing through the VLT and the NACO instrument with the employed filter and camera setting is generated with the *imgen* tool of the ESO ECLIPSE pipeline (Devillard 2001). The peak flux of the theoretical PSF is again determined with a two-dimensional Gaussian fit and normalized by the total flux of the theoretical PSF image. The Strehl ratio is then the ratio of the normalized, measured PSF peak flux of the reference star and the normalized PSF peak flux of the theoretical, instrumental PSF. The image names, the position of the reference star in each science frame and the derived FWHMs and Strehl ratios are written to an output list, which is utilised in the next step of the pipeline.

2.2.5 Image combination

To avoid that science frames obtained with a bad AO correction deteriorate the final image, frames with a FWHM of the reference star larger than either 1.5 times the minimum FWHM in the dataset or a freely chosen maximum FWHM may be excluded from the image combination. As an option to improve the spatial resolution in the combined image, the included science frames are linearly weighted by the inverse of the FWHM or the Strehl ratio of the reference star with the total weight of all frames being equal to one.

The relative offsets of all frames to the reference image are determined by maximising the cross-correlation between the selected images and the reference image using the three routines *precor*, *crossdriz* and *shiftfind* from the *dither* package (Koekemoer et al. 2002). The reference image is

selected as the image for which the position of the reference star is closest to its median position in all images. This ensures the maximal overlap between the reference image and the other images facilitating the determination of the relative offsets. The *precor* routine is a preparatory step before the cross-correlation which separates the real physical objects in each image from noise, cosmic rays and hot pixels. It determines the number of pixels within a moving box with counts above a given threshold. If the number of pixels above the threshold is equal to or larger than a set minimum value, the box is left unchanged, otherwise all pixels within the box are set to zero. The altered image is then written to an output image which has the appearance of a positive pixel mask at the position of stars brighter than the chosen flux threshold. It thus avoids cross-correlating noise patterns and facilitates the determination of the image shifts from real stellar positions. In the pipeline the box size is always set to 5×5 pixels and the minimum number of pixels above the threshold is fixed to 15. These values are optimised for the NACO datasets, although different settings yield only negligible differences in the derived image shifts. The threshold is determined anew for each dataset to be ten times the background value of the reference image for all NACO data of Field 1 and the first epoch K_s-band data of the outer fields (Chapter 4). The second epoch of K_s-band data of the outer fields was obtained in cube mode (see Sect. 4.1.1.1 for details). Due to the increased noise in the single DIT frames, the threshold was set to the median plus five times the standard deviation of the background in the reference image. The same prescription for the threshold was found to be also appropriate for the L'-data of the Quintuplet cluster (see Chapter 5), because of its intrinsically higher thermal background noise. The routine *crossdriz* cross-correlates each image with the reference image using the output images of *precor* and generates for each image a cross-correlation image. If the cross-correlation was successful a pronounced peak is apparent in the cross-correlation image, where the respective distance from the image centre corresponds to the offset between the image and the reference image. The peak position, and hence the relative offset for each image, is determined by a two-dimensional Gaussian fit with the routine *shiftfind*.

The final image combination step is performed using the PyRAF/IRAF task *drizzle* (described in detail in Fruchter & Hook 2002) with the selected science frames, weighted either by the inverse of the FWHM or the Strehl ratio (see above), and the relative offsets as input. For each science frame an individual combined bad pixel mask (Sect. 2.2.2) and a ghost mask (Sect. 2.2.4.1) can be provided. The *drizzle* algorithm maps each pixel of an input image onto the correct position in the combined image and distributes its flux among the output pixels proportional to the overlap area. Input pixels, which are contained in the bad pixel mask or the ghost mask of a science frame, are not used for deriving the combined image. As the flux of each output pixel is weighted by the sum of the overlap areas of contributing input pixels, pixels masked in some input frames do not affect the count values in the combined image as long as a sufficient number of good pixels from other input frames fall onto the masked area. The fractional number of input pixels contributing to each output pixel of the combined image is written to the so-called weight image. Finally, the position of the reference star in the combined image and the updated linearity limit are derived.

For all NACO datasets presented in this thesis the frames to be combined were linearly weighted by the inverse of the FWHM of the reference source. Pixels either contained in the individual bad pixel mask or the ghost mask of the respective frame were excluded.

3 The present-day mass function in the central part of the Quintuplet cluster

The analysis of the central part of the Quintuplet cluster as covered by Field 1 (see Fig. 1.1) is based on near-infrared observations obtained at the ESO VLT during two epochs in 2003 and 2008. The time baseline of 5.0 yr in combination with the high angular resolution and astrometric precision provided by the NACO instrument enables the identification of the cluster members primarily based on their common proper motions with respect to stars in the Galactic field. The present-day mass function in the central 0.5 pc of the cluster was then derived based on this clean sample.

Section 3.1 introduces the datasets covering Field 1. The remaining sections of this chapter (Sects. 3.2 to 3.8) are an excerpt of a publication in Astronomy & Astrophysics (Hußmann et al. 2012), which concisely describes the analysis of the data presented in Sect. 3.1 and discusses the results. As the Quintuplet cluster and the performed data reduction could be introduced and described in more details in Chapters 1 and 2 of this thesis than in the respective sections in Hußmann et al. (2012), the excerpt begins with Sect. 3 of the publication. Furthermore, Sect. 10 of the publication is omitted as a complete summary of the results of this thesis is presented in Chapter 6. In Sect. 3.2 of this thesis the source extraction, the photometric calibration and the determination of the astrometric and photometric uncertainties are described. The completeness of the datasets is determined based on artificial star experiments in Sect. 3.3. A sample of Quintuplet proper motion members is established in Sect. 3.4, and refined by a colour selection in the CMD and the exclusion of spectroscopically identified late-type stars in Sect. 3.5. The initial stellar masses are inferred from four isochrones of different ages and different stellar models (Sect. 3.6). The PDMF is derived in Sect. 3.7 and its slope is compared to mass function slopes from the literature of other young massive clusters in our Galaxy in Sect. 3.8.

3.1 Observational data and data reduction

The central part of the Quintuplet cluster (Field 1, see Fig. 1.1) is covered by four datasets observed in two epochs in 2003 and 2008. All datasets were obtained at the ESO VLT with AO correction provided by the NACO instrument utilising the bright Quintuplet star Q2 ($K_s \sim 6.6$ mag) as natural guide star for the infrared wavefront sensor. The pixel-scale of the employed medium resolution camera S27 is 0.02710″, therefore each frame (1024×1024 pixel) covers a FOV of 27.8″pixel^{-1}. The observations were all carried out in service mode to ensure that the data are taken under the requested seeing conditions and exhibit the required AO performance. The main properties of the four datasets are listed in Table 3.1. The stated FWHM is the FWHM of the empirical PSF extracted from the combined image during the PSF fitting (see Sect. 3.2.1). The Strehl ratio is determined using this PSF as the observed PSF and the appropriate theoretical PSF retrieved with the *imgen* tool from the ESO Eclipse pipeline (see Sect. 2.2.4.2).

Table 3.1: Overview of the used VLT/NACO datasets (adapted from Hußmann et al. 2012).

Date	Filter	No. of frames	DIT (s)	NDIT	$t_{\rm int}{}^a$ (s)	Airmass	Seeing (″)	FWHM (″)	Strehl ratio
2003-07-22	H	16	2.0	30	960	1.00–1.02	0.47–0.60	0.078	0.15
2003-07-22	K_s	16	20.0	2	640	1.03–1.06	0.36–0.49	0.080	0.22
2003-07-23	K_s	16	2.0	30	960	1.03–1.07	0.31–0.47	0.082	0.26
2008-07-24	K_s	33	2.0	15	990	1.00–1.01	0.49–0.60	0.080	0.26

Notes. $^{(a)}$ Total integration time of the central part of the combined image with maximum overlap.

3.1.1 Observations in 2003

The first epoch, obtained on July 22-23th 2003, was retrieved from the ESO archive (PI: F. Eisenhauer, Program ID 71.C-0344(A)) and consists of three datasets: two datasets in the K_s-band with DITs of 2.0 s and 20.0 s and one H-band dataset with a DIT of 2.0 s all of which were obtained with the Aladdin 2 detector. Each dataset consists of 16 dithered science frames and covers a common area of $40'' \times 40''$. For each dataset, 16 sky frames were observed in two blocks of 8 frames each between and after the science observations. For none of the datasets an apparent difference between the sky frames obtained in the first or second block could be found. Therefore all sky frames belonging to a dataset were used to generate the respective sky in order to minimise stellar residua. To still account for variations of the overall sky brightness, the sky was scaled to the background level of each science frame before it was subtracted.

All datasets from the first epoch were not affected by the 50 Hz noise and had not to be corrected. Due to the low number of science frames in each dataset and the satisfactory AO performance, all frames were combined to one final image. The FWHM of the PSF in the final combined image was 0.08″ for all three first epoch datasets (see Table 3.1). Figure 3.1 shows a JHK_s composite image of the NACO data of Field 1.

3.1.2 Observations in 2008

For the second epoch, the cluster was observed in the K_s-band with a DIT of 2.0 s on July 24th 2008, 5.0 yr after the first epoch (PI: W. Brandner, Program ID 81.D-0572(B)). The observations were carefully designed to provide high astrometric accuracy with the intention to accurately measure the proper motions of the cluster stars. This was accomplished by exactly reproducing the pointing and the dither pattern of the K_s-band observations of the first epoch. The orientation and the angular distance to the optical axis of each star, i.e. its optical path, and hence the optical distortions are then almost identical for each individual pointing of the dither pattern in both epochs, which minimises the effect of the distortions on the derived proper motions. Furthermore, the large number of 44 science frames permits to select frames based on their FWHM to enhance the spatial resolution in the final image without losing photometric depth and thus improves the achievable astrometric accuracy. Ten sky frames were obtained in one block subsequent to the science frames in order not to exceed the 1 hr time limit for NACO observation blocks by repeatedly moving between the science and the sky field.

All dark, sky and science frames of the second epoch are affected by the 50 Hz noise and were corrected as described in Sect. 2.2.3. Due to too small dithers between the sky frames strong stellar residua remained in the sky derived only from these frames. Therefore, the sky finally used for the data reduction was generated from both sky and science frames and again scaled to the background level

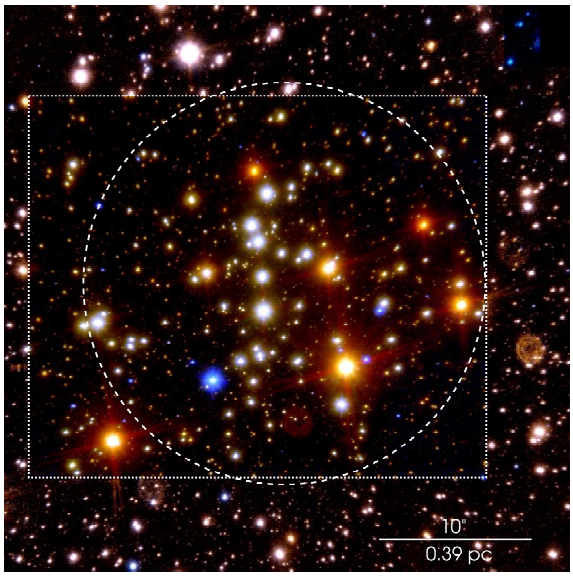

Figure 3.1: VLT/NACO JHK_s composite image of the Quintuplet cluster. Outside the dotted rectangle only H- and K_s-band data are available. The dashed circle with a radius of 500 pixel or 0.5 pc indicates the region used for the derivation of the mass function (see Sect. 3.4.2). Due to bad AO correction, the J-band dataset was unsuitable to perform photometry and astrometry and was used only for this composite image.

of each science frame. From the 44 science frames, 33 frames with the smallest FWHM ($< 0.083''$) were selected and combined to a final image. The achieved PSF FWHM in the final combined image of the second epoch was $0.080''$ (Table 3.1) and hence the same as for the first epoch datasets of 2003.

The following sections of this chapter as well as Appendices A and B are a reproduction of Sections 3 to 9 and Appendices B and C of the following publication:
The present-day mass function of the Quintuplet cluster based on proper motion membership; Hußmann, B., Stolte, A., Brandner, W., Gennaro, M., & Liermann, A. 2012, A&A, 540, A57, reproduced with permission ©ESO.

3.2 Photometry

3.2.1 Source extraction

Stellar fluxes and positions were determined with the *starfinder* algorithm (Diolaiti et al. 2000), which is designed for high precision astrometry and photometry on AO data of crowded fields. The point spread function (PSF) is derived empirically from the data by median superposition of selected stars after subtraction of the local background and normalization to unit flux. Using an empirical PSF is preferable for astrometric AO data, as the steep core and wide halo are not well reproduced by analytic functions. Stars whose peak flux exceed the linearity limit of the detector and are included in the list of stars for the PSF extraction are repaired by replacing the saturated core with a replica of the PSF, scaled to fit the non-saturated wings of the star[1]. Only if the saturated stars are repaired, they are

[1] Stars, whose peak flux exceeds the linearity limit of the detector are referred to as saturated stars for the remainder of this paper.

Table 3.2: Number of stars for PSF extraction.

Dataset No.	No. of PSF stars	No. of saturated PSF stars
1	37	17
2	239	136
3	48	29
4	69	15

definitely detected and fitted by the algorithm, so that their contribution on the flux of neighbouring stars can be subtracted. This is of special importance for faint stars located within the halo of a saturated star in order to measure their fluxes precisely. As spatially varying PSFs are not supported in *starfinder*, the PSF was assumed to be constant across the field (but see Sect.3.2.2). Isolated, bright stars uniformly spread across the image were selected for PSF extraction. All saturated stars were included in the list of PSF stars in order to be repaired. The total number of selected PSF stars and the number of saturated stars among them are listed in Table 3.2. The comparably small number of saturated stars of the last dataset is due to the higher linearity limit of the Aladdin3 detector.

3.2.2 Relative photometric calibration

The simplification of a constant PSF across the whole image led to spatially varying PSF fitting residuals and in turn to small-scale zeropoint variations across the field. This is typical for AO data and is mostly a consequence of anisoplanatism at increasingly larger distances from the natural guide star. As the extracted PSF resembles an average of the different PSFs across the image, the variation of the residuals after PSF subtraction is not centred at the position of the guide star. In the case of both the 2003 and 2008 data, the residual image showed a radial variation of the PSF fitting residual overlaid with slow azimuthal changes. In order to correct for these local zeropoint variations, a spatially varying correction factor was determined from the flux ratio *FR* of the residual flux in the PSF subtracted image and the stellar flux within an aperture around the centroids of isolated stars. The flux ratio *FR* was fitted in dependence of the distance to the image centre for angular sectors of 45° (0° − 45°, 45° − 90°, ...) either by a constant offset or a small linear trend. The correction factor $f_{\rm corr}(r)$, which is to be multiplied to the fluxes of all stars within an angular sector, follows from the respective fit of the flux ratio $FR_{\rm fit}(r)$:

$$f_{\rm corr}(r) = 1 + FR_{\rm fit}(r)\,. \tag{3.1}$$

The error of $f_{\rm corr}(r)$ is identical to the fitting error of $FR_{\rm fit}(r)$, which is $\Delta FR_{\rm fit}(r) = \Delta c$ if the flux ratio in the respective angular sector was fitted by a constant offset c and $\Delta FR_{\rm fit}(r) = \sqrt{(r\Delta b)^2 + (\Delta c)^2}$ if the flux ratio was fitted by a linear trend with $FR_{\rm fit}(r) = br + c$.

This procedure resulted in the most consistent photometric calibration across the observed field. Besides the small-scale zeropoint variations the spatial variation of the PSF affects the centroiding accuracy of detected stars. This effect is described in Sect. 3.4.2.

3.2.3 Absolute photometric calibration

Reference sources for the photometric calibration were taken from the Galactic Plane Survey (GPS; Lucas et al. 2008), which is part of the UKIRT Infrared Deep Sky Survey (UKIDSS; Lawrence et al. 2007). Magnitudes of stars within the UKIDSS catalogue are determined from aperture photometry using an aperture radius of 1″ and are calibrated using the Two Micron All Sky Survey (2MASS;

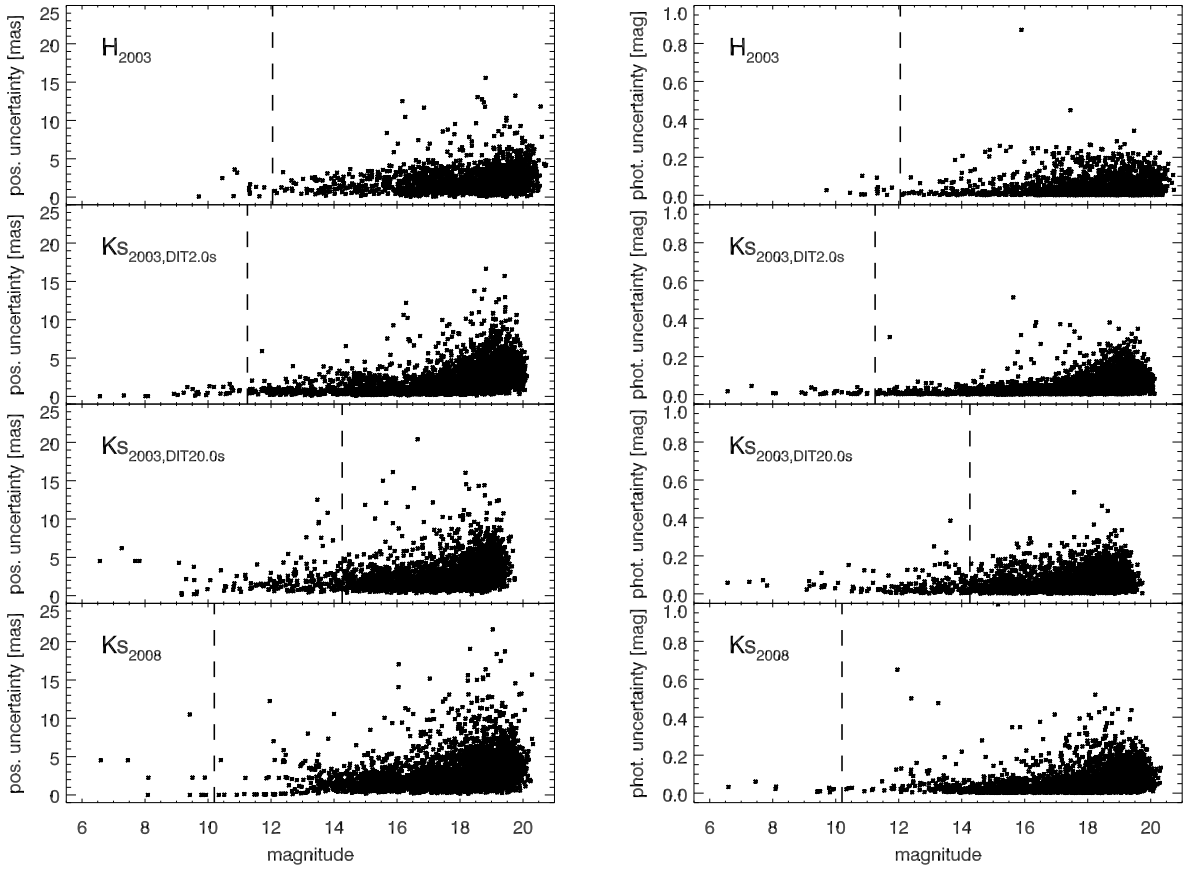

Figure 3.2: Plot of the astrometric uncertainty (*left panels*) and the photometric uncertainty (*right panels*) vs. the magnitude for all four NACO datasets. The plotted photometric uncertainty does only include the PSF fitting uncertainty. The dashed lines mark the linearity limit of the respective dataset.

Skrutskie et al. 2006). Data from the Sixth Data Release (DR6) for the Quintuplet cluster was retrieved from the UKIDSS archive (Hambly et al. 2008). For a set of calibration stars (29 in *H*-, 13 in K_s-band), which could unambiguously be assigned to calibrated sources in the UKIDSS catalogue, the individual zeropoints were determined. Due to the high spatial resolution of the NACO data several fainter stars can be resolved within the UKIDSS 1″ aperture around each calibrator. As these stars do contribute to the measured flux in the UKIDSS aperture, the PSF-flux of all stars falling within a radius of $r = 1'' - 0.5 \times \mathrm{FWHM_{PSF}}$, where $\mathrm{FWHM_{PSF}}$ is the FWHM of the extracted NACO PSF, was added and compared to the magnitude of each calibrator in the UKIDSS catalogue. The final zeropoint was then determined from the average of the individual zeropoints of the calibration stars. The zeropoints of the two K_s-band datasets from the first epoch were determined subsequently using the calibrated second epoch data. No significant colour terms were found between the NACO *H*, K_s and the UKIDSS *H*,*K* filter systems.

3.2.4 Error estimation

The estimation of the photometric and astrometric uncertainties follows the approach described in Ghez et al. (2008) and Lu et al. (2009). The reduced science frames for each dataset were divided into three subsets of comparable quality and coverage. Each subset of 5 (first epoch) or 11 frames (second

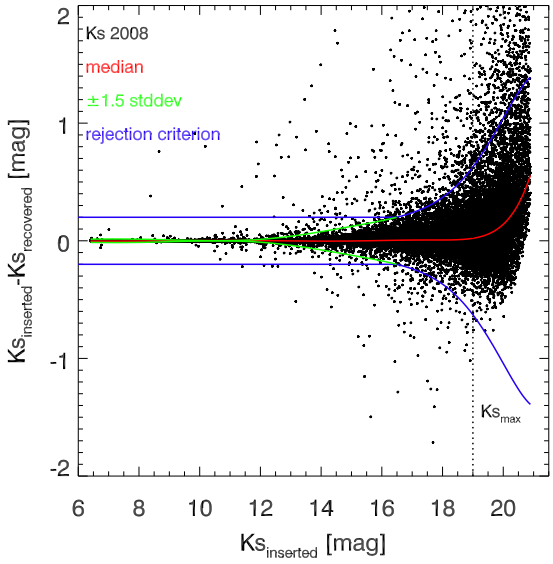

Figure 3.3: Difference of the inserted and recovered magnitudes of artificial stars inserted into the combined image of the K_s-band data in 2008 plotted vs. the magnitude. A high-order polynomial fit to the median and the standard deviation (multiplied by a factor of 1.5) of the magnitude difference within magnitude bins of 1 mag are shown as well. The vertical dotted line indicates the maximum K_s-band magnitude at $K_s = 19$ mag of stars to be used for the proper motion analysis.

epoch) was combined with *drizzle* and the photometry and astrometry of the resulting auxiliary image was derived with *starfinder* in the same way as for the deep images. The photometric and astrometric uncertainty was derived as the standard error of the three independent measurements for each star detected in all three auxiliary frames. As no preferential direction is expected for the positional uncertainty, the astrometric uncertainty of each star is computed as the mean of the positional uncertainty in the x- and y-direction. The astrometric and photometric uncertainties as derived from the auxiliary frames are shown in dependence of the magnitude in Fig. 3.2 for all datasets.

In order to remove false detections from the three K_s-band catalogues, only stars which were detected in all three auxiliary images of the respective dataset, and hence with measured astrometric and photometric uncertainties assigned, were kept in the respective source catalogue. For the H-band data this criterion was not applied. The H-band was matched (see Sect. 3.5) with a K_s-band catalogue containing only stars detected in both epochs. It is assumed that a star found in the K_s-band images of both epochs is a real source and if it is missing in one of the H-band auxiliary images this is a consequence of the substantially lower photometric depth of the auxiliary image.

The photometric errors as stated in the final source catalogue (Table 3.4) do include the respective zeropoint uncertainties, the photometric uncertainties due to the flux measurement from PSF fitting, and the error of the correction factors (Sect. 3.2.2).

3.3 Completeness

In order to quantify the detection losses due to crowding effects, the local completeness for each dataset was determined from the recovery fraction of artificial stars inserted into each combined image. The artificial star experiment for the H-band data covers a magnitude range from 9.5 to 21.5 mag. For each magnitude bin with a width of 0.5 mag, 42 artificial star fields were generated. Each artificial star

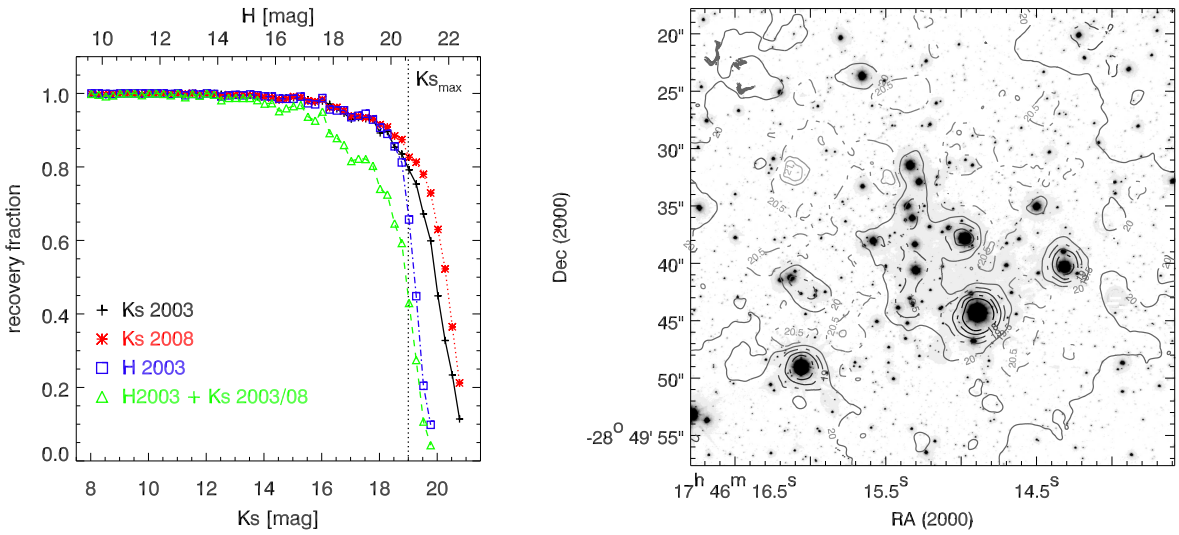

Figure 3.4: *Left panel*: Recovery fractions of artificial stars inserted within the inner 500 pixel from the centre of the observed field plotted vs. the respective magnitude in the K_s- (lower abscissa) or H-band (upper abscissa). The full and dotted lines correspond to the recovery fractions for the K_s-band data in 2003 and 2008, respectively and the dash-dotted line shows the completeness in the H-band. The dashed line shows the total completeness for the stars after matching the two K_s-band and the H-band datasets. Only stars with $K_s < 19$ mag are used for the proper motion analysis, as indicated by the vertical dotted line. *Right panel*: K_s-band image from the second epoch with the overplotted contours representing a completeness level of 50% for the labelled magnitudes.

field was created by adding 100 artificial stars, which are scaled replica of the empirical PSF, inserted at random positions and with random fluxes within the respective flux interval, into the combined image.

For the three K_s-band datasets, the artificial stars were inserted at the same physical positions as in the H-band image and with a magnitude in K_s yielding a colour for the respective artificial star of $H - K_s = 1.6$ mag, which resembles the colour of main sequence (MS) stars in the Quintuplet cluster (see Sect. 3.5). The photometry on the images with added artificial stars was performed in the same way as for the original images. In addition to artificial stars which were not re-detected by *starfinder*, stars, whose recovered magnitudes deviated strongly from the inserted magnitudes, were considered as not recovered. The criterion to reject recovered stars due to their magnitude difference between input and output magnitude was derived from polynomial fits to the median and the standard deviation of the magnitude difference within magnitude bins of 1 mag (Fig. 3.3). Stars with absolute magnitude differences larger than 1.5 times the fit to the standard deviation are treated as not recovered, but only if their absolute magnitude difference exceeds 0.20 mag. The median of the magnitude difference exposes a systematic increase towards the faint end, exceeding 0.05 mag for $K_s > 19.4$ mag or $H > 20.25$ mag. This trend indicates that for the faintest stars the measured fluxes contain systematic uncertainties. As we restrict the analysis to stars brighter than $K_s < 19$ mag, sources at these faint magnitudes are excluded from the proper motion and mass function derivation.

The left panel in Fig. 3.4 shows the overall recovery fraction for all datasets (K_s 2003 and 2008, and H 2003) within a radius of 500 pixels ($\hat{=}13.6''$) from the image centre, the part of the image actually used for the determination of the present-day mass function (see Sect. 3.4.2). The recovery fraction for the K_s-band data from 2003 is a combination of the recovery fractions for the two K_s-band datasets of that epoch. The dataset with the longer DIT of 20.0 s is used only for magnitudes fainter than the

linearity limit of this dataset at 14.3 mag. For brighter magnitudes, the recovery fraction of the 2003 K_s-band data with the short DIT of 2.0 s is drawn. The total recovery fraction also shown in the figure is the product of all three recovery fractions and is most relevant for the completeness correction of the mass function, as i) only stars which are detected in both epochs can be proper motion members and ii) only for stars with measured H-band magnitudes can masses be derived reliably.

Completeness varies as a function of position due to the non-uniform distribution of brighter stars and hence is a function of the stellar density and magnitude contrast between neighbours (see e.g., Eisenhauer et al. 1998; Gennaro et al. 2011). A spatially-dependent approach to determine the local completeness value becomes especially important if the cluster exhibits a non-symmetric geometry or in the presence of very bright objects, which heavily affect the completeness values in their surrounding. Both effects are present in the Quintuplet cluster. In order to assign a local completeness value to each detected star, the method described in Appendix A of Gennaro et al. (2011) was applied to derive completeness maps for each combined image containing the recovery fraction for every pixel as a function of magnitude. The procedure encompasses three steps performed for each magnitude bin (for a detailed description the reader is referred to Gennaro et al. 2011): 1.) Determine for each artificial star its ν nearest neighbours among the inserted stars ($\nu = 16$ for all datasets). The local, averaged completeness value at the position of the considered artificial star follows from the fraction of the recovered nearest neighbours (including the star itself). 3.) Interpolate these local completeness values into the regular grid of image pixels. 4.) Smooth the obtained map with a boxcar kernel with a width of the sampling size in order to remove potential artificial features introduced by the previous step. The sampling size $\langle d \rangle$ is the typical separation of independent measurements of the local completeness value and depends on the image area A, the number of inserted stars N and the chosen number of nearest neighbours ν (see Eq. A1 in Gennaro et al. 2011):

$$\langle d \rangle = \sqrt{\frac{A}{\pi N}} \times \sqrt{\nu} \approx 20\,\mathrm{FWHM_{PSF}} \approx 1.6\,''\,. \tag{3.2}$$

For the final step the completeness maps of all magnitude bins are used. To ensure that the completeness decreases monotonically with increasing magnitude, a Fermi-like function is fitted to the completeness values at every pixel in the image as a function of magnitude. The completeness (or recovery fraction) for every real star can then be computed from the fit parameters at the position of the star in each image. The right panel in Fig. 3.4 shows the combined K_s-band image for the 2008 epoch with superimposed 50%-completeness contours and limiting magnitudes labelled. The very bright stars with their extended halos hamper the detection of nearby faint stars causing the recovery fraction to be non-uniform across the field, as expected. The completeness of a star entering the mass function is the product of its completeness in the H-band, the 2008 epoch K_s data, and either the 2.0 s DIT ($K_{s,2003} < 14.3$ mag) or the 20.0 s DIT ($K_{s,2003} > 14.3$ mag) 2003 epoch K_s dataset as determined from the respective completeness maps:

$$f_{\mathrm{comp}} = f_{\mathrm{comp,Ks2008}} \times f_{\mathrm{comp,Ks2003}} \times f_{\mathrm{comp,H2003}}\,. \tag{3.3}$$

For stars brighter than $H = 13.5$ mag or $K_s = 10.4$ mag the completeness was assumed to be 100%.

3.4 Proper motion membership

Due to the high field star density for lines of sight towards the Galactic centre the distinction between cluster and field stars becomes particularly important. As most of the field stars are located within

the Galactic bulge they have similar extinction values as the cluster and cannot be distinguished from cluster members on the basis of their colours alone. The high astrometric accuracy of the AO assisted VLT observations in combination with the time baseline of 5.0 yr allows for the measurement of the individual proper motions of stars at the distance of the Quintuplet cluster. The primary applied method to discern the cluster members from the field stars is based on the measured proper motions.

3.4.1 Geometric transformation

In order to determine the spatial displacements, two geometric transformations were derived to map each position in the two first epoch K_s images (2003) with short (2.0 s) and long (20.0 s) DIT onto the corresponding position in the second epoch K_s image (2008). The second epoch is used as reference epoch because of the higher astrometric accuracy, deeper photometry and brighter linearity limit of this dataset. Only the K_s-band datasets were used to determine the spatial displacements, as due to their higher Strehl ratios the stellar cores are better resolved than in H-band, providing the better centroiding accuracy and hence most accurate astrometry.

Under the assumption that internal motions are not resolved so far, the cluster itself served as the reference frame. The geometric transformation was derived in an iterative process. First, a rough transformation was determined with the IRAF task *geomap* using the positions of manually selected bright, non-saturated stars uniformly distributed across the images of both epochs. The respective catalogue of the first epoch dataset (2003) was then mapped onto the catalogue of the second epoch (2008) to get a mutual assignment of stars found in both catalogues. From these stars the most likely cluster candidates were selected to provide the reference positions for the refined, final geometric transformation. As the bright stars used for the preliminary transformation are likely cluster members, the distribution of spatial displacements in the x-,y-direction of cluster star candidates are expected to scatter around the origin. Therefore, only stars with spatial displacements within a radius of 0.8 pixel$\hat{=}$4.3 mas/yr from the origin were selected for the derivation of the final transformation, which excludes most of the presumed field stars. Further, as the bulk of cluster stars are probably brighter than most stars in the field, only non-saturated bright and intermediate bright stars ($11.5 < K_s < 15.5$ mag for a DIT of 2.0 s and $14.0 < K_s < 17.0$ mag for a DIT of 20.0 s) provide the reference positions. The final geometric transformations were derived with *geomap* in an interactive way. The residual displacements in the x-, y-directions between the transformed first epoch and the second epoch coordinates were minimized by iteratively removing outliers and carefully adapting the order of the polynomial fit (= 3 for the final transformations). The final rms deviation of the geometric transformation was 0.2 mas/yr in the x- and 0.3 mas/yr in the y-direction for the dataset with a DIT of 2.0 s, and 0.3 mas/yr in the x- and y-direction for the dataset with a DIT of 20.0 s. For a total cluster mass of $M_{cl} \approx 6000\,M_{\odot}$ within a radius of $r \leq 0.5$ pc (see Sect. 3.7) the internal velocity dispersion is expected to be on the order of $0.15 - 0.2$ mas/yr or $6 - 8$ km/s. As this is smaller than the uncertainty of the geometric transformation alone, intrinsic motions are not resolved. Therefore the selection of cluster stars as geometric reference sources is justified.

3.4.2 Data selection and combination

Each of the two transformed star catalogues of the K_s-band data from the first epoch was matched with the star catalogue of the second epoch using a matching radius of 4 pixels ($\hat{=}$108 mas $= 1.4 \times$ $\mathrm{FWHM_{PSF}}$). The matching radius was chosen small enough to avoid mismatches between close neighbouring stars, but large enough to include all moving sources at GC distances below the escape velocity of the GC. A displacement of 108 mas within the time baseline of 5.0 yr for a distance of 8.0 kpc to

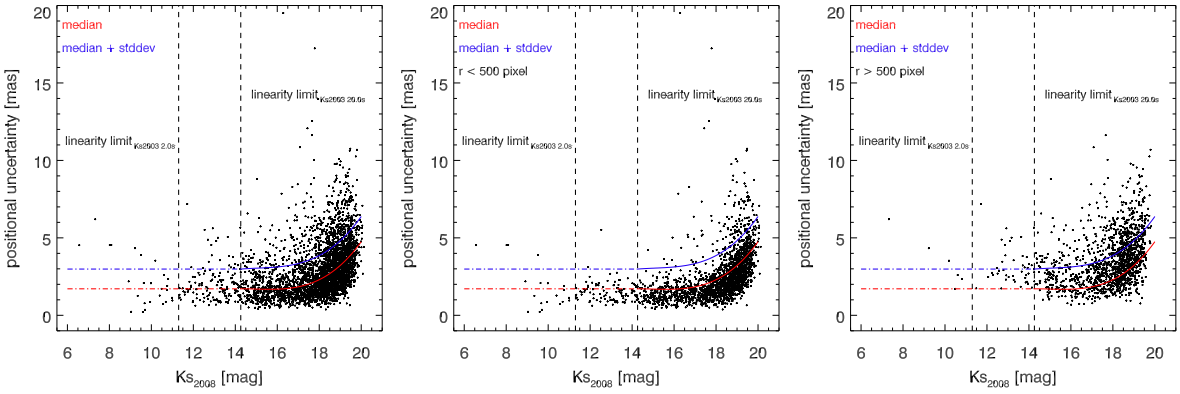

Figure 3.5: *Left panel*: Plot of the combined astrometric uncertainty from the two epochs of K_s-band data plotted vs. the magnitude of the second epoch (for details of the error estimation see Sect. 3.2.4). The median and standard deviation of the astrometric uncertainty above the linearity limit (at 14.3 mag) of the dataset in 2003 with 20.0 s DIT were fitted by polynomials. This fit of the median (lower line) and the sum the median and standard deviation (upper line) are drawn in all three plots. *Middle panel*: Astrometric uncertainty of stars residing within a circle with $r < 500$ pixel $\hat{=}$ 13.6″ around the centre of the observed field. *Right panel*: Astrometric uncertainty of stars residing outside this radius, which are excluded from further analysis.

the GC (Ghez et al. 2008) corresponds to a proper motion of 820 km/s. The combined astrometric uncertainty $\sigma_{\rm pos} = \sqrt{\sigma^2_{\rm pos,Ks2003} + \sigma^2_{\rm pos,Ks2008}}$ was derived for both of these catalogues. In the left panel of Fig. 3.5, the combined astrometric uncertainty is plotted against the magnitude. The datapoints below the linearity limit of the long exposure in 2003 at $K_s = 14.3$ mag originate from the match of the second epoch with the data with a DIT of 20.0 s, the datapoints at brighter K_s magnitudes are from the match with the data obtained with a shorter DIT of 2.0 s. For the matched catalogue using the first epoch dataset with a DIT of 20.0 s, the median and the standard deviation of the astrometric uncertainties within bins of 0.5 mag width were fitted by a third and second order polynomial, respectively. The fit to the median and the sum of both fits are shown in all three panels of Fig. 3.5 for comparison. The usage of one averaged PSF for the whole image results in the observed radial increase of the PSF fitting residuals (see Sect. 3.2.2). The centroiding accuracy is therefore expected to decrease towards larger radii resulting in a larger astrometric uncertainty. The centre and right panel of Fig. 3.5 exemplify this behaviour by using only stars with a distance of less than or greater than 500 pixel $\hat{=}$ 13.6″ from the centre of the combined images in both epochs, respectively. The decrease in the scatter and magnitude of the astrometric uncertainties at smaller radii is striking. The median of the astrometric uncertainty for $12 < K_s < 18$ mag is 1.46 mas for stars within a radius of 500 pixel, but 2.64 mas for stars outside that radius. Therefore, the further analysis is restricted to stars within a radius of 13.6″ from the centre of the observed field of view for the remainder of this paper. The astrometric uncertainties rise steeply near the detection limit at about 20 mag (see centre panel in Fig. 3.5). For stars fainter than 19 mag, almost no stars exhibit an uncertainty below the median value of stars with intermediate brightness ($14 < K_s < 17$ mag). Stars with a K_s-band magnitude fainter than 19 mag are therefore excluded from the sample. As last selection based on the combined uncertainty, stars fainter than $K_s = 14.3$ mag are removed if their uncertainty is above the sum of the fits of the median and standard deviation derived from the combined uncertainty of all observed stars (see Fig. 3.5). The percentage of rejected stars varies between 0 and 9.4% for the affected magnitude bins and does not show a systematic trend with magnitude, therefore no systematic bias is introduced by this selection. After the above mentioned selections, the two matched catalogues were combined. Stars fainter than

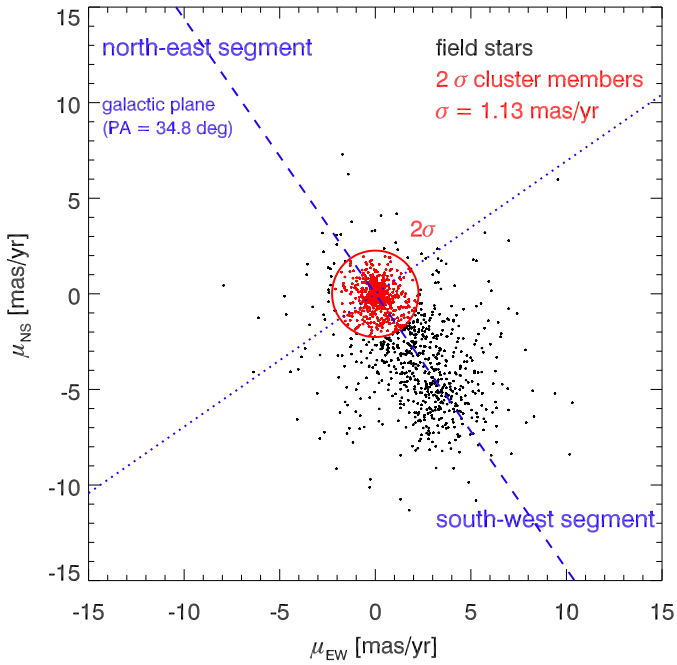

Figure 3.6: Proper motion diagram of stars with $K_s \leq 19$ mag. The dashed line marks the direction parallel to the Galactic plane, the dotted line is oriented vertically with respect to the Galactic plane and splits the proper motion diagram into the north-east and the south-west segment. Stars within a radius of $2\,\sigma$ as derived from the Gaussian fit in Fig. 3.7 (right panel) around the origin are selected as cluster members.

$K_s = 14.3$ mag were taken from the match with the DIT 20.0 s first epoch data, brighter stars originate from the matched catalogue using the dataset from the first epoch with a DIT of 2.0 s. The final K_s-band catalogue contains a total of 1304 stars.

3.4.3 The proper motion diagram

Individual stars are plotted in the proper motion diagram (Fig. 3.6) with proper motions in the east-west-direction on the x- and proper motions in the north-south direction on the y-axis. As the cluster is used as the reference frame, the distribution of cluster members is centred around the origin and overlaps with the elongated distribution of the field stars. The orientation of the field stars is approximately parallel to the plane of the Galaxy (dashed line in Fig. 3.6). The dotted line running through the origin and vertically to the Galactic plane splits the proper motion diagram into two halfs being referred to as the north-east segment (upper half) and the south-west segment (lower half).

Figure 3.7 shows histogram plots of the distribution of the proper motions parallel (left panel) and vertical to the Galactic plane (centre panel). The distribution of proper motions in the direction parallel to the Galactic plane is strongly peaked at the origin, with a very steep decline in the north-west segment, and a slightly broadened decline and overlap with the broad field star distribution in the south-west segment, as expected from Fig. 3.6. The proper motions vertical to the Galactic plane are almost distributed symmetrically with respect to the Galactic plane (centre panel in Fig. 3.7), confirming the assumed orientation of the field star distribution in the proper motion diagram. This and the exposed offset of the field star distribution in the proper motion diagram indicate a movement of the Quintuplet Cluster parallel to the Galactic plane towards the north-east with respect to the field as was found previously for the Arches Cluster (Stolte et al. 2008). The sample of stars with proper

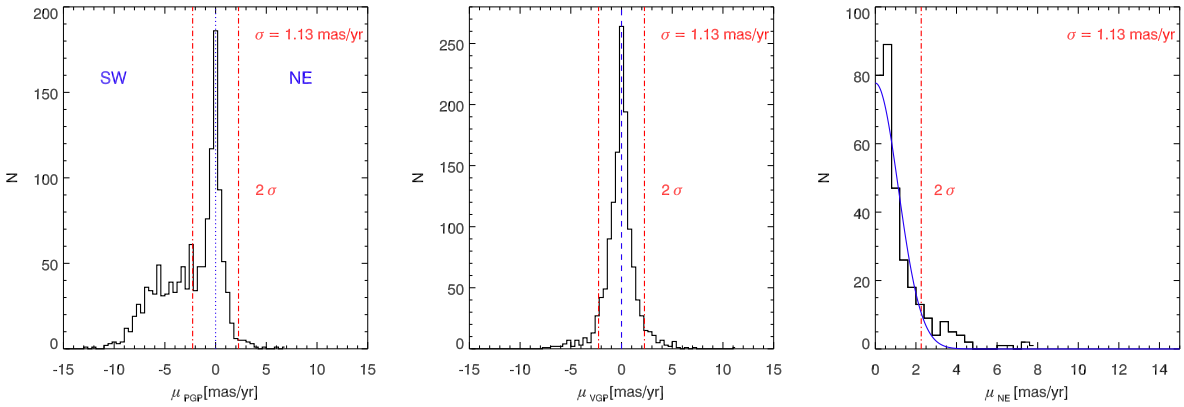

Figure 3.7: *Left panel*: Histogram of proper motions parallel to the Galactic plane. *Middle panel*: Histogram of proper motions vertical to the Galactic plane. *Right panel*: Histogram of the 2-dimensional proper motions located in the north-east-segment of the proper motion diagram. The histogram was fitted with a Gaussian function and a $2\,\sigma$ cut was used as the selection criterion for cluster membership (dash-dotted lines in all three panels).

motions in the north-east segment is least contaminated by field stars and was therefore used to derive the membership criterion. The distribution of proper motions in the north-east segment was fitted with a Gaussian function (right panel in Fig. 3.7). Stars whose proper motions are within a circle of radius $2\,\sigma = 2.26\,\mathrm{mas/yr}$, where σ is the width of the Gaussian fit, are selected as cluster members (see Fig. 3.6). Two of the initial five Quintuplet members (Q1, Q9; Nagata et al. 1990; Okuda et al. 1990) do not fall inside this circle. Their fluxes are exceeding the linearity limits by a factor of 8-30, such that their positions are not well determined. Note that this only affects the very brightest sources, for which spectroscopic member identification is available (Figer et al. 1999b; Liermann et al. 2009). These two stars were added manually to the sample of proper motion members.

3.5 Colour-magnitude diagrams

The K_s source catalogues of proper motion members and non-members were matched with the source catalogue of the first epoch H-band data. The corresponding colour-magnitude diagrams (CMD) are shown in Fig. 3.8 and use only magnitudes in H and K_s from the first epoch to avoid additional scatter being introduced by variable stars. Stars whose fluxes exceed the respective linearity limit in either H and/or K_s at $H = 12.05\,\mathrm{mag}$ and $K_s = 11.25\,\mathrm{mag}$ are marked with crosses. All 1221 stars (member and non-members) with measured proper motion and $(H - K_s)$ colour are included in the final source catalogue (see Table 3.4).

Cluster and field stars separate well as can be seen by characteristic features of the field population (right panel), that are absent in the cluster selection (left panel). For example an elongated overdensity is observed, which starts at about $H = 17\,\mathrm{mag}$, $H - K_s = 1.8\,\mathrm{mag}$ and extends to redder colours along the reddening path adopting the extinction law by Nishiyama et al. (2009). It is consistent with arising from red clump stars located in the Galactic bulge. Assuming the intrinsic K-band magnitude for red clump stars of $K = -1.61\,\mathrm{mag}$ by Alves (2000), the assumed intrinsic colour of $H - K_s = 0.07$ of Nishiyama et al. (2006), a distance to the Galactic centre of 8 kpc (Ghez et al. 2008) and an approximate extinction of $A_{K_s} = 2.35\,\mathrm{mag}$, which is also appropriate for the cluster MS (see Sect. 3.6), yields $H_{RC} = 17.05\,\mathrm{mag}$ and $(H - K_s)_{RC} = 1.79\,\mathrm{mag}$.

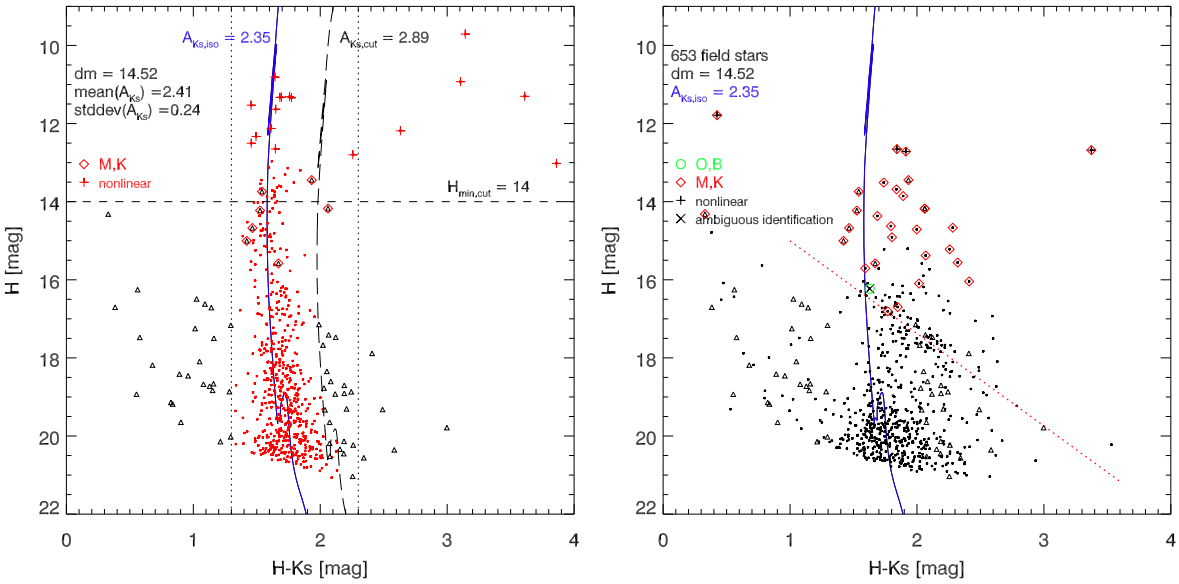

Figure 3.8: *Left panel*: Colour-magnitude diagram of cluster member candidates on the basis of their proper motions. A 4 Myr isochrone with solar metallicity, combined using a Padova MS-isochrone and a Pisa-FRANEC PMS-isochrone, shifted to a distance of 8 kpc and a foreground extinction of $A_{K_s} = 2.35$ mag, is shown for reference. Stars, with fluxes exceeding the linearity limit of the detector are drawn as crosses in all figures throughout this paper. A two-step colour-cut was applied for stars with $H > 14$ mag to remove field stars with similar proper motions as the cluster from the cluster sample (see Sect. 3.5 for details). The vertical short-dashed lines mark the first colour-cut, while in the second step of the colour-cut highly reddened objects to the right of the second isochrone ($A_{K_s} = 2.89$ mag, long-dashed line) are removed. The dots represent the sample of cluster stars after the colour-cut, stars rejected based on their colour are drawn as triangles. Spectroscopically identified field supergiants from the LHO catalogue (Liermann et al. 2009) are marked with diamonds and are removed from the final cluster sample. *Right panel*: Colour-magnitude diagram of stars classified as belonging to the field according to their proper motion (dots) and of stars removed from the member sample based on their colour or known spectral type (triangles). One star, classified as belonging to the field by its proper motion, has an O-star as (ambiguous) counterpart in the LHO catalogue (see Sect. 3.5) and is marked with a circle. The tilted dotted line is the line of reddening according to the extinction law by Nishiyama et al. (2009) running through the population of red clump stars from the Galactic bulge.

Several blue foreground stars with colours $H - K_s \leq 1.3$ mag are seen to the left of the cluster member sequence (Fig. 3.8, left panel). These sources are likely disc main sequence stars following the differential rotation of the outer Milky Way rotation curve. With expected velocities of ~ 200 km/s, they cannot be distinguished from the cluster population on the basis of their proper motion alone. Furthermore a few very red objects, which could be non-members by comparison with the field CMD, remain in the proper motion sample. In order to remove these contaminants a two-step colour-cut was applied to stars fainter than $H = 14$ mag. First the blue foreground and red background stars were removed by keeping only stars with $1.3 \leq H - K_s \leq 2.3$ mag. In a second step the individual extinction of the remaining stars fainter than $H = 14$ mag was determined from the intersections of the lines of reddening with a 4 Myr isochrone assuming a distance to the cluster of 8 kpc. The method to derive the individual extinction and the used isochrone are explained in detail in Sect. 3.6. The isochrone was shifted to an extinction of $A_{K_s} = 2.89$ mag, corresponding to the sum of the mean ($\overline{A_{K_s}} = 2.41$ mag) and twice the standard deviation ($\sigma_{A_{K_s}} = 0.24$ mag) of the individual extinctions of the cluster members remaining after the first colour-cut, and stars redder than the shifted isochrone were also removed

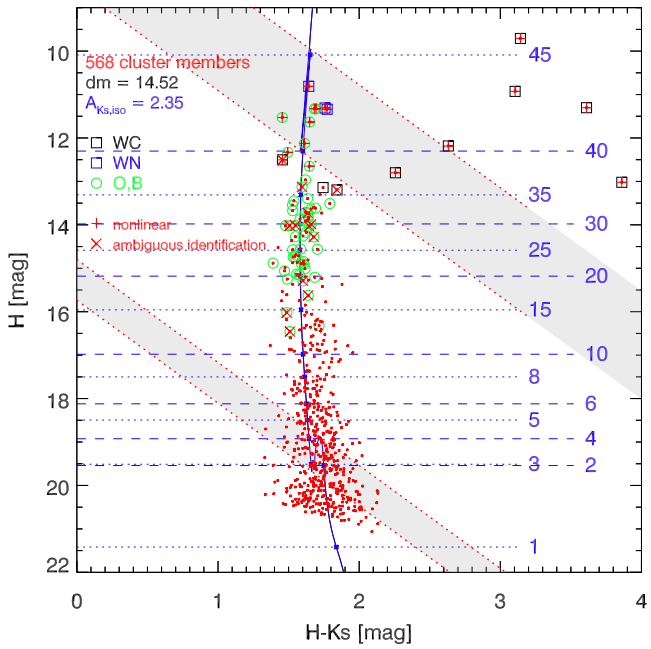

Figure 3.9: Colour-magnitude diagram of the final cluster sample. Stars with counterparts in the LHO catalogue are flagged with symbols according to their spectral type (box: WR-stars, circle: OB-stars, stars with ambiguous identification are additionally marked with an X-cross). The horizontal dashed and short-dashed lines mark the initial masses along the isochrone in units of $M_{\odot}$. The tilted dotted lines show the lines of reddening according to the extinction law by Nishiyama et al. (2009) and enframe the two regions in the CMD (shaded in grey in Fig. 3.9, 3.10 and 3.11), within which the isochrone has multiple intersections with the line of reddening, and consequently no unique mass can be inferred for a given star.

from the sample of cluster stars.

The designated cluster members and non-members were compared with the K-band spectral catalogue of Liermann et al. (2009; further abbreviated as LHO catalogue) for a spectral classification of the brighter stars and in order to assess the selection of cluster stars based on their proper motions and colours. Only observed stars with a K_s-band magnitude brighter than 15.5 mag, which is about 1 mag fainter than the faintest star in the LHO catalogue, were included in the comparison. Eighty-five stars from the spectral catalogue could be assigned to 92 observed stars (69 members, 23 field stars). The ambiguous assignments of 6 stars from the LHO catalogue to 13 observed stars (all members) are caused by the lower spatial resolution of the SINFONI-SPIFFI instrument of 0.250″ for the used 8″ × 8″ field of view. The spectral classification for the matched stars is indicated in a simplified form by the overplotted symbols in Fig. 3.8, Fig. 3.9 and Fig. 3.10. Stars with ambiguous assignments are additionally marked with an X-cross. One star (LHO 110) was re-classified in Liermann et al. (2010) from O6-8 I f to WN9h and is treated accordingly in the figures. The numbers and spectral classifications from the LHO catalogue are noted in the source catalogue (Table 3.4). Six late-type M,K supergiants are still contained within the cluster sample after the colour-cut and are very likely remaining contaminants with motions similar to the cluster members from the Galactic bulge considering the young age of the cluster. These stars and stars rejected by the colour-cut were removed from the final cluster sample and added to the proper motion non-members in the field star CMD (plotted as triangles in the right panel of Fig. 3.8). The one early-type star (O4-7 I f) among the designated field stars is located at the edge of the analysed area of the data and very close to a

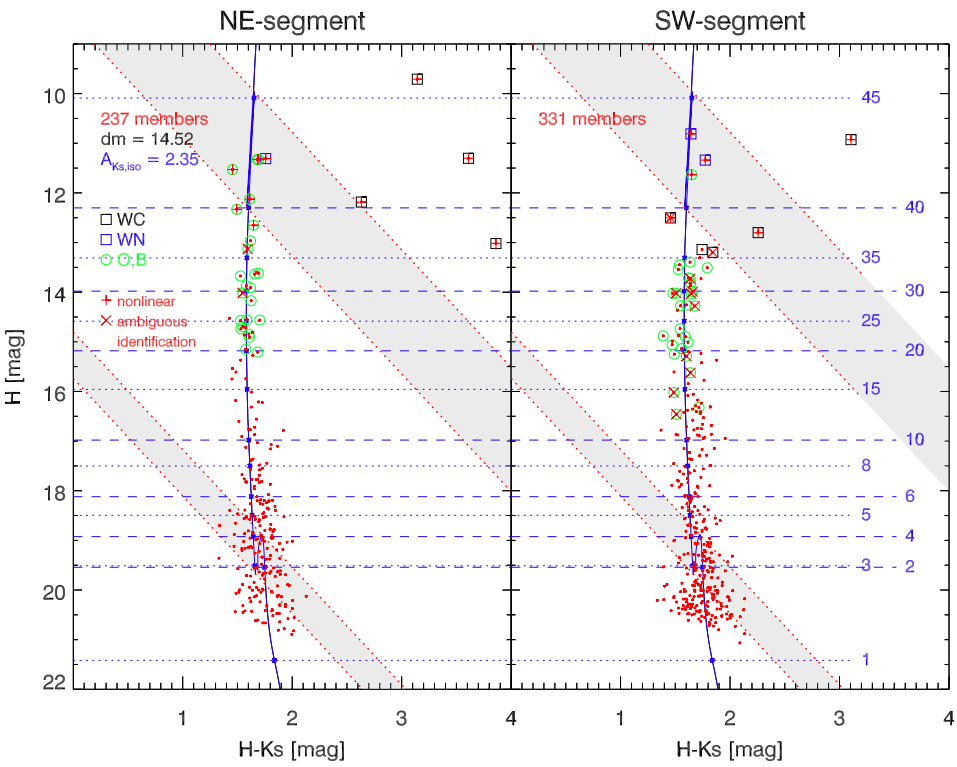

Figure 3.10: Colour-magnitude diagram of all stars of the final cluster sample with proper motions residing in the north-east (*left panel*) or south-west segment (*right panel*) of the proper motion diagram (Fig. 3.6). See Figs. 3.8 and 3.9 for details.

second star just outside this region. It is therefore unclear if the spectral classification really belongs to this star or its neighbour, hence the star was not added to the final cluster sample. For 12 of the 62 stars in the LHO catalogue, which could be assigned to designated cluster members, the sources in our catalogue exceed the K_s-band linearity limit by more than 1 mag. This impedes the repair of the core by *starfinder* and the correct measurement of the position and proper motion. Disregarding these 12 stars, the percentage of contaminating M,K supergiants, which cannot be discerned from the cluster members based on their proper motion or colour, amounts to $6/(62-12) = 12\%$. Even after the removal of the 6 M,K supergiants some field stars may still remain in the final cluster sample, as only down to about $H = 15.5$ mag most stars have a counterpart in the LHO catalogue. The number of these contaminants is estimated in Appendix B.

The CMD of the final sample of cluster stars is shown in Fig. 3.9 and, separated into the north-east and south-west segment of the proper motion diagram, in Fig. 3.10. The slight overdensity located at $H - K_s = 1.8$ mag, $H = 17$ mag indicates a remaining contamination with red clump stars, which is more pronounced for stars with proper motion in the south-west segment. The CMD for the south-west segment contains 94 stars more than for the north-east segment mainly at the faint end of the observed population, which appears slightly broadened. This is expected from the proper motion diagram as the field star population overlaps with the cluster stars in the south-west segment causing a larger contamination for this segment. The astrometric uncertainty and therefore the scatter in the proper motion diagram increases for fainter magnitudes and therefore the confusion with faint field stars is more severe. The cluster members in the north-east segment therefore constitute the cleanest

sample.

3.6 Mass derivation

Based on the presence of WC stars, O I stars and a red supergiant within the Quintuplet cluster, Figer et al. (1999b) derived an average age of 4 ± 1 Myr assuming a coeval population. More recently the ages of 5 WN stars were determined by comparison of their luminosities and effective temperatures as derived from spectral line fitting with stellar evolution models to be about 2.4 – 3.6 Myr pointing to a somewhat younger age of the cluster (Liermann et al. 2010). To study the influence of the assumed cluster age on the slope of the mass function, three isochrones with ages of 3, 4 and 5 Myr were used to derive the initial stellar masses. The isochrones are a combination of Padova main sequence (MS) isochrones and pre-main sequence (PMS) isochrones derived from Pisa-FRANEC PMS stellar models (see Gennaro et al. 2011; Marigo et al. 2008; Degl'Innocenti et al. 2008). As the NACO photometry is calibrated by means of UKIDSS sources (see Sect. 3.2.3), the combined isochrones, for simplicity referred to as 3, 4 and 5 Myr Padova isochrones in the following, were transformed from the 2MASS into the UKIDSS photometric system using the colour equations from Hodgkin et al. (2009, Eqs. 6 - 8). To cover the effect of a different set of stellar models on the derived masses, a 4 Myr Geneva MS isochrone with enhanced mass loss for high mass stars, $M > 15\,M_{\odot}$, (Lejeune & Schaerer 2001) was included in the comparison. The conversion of this isochrone into the UKIDSS filter system encompassed two steps. The isochrone was first transformed from the Bessell & Brett (1988) to the 2MASS photometric system using the updated[2] transformation by Carpenter (2001) and subsequently from the 2MASS to the UKIDSS filter system using the above mentioned conversion.

For all isochrones, solar metallicity according to the description of the underlying stellar models[3] was assumed, and a distance to the Galactic centre of 8.0 kpc (Ghez et al. 2008) was applied as the distance to the Quintuplet cluster. The four isochrones shown in Fig. 3.11 were reddened by a foreground extinction of $A_{K_s} = 2.35$ mag using the extinction law of Nishiyama et al. (2009) ($A_H : A_{K_s} = 1.73 : 1$) to match the observed MS of the cluster members. This extinction law is one of the most recent determinations of the extinction in the near-infrared along the line of sight towards the Galactic centre and consistent with other current findings, e.g., by Straižys & Laugalys (2008) or Schödel et al. (2010).

The individual mass and extinction of each star in the final cluster sample was determined from the intersection of the line of reddening through the star with the respective isochrone in the CMD. Due to the local maximum of the PMS at the low-mass end as well as the extended loop at the transition from the end of the hydrogen core burning to the contraction phase at the high-mass end, the de-reddening path of a star may have several intersections with the isochrone, thus leading to an ambiguous mass assignment (the affected areas in the colour-magnitude plane are shaded in grey in Figs. 3.9, 3.10 and 3.11). For these stars, the masses at each intersection were averaged. The post-MS phase after the exhaustion of hydrogen in the stellar core is very rapid (a few 10^3 yr according to the stellar models) and apparent in the isochrones as the branch with increasing H-band brightnesses, re-rising after the decline connected to the contraction phase. Due to its short duration, which causes the Hertzsprung gap in the Hertzsprung-Russel diagrams of stellar clusters, only the two intersection points with the upper part of the MS and with the subsequent falling branch of the isochrone were averaged. Two

[2] Carpenter, J.M., 2003 see `http://www.astro.caltech.edu/~jmc/2mass/v3/transformations/`

[3] solar metallicity for the Geneva isochrone: X = 0.68, Y = 0.3, $Z = 0.020$ (Lejeune & Schaerer 2001);
solar metallicity for the Padova isochrones: X = 0.708, Y = 0.273, $Z = 0.019$ for $M < 7\,M_{\odot}$ (Marigo et al. 2008; Girardi et al. 2000), X = 0.7, Y = 0.28, $Z = 0.020$ for $M > 7\,M_{\odot}$ (Bertelli et al. 1994; Bressan et al. 1993)

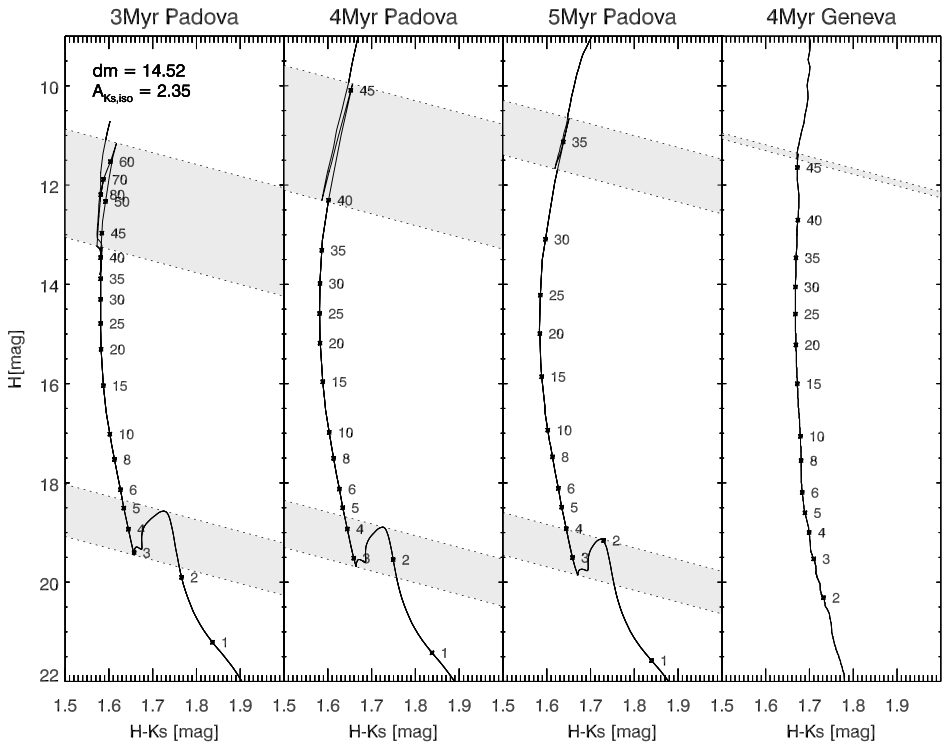

Figure 3.11: Comparison of the four isochrones used to determine stellar masses. For all shown isochrones, solar metallicity, a distance to the cluster of 8 kpc and a foreground extinction of $A_{K_s} = 2.35$ mag is adopted. As in Fig. 3.9 and Fig. 3.10, the dotted lines enframe regions in the CMD with ambiguous mass assignments (shaded in grey) and the initial masses are labelled along the isochrones.

O stars from the LHO catalogue have no intersection with the Geneva isochrone on the MS or the falling branch, therefore an initial mass of 47.3 $M_{\odot}$, which is the maximum mass along this isochrone used for the mass determination (see Table 3.3), was assigned to them.

11 Wolf-Rayet stars out of the 21 observed in the Quintuplet Cluster are contained within our sample of cluster members. The masses for these stars could not be determined from the isochrones but the mass range of Wolf-Rayet stars was inferred from the underlying stellar models by Bressan et al. (1993) for the Padova isochrones and by Meynet et al. (1994) and Schaller et al. (1992) for the Geneva isochrone (see Table 3.3).

Considering only stars above the PMS/MS transition region, the individual extinction A_{K_s} of each star as inferred from the 3, 4 and 5 Myr Padova isochrones agrees within ±0.02 mag (±0.005 mag for $5.5 < \mathrm{m} < 30\,M_{\odot}$). Using the 4 Myr Geneva isochrone yields systematically smaller values of the individual extinction by 0.08 – 0.12 mag. The individual extinction value denoted in the final source catalogue (Table 3.4) refers to the 4 Myr Padova isochrone.

3.7 Mass functions

In order to avoid potential biases introduced by bins with a very small number of objects or large differences in the number of stars between the low- and high-mass bins, we adopted the method proposed by Maíz Apellániz & Úbeda (2005). Here, the widths of the different bins are adjusted such that each bin houses approximately the same number of stars (Method A). If the number of stars in

Table 3.3: Summary of isochrone properties relevant for the mass derivation.

Isochrone name	Description	Wolf-Rayet mass	Stars with ambiguous mass assignments			
			PMS → MS		MS → post-MS	
			Mass range	No. of stars	Mass range	No. of stars
		($M_\odot$)	($M_\odot$)		($M_\odot$)	
3 Myr Padova	MS[a] + PMS[b]	85 – 100	2.1 – 5.5	150	42.3 – 84.4	11
4 Myr Padova	MS[a] + PMS[b]	51 – 65	1.9 – 4.6	146	39.9 – 50.8	5
5 Myr Padova	MS[a] + PMS[b]	37 – 40	1.8 – 4.0	146	33.5 – 35.4	3
4 Myr Geneva	MS[c]	48 – 60			45.8 – 47.3	0

Notes. [(a)] Padova isochrone with solar metallicity for $m > 4\,M_\odot$ (Marigo et al. 2008). [(b)] Pre-main sequence parts of the isochrones ($m \leq 4\,M_\odot$) are derived from Pisa-FRANEC PMS stellar models (Degl'Innocenti et al. 2008, see Gennaro et al. 2011 for the combination with the Padova isochrones). [(c)] Geneva isochrone with solar metallicity and enhanced mass loss for high mass stars, $M > 15\,M_\odot$, (Lejeune & Schaerer 2001).

the sample did not split up evenly for the chosen number of bins, the bins to contain one additional star from the remaining stars were chosen randomly. The stars were then sorted according to their masses and distributed among the bins. For each isochrone the mass function (MF) and slope were determined for dividing the cluster sample into 4, 8, 12, 16 and 20 bins. The boundary between two adjacent bins was set to the mean of the most/least massive star in the respective bins. The minimum mass used for each mass function was set to the lowest mass of a star with a unique mass assignment for the respective isochrone, i.e. lying above the ambiguity region caused by the PMS/MS transition. Stars with ambiguous mass assignments at the upper end of the MS were kept for the mass function, as due to their small number they all contribute to the uppermost bin in the mass function. The upper mass limit or uppermost bin boundary $m_{\rm up}$ was calculated from the data to be (see Maíz Apellániz & Úbeda 2005)

$$m_{\rm up} = m_n + 0.5\,(m_n - m_{n-1})\ , \tag{3.4}$$

with n being the total number of stars. The number of stars in each bin n_i was normalized by the respective bin width Δm_i. The logarithm of the normalized number of stars per bin as a function of the logarithm of the medium mass of each bin was fitted with a straight line using the IDL routine *LINFIT*, which performs a χ^2 minimisation.

The uncertainty of the number of stars per bin Δn_i is derived by Maíz Apellániz & Úbeda (2005) from the standard error of a binomial distribution $(n p_i\,(1 - p_i))^{1/2}$, where the unknown true probability for a star to reside in the $i^{\rm th}$ bin p_i is approximated by the measured value n_i/n:

$$\Delta n_i = \sqrt{\frac{n_i\,(n - n_i)}{n}}\ . \tag{3.5}$$

Note that this uncertainty differs from the Poisson error $\sqrt{n_i}$, which is usually applied to binned data. For the linear fit each bin was weighted by its statistical weight $w_i = 1/{\Delta n_i}^2$. The statistical weight w_i assigned to the logarithm of the normalized number of stars per bin $(\log_{10}(n_i/\Delta m_i))$ follows from error propagation of Δn_i in the logarithmic plane (see Eq. 7 in Maíz Apellániz & Úbeda 2005):

$$w_i = \frac{n\,n_i\,2\ln 10}{n - n_i}\ . \tag{3.6}$$

It is basically the same for every bin as the number of stars per bin varies by a maximum of one.

Table 3.4: Catalogue of stellar sources with measured proper motions and colours in the Quintuplet cluster.

No.	ΔR.A.[a] (″)	ΔDecl.[a] (″)	K_s (mag)	σ_{K_s} (mag)	H (mag)	σ_H (mag)	A_{K_s}[b] (mag)	Compl.[c]	$\mu_{\alpha\cos(\delta)}$ (mas/yr)	μ_δ (mas/yr)	$\sigma_{\mu_{\alpha\cos(\delta)}}$[d] (mas/yr)	σ_{μ_δ}[d] (mas/yr)	σ_μ[d] (mas/yr)	Seg.[e]	LHO No.[f]	Type[f]	Member[g]	$m_{\mathrm{Pad,3\,Myr}}$[h] ($M_\odot$)	$m_{\mathrm{Pad,4\,Myr}}$[h] ($M_\odot$)	$m_{\mathrm{Pad,5\,Myr}}$[h] ($M_\odot$)	$m_{\mathrm{Gen,4\,Myr}}$[h] ($M_\odot$)
1	-7.58	3.99	7.69	0.08	11.30	0.04	-	1.00	-2.30	0.91	0.93	0.95	0.98	NE	75	WC9?d	y	85-100	51-65	37-40	48-60
2	-5.16	9.25	9.16	0.08	13.02	0.03	-	1.00	-2.13	-0.87	0.25	0.49	0.44	NE	102	WC9?d	y	85-100	51-65	37-40	48-60
3	-0.00	0.00	6.57	0.06	9.71	0.03	-	1.00	-2.09	0.25	0.93	0.95	0.98	NE	42	WC9d + OB	y	85-100	51-65	37-40	48-60
4	1.09	6.45	7.82	0.06	10.93	0.02	-	1.00	0.93	0.54	0.93	0.96	0.98	SW	84	WC9d	y	85-100	51-65	37-40	48-60
5	5.35	3.70	9.17	0.05	10.81	0.02	2.36	1.00	-0.59	-1.21	0.22	0.30	0.37	SW	71	WN9	y	85-100	51-65	37-40	48-60
6	16.21	3.04	9.55	0.12	11.31	0.10	2.53	1.00	-1.21	0.52	0.82	0.84	0.86	NE	67	WN9	y	85-100	51-65	37-40	48-60
7	9.04	6.26	9.55	0.04	12.18	0.02	-	1.00	-0.38	1.13	0.23	0.29	0.37	NE	79	WC9d	y	85-100	51-65	37-40	48-60
8	5.06	11.40	9.57	0.05	11.34	0.05	2.55	1.00	0.59	-0.30	0.80	0.33	0.55	SW	110	WN9h	y	85-100	51-65	37-40	48-60
9	6.08	9.30	9.65	0.05	11.33	0.03	2.43	1.00	-0.47	0.29	0.23	0.38	0.40	NE	100	O6-8 I f e	y	56.38	46.05	34.53	47.28
10	5.65	8.24	9.63	0.05	11.33	0.03	2.45	1.00	0.50	0.50	0.23	0.30	0.37	NE	96	O6-8 I f e	y	56.30	46.00	34.50	47.28

Notes. This table is available in its entirety in a machine-readable form at the CDS via anonymous ftp to `cdsarc.u-strasbg.fr` (`130.79.128.5`) or via `http://cdsweb.u-strasbg.fr/cgi-bin/A+A/540/A57`. A portion is shown here for guidance regarding its form and content.

[a] Positional offset in right ascension and declination relative to the AO guide star Q2 (R.A. = 17:46:14.690, Dec. = -28:49:40.71 [J2000]). [b] Individual extinction of each star as derived using the 4 Myr Padova isochrone. [c] The combined completeness for each star is the product of its completeness in the K_s-band datasets of both epochs (2003 and 2008) and in the H-band dataset from 2003. [d] See Appendix A for details of the error determination. [e] Indicates the segment in the proper motion diagram in which the star resides. [f] Numbers and spectral identifications from the spectral catalogue by Liermann et al. (2009). Sources in the LHO catalogue which have more than one counterpart in this table are marked with an asterisk. [g] Cluster membership: cluster members are indicated by ”y”, field stars according to their measured proper motions are indicated by ”n”. Proper motion members rejected based on their spectral type (M,K supergiants) or their colour are marked with ’n st’ or ’n cc’, respectively. [h] Initial masses as determined from the 3, 4, 5 Myr Padova isochrones (with PMS part derived from Pisa-FRANEC PMS stellar models, see Gennaro et al. 2011) and the 4 Myr Geneva isochrone. All isochrones assume solar metallicity. For Wolf-Rayet stars the stated mass ranges are inferred from the underlying stellar models of the respective isochrone.

Besides the binning method just described, the mass function was also determined using an equal logarithmic width for each bin (Method B), which is still the most common binning method for deriving mass function slopes (see Maíz Apellániz & Úbeda 2005 for a discussion of the biases of this method). The lower and upper mass limits were determined in exactly the same way as above and the logarithmic bin widths were set by dividing the so defined mass range into 4, 8, 12, 16 and 20 bins. The weights applied to each bin were again calculated with Eq. (3.6) and are decreasing going to higher masses due to the lower number of stars contained in the high mass bins. In order to study the influence of the weights on the slope for this binning method, the slope was derived from a linear fit to the MF with and without weighting.

The reported slopes of the mass function α refer to a power-law distribution in linear units ($dn/dm \propto m^{\alpha}$) with the standard Salpeter slope being $\alpha = -2.35$ in this notation (Salpeter 1955). If not mentioned otherwise, the mass function and its slope were determined using all cluster members from both the north-east and south-west segment (see Fig. 3.10) and distributing the stars into bins with (almost) constant number of stars (Method A). All shown linear fits to the respective mass functions were derived from the completeness corrected mass function using for each star its individual completeness correction (see Sect. 3.3).

The minimum mass of a star with unique mass assignment was 5.5, 4.6 and 4.0 $M_{\odot}$ for the 3, 4 and 5 Myr Padova isochrone, respectively. The minimum mass for the 4 Myr Geneva isochrone was set to 4.5 $M_{\odot}$ in order to use exactly the same stars as for the Padova isochrone of the same age. As mentioned in Sect. 3.6, it was not possible to infer the individual masses of the WR stars from the isochrones. Therefore, a constant mass within the mass ranges of the Wolf-Rayet stars deduced from the stellar models (see Table 3.3) was assigned to each identified Wolf-Rayet star in the cluster sample in dependence of the assumed cluster age. The uppermost bin boundary, calculated with Eq. (3.4), is then identical to the assigned WR mass. The chosen WR mass has a significant impact on the derived slopes due to the fairly large mass range of the Wolf-Rayet stars for cluster ages of 3 and 4 Myr. A larger assigned WR mass biases the mass function to a steeper slope due to the normalization of n_i by the bin width Δm_i. The maximum difference between the slopes using the minimum and maximum WR masses for each of the isochrones was 0.21, which is about twice the typical formal fitting error of the slope. To avoid the described bias, the Wolf-Rayet stars were not included in the mass function. After the exclusion of the Wolf-Rayet stars, the uppermost bin boundary is determined by the two most massive stars in the respective sample (see Eq. 3.4).

In order to quantify the effect of the random selection of bins to contain one additional star from the remainder of the division of the total number of stars by the number of bins (Method A), the distribution process and the fit to the resulting MF was repeated 1000 times. The reported slopes for this binning method are the mean slope of all these repetitions. The maximum difference between the slopes of the same MF due to different random distributions of the surplus stars was 0.03, which is very small compared to the formal fitting errors.

The slope of the mass function of each isochrone was determined using 4, 8, 12, 16 and 20 bins. Using only 4 bins results in slopes being systematically shallower than for the other numbers of bins by up to 0.10. The choice of 20 bins introduces a bias in the case of the 3 Myr isochrone. Due to the large number of massive stars with averaged masses for this isochrone (see Table 3.3), these stars fill up the uppermost bin completely. The mass range of stars with averaged masses is compressed, which in turn leads to a decreased binwidth of the last bin. As the number of stars is normalized by the bin width, the normalized number of stars in the last bin is increased leading to a flatter slope. The most reliable mass function slopes are therefore obtained using 8, 12 or 16 bins. The maximum difference of the obtained slopes for a given isochrone between these three bin numbers was 0.03. Given this

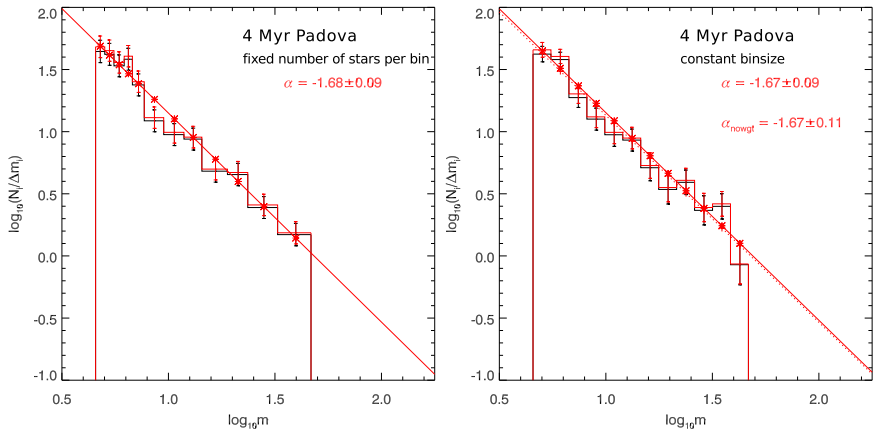

Figure 3.12: Comparison of the mass function and derived slopes for different methods of binning the data and performing the linear fit. Only the fit and derived slope for the completeness corrected mass function are shown. *Left panel*: Mass function of the Quintuplet cluster with initial masses derived from the 4 Myr Padova isochrone. Only stars with $m > 4.6\,M_{\odot}$, i.e. stars above the ambiguity region in the CMD due to the PMS, are used. Wolf-Rayet stars are not included in the mass function, as the large uncertainty of their mass might bias the derived slopes. The bin sizes are adjusted such that each of the 12 bins holds approximately the same number of stars. *Right Panel*: Mass function of the same data but distributing the stars into 12 bins of a uniform logarithmic width of 0.084 dex adopting the same lower and upper mass limits as in the left panel. The solid line shows the weighted linear fit, the dotted line the unweighted fit.

negligible influence of the bin number, all results presented in the following are determined using 12 bins (see also Table 3.5).

Figure 3.12 shows the comparison of the mass functions and the derived slopes for distributing the data in bins with (almost) constant number of stars (Method A, left panel) and for using bins of equal logarithmic width of $\Delta \log_{10} m = 0.084$ dex (Method B, right panel) for the 4 Myr Padova isochrone. In the shown example and in general the three slopes of the weighted fit to the mass function derived with a uniform number of stars per bin and the weighted and unweighted fit to the mass function with an equal logarithmic bin width agree well within the errors, if the full sample of stars is fitted. The use of a constant logarithmic bin size with applied weights following the prescription of Maíz Apellániz & Úbeda (2005) generates consistent results compared to the use of bins with variable widths and equal numbers of stars also if only stars from the north-east or south-west segment of the proper motion diagram are included in the mass function. In contrast, the unweighted fit responds much more sensitively to fluctuations of the number of stars in the higher mass bins, especially if the last bin included in the fit is depleted, which is the case for the south-west segment. For the remainder of this paper only the results determined from mass functions with an equal number of stars per bin are considered.

The first row in Fig. 3.13 shows the mass function for the 4 Myr Padova isochrone for all cluster members (left panel), for stars in the north-east-segment (centre panel), and for stars in the south-west segment (right panel). All three slopes agree well, although a lack of stars in the mass function of the north-east segment in the mass range of $11 - 22\,M_{\odot}$ compared to the south-west segment is evident. This surplus of stars for the south-west segment is also apparent in the CMD (Fig. 3.10) and could indicate a remaining contamination with red clump stars. Further contaminations suggested by the difference in the number of cluster members in the north-east and south-west segment are likely removed by only using stars with intermediate brightness and masses above $4.6\,M_{\odot}$.

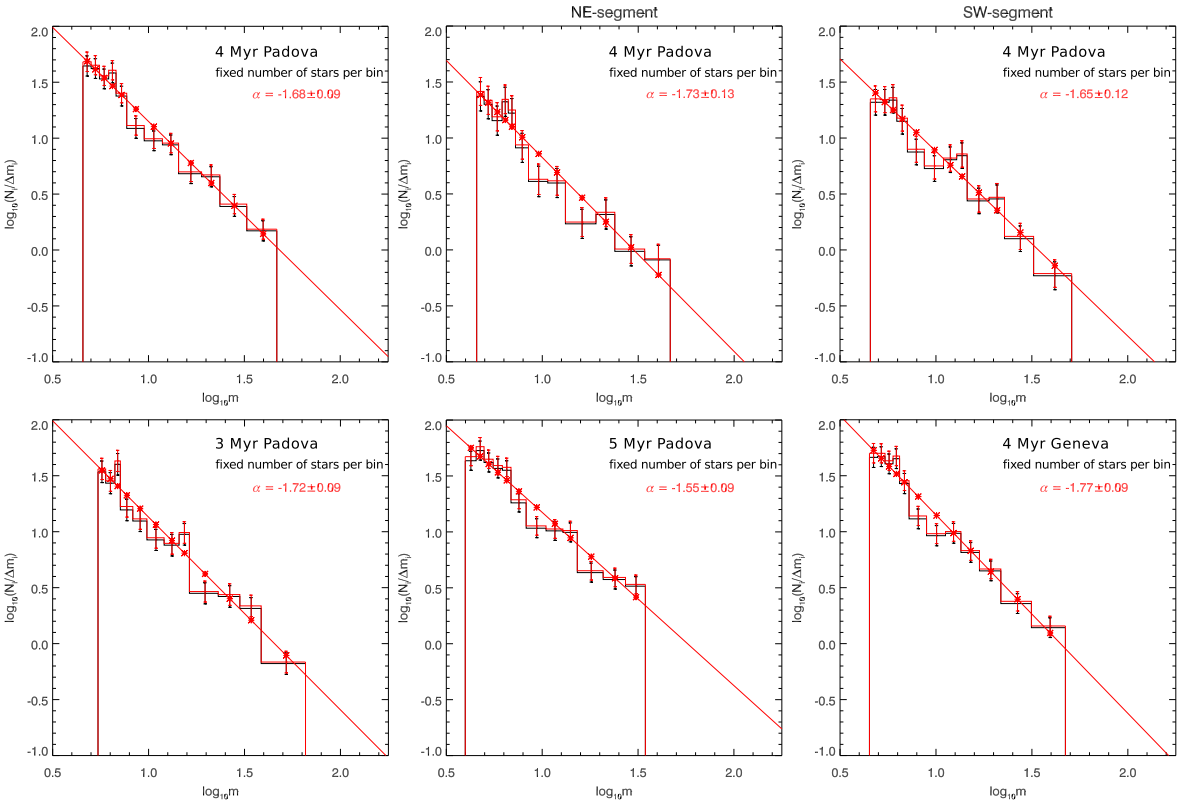

Figure 3.13: *Upper panels*: Mass functions for the 4 Myr MS-Padova isochrone using all stars (*left*), or only stars located in the north-east- (*middle*), or south-west-segment (*right*) of the proper motion diagram (Fig. 3.6) *Lower panels*: Resulting mass function if stellar masses are derived from a 3 or 5 Myr Padova MS-isochrone (*left* and *middle*) or 4 Myr Geneva isochrone (*right*). For all shown mass functions the stars were distributed in 12 bins of variable width with equal numbers of stars per bin. As in Fig. 3.12, the Wolf-Rayet stars were removed and only stars above the ambiguity region in the CMD due to the PMS are included. The resulting minimum masses are 5.5, 4.6, 4.0, and 4.5 $M_{\odot}$, for the 3, 4, 5 Myr Padova and the 4 Myr Geneva isochrone, respectively.

For the Padova isochrones the slope of the mass function decreases with increasing age going from 3 to 5 Myr from (-1.72 ± 0.09) to (-1.55 ± 0.09). As can be seen in Fig. 3.11, the range of initial masses along the upper part of the MS starting at about 20 $M_{\odot}$ strongly decreases with age. This causes the same number of brighter stars in the CMD being squeezed into a smaller mass interval for the older ages, which therefore results in a flattening of the slopes with increasing age. The initial masses derived using the 4 Myr Padova isochrone are 0% – 7% larger for stars with $m < 37\ M_{\odot}$ than the initial masses determined with the 4 Myr Geneva isochrone. For stars with even higher masses the Geneva isochrone yields slightly larger masses. This varying difference in the deduced masses causes the slope derived from the Geneva isochrone to be steeper by 0.09 in comparison with the Padova isochrone of the same age. Nonetheless, the two derived slopes agree within the fitting uncertainties.

All slopes derived binning the data into 12 bins containing approximately the same number of stars per bin are summarized in Table 3.5. The slopes are all internally consistent: 1.) For each isochrone the slope derived for the south-west segment is flatter than the slope for the north-east segment, and the slope of the full sample is very close to the average of the slopes of both segments. 2.) Independent of

Table 3.5: Overview of derived slopes of the mass function binning the data into 12 bins containing approximately the same number of stars.

Isochrone name	Segment[a]	No. of stars	n_i[b]	$m_{\rm min}$ ($M_\odot$)	$m_{\rm max}$ ($M_\odot$)	α [c]	$\Delta\alpha_{\rm fit}$[d]	$\Delta\alpha_{\rm binning}$[e]
3 Myr Padova	NE + SW	220	18 – 19	5.5	65.8	−1.72	0.09	0.03
4 Myr Padova	NE + SW	261	21 – 22	4.6	46.7	−1.68	0.09	0.01
5 Myr Padova	NE + SW	289	24 – 25	4.0	34.5	−1.55	0.09	0.01
4 Myr Geneva	NE + SW	261	21 – 22	4.5	47.3	−1.77	0.09	0.01
3 Myr Padova	NE	99	8 – 9	5.5	65.8	−1.76	0.13	0.07
4 Myr Padova	NE	119	9 – 10	4.6	46.5	−1.73	0.13	0.02
5 Myr Padova	NE	132	11	4.0	34.5	−1.63	0.13	0.00
4 Myr Geneva	NE	119	9 – 10	4.5	47.3	−1.82	0.13	0.03
3 Myr Padova	SW	121	10 – 11	5.5	65.6	−1.68	0.13	0.01
4 Myr Padova	SW	142	11 – 12	4.6	51.0	−1.65	0.12	0.01
5 Myr Padova	SW	157	13 – 14	4.0	36.2	−1.52	0.12	0.01
4 Myr Geneva	SW	142	11 – 12	4.5	48.1	−1.70	0.12	0.01

Notes. [(a)] Segment in the proper motion diagram (Fig. 3.6). [(b)] Number of stars per bin. [(c)] Average of the slopes derived for 1000 realizations of randomly distributing the remainder of the division of the number of stars by the number of bins into the bins by increasing the number of stars in the selected bin by one. [(d)] Formal uncertainty of the linear fit. [(e)] Maximum difference between the slopes due to the random distribution of the surplus stars.

the sample (NE + SW, NE, SW), the slope of the mass function decreases with the assumed cluster age for the Padova isochrones, and the use of the 4 Myr Geneva isochrone results in a steeper slope than for the 4 Myr Padova isochrone. For the north-east and south-west segment all slopes agree within the formal fitting uncertainties irrespective of the isochrone. For the full sample, the error margins of the slope derived for the 5 Myr Padova isochrone have barely no overlap with the error margins of the 4 Myr Geneva isochrone. The average value of the slopes of all considered isochrones, using the full sample of cluster members, therefore provides a robust estimate for the mass function slope of the Quintuplet cluster. The average slope is −1.68, which is the same value as the slope of the 4 Myr Padova isochrone. The maximum differences between this average and the four regarded slopes are +0.13 and −0.09, respectively, and provide the conservative estimate of the uncertainty of the average slope.

Our best value of the slope of the present-day mass function of the Quintuplet cluster for stars within a radius of 0.5 pc from the cluster centre, an initial mass of $m_{init} > 5\,M_\odot$ and excluding spectroscopically identified Wolf-Rayet stars, is $\alpha = -1.68^{+0.13}_{-0.09}$. It should be noted that we determined the slope using the *initial* masses as inferred from the isochrones. Furthermore, binarity is not accounted for, as we cannot observe a binary sequence in the CMD of the Quintuplet cluster. Therefore, the reported slopes refer to the system mass function. Weidner et al. (2009) performed a numerical study to determine the influence of unresolved multiple systems on the initial mass function. Assuming 100% of the stars being part of multiple systems and using three different pairing methods they find that the difference of the slopes of the single star and the observed system IMF for the high mass stars ($m > 2\,M_\odot$) is normally smaller than the usual error bars of observational slopes. In general, the system IMF tends to be steeper by about 0.1 than the single star IMF. Da Rio et al. (2009) derive a maximum difference between the single star and the system IMF of 0.2 for stars with $m > 1 M_\odot$ by using random pairing and varying the binary fraction between 0 and 1. Non-resolved multiple systems

are therefore unlikely to fabricate the flat MF slope of $\alpha = -1.68$ observed in the Quintuplet cluster within a radius of 0.5 pc compared to the canonical slope of −2.3 (Kroupa 2001).

A residual contamination of field stars in the final cluster sample, that could possibly not be removed on the basis of their proper motions or colours alone, may also bias the reported mass function slopes. In Appendix B the number of contaminating stars remaining in the cluster sample is estimated within six mass bins and its influence on the MF slope is assessed for the 4 Myr Padova isochrone. Depending on the number of residual field stars in each mass bin, the retrieved slopes vary in the range between −1.50 and −1.74. The steepest slope is still well contained within the formal fitting error of the slope derived without accounting for potential residual field stars. Within the errors the slopes stated in Table 3.5 can be regarded as lower (steep) bounds for the true PDMF slope of the Quintuplet cluster.

The total mass of stars in the final cluster sample amounts to 4390 $M_\odot$ adopting the initial masses derived from the 4 Myr Padova isochrone and an average mass of 58 $M_\odot$ for each of the 11 WR stars. Extrapolating the MF ($\alpha = -1.68$) down to a minimum mass of 0.5 $M_\odot$ results in a total mass of the Quintuplet cluster within a radius of 0.5 pc of 6010 $M_\odot$.

3.8 Discussion

All derived slopes of the mass function in the central part of the Quintuplet cluster above a mass of 5 $M_\odot$ are systematically flatter than the canonical slope of the initial mass function of $\alpha = -2.3 \pm 0.7$ for the same mass regime (Kroupa 2001), albeit still marginally contained within its large 99% confidence limits. This indicates that the cluster within a radius of 0.5 pc is depleted of lower mass stars.

This result is not unexpected with respect to findings in other Galactic young massive clusters (see Table 3.6), which reveal signs of mass segregation by steepening slopes of their mass function for larger distances to the cluster centre. The mass function of the young cluster NGC 3603 (age 1 − 2.5 Myr) exhibits a gradually steeper slope for larger annuli from $\alpha = -1.31$ within $R < 0.15$ pc to −1.75 for $0.4 < R < 0.9$ pc (Harayama et al. 2008). Up to a maximum observed distance of 3.3 pc from the assumed cluster centre the slope remains almost constant ranging from −1.80 to −1.86. The global slope of −1.74 for $0.4 < m < 20\ M_\odot$ is well below the canonical IMF slope of −2.3, suggesting a top-heavy IMF for this cluster. Westerlund 1 (Wd 1), with an age of about 3 to 5 Myr, exhibits a flattened MF with $\alpha = -1.6$ for stars in the mass range of $3.4 < m < 27\ M_\odot$ within $R < 0.75$ pc, which successively steepens at larger radii up to $\alpha = -2.7$ for $R > 2.1$ pc (Brandner et al. 2008). These general findings were confirmed in a follow-up paper by Gennaro et al. (2011), which drops the assumption of radial symmetry for the cluster and determines the mass function in a two-dimensional approach. Their global mass function slope is with $\alpha = -2.55^{+0.20}_{-0.08}$ even steeper than the canonical slope. The Arches cluster (age ∼ 2.5 Myr), is located at a projected distance to the Galactic centre of 26 pc, which is almost equal to the projected distance of 30 pc for the Quintuplet cluster. Hence both clusters might have formed in the same environment, albeit at different times, and evolved in the strong tidal field of the Galactic centre. The slope of the mass function of the central part of the Arches cluster was first determined by Figer et al. (1999a) and found to be top-heavy with a slope of $\alpha = -1.65$ for $0.1 < R < 0.35$ pc. Stolte et al. (2002) found a slightly steeper slope of $\alpha = -1.8 \pm 0.2$ within $R < 0.4$ pc. Outside this radius the slope steepens to $\alpha = -2.70 \pm 0.7$, indicating again mass segregation towards the cluster centre. The authors correct for a radial extinction gradient outside of 0.2 pc and use the present-day masses determined from a 2 Myr Geneva isochrone. A more recent study by Espinoza et al. (2009) finds a much steeper slope of -2.1 ± 0.2 for $R < 0.4$ pc consistent with a canonical IMF, but still a flattening towards the cluster core with $\alpha = -1.88 \pm 0.20$ inside of $R = 0.2$ pc. Espinoza et al. (2009) account for differential extinction by individually dereddening the stars and infer initial

Table 3.6: Comparison of mass function slopes in the centres of Galactic young massive clusters.

Cluster name	Age (Myr)	Distance (kpc)	Mass range ($M_\odot$)	R (pc)	α	R (pc)	α	R (pc)	α	References
Quintuplet	3–5	8.0	> 5			< 0.5	$-1.68^{+0.13}_{-0.09}$			this work
Arches	2.5	8.0	> 10	< 0.2	-1.88 ± 0.20	< 0.4	-2.1 ± 0.2			1
NGC 3603	1–2.5	6.0 ± 0.8	4–20	< 0.15	-1.31	0.3–0.4	-1.72			2
Westerlund 1	3–5	3.55 ± 0.17	3.4–27					< 0.75	-1.6	3

References. (1) Espinoza et al. (2009); (2) Harayama et al. (2008); (3) Brandner et al. (2008).

masses instead of present-day masses from a 2.5 Myr Geneva isochrone. Espinoza et al. (2009) have also shown that variations in the MF slope caused by the choice of metallicity and a wider range of cluster ages (2.0 – 3.2 Myr) are smaller than the fitting uncertainties. The steeper slopes are then most likely a consequence of the individual dereddening of each star prior to the stellar mass estimation. This suggests that individual dereddening is one of the most crucial aspects under variable extinction conditions to obtain realistic MF slopes. For the Quintuplet analysis presented above, individual dereddening was taken into account as well, and the initial stellar masses were used to create the MF. In this respect our slopes of the mass function of the Quintuplet cluster should be directly comparable with their results. However, as proper motions were not available, their membership selection is solely based on a strict colour-cut leaving the remaining contamination by field stars unclear. In summary the MF slopes for the inner parts of the Quintuplet cluster, NGC 3603 and Wd 1 are all consistently flatter than the standard IMF slope. The question if the MF of the Quintuplet cluster steepens towards larger distances from the cluster core as for Wd 1 and NGC 3603 requires the measurement of the MF also in the outer parts. The flattening of the slope in the cluster centres may be caused by the internal dynamical evolution of the cluster alone as in the case of Wd 1 and NGC 3603, where the Galactic tidal field is negligible, or by a combination of the internal and the external dynamical evolution in the tidal field of the Galactic centre as in the case of the Quintuplet cluster.

For the Arches cluster, Kim et al. (2006) have quantified the effect of the internal cluster dynamics and the evaporation in the Galactic tidal field on the mass function measured within an annulus of 0.19 – 0.35 pc. Their Fokker-Planck calculations and N-body simulations yield a flattening of the mass function by 0.1 to 0.2 within the present cluster lifetime of 2.5 Myr. At an older age of about 3 – 5 Myr, the much more dispersed appearance of the Quintuplet with respect to the Arches cluster suggests that the Quintuplet cluster is dynamically more evolved and more affected by tidal effects. If the Quintuplet cluster started with a similar initial density and total mass as the Arches cluster the expected initial MF slope would be at least -1.9. The longer evolution time of the cluster might be responsible for a further flattening of the MF slope in the cluster core during the age of the Quintuplet cluster. While the dynamical evolution provides a tempting explanation for the flattened MF in the cluster centre, N-body simulations are required to confirm or disprove whether the flat PDMF of the Quintuplet cluster can be explained by dynamical effects alone.

4 The present-day mass function in the outer parts of the Quintuplet cluster

In order to derive the radial variation of the PDMF of the Quintuplet cluster, the outer parts of the cluster were probed in four connected fields (Fields 2 to 5, see Fig. 1.1) to the east and south of the cluster centre by NACO K_s-band observations in 2008 and 2009. To establish a proper motion membership sample in the same fashion as for the central part of the cluster, a second epoch of NACO observations in the K_s-band was obtained in 2011 and 2012. Datasets of the cluster taken with the Wide Field Camera 3 (WFC3) onboard the Hubble Space Telescope (HST)[1] in the $F127M$ and $F153M$ filters (see Table 4.3) provided colour information for stars located in the outer fields. The membership samples were established for each field individually based on the measured proper motions and a subsequent colour selection. The PDMF was then determined in two radial annuli ranging from 0.5 to 1.2 pc and from 1.2 to 1.8 pc (2.1 pc), respectively.

The NACO and WFC3 datasets, the performed reduction and analysis of the data and the determination of the completeness from artificial star experiments are detailed in Sect. 4.1. The selection of a proper motion membership sample for each of the four Quintuplet outer fields based on membership probabilities is described in Sect. 4.2. The CMDs of the outer fields, the applied colour selection to derive the final member selection and the mass determination are explained in Sect. 4.3. Finally, the slope of the PDMF in the outer parts of the Quintuplet cluster is determined within two annuli and the PDMF of the cluster is discussed in Sect. 4.4.

4.1 Datasets and data reduction of the Quintuplet outer fields

4.1.1 VLT/NACO K_s-band data

4.1.1.1 Datasets

Four fields in the outskirts of the Quintuplet cluster to the south and east of Field 1 (see Fig. 1.1) were covered by service mode observations in the K_s-band in 2008 and 2009 (observation periods P81 and P82[2], PI: W. Brandner, Program ID 081.D-0572(B)). For the AO correction with the NAOS instrument the four natural guide stars indicated in Fig. 1.1 were used as guide probes for the infrared wavefront sensor. The stated K_s-band magnitudes of the guide stars are taken from the 2MASS catalogue (Skrutskie et al. 2006).

Second epoch observations of Fields 2 to 5 in the K_s-band were proposed and scheduled for service mode observations in 2010 (P85, PI: A. Stolte, Program ID 085.D-0446(B)). Unfortunately, neither in this observation period nor in P86 data of the Quintuplet outer fields were obtained due to unfavourable observing conditions. The observations were reattempted in P87, but only for Field 2 data with the

[1] This thesis is based in part on observations made with the NASA/ESA Hubble Space Telescope, obtained from the data archive at the Space Telescope Science Institute. STScI is operated by the Association of Universities for Research in Astronomy, Inc. under NASA contract NAS 5-26555.

[2] ESO observation periods have a duration of 6 months. Observation periods with odd numbering last from April 1 to September 30, periods with even numbering from October 1 to March 31.

Table 4.1: Overview of the VLT/NACO datasets covering the outer parts of the Quintuplet cluster.

Field	Date	Filter	Frames[a]	DIT (s)	NDIT	$t_{\rm int}$[b] (s)	Airmass	Seeing ($''$)	FWHM[d] ($''$)	Strehl ratio[d]
2	2008-07-24	K_S	34	2.0	15	1020	1.01 – 1.03	0.44 – 0.61	0.070	0.42
2	2011-09-19	K_S	464[c]	2.0	1	928	1.34 – 1.48	0.55 – 0.75	0.095	0.10
3	2009-04-07	K_S	32	2.0	15	960	1.00 – 1.02	0.56 – 0.81	0.085	0.21
3	2012-06-14	K_S	827[c]	2.0	1	1654	1.01 – 1.04	0.57 – 0.83	0.098	0.09
4	2009-04-10	K_S	32	2.0	15	960	1.07 – 1.11	0.51 – 0.62	0.077	0.27
4	2012-06-14	K_S	515[c]	2.0	1	1030	1.00 – 1.01	0.67 – 0.88	0.100	0.08
5	2009-04-10	K_S	31	2.0	15	930	1.02 – 1.05	0.57 – 0.96	0.080	0.28
5	2012-08-02	K_S	269[c]	2.0	1	538	1.01 – 1.02	0.56 – 0.80	0.087	0.14

Notes. [(a)] Number of dithered frames used to generate the final combined image. [(b)] Total integration time of the central part of the image with maximum overlap. [c] Dataset was obtained in cube mode, i.e. each single DIT is stored as a layer of a data cube. Each data cube contained 30 DITs. [d] Determined from the extracted PSF of the combined image.

astrometric accuracy required to establish a proper motion membership sample could be obtained. Fortunately, a second epoch of K_S-band data could be acquired for all missing fields (Fields 3, 4 and 5) during two observing runs in visitor mode in 2012 (PI: A. Stolte, Program ID 089.D-0121(A) and PI: C. Olczak, Program ID 089.D-0430(A)).

An observing program to observe the outer fields also in the H-band was likewise scheduled for P85, but could not be executed. The program was transferred to the observation period P86 (October 2010 to March 2011) and reattempted, but to no avail[3]. Therefore the information of the stellar colours necessary to derive reliable masses and to remove contaminating field stars from the sample of proper motion cluster members had to be determined from WFC3 observations (see Sect. 4.1.2).

The settings of the first epoch observations of the four outer fields were the same as for the K_S-band observations of Field 1 in 2008 using the medium resolution camera S27, a DIT of 2.0 s, NDIT of 15 and covering each field with 44 frames. Ten sky frames were obtained subsequent to the science observations (cf. Sect. 3.1.2). The area on the sky covered by each of the four outer fields after removal of a margin to avoid regions with low coverage or uncorrected 50 Hz noise (see below and Sect. 2.2.3) is about $28'' \times 25''$.

The second epoch observations from 2011 and 2012 were obtained in cube mode, such that each single DIT is stored in a separate layer of a data cube (see Sect. 5.9 in Girard et al. 2011). The advantage of this mode is the possibility to select from the single DIT frames of each pointing only the ones with a good AO performance. For our earlier NACO observations, each of the NDIT single DITs were averaged by CONICA's read-out controller into a single layer frame as cube mode was not yet available. Field 2 was covered with 22 data cubes and 10 sky cubes were obtained subsequent to the science observations. The other Quintuplet outer fields were observed in visitor mode and the number of data cubes was adjusted according to the observing conditions. The number of data cubes was 34, 20 and 12 for Field 3, 4, and 5, respectively, and 8 sky cubes were obtained for each field. Each data or sky cube contained 30 single frames with a DIT of 2.0 s. The properties of the K_S-band datasets covering the outer parts of the Quintuplet cluster are summarised in Table 4.1.

All K_S-band datasets of both epochs were reduced using the custom-made data reduction pipeline

[3]The data quality of the only outer field observed with VLT/NACO in the H-band (Field 3) was discarded due to the insufficient AO performance and very pronounced anisoplanatism in favour of the WFC3 datasets.

Table 4.2: Overview of the VLT/ISAAC datasets of the Quintuplet cluster used as reference for the photometric calibration of the outer fields.

Date	Filter	No. of frames	DIT (s)	NDIT	$t_{\rm int}$[a] (s)	Airmass	Seeing ($''$)	FWHM[b] ($''$)
2001-04-09	J_s	7	1.8	20	248	1.00 – 1.01	0.49 – 0.62	0.46
2001-04-09	H	9	1.8	20	319	1.00 – 1.00	0.48 – 0.63	0.44
2001-04-09	K_s	9	1.8	20	319	1.00 – 1.01	0.46 – 0.63	0.40

Notes. [(a)] Total integration time of the central part of the image with maximum overlap. [b] Determined from the extracted PSF of the combined image.

described in Sect. 2.2[4]. The dark, sky and science frames all required a correction of the 50 Hz noise. As for Field 1, the small dithers between the sky frames resulted in significant stellar residua in the sky derived from the sky frames alone, such that the finally applied sky was generated using all sky and object frames. The only exception was the second epoch data of Field 4, were only sky frames could be used to generate a smooth sky. The quality of each reduced science frame was assessed by determining the FWHM of a reference source present in all frames of the respective dataset. Based on the measured FWHM, between 14% and 30% of the frames of a dataset were excluded from the image combination with the *drizzle* algorithm (see Table 4.1).

4.1.1.2 Source detection and photometric calibration

With the exception of Field 2, where the natural guide star is at the centre, the guide stars are located close to the corners of the respective outer fields. Due to the larger distances of stars from the respective guide star, large areas of the Fields 3, 4 and 5 exhibit a pronounced anisoplanatism with distinctively elongated stars. As the *starfinder* algorithm uses a constant, empirical PSF for the source extraction, elongated stars were frequently fitted by multiple components. In some cases the secondary, fake components comprised a significant fraction of the stellar flux of up to 0.3 mag. Due to this large systematic magnitude error of stars with larger guide star distances and the associated scatter, which prevents a reliable determination of the zeropoint, the IRAF *daophot* package instead of *starfinder* was used for the source detection and the PSF fitting for all outer fields (Stetson 1987). Unlike the *starfinder* algorithm, *daophot* uses an analytical function to fit the PSF, but allows for a linear or quadratic spatial variation of the PSF. The selected PSF stars are first fitted with an analytical function[5]. The flux residua of the PSF stars after subtraction of the fitted analytical function are averaged into a constant two-dimensional look-up table. The spatial variation of the PSF is accounted for by determining the Taylor expansion of the change of the residua of the PSF stars with the location in the image to the first or second order. The Taylor expansions are stored into two or five additional look-up tables for a linear or quadratically varying PSF, respectively (Stetson 1992). For all datasets of the outer fields, the flattest residua were achieved using the *daophot* package with a quadratically varying PSF.

[4]Dr. Andrea Stolte performed the data reduction and image combination of the second epoch data of Fields 3 and 4 and of the ISAAC data used for photometric calibration (see Sect. 4.1.1.2). Further, the source detection with the *daophot* package (Sect. 4.1.1.2) for all outer fields with exception of the second epoch data of Fields 2 and 5 was also carried out by Dr. Andrea Stolte.

[5]The best fitting function yielding the smallest residua can be selected automatically. The possible choices are: Gaussian function, Moffat function, Lorentz function or Penny function (Gaussian + Lorentzian function).

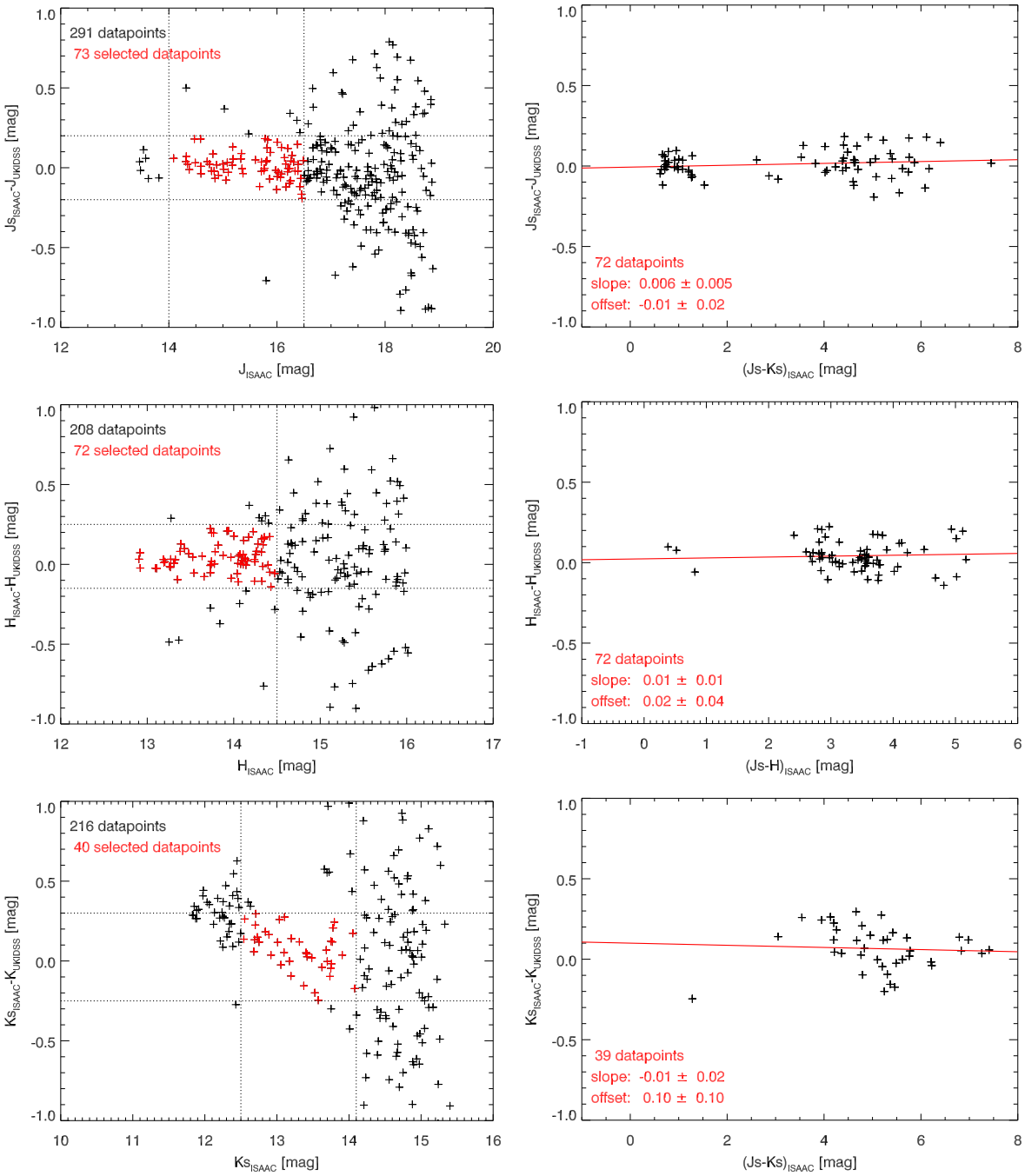

Figure 4.1: *Left panels*: Magnitude difference of stars common in the ISAAC J_sHK_s datasets and the UKIDSS *JHK* catalogue plotted vs. the respective ISAAC magnitude. Stars which are selected for the derivation of the potential colour terms between the two filter systems are drawn in red. The left dotted line indicates the ISAAC non-linearity limit, while the right dotted line provides the selection at the faint limit. The increasing scatter towards fainter magnitudes is due to the difference in the resolution between the higher resolved ISAAC data and the UKIDSS catalogue and indicates that the UKIDSS photometry becomes unreliable beyond the applied selection. *Right panels*: Magnitude differences of the stars selected in the *left panels* plotted vs. $(J_s - K_s)_{\mathrm{ISAAC}}$ (*top right* and *bottom right*) or $(J_s - H)_{\mathrm{ISAAC}}$ (*middle right*). Linear fits to the datapoints are shown as well (red lines).

Table 4.3: Overview of the used VLT/NACO, VLT/ISAAC, and UKIDSS broad band filters and the HST/WFC3 medium band filters.

NACO[a]			ISAAC[b]			UKIDSS[c]			WFC3[d]		
Filter	λ_c	$\Delta\lambda$	Filter	λ_c	$\Delta\lambda$	Filter	λ_c	$\Delta\lambda$	Filter	λ_c	$\Delta\lambda$
	μm	μm		μm	μm		μm	μm		μm	μm
J	1.27	0.25	J_s	1.24	0.16	J	1.25	0.16	$F127M$	1.27	0.07
H	1.66	0.33	H	1.65	0.30	H	1.64	0.29	$F153M$	1.53	0.07
K_s	2.18	0.35	K_s	2.16	0.27	K	2.20	0.34			

Notes. [(a)] Central wavelength (λ_c) and filter width ($\Delta\lambda$) from Table 5-4 in Ageorges et al. (2007). [(b)] λ_c and $\Delta\lambda$ from Table 2 in Mason et al. (2010). [(c)] $\Delta\lambda$ is inferred from the cut-on and cut-off wavelengths as stated in Tokunaga et al. (2002, Table 1). [(d)] λ_c and $\Delta\lambda$ are inferred from the cut-on and cut-off wavelengths. The cut-on and cut-off wavelengths were determined from the transmission curve of the respective filter (available from `ftp://ftp.stsci.edu/cdbs/comp/wfc3/`).

The UKIDSS catalogue contains only very few suited calibrators for some of the outer fields. Therefore, a set of VLT/ISAAC observations covering all observed Quintuplet fields was calibrated versus the UKIDSS catalogue to provide a large number of well-resolved calibrators. The ISAAC observations (see Table 4.2) were obtained in April 9th 2001 and imaged an area on the sky of about $3.9' \times 3.9'$ centred at the Quintuplet cluster with a pixel scale of $0.148''$pixel^{-1} in the J_s-, H- and K_s-band (PI: A. Stolte, Program ID 67.C-0591(B)). Stellar positions and fluxes in the combined ISAAC images were measured with the *starfinder* algorithm and matched with the UKIDSS JHK catalogue. Sources either saturated in the UKIDSS catalogue or in the ISAAC images were removed, and sources which could not be reliably assigned to their UKIDSS counterparts were manually rejected. As in the case of the direct calibration of the NACO data of Field 1 (see Sect. 3.2.3), the PSF fluxes of all stars in the ISAAC images falling within the UKIDSS $1''$ aperture around each calibrator were added and compared to the magnitude in the UKIDSS catalogue. Ultimately 58, 59 and 33 calibrators were used to determine the zeropoints in the J_s-, H-, and K_s-band, respectively.

In order to determine if colour terms between the ISAAC and the UKIDSS filter systems (see Table 4.3) are present, a set of common, unsaturated stars in both catalogues was selected for each filter (see left panels in Fig. 4.1). While for the determination of the zeropoint the ISAAC PSF fluxes of stars within the UKIDSS aperture of $1''$ around each calibrator could be added, this procedure could not be used for the derivation of the colour terms. Adding the fluxes of stars with different intrinsic properties would alter the colour of each calibrator source, and hence bias the derived colour terms. The scatter of the magnitude differences $m_{\rm ISAAC} - m_{\rm UKIDSS}$ is therefore larger than for the derivation of the zeropoints. The magnitude differences as a function of $(J_s - K_s)_{\rm ISAAC}$ or $(J_s - H)_{\rm ISAAC}$ were fitted by a straight line (see right panels in Fig. 4.1). A definite colour term could not be detected for any of the three filters as the formal fitting error was in all cases equal to or larger than the derived slope. For the J_s-band and to a lesser degree for the H-band significant colour terms can be confidently ruled out due the large number of used stars and the covered colour range. For the K_s-band filter the presence of a colour term cannot be excluded or confirmed due to the lack of blue stars, the rather contracted colour range and the comparatively large scatter of the datapoints. As no significant colour terms between the J- and H-band filters of both filter systems is present and a colour term between the K-band filters could not be safely measured, no colour term correction was applied to the ISAAC J_sHK_s photometry.

The zeropoints of the NACO K_s-band datasets of all the outer fields obtained in 2008/2009 were subsequently determined with respect to the calibrated ISAAC K_s-band source catalogue. The con-

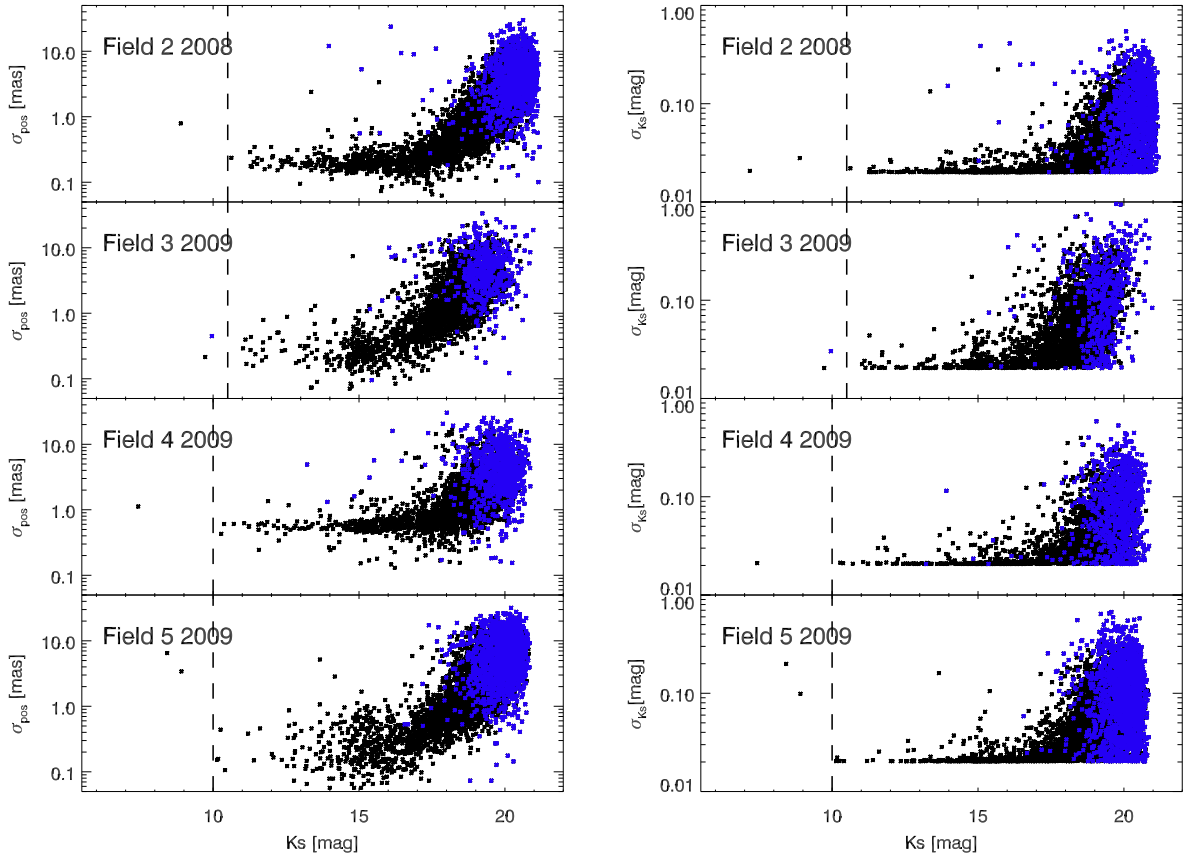

Figure 4.2: Astrometric (*left panels*) and photometric uncertainties (*right panels*) plotted vs. magnitude of the four NACO K_s-band datasets of the Quintuplet outer fields from the first epoch in 2008 or 2009. Stars which are only detected in two of the three auxiliary frames are drawn in blue. The plotted photometric uncertainties include the PSF fitting uncertainties and the standard error of the zeropoint of the calibration vs. the ISAAC K_s-band data. The dashed vertical lines indicate the approximate linearity limit of the respective NACO dataset.

sistency of the photometric calibration of Fields 2, 3 and 5 was confirmed using common stars in the overlap regions of Field 2 with Field 3 and of Field 2 with Field 5 (Fig. 1.1). In both cases the mean zeropoint offsets of these common stars with $K_s < 18$ mag and after rejection of outliers outside of $\pm 2\,\sigma$ from the mean was ±0.01 mag. Hence the photometric calibration of Fields 2, 3 and 5 are in very good agreement. For Field 4, a similar consistency check was not possible due to the missing overlap between Fields 4 and 5. The second epoch (2011/2012) K_s-band data of each field was calibrated with respect to the first epoch data.

4.1.1.3 Estimation of photometric and astrometric errors

The photometric and astrometric uncertainties of the four NACO K_s-band datasets of the outer fields were estimated in the same way as described in Sect. 3.2.4. The frames of each dataset were divided into three subsets which were subsequently combined into three auxiliary images. For the PSF fitting with *daophot*, the same PSF as derived for the respective deep image was used. Again the standard errors of the three independent measurements of the x-, y-position and the flux of each star in the three auxiliary frames were adopted as the positional and the photometric uncertainties. As faint stars

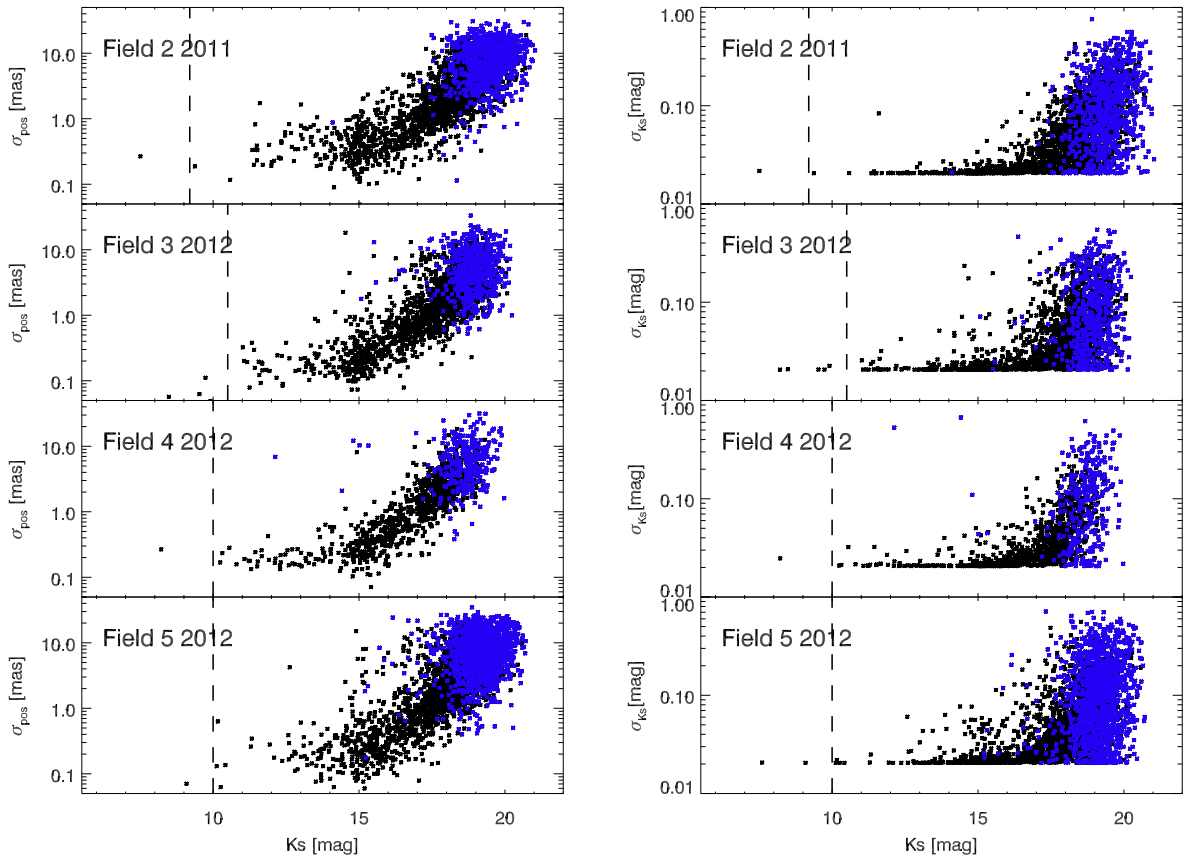

Figure 4.3: Astrometric (*left panels*) and photometric uncertainties (*right panels*) plotted vs. magnitude of the four NACO K_s-band datasets of the Quintuplet outer fields from the second epoch in 2011 or 2012. Stars which are only detected in two of the three auxiliary frames are drawn in blue. The plotted photometric uncertainties include the PSF fitting uncertainties and the standard error of the zeropoint of the calibration vs. the ISAAC K_s-band data. The dashed vertical lines indicate the approximate linearity limit of the respective NACO dataset.

were frequently detected only in two of the three auxiliary frames, the uncertainties of these stars were estimated as half the difference of the two independent measurements. All stars which were detected in at least two auxiliary frames were kept in the source catalogue. Figures 4.2 and 4.3 show the astrometric uncertainties which are the mean of the positional uncertainties in the x-, and y-direction, and the photometric uncertainties in dependence of the magnitude for the four outer fields in both epochs. The shown photometric uncertainties include the standard error of the zeropoint. The uncertainties scatter only slightly for stars brighter than $K_s = 17.5$ mag, whereas for fainter stars the scatter increases steeply. The second epoch data, with the exception of Field 3, exhibit larger uncertainties with a more pronounced scatter at the faint end. For all outer fields, the scatter of the uncertainties of the brighter stars is smaller than for Field 1 (cf. Fig. 3.2). For the outer fields the astrometric uncertainties of stars with $K_s < 17.5$ mag have median values between 0.2 and 0.6 mas, while a much larger median value of 1.6 mas was derived for the K_s-band data of Field 1 from 2008, where *starfinder* was used as the PSF fitting tool. The *daophot* photometry shows generally a lower scatter on the auxiliary frames than the *starfinder* photometry, and magnitudes are more closely reproduced with the *daophot* PSF fitting. This indicates that the PSF fitting with the *daophot* package compared to the PSF fitting with *starfinder* is less sensitive to the small differences in the noise between auxiliary images. Fritz et al.

(2010) determined for the S13 camera the astrometric uncertainty with *starfinder* on a set of subsequent single frames (see their Fig. 4, red dashed line). Their derived astrometric uncertainty increased from $\sim$ 0.4 to 2.5 mas in the magnitude range from K_s = 12 to 17 mag which is of the same order as found for Field 1. For the S27 camera Trippe et al. (2008) derived the astrometric uncertainty by comparing the stellar positions (K_s < 18 mag) which were determined by fitting a two-dimensional elliptical Gaussian to detected sources in a set of mosaics. They find a typical uncertainty of $\sim$ 0.7 mas which is larger than the median value of the astrometric uncertainties in the outer fields. As in contrast to Trippe et al. (2008) the single frames were not corrected for instrumental geometric distortions before generating the combined images, the astrometric uncertainties of the outer fields are expected to be larger. The astrometric uncertainties determined for the outer fields are therefore likely underestimated. Nevertheless, as the 'true' centroiding error is not known and the derived uncertainties trace at least the relative measurement accuracies, they are applied as the measurement errors.

4.1.2 HST/WFC3 data

Although *H*-band observations of the Quintuplet Fields 2 to 5 were scheduled for the ESO observation period P85 and reattempted in P86, no data of sufficient quality was obtained due to bad atmospheric conditions. Therefore, in order to get colour information for the outer fields of the Quintuplet cluster, which is necessary to determine masses from the isochrones in the CMD, observations obtained in 2010 with WFC3 on-board the HST were analysed. In the following, the datasets, the data reduction and the photometric calibration of the WFC3 observations are described.

4.1.2.1 Datasets and data reduction

The Wide Field Camera 3 was installed during the HST servicing mission 4 in May 2009 as a replacement for the Wide Field Planetary Camera 2 (Rajan 2010)[6]. It offers two different channels, the Ultraviolet-Visible (UVIS) channel for observations in the wavelength range of 200 to 1000 nm and the Infrared (IR) channel for wavelengths between 800 to 1700 nm. The IR channel covers a FOV of $136'' \times 123''$ with a pixel scale projected onto the sky of approximately $0.135'' \times 0.121''$. The asymmetry of the FOV and of the pixel scale is caused by the 22° tilt of the focal plane with respect to the incoming light beam (Rajan 2010). Further geometric distortions are introduced by the intricate optical design with multiple foldings of the light path and variations of the detector plate scale. These geometrical distortions can be corrected with a typical accuracy of 0.1 pixel (Rajan 2010) by applying the newest distortion coefficient table with the PyRAF task *multidrizzle*[7].

Two datasets observed with the WFC3 IR-channel on August 10th and 16th 2010 with the $F127M$ and $F153M$ medium-band filters (PI: A. Ghez, proposal ID: 11671) were retrieved from the Mikulski Archive for Space Telescopes (MAST). The data were reduced upon retrieval (March 12th 2012) with the standard WFC3 calibration pipeline (*calwf3*, version 2.6.2) using the most current calibration files at that time. The automatic data reduction of the raw exposures encompasses the subtraction of the bias level and the dark current, the correction of the detector non-linearity, the up-the-ramp fitting of the multiple non-destructive read-outs, the flat-fielding and the identification of bad pixels (for details of the calibration process of the *calwf3* pipeline see Rajan 2010). As for the linear fit of the signal versus time, only those read-outs are used where the saturation limit is not exceeded, i.e. a pixel in the

[6] For the online version of the WFC3 data handbook see `http://www.stsci.edu/hst/wfc3/documents/handbooks/currentDHB/wfc3_cover.html`.

[7] The distortion coefficient table as well as other reference files used for the calibration of WFC3 data can be obtained from `http://www.stsci.edu/hst/observatory/cdbs/SIfileInfo/WFC3/reftablequeryindex`.

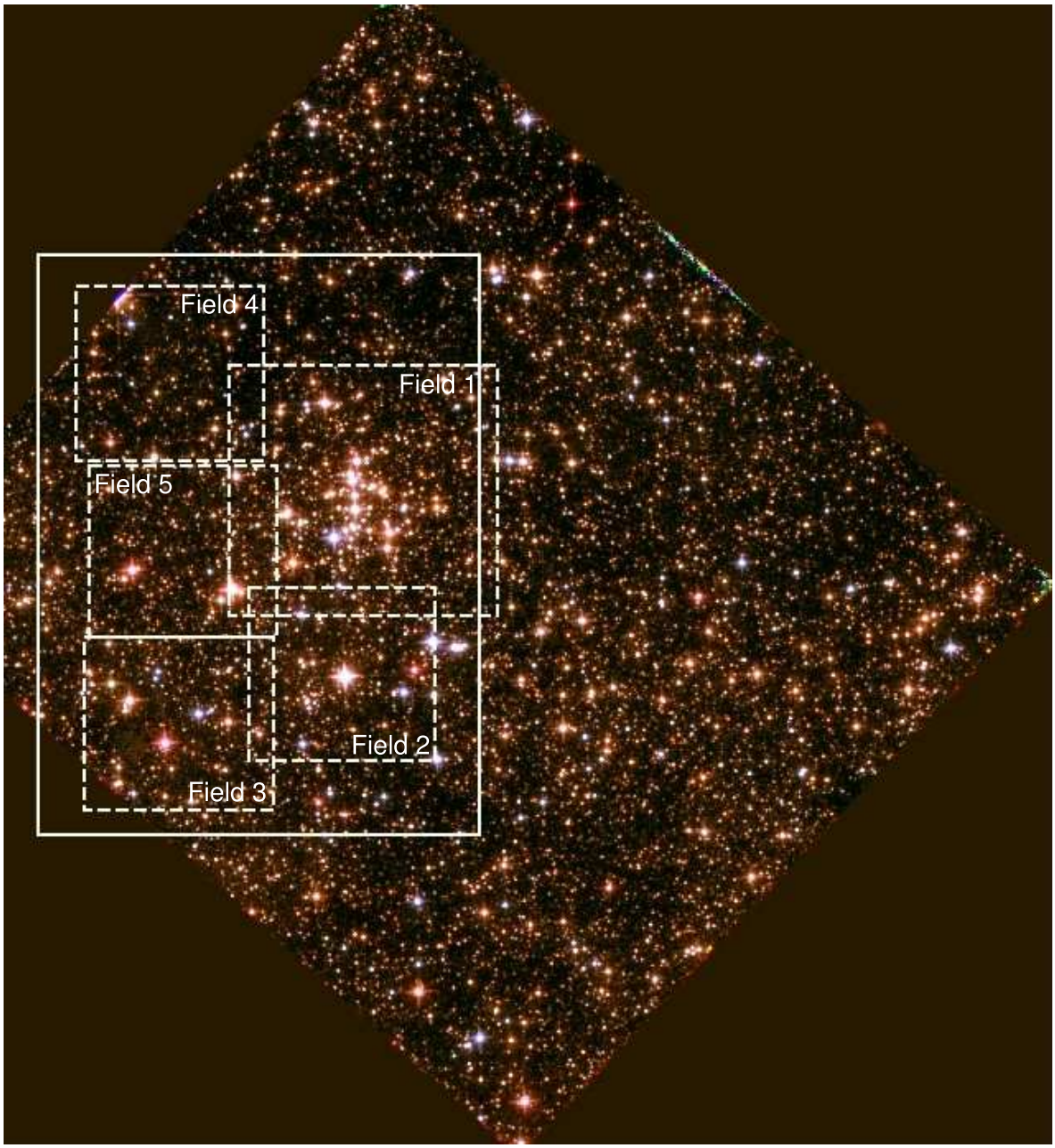

Figure 4.4: Three-colour composite image using the $F127M$, $F139M$ and $F153M$ WFC3 data of the Quintuplet cluster. The areas covered by the observed NACO Fields are indicated by the dashed rectangles. The part of the combined WFC3 image for which the source detection was performed is marked with the solid rectangle.

Table 4.4: Overview of the used WFC3 observations.

Date	Filter	No. of frames	$n_{\mathrm{samp}}{}^{a}$	t_{exp} (s)	t_{int} (s)	FWHM^{b} ($''$)
2010-08-10	$F127M$	12	13	599.2	7190.8	0.211
2010-08-16	$F153M$	21	13	349.2	7333.2	0.206

Notes. $^{(a)}$ Number of non-destructive read-outs including the zeroth read. $^{(b)}$ Determined from the extracted PSF.

reduced image is only saturated if it is saturated in all its read-outs. This applies almost exclusively to bad pixels, such that only the Pistol star and Q7 observed in the $F153M$ filter are saturated. The reduced images as downloaded from MAST were further processed locally.

Image pixels, with count levels exceeding about half their full well depth (i.e. $> 50,000$ electrons) expose a faint afterglow in subsequent exposures (Rajan 2010)[8]. This image persistence can in extreme cases take up to several hours to abate. The persistence within each exposure is automatically predicted during data processing and the corresponding persistence images can be retrieved via a web interface[9]. The WFC3 datasets covering the Quintuplet cluster were actually affected by persistence due to the large number of bright stars. For the brightest stars, the count rates of their afterglow are even comparable to the brightness of stars at the faint end. As the applied dither steps and the overall dither patterns are larger than the PSF FWHM (~ 1.5 pixel), the persistence afterglow of a bright star can be located in its wing and therefore influence the detection of faint stars in the stellar halo. The persistence images were therefore subtracted from the reduced images.

The individual, dithered observations were combined with the PyRAF task *multidrizzle* into one final image for each filter. The relative alignment of the individual images as derived from the WCS (World Coordinate System) information of the images was refined by determining additional shifts and rotations due to slight pointing differences with the PyRAF task *tweakshifts*. During the image combination the individual exposures were corrected for the geometric distortions and hot pixels, and pixels affected by cosmic rays were detected and added to the bad pixel mask. The drizzling of the images observed with sub-pixel dithers allows for a finer sampling of the otherwise undersampled WFC3 PSF. The output pixels of the combined images were chosen to be $0.07''$, such that the FWHM of the PSF in the drizzled image is about 2.5 pixel and therefore well-sampled. The input pixels were shrunk to 0.7 times its input size, i.e. the parameter *pixfrac* was set to 0.7, in order to enhance the resolution of the final image.

The properties of the datasets observed with the $F127M$ and $F153M$ filters are summarized in Table 4.4.

4.1.2.2 Source detection and photometric calibration

From the full area covered by the WFC3 observations, a $70'' \times 92''$ region encompassing all five fields of the NACO observations was extracted to speed up the source detection with the *starfinder* algorithm (see Fig. 4.4). A constant, empirical PSF was extracted using 38 preferentially isolated and uniformly distributed PSF stars for each of the two filters. The two stars (Pistol star, Q7) saturated in the F153M data are included in the list of PSF stars in order for their saturated cores to be repaired by *starfinder*. This allows for the detection and PSF fitting of these two stars, such that their contribution

[8] See also `http://www.stsci.edu/hst/wfc3/ins_performance/persistence/`.
[9] `http://archive.stsci.edu/prepds/persist/search.php`.

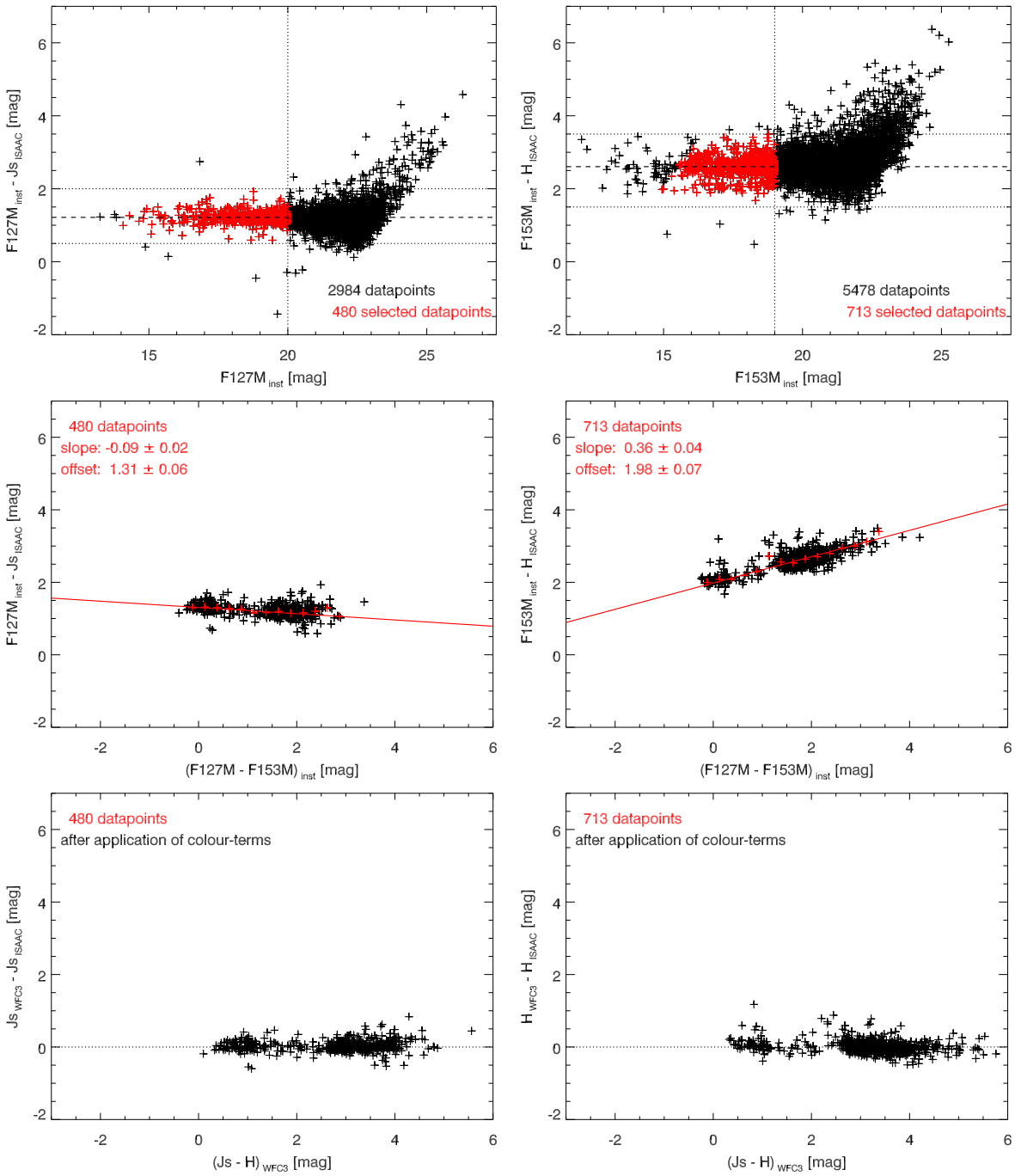

Figure 4.5: *Top left*: Difference of the instrumental WFC3 $F127M$ magnitude and the calibrated ISAAC J_s-band magnitude vs. the instrumental $F127M$ magnitude. Stars selected for the derivation of the colour term between the $F127M$ and the J_s-band filter are drawn in red. *Middle left*: Magnitude difference of the selected stars vs. the instrumental colour $(F127M - F153M)_{\rm inst}$. The red crosses mark the median values within colour bins of 0.25 mag. A linear fit to the median values weighted by the standard deviation of each bin is shown as well. *Bottom left*: Magnitude difference of the selected stars vs. the colour $(J_s - H)_{\rm WFC3}$ after the conversion of the WFC3 magnitudes to the ISAAC filter system. *Right panels*: Corresponding plots as in the *left panels* for the determination of the colour term between the F153M and the ISAAC H-band filter. The second, lower branch visible in the *top right* panel around $F127M_{inst} - H_{\rm ISAAC} = 2.1$ mag is concentrated at about $(F127M - F153M)_{\rm inst} = 0$ mag in the *middle right panel*.

to the fluxes of neighbouring stars can be subtracted.

As for the NACO data of the outer fields, the photometric calibration of the WFC3 source catalogues was performed with respect to the calibrated ISAAC data of the Quintuplet cluster. The WFC3 $F127M$ and $F153M$ filters are calibrated vs. the ISAAC J_s- and H-band filters, respectively (cf. Table 4.3). Figure 4.5 shows in the upper panels the magnitude differences of common stars in the WFC3 and ISAAC source catalogues for the $F127M$ and J_s-band filter (left) and the $F153M$ and H-band filter (right). In the top right panel of Fig. 4.5, most stars scatter around a magnitude difference of $F153M_{\rm inst} - H = 2.6$ mag, while a second branch of stars at about $F153M_{\rm inst} - H = 2.1$ mag is also visible. For the determination of potential colour terms between the medium-band WFC3 and the broad-band ISAAC filters only stars fainter than the saturation limits in the ISAAC J_s-band ($J_s = 12.8$ mag) or H-band data ($H = 12.9$ mag) were selected. In order not to be influenced by the increasing and asymmetric scatter of the magnitude differences towards fainter magnitudes, stars with $F127M_{\rm inst} \geq 20$ mag or $F153M_{\rm inst} \geq 19$ mag were excluded. Further, the few outliers outside $F127M_{\rm inst} - J_s = [0.5, 2.0]$ or $F153M_{\rm inst} - H = [1.5, 3, 5]$ were removed as well. For the selected stars, the respective magnitude differences between the WFC3 and the ISAAC filters were plotted with respect to the instrumental colour $F127M_{\rm inst} - F153M_{\rm inst}$ (see middle panels in Fig. 4.5). The reason to use instrumental WFC3 colours instead of the calibrated ISAAC colours ($J_s - H$) to derive a colour term is the superior resolution and larger sensitivity of the WFC3 compared to the ISAAC data. Otherwise a large number of faint, but well measured stars in the WFC3 data, which are missing in the ISAAC source catalogues, could not be photometrically calibrated. The stars forming the second branch in the top right panel of Fig. 4.5 result from the pronounced colour term as all stars which populate this branch have an instrumental WFC3 colour of about 0 mag (middle right panel). In order to be less affected by the scatter in more sparsely populated colour ranges, the colour term was determined by fitting the median values within colour bins of 0.25 mag, weighted by the respective standard deviation in each bin, with a straight line. The linear fits as well as the median values are shown in red in the middle panels of Fig. 4.5. The bottom panels show the magnitude differences as a function of the WFC3 colours after the WFC3 magnitudes were converted into the ISAAC filter system. Besides the obvious shifts in colour compared to the middle panels in Fig. 4.5, these plots illustrate the increased spread of the colour range once the colour terms are applied. To complete the photometric calibration of the WFC3 data, a slight remaining zeropoint offset was corrected for both WFC3 filters. The conversion equations from the WFC3 to the ISAAC filter system are:

$$J_{s,\rm WFC3} = F127M_{\rm inst} - c_{F127M} \cdot (F127M_{\rm inst} - F153M_{\rm inst}) + zp_{F127M} \quad (4.1)$$

$$H_{\rm WFC3} = F153M_{\rm inst} - c_{F153M} \cdot (F127M_{\rm inst} - F153M_{\rm inst}) + zp_{F153M}\,, \quad (4.2)$$

with $c_{F127M} = -0.09 \pm 0.02$ and $c_{F153M} = 0.36 \pm 0.04$ being the respective colour terms. In the following section, WFC3 magnitudes in the $F127M$ and $F153M$ filters which are converted to the ISAAC filter system are designated as $J_{s,\rm WFC3}$ and $H_{\rm WFC3}$, respectively.

4.1.2.3 Estimation of photometric and astrometric errors

The estimation of the astrometric and photometric uncertainties due to the PSF fitting proceeded in the same way as for the NACO datasets. For both datasets, three auxiliary frames were combined with *multidrizzle* from three subsets, consisting of either four ($F127M$) or seven frames ($F153M$) of the respective dataset each. The source detection and PSF fitting was performed with *starfinder* in the same manner as for the deep images using the empirical PSF extracted from the respective deep image. Again, only stars which are detected in at least two auxiliary frames are considered in the

further analysis in order to exclude spurious detections. For the determination of the photometric uncertainties due to the PSF fitting, no conversion between the WFC3 and ISAAC filter systems was applied. The derived photometric uncertainties refer therefore to the standard errors $\sigma_{F127M,\mathrm{inst}}$ and $\sigma_{F153M,\mathrm{inst}}$ of the instrumental magnitudes.

Fig. 4.6 shows the astrometric uncertainty (top panels), i.e. the mean of the uncertainties in the x- and y-direction, and the photometric uncertainty of the instrumental magnitudes (middle panels) as a function of the magnitude for both filters. For stars brighter than about $J_{s,\mathrm{WFC3}} < 21.5$ mag or $H_{\mathrm{WFC3}} < 18.5$ mag, the median of the astrometric and photometric uncertainties is relatively constant (red lines in Fig. 4.6). The median of the astrometric uncertainties of these stars is 4.4 mas and 3.0 mas for the $F127M$ and the $F153M$ dataset, respectively. Considering the short time baselines between the NACO data of the outer fields and the WFC3 observations of 1.3 yr (Field 3, 5) and 2.0 yr (Field 2), the astrometric uncertainties in units of mas/yr of the WFC3 data alone are of similar size or larger than the proper motion membership criterion applied for Field 1 of $2\,\sigma = 2.26$ mas/yr (see Sect. 3.4.3). A selection of the cluster members based on proper motions derived from the NACO data and the drizzled WFC3 images is therefore not feasible.

The median of the photometric uncertainties $\sigma_{F127M,\mathrm{inst}}$ and $\sigma_{F153M,\mathrm{inst}}$ for $J_{s,\mathrm{WFC3}} < 21.5$ mag or $H_{\mathrm{WFC3}} < 18.5$ mag amounts to 0.04 mag and 0.03 mag, respectively. For fainter magnitudes the photometric and astrometric uncertainties and especially the scatter increase strongly. The uncertainties derived for the $F127M$ dataset are in general larger than for the $F153M$ dataset. This may be caused by the lower number of only four frames contributing to each auxiliary frame and hence the smaller signal to noise ratio of the $F127M$ auxiliary frames. In addition, as the individual frames obtained with WFC3 are undersampled, a larger number of frames per auxiliary frame obtained with sub-pixel dithers improves the sampling in the drizzled image. This effect may contribute to the smaller astrometric and photometric uncertainties of the $F153M$ dataset.

Besides the photometric uncertainties related to the PSF fitting, the contributions of the photometric calibrations to the photometric errors have to be considered as well. The total photometric uncertainties of the converted WFC3 magnitudes follow from error propagation of Eqs. (4.1) and (4.2):

$$\sigma_{J_{s,\mathrm{WFC3}}} = \sqrt{\sigma^2_{m_1,\mathrm{inst}} + (\sigma_{c_1} \cdot (m_{1,\mathrm{inst}} - m_{2,\mathrm{inst}}))^2 + (c_1 \cdot \sigma_{m_1,\mathrm{inst}})^2 + (c_1 \cdot \sigma_{m_2,\mathrm{inst}})^2 + (\sigma_{zp_1})^2} \quad (4.3)$$

$$\sigma_{H_{\mathrm{WFC3}}} = \sqrt{\sigma^2_{m_2,\mathrm{inst}} + (\sigma_{c_2} \cdot (m_{1,\mathrm{inst}} - m_{2,\mathrm{inst}}))^2 + (c_2 \cdot \sigma_{m_1,\mathrm{inst}})^2 + (c_2 \cdot \sigma_{m_2,\mathrm{inst}})^2 + (\sigma_{zp_2})^2}\,, \quad (4.4)$$

where the subscripts 1 and 2 refer to the $F127M$ and $F153M$ filters, respectively. The applied zeropoint errors were the standard errors of the residual zeropoint offsets after the correction of the colour terms. The total photometric uncertainties are shown in the bottom panels of Fig. 4.6 for both filters. The median of the total photometric uncertainties of the F127M and F153M datasets for magnitudes brighter than $J_{s,\mathrm{WFC3}} < 21.5$ mag and $H_{\mathrm{WFC3}} < 18.5$ mag are 0.06 mag and 0.09 mag, respectively. The second sequence – stars with smaller photometric uncertainties than the median value – visible in both filters originates from stars with instrumental WFC3 colours $F127M_{\mathrm{inst}} - F153M_{\mathrm{inst}}$ close to zero (see Eqs. (4.3) and (4.4) and cf. Fig. 4.5), i.e. blue foreground stars.

After the source detection, the photometric calibration, and the estimation of the astrometric and photometric uncertainties of all NACO and WFC3 datasets, a combined source catalogue for each of the four Quintuplet outer fields was generated using the positions of the first epoch K_s-band data as reference. Therefore, only stars which are detected in the K_s-band in both epochs and in both WFC3 filters are used for further analysis. The detection of a star in both the $F127M$ and the $F153M$ datasets is the requirement for the conversion of its flux from instrumental WFC3 magnitudes into J_s-

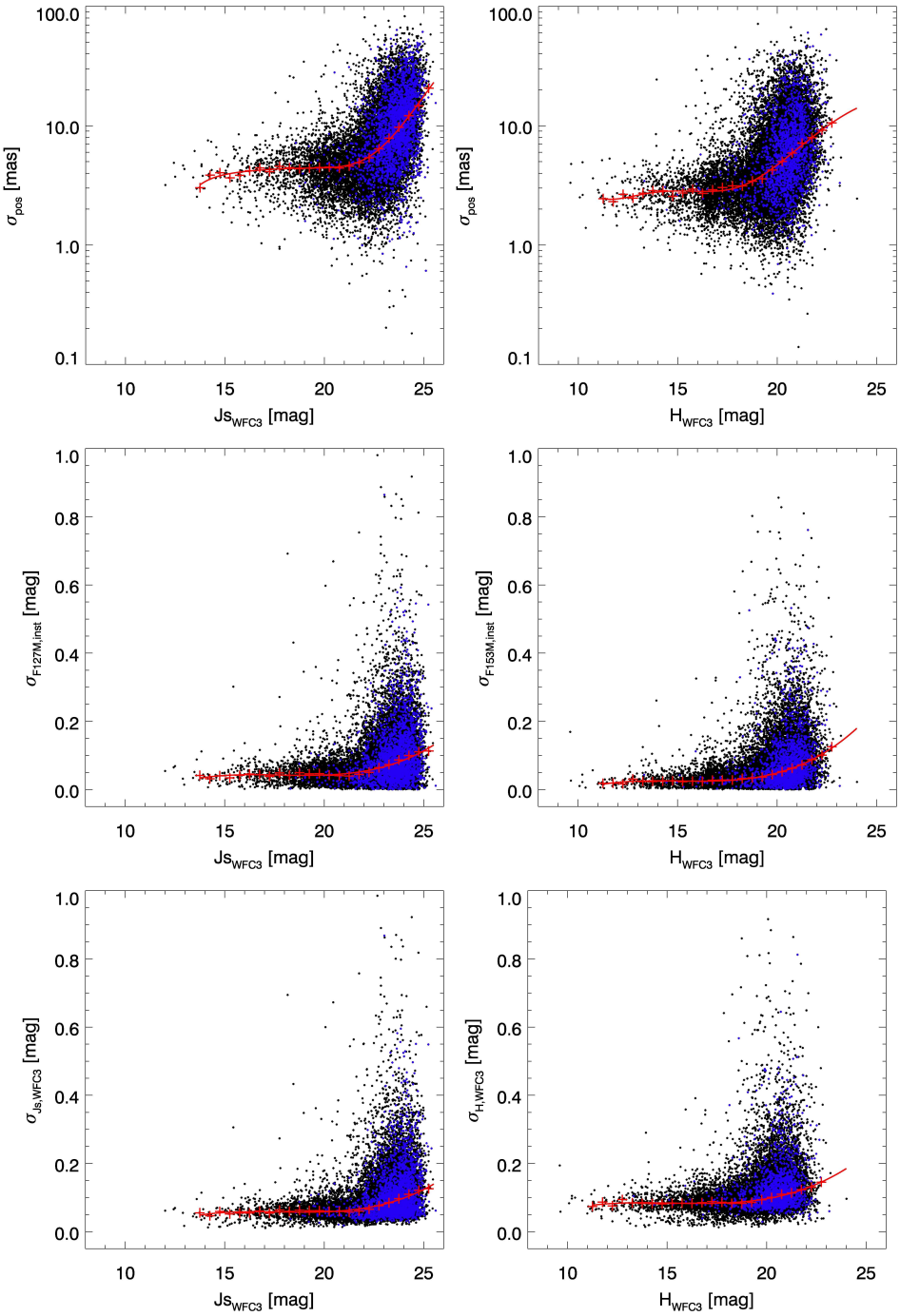

Figure 4.6: *Top panels*: Astrometric uncertainties for the WFC3 $F127M$ (*left*) and $F153M$ datasets (*right*) vs. the respective magnitudes (converted to the ISAAC filter system with Eqs. (4.1) and (4.2)). Stars which are only detected in two of the three auxiliary frames are drawn in blue. The median values within magnitude bins of 0.5 mag and a polynomial fit to the median are shown in red. *Middle panels*: Uncertainties $\sigma_{F127M,\mathrm{inst}}$ and $\sigma_{F153M,\mathrm{inst}}$ of the instrumental magnitudes. *Bottom panels*: Total photometric uncertainties of J_s (*left*) and H (*right*), including the uncertainties of the instrumental magnitudes, the error of the colour term, and the error of the zeropoint (see Eqs. (4.3), and (4.4)).

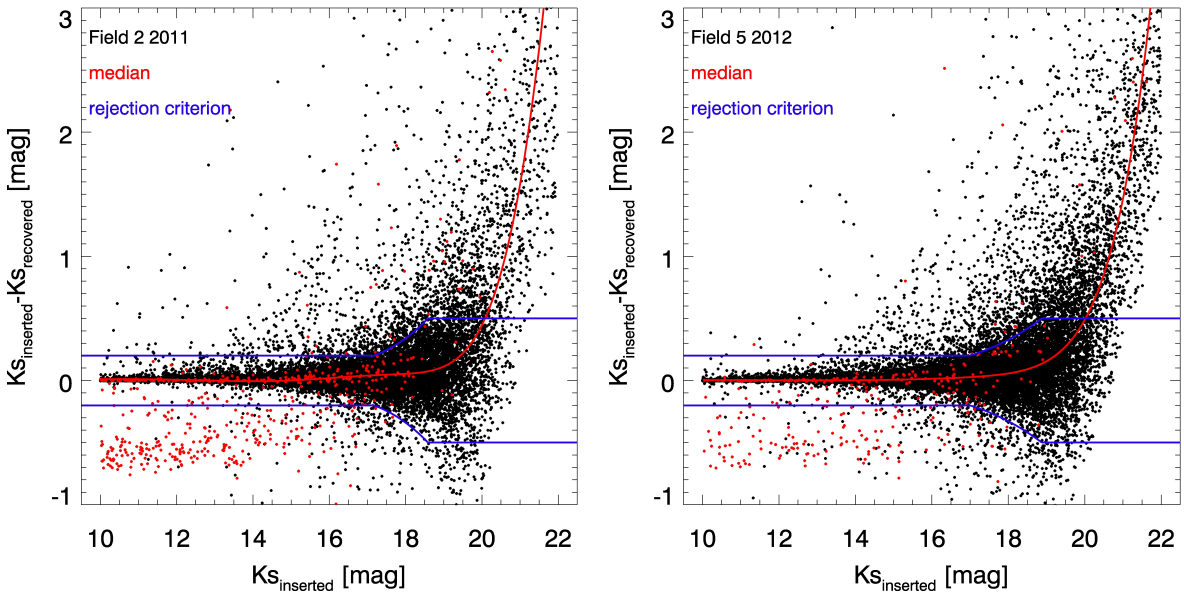

Figure 4.7: Magnitude difference of the inserted and recovered artificial stars plotted vs. the K_s-band magnitude for the second epoch data of Fields 2 (*left panel*) and 5 (*right panel*). The median of the magnitude difference (red line) and the criterion to reject recovered stars based on the magnitude difference (blue line) are shown as well. Artificial stars drawn in red are located in the upper left corner of Field 2 or the upper right corner of Field 5, respectively, and show a systematic zeropoint offset for $K_s < 16$ mag as compared to the rest of the respective field. The affected areas are therefore excluded from the derivation of the completeness maps and the source catalogues of these two fields.

and H-band magnitudes (see Sect. 4.1.2.2).[10]

4.1.3 Completeness

The completeness in the outer parts of the Quintuplet cluster was determined with the same approach as for the central field which follows the method described in Gennaro et al. (2011, see also Sect. 3.3). Artificial star experiments were performed for all NACO and both WFC3 datasets. In order to determine the individual completeness of each star and hence accounting for spatial variations of the completeness due to the presence of bright stars or crowding effects, a set of magnitude dependent completeness maps was generated from the local recovery fractions of artificial stars in the K_s-band for each of the outer fields. In the same vein a set of completeness maps based on the combined artificial star catalogue in J_sH (see Sect. 4.1.3.1) were created for the extracted WFC3 field (see Fig. 4.4). The individual completeness of each star in either the K_s-band or in J_sH was then calculated from the parameters of a Fermi-like function fitted as a function of magnitude to the values of these completeness maps at the position of the respective star (see Sect. 4.1.3.2, Gennaro et al. 2011).

4.1.3.1 Artificial star experiments and overall completeness

The artificial star experiments for the K_s-band data of the outer fields cover the magnitude range from 10.0 to 22.0 mag. The artificial stars were inserted as scaled replica of the PSF of the respective dataset

[10] In the following sections the subscript WFC3 is dropped and $F127M$ and $F153M$ magnitudes converted into the ISAAC filter system are simply referred to as J_s- and H-band magnitudes, respectively.

with the IRAF *addstar* routine of the *daophot* package. For each K_s-band dataset the artificial stars were inserted at the same position and with the same magnitude in both epochs. Per dataset a total of 50400 artificial stars was added, whereas only 100 artificial stars were inserted at a time in order not to influence the crowding properties of the original data. With this number of artificial stars the effective sampling size of the completeness maps within magnitude bins of 0.5 mag and using the 16 nearest neighbours ($\nu = 16$) of each artificial star is approximately $\langle d \rangle = 1.4''$ (cf. Eq. 3.2, see also Appendix A in Gennaro et al. 2011). The source detection and photometry on the artificial star fields was performed in the same way as for the original datasets. In addition to artificial stars which were not detected, stars with measured magnitudes strongly deviating from the inserted magnitudes were treated as not recovered. These artificial stars are either confused with nearby real stars during the matching of the list of inserted artificial stars with the respective source catalogue, or they are blended with other stars. A confusion of an artificial star with a real star can only occur if the artificial star is inserted within the chosen matching radius of = 2 pixel from a real star and if the respective real star is of comparable or larger brightness than the artificial star. These two conditions are fulfilled only for about 1% of the inserted artificial stars even at $K_s = 18$ mag such that confusion is only a minor contribution to the artificial stars which are rejected due to the large deviation of their magnitude. Blending, i.e. the wrong attribution of the flux of nearby stars to a certain star during the PSF fitting, is therefore the major source for large differences between the inserted and recovered magnitudes and naturally influences the measured brightness of faint artificial stars most severely. The rejection criterion was chosen to be magnitude dependent between a minimum absolute magnitude difference of 0.2 mag for the brighter stars and a maximum absolute magnitude difference of 0.5 mag at the faint end. Between these two extremes a fit to the standard deviation of the magnitude difference within magnitude bins of 0.5 mag was applied as the rejection criterion (see Fig. 4.7). As expected, the percentage of stars removed by this rejection criterion increases due to the increased scatter towards fainter stars. For $17.0 < K_s < 17.5$ mag[11], the percentage of artificial stars rejected due to their large magnitude difference ranges between 4% (Field 2, first epoch) and 13% (Field 3 and 4, second epoch) of the recovered stars within this magnitude range. In the end, the influence of the application of the rejection criterion on the mass function slope was found to be negligible. As for Field 1 (see Sect. 3.3), the steep increase of the median of $K_{s,\mathrm{inserted}} - K_{s,\mathrm{recovered}}$ marks the limit for a reliable photometry of fainter stars. The magnitude at which the median exceeds 0.05 mag varies between $K_s = 17.5$ (Field 4, second epoch) and $K_s = 19.0$ mag (Field 2, first epoch) and reflects the general quality of the respective dataset.

For the second epoch data of Fields 2 and 5, a second sequence of stars with large negative magnitude differences of about -0.7 mag is visible for $K_s < 16$ mag. These stars are almost exclusively located in the upper left or upper right image corner of Fields 2 and 5 (Fig. 4.7, red datapoints), respectively, which indicates that the elongated PSF in these regions is not well reproduced by the analytic *daophot* PSF even with a quadratic spatial variation. In total about half of the recovered stars within these regions have magnitude differences < -0.2 mag and are excluded with the default rejection procedure, which would strongly bias the completeness in these image areas. Therefore the affected areas in Fields 2 and 5 (second epoch) are excluded from the derivation of the completeness and the further analysis (see bad area mask shown in Fig. 4.11).

The PSF fitting for the two WFC3 datasets was not performed with the *daophot* package but with the *starfinder* algorithm and the artificial star experiments were done slightly differently compared to the NACO K_s-band datasets. Due to the larger size of the WFC3 images and in general the longer duration of a PSF fitting run with *starfinder* the total number of inserted stars had to be decreased

[11] The proper motion analysis (see Sect. 4.2) and the subsequent analysis are restricted to $K_s < 17.5$ mag.

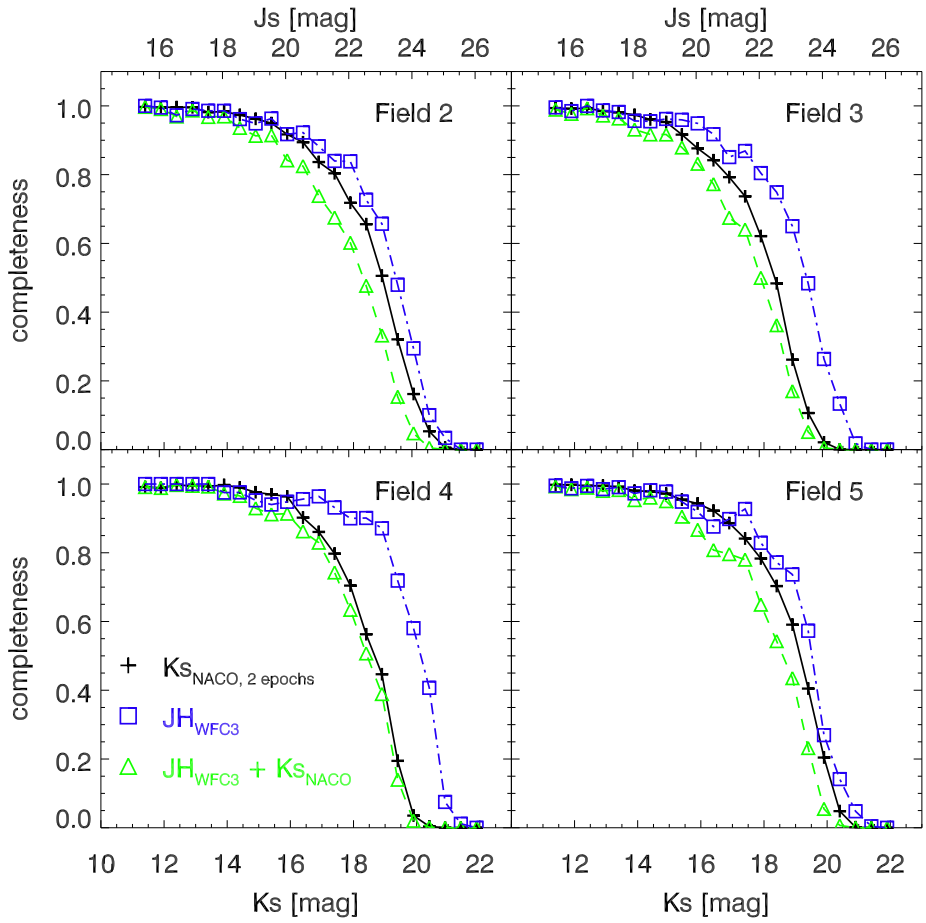

Figure 4.8: Average completeness of artificial stars vs. the respective K_s-band (lower abscissa) or J_s-band magnitude (upper abscissa) for the four Quintuplet outer fields. Only artificial stars within good image areas are included in these plots (cf. Fig. 4.11). The black solid lines show the combined completeness of the K_s-band data in both epochs and the blue dash-dotted lines show the combined completeness in the J_s- and H-band data. The overall completeness in the J_s-, H- and the K_s-band datasets of both epochs of a MS star ($J_s - K_s = 4.15$ mag) is represented by the green line.

and hence the effective sampling size was increased. Within each magnitude bin, 1900 artificial stars were inserted, again 100 stars at a time. The resulting effective sampling size is $\langle d \rangle = 4.1''$ ($\nu = 16$) and hence much coarser than for the NACO K_s-band data. The 100 artificial stars which were inserted together into the respective combined image resided within the same 0.5 mag bin (cf. Sect. 3.3). As in the case of the NACO K_s-band data, the artificial stars were placed at the same position into the $F127M$ and the $F153M$ datasets with a colour of $J_s - H = 2.8$ mag which resembles the (calibrated) colour of the cluster MS[12]. The (calibrated) magnitude ranges of the artificial stars are $J_s = [15.3, 26.3]$ and $H = [12.5, 23.5]$. As for the K_s-band data, recovered artificial stars with strongly deviating magnitudes were treated as not recovered. The rejection criterion varied between a minimum absolute magnitude difference of 0.1 mag and a maximum absolute magnitude difference of

[12] Although the artificial star experiments for the WFC3 data were performed using the instrumental magnitudes $F127M_{\rm inst}$ and $F153M_{\rm inst}$, the magnitudes stated in the text or the figures have been converted into the ISAAC filter system for convenience.

0.6 mag at the faint end. Stars on the MS of the outer Quintuplet fields scatter around $J_s - H = 2.8$ mag and $J_s - K_s = 4.15$ mag (cf. Fig. 4.24). A MS star with $K_s = 17.5$ mag – the applied magnitude cut for the proper motion membership sample (Sect. 4.2.1.2) – therefore has a J_s- and H-band magnitude of ~ 21.65 mag and ~ 18.85 mag, respectively. The percentage of stars rejected due to their large difference of the inserted and the recovered magnitudes for artificial stars in the appropriate 0.5 mag magnitude ranges of $J_s = [21.3, 21.8]$ and $H = [18.5, 19.0]$ are 5.1% and 7.1%, respectively. The median of the magnitude difference exceeds 0.5 mag at $J_s = 22.6$ mag and $H = 19.8$ mag and therefore at about 1 mag fainter magnitudes than of stars on the MS for which the proper motion membership is assessed.

As proper motions can only be determined for stars detected in both epochs, only the combined completeness in the K_s-band within each field is relevant to assess the completeness of the proper motion membership sample established in Sect. 4.2. The combined K_s-band completeness is determined by considering only those artificial stars as detected which are recovered in both epochs. All other stars were marked as lost in the respective combined artificial star catalogue. The same procedure is applied for the $F127M$ and the $F153M$ dataset, as stars have to be detected in both filters in order to convert their instrumental magnitudes $F127M_{\rm inst}$ and $F153M_{\rm inst}$ into J_s- and H-band magnitudes (see Sect. 4.1.2.2). As the number of artificial stars and therefore the position at which they were inserted differ between the artificial stars experiments for the K_s-band and the two WFC3 datasets, a similar determination of the combined completeness in J_sHK_s is not feasible.

Figure 4.8 shows the average completeness[13] in each of the four Quintuplet outer fields determined in magnitude bins of 0.5 mag as a function of magnitude. For the combined J_sH-completeness, the bin boundaries are shifted by 4.15 mag with respect to the bin boundaries of the combined K_s-completeness of both epochs in order to account for the colour of stars on the cluster MS (cf. Fig. 4.24). The spatially averaged completeness in J_sHK_s of MS stars can then be estimated by multiplying the combined K_s-completeness with the combined J_sH completeness in the respective shifted magnitude bins. As correlations of the completeness in the K_s-band and J_s- and H-band datasets, such as local detection losses in the neighbourhood of bright stars, are not accounted for, the overall completeness in J_sHK_s is expected to be slightly underestimated. The large combined completeness in J_sH for $K_s > 16$ mag for Field 4 is due to the small number of bright stars within the used area (cf. Fig 4.4 and 4.11).

4.1.3.2 Completeness maps

Following the method of Gennaro et al. (2011), a set of completeness maps covering the magnitude range $10.0 < K_s < 22.0$ mag in magnitude bins of 0.5 mag was derived from the respective combined artificial star catalogue for each of the four outer fields. Likewise, completeness maps ($15.3 < J_s < 26.3$ mag, bin width 0.5 mag) were generated for the extracted WFC3 field (see Fig. 4.4) using the combined J_sH artificial star catalogue. As mentioned in the previous section, the effective sampling sizes of the completeness maps ($\nu = 16$) were $\langle d \rangle = 1.4''$ and $4.1''$ for the four outer fields observed in the NACO K_s-band and the WFC3 data, respectively. The completeness in each image pixel was then fitted as a function of magnitude with a Fermi-like function using the completeness maps derived for the K_s-band data of the outer fields or the WFC3 data, respectively. The individual completeness value of each star in K_s or J_sH can then be derived from the respective fit parameters at the position of

[13] The term average completeness refers to the fact that it resembles the spatially averaged completeness in the respective magnitude bin, in contrast to the individual completeness values for each star as derived in Sect. 4.1.3.2 which trace the spatial variations of the completeness due to crowding or bright stars.

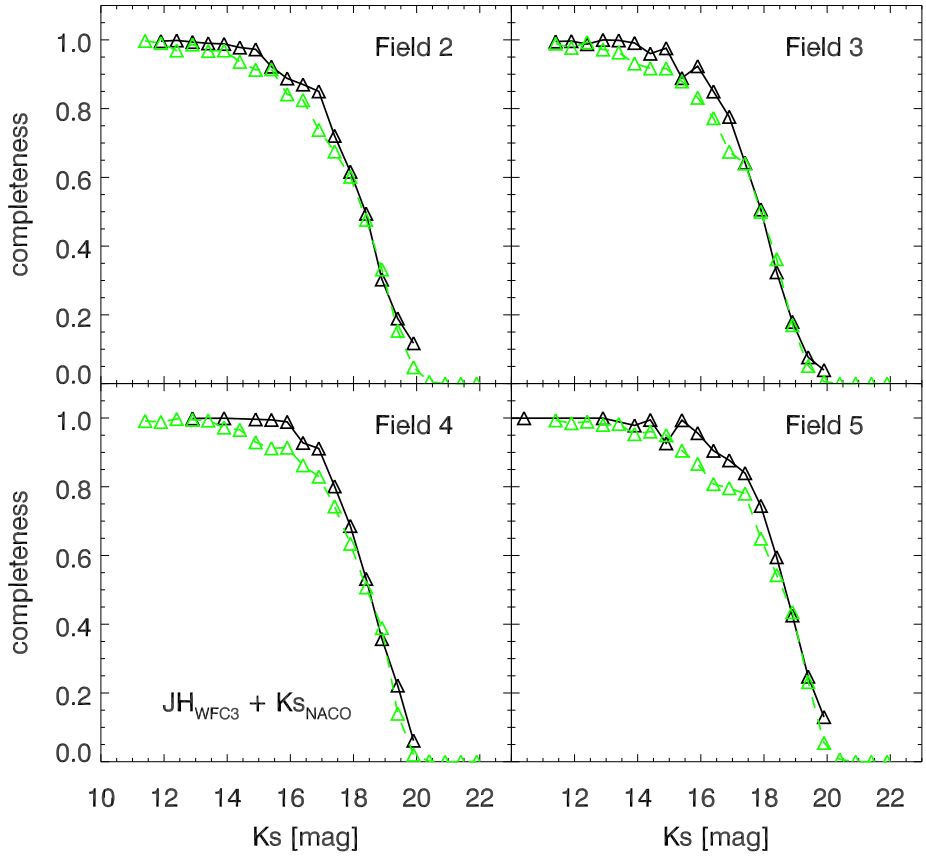

Figure 4.9: Comparison of mean of the individual completeness values in J_sHK_s of observed stars (black line) with the average completeness in J_sHK_s derived directly from the combined artificial star catalogues in K_s-band and J_sH (green line, see Fig. 4.8) within magnitude bins of 0.5 mag width.

the star and its K_s- or J_s-band magnitude. The overall completeness of a star in J_sHK_s is determined as the product of its individual completeness value in the K_s-band and in J_sH.

The average of the individual completeness values of all stars as derived from the completeness maps is expected to resemble the spatial average of the completeness as shown in Fig. 4.8, assuming that stars are uniformly distributed across the field irrespective of their brightness and that no strong spatial variation of the extinction is present. For comparison, the average of the individual completeness values in J_sHK_s within magnitude bins of 0.5 mag width is compared in Fig. 4.9 to the spatial average of the completeness as directly determined from the artificial star catalogues. As the artificial star experiments were designed to trace the completeness of stars on the cluster MS, only the individual completeness values of stars with colours within ±0.5 mag from the cluster MS ($J_s - H = 2.8$ mag, $J_s - K_s = 4.15$ mag) were considered. Apparently, the average of the individual completeness values for $K_s < 17.5$ mag (Field 2 and 3) and $K_s < 18.5$ mag (Field 4 and 5) derived from the spatially resolved completeness maps is larger than the spatially averaged completeness. For $K_s < 17.5$ mag, the maximum difference is about 10% and the mean difference is about 5%. A possibility to explain this discrepancy is that the Fermi-function is not a perfect representation of the drop of the completeness in all image parts. The fit tends to overestimate the completeness in the transition region between a completeness of nearly 100% and the steep decline at the faint end (see Fig. 4.10), i.e. in the magnitude range ($15 < K_s < 18$ mag) the discrepancy is most evident. The actual impact of

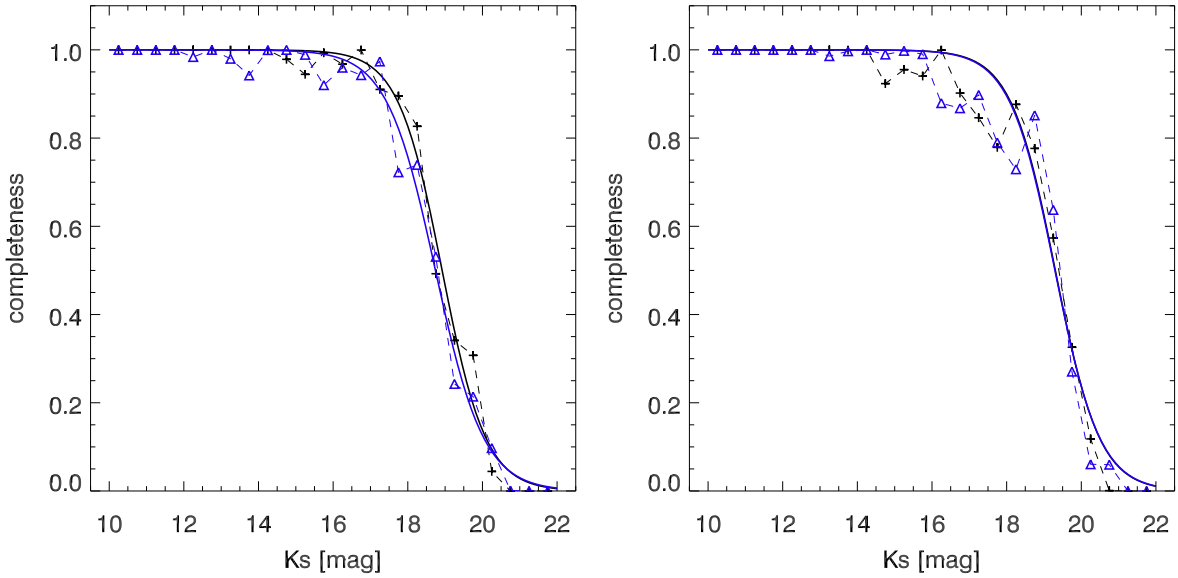

Figure 4.10: Fit of the completeness values at selected pixel positions of the completeness maps of Field 4 with a Fermi-like function as a function of the magnitude. The *left panel* shows an illustrative example of the fit in two regions, where the magnitude dependence of the completeness is well represented by the fitting function. For the examples in the *right panel* the fit overestimates the completeness just before the steep drop of the Fermi-like function due to irregularities in the true recovered completeness values which do not follow a functional form in these selected pixels.

this potential overestimation of the completeness on the mass function and its slope is expected to be small. The minimum of the spatially averaged completeness in J_sHK_s relevant for the derivation of the mass function in the outer fields is about 60% (see Fig. 4.9, Field 3 at $K_s = 17.5$ mag). Assuming that on average the individual completeness values are overestimated by about 10% the maximum percental difference of the logarithm of the number of stars $\log_{10} n$ in the lowermost mass bin is not exceeding 7%. As the spatial completeness variations in the Quintuplet fields are pronounced, especially in the neighbourhood of the bright WR stars or RSGs (such as Q7 in Field 5), and the effect of the slight overestimation of the individual completeness on the mass function slope is expected to be small or even negligible, the individual completeness values are preferred to the spatial average of the completeness as derived from the combined artificial star catalogues and are applied in the derivation of the mass function slope (see Sect. 4.4).

4.1.4 Data selection

In order to use only those image parts with a comparable quality, a bad area mask was generated for each of the four Quintuplet outer fields. The respective mask contains the rejected areas of both epochs of K_s-band data. As the coverage of the dithered frames decreases towards the edges of each dataset, the noise and the number of not repaired bad pixels increases. The bad area masks cover therefore a margin of 30 pixel at the left and right and a 40 pixel margin at the top and bottom edge of each combined image. For Field 2, a pronounced noise pattern at the centre of the left and right edge protruded further into the combined image. The affected areas were additionally covered by the bad area mask for this field (see black dotted lines in Fig. 4.11). As mentioned in Sect. 4.1.3.1, the artificial star experiments performed for the second epoch data of Fields 2 and 5 indicated that the PSF

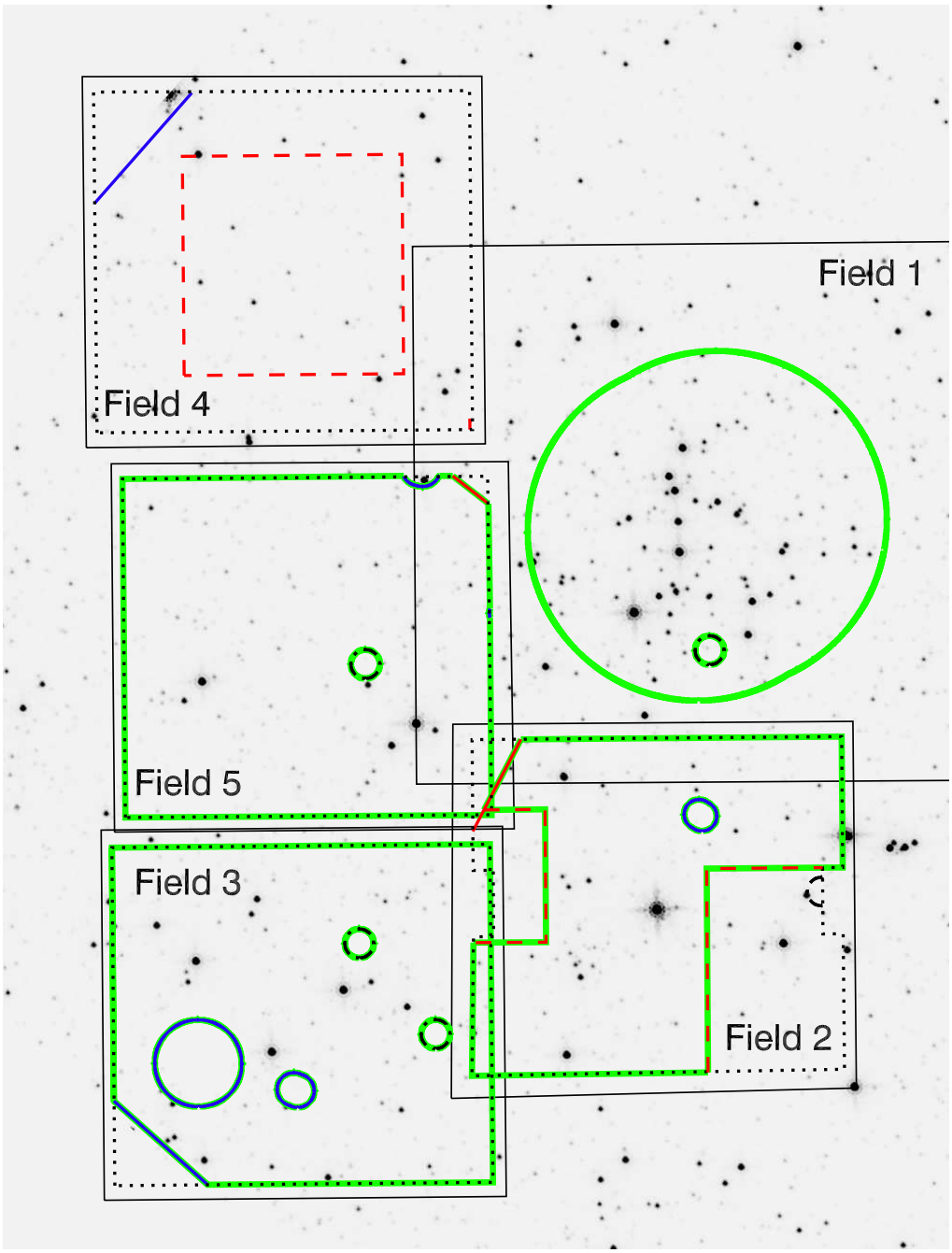

Figure 4.11: Bad area masks plotted on the selected area of the WFC3 *F*127*M* combined image. The black solid lines show the extent of the four Quintuplet outer fields as covered by the NACO K_s-band data. The margin of each field disregarded to avoid areas with low coverage is drawn as black dotted line. The image corners in Fields 2 and 5, where the artificial star experiments indicate that the PSF fitting is unreliable (see Sect. 4.1.3.1), are marked by the red solid lines. Optical ghosts within the NACO data are drawn with black dash-dotted lines. Bad or missing areas in the WFC3 datasets are indicated in blue. For Fields 2 and 4, further selections were performed after inspection of the respective CMD (red dashed lines, see Sects. 4.3.1.2 and 4.3.1.3). The areas which were actually used to derive the MF are enframed in green.

fitting is not reliable in the top left or top right image corner of Field 2 and Field 5, respectively. These corners were therefore covered as well by the bad area mask of Fields 2 and 5 (red solid line). The thus derived bad area masks were applied before the proper motion diagrams (PMDs) of the respective fields were generated[14].

As bright optical ghosts present in Fields 2, 3 and 5 mostly affect the completeness, these image parts were excluded only after the derivation of the proper motion membership sample. Stars appearing in the CMDs of the outer fields (see Sect. 4.3) are required to be detected in both WFC3 datasets. Therefore areas either not covered by the WFC3 datasets or within extended regions of insensitive pixels are included in the bad area masks (blue lines). The smaller, roundish bad areas in the WFC3 data are regions with lowered sensitivity. They are termed 'IR blobs' and originate from areas of reduced reflectivity of the mirror directing the incoming light either to the UVIS or the IR channel (Rajan 2010, Sect. 6.4). The large feature in Field 3 is the so-called 'death star' and consists of unresponsive pixels (Rajan 2010, Sect. 6.8.2).

As described in Sect. 4.3.1.3, parts of Field 2 may be affected by increased extinction as they are devoid of proper motion members within the applied colour selection. The suspicious image areas marked by the red dashed lines in Fig. 4.11 were consequently not treated as probed image area (see Sect. 4.4.1). For Field 4, features in the CMD indicate that either the photometry may be severely influenced by the particularly strong anisoplanatism, or a pronounced spatial variation of the foreground extinction is present in this field. For testing purposes a rectangular selection for this field was applied (see Sect. 4.3.1.2) which is also indicated by the red dashed line in Fig. 4.11.

The areas finally contributing to the MFs of the Quintuplet outer fields are highlighted in green in Fig. 4.11.

4.2 Proper motion membership

The importance of individual proper motions for disentangling the cluster and the field population is even more important for the outer fields than for Field 1 due to the decline of the cluster density profile. As the second epoch data of Field 2 was available almost a year earlier than for Fields 3, 4, and 5 the determination of the individual proper motions was performed first for this field. It also served as test case for the derivation of a proper motion membership sample based on membership probabilities. The analysis of the remaining outer fields was executed in the same way as for Field 2 for consistency.

4.2.1 Proper motion measurement

4.2.1.1 Geometric transformation

The individual proper motions were measured in the same way as for Field 1 using the cluster as frame of reference (see Sect. 3.4.1). Due to the superior AO performance indicated by the smaller astrometric uncertainties for Fields 2, 4 and 5 (see Figs. 4.2 and 4.3), the first epoch data served as the reference epoch for the geometric transformation. For consistency, and because the astrometric uncertainties for the first epoch data of Field 3 are not much larger than the uncertainties in the second epoch, the first epoch was also used as the reference epoch for this field. After matching the respective first and second epoch source catalogues using a preliminary coordinate transformation, cluster star

[14] As the PMD of Field 2 was derived first, a different selection of the good image area based on the weight image from the image combination was adopted. The described bad areas mask of Field 2 was applied after the proper motion membership sample was established.

Table 4.5: Final rms of the geometric transformation between the first and second epoch data of the outer fields.

Field	Timebase (yr)	rms_x [a] mas/yr	rms_y [a] mas/yr
2	3.2	0.4	0.4
3	3.2	0.3	0.3
4	3.2	0.5	0.5
5	3.3	0.3	0.4

Notes. [(a)] The x- and y-axis are orientated east-to-west and south-to-north, respectively.

candidates were selected based on their position in the preliminary PMD, their magnitude, and their colour. As cluster stars are expected to be close to the origin in the PMD (see Sect. 3.4.3) sources to be used as reference sources for the final transformation were required to be within 4.7, 2.7, 4.2 and 5.2 mas/yr for Fields 2, 3, 4 and 5, respectively[15]. To maximise the number of reference stars for the transformation, while at the same time excluding saturated and very faint stars, only cluster candidates in the magnitude range from K_s = 10 to 17 mag (Fields 2 and 5), 10 to 17.5 mag (Field 3) or 10 to 18 mag (Field 4) were selected as cluster star candidates. As for the outer fields the number of cluster stars is much smaller than the number of field stars, the reference sources for the final transformation were additionally required to have colours similar to the cluster MS. For Field 2, only reference sources with $1.3 < H - K_s < 2.3$ mag[16] (see Fig. 3.8) and for Fields 3, 4 and 5 only stars with $3.5 < J_s - K_s < 4.5$ mag (see Fig. 4.24) were used as reference stars for *geomap* to derive the final geometric transformation required to map the positions in the second epoch onto the correct positions in the K_s-band images from the first epoch. The final rms of the geometric transformations are summarized in Table 4.5.

4.2.1.2 Proper motion diagram

The PMDs of the four Quintuplet outer fields are shown in Fig. 4.12. The proper motion uncertainties as defined in Eq. A.3 are displayed as a function of the first epoch K_s-band magnitude in Fig. 4.13. The PMD of Field 2 (top left panel in Fig. 4.12) shows the proper motions in the east-west and north-south direction of all stars with $K_s < 19.0$ mag which corresponds to the magnitude selection applied for Field 1 (Sect. 3.4.2). The scatter of the proper motion is increased compared to the PMD of Field 1 (Fig. 3.6) and the field star distribution becomes more prominent, as expected at increasing distance from the cluster centre. The uncertainty of the proper motion up to a magnitude of 17.5 mag exhibits little scatter with a median value of 0.54 mas/yr, but rises steeply for fainter magnitudes. For Field 2, K_s = 17.5 mag would therefore be a strict, but appropriate magnitude limit. Stars brighter than K_s = 17.5 mag are indicated as blue dots in the top left panel of Fig. 4.12.

The distribution of proper motions parallel and vertical to the Galactic plane for Field 2 is illustrated in Fig. 4.14 (left and middle panel) for stars with $K_s < 19.0$ mag (black) and $K_s < 17.5$ mag (blue). If Fig. 4.14 is compared to the respective histogram plots for Field 1 (Fig. 3.7), it is evident that the ratio of cluster to field stars drops drastically in the outer parts of the cluster even if the faintest stars are excluded. A significant contamination of a proper motion member sample can therefore not be avoided, although the final member sample can be substantially cleaned by applying an additional

[15] The criterion was based on the scatter of stars around the origin in the preliminary PMD.

[16] As the proper motions for Field 2 were derived before the WFC3 data had been calibrated, the H-band magnitudes for the colour selection of the reference sources originate from the ISAAC data.

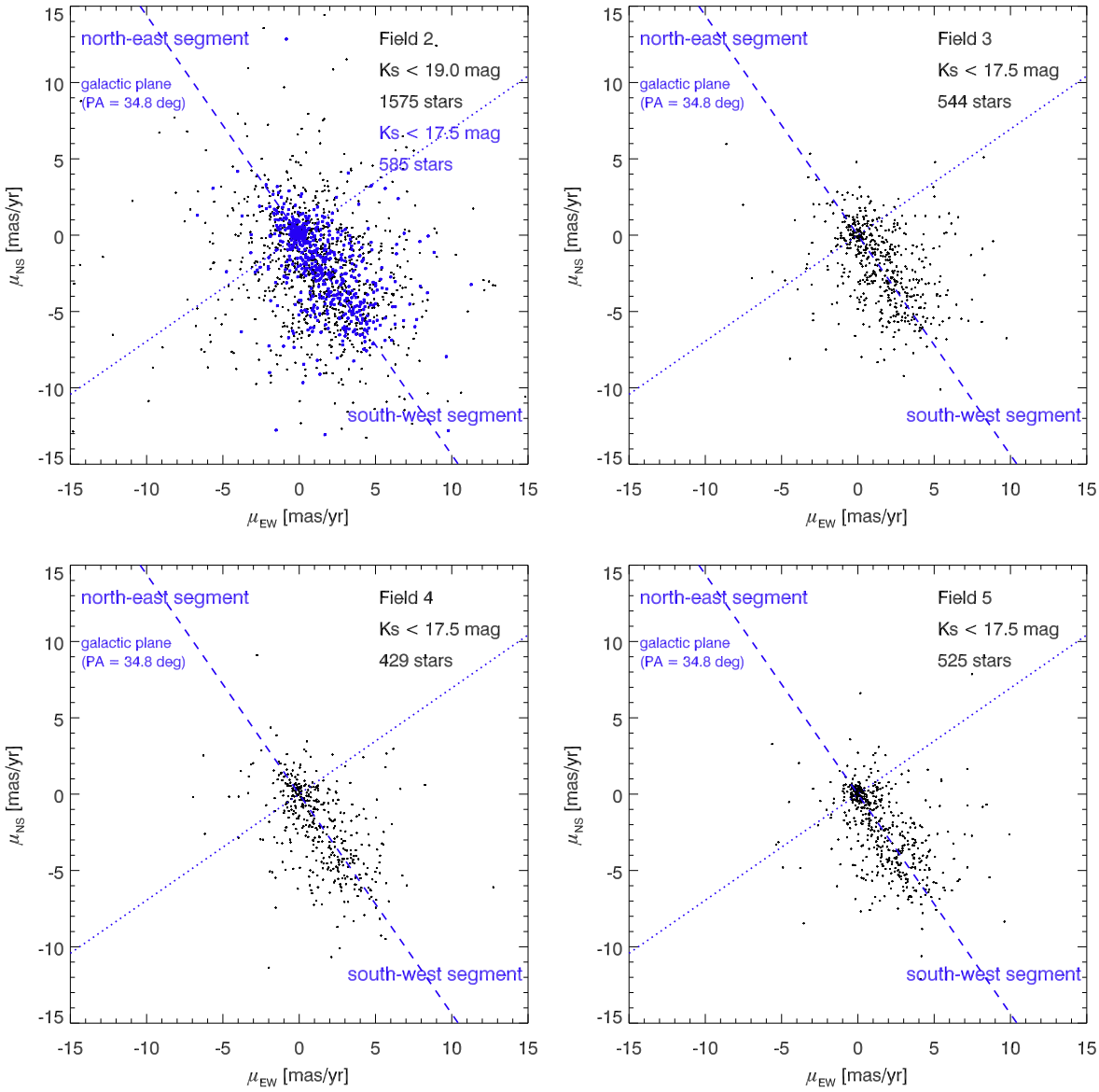

Figure 4.12: PMDs of all four outer fields derived from the NACO K_s-band data. For Field 2 (*top left panel*) all stars with $K_s < 19.0$ mag are drawn for a comparison with the PMD of the central part of the cluster (see Fig. 3.6), whereas for Fields 3, 4 and 5 only stars with $K_s < 17.5$ mag are shown (drawn in blue for Field 2).

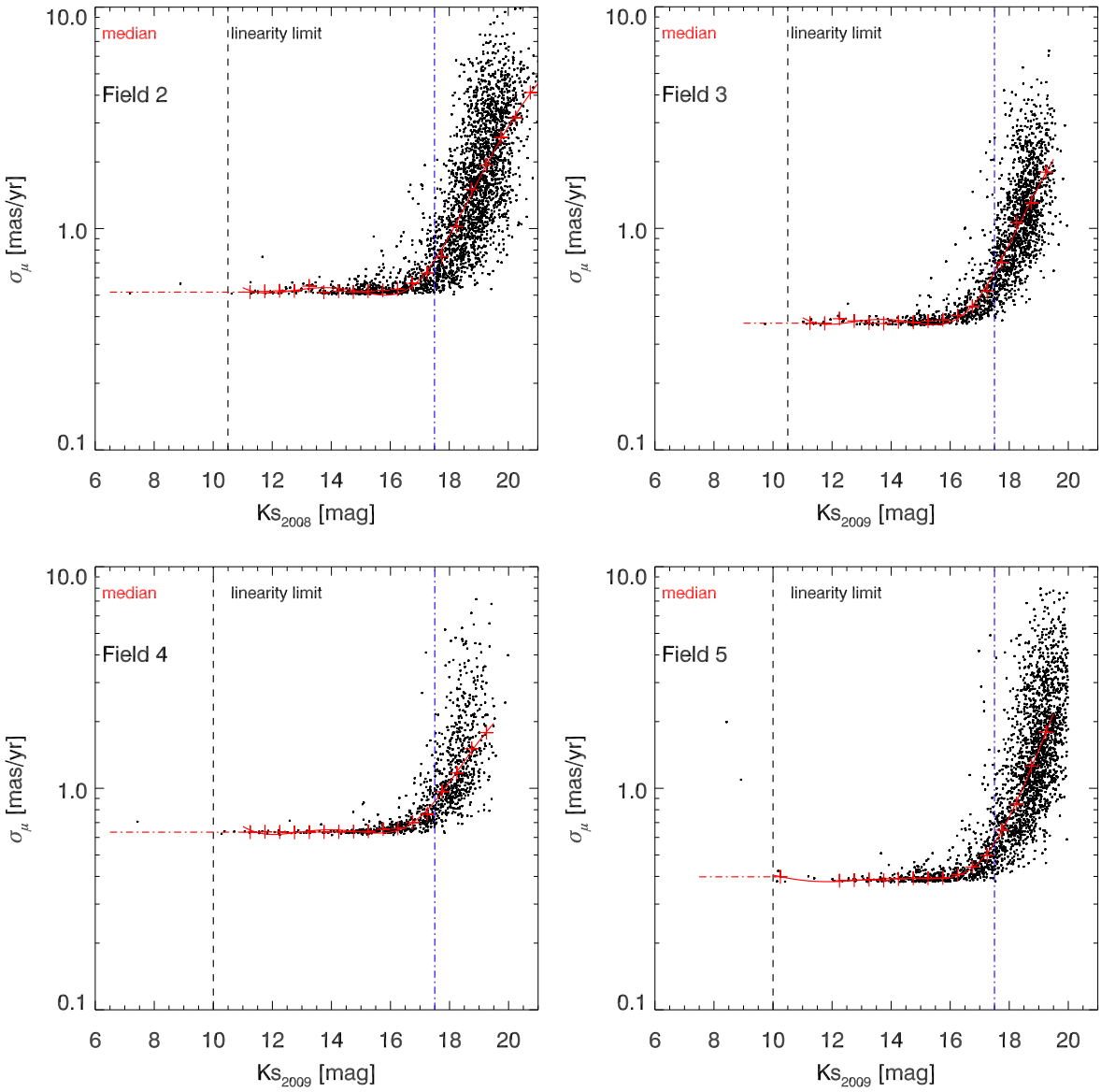

Figure 4.13: Proper motion errors in the Quintuplet outer fields as a function of the K_s-band magnitude of the first epoch. The median of the proper motion errors within magnitude bins of 0.5 mag and a corresponding polynomial fit are shown in red. The blue dash-dotted line indicates the selected magnitude limit at K_s = 17.5 mag for the proper motion membership sample.

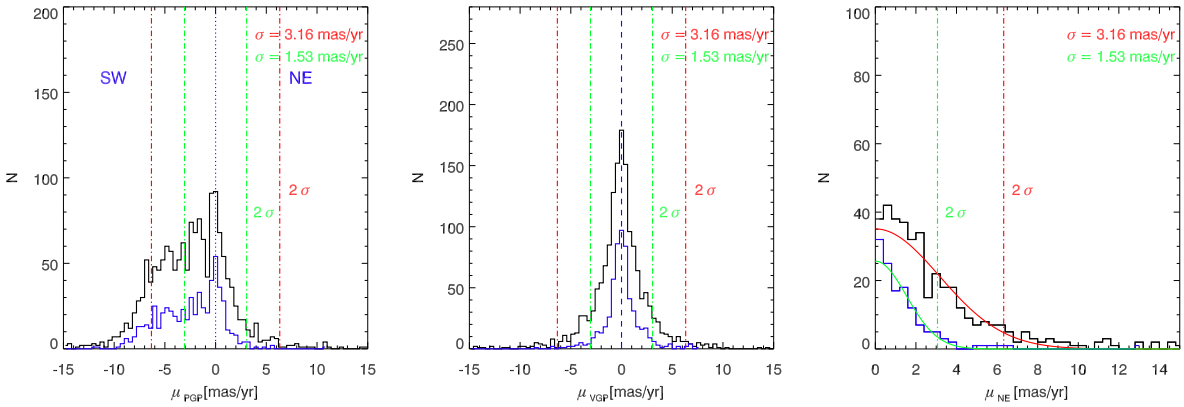

Figure 4.14: Proper motion histograms for Field 2 using all stars with $K_s < 19.0$ mag (black) or $K_s < 17.5$ mag (blue). *Left panel*: Histogram of proper motions parallel to the Galactic plane. *Middle panel*: Histogram of proper motions vertical to the Galactic plane. *Right panel*: Histogram of the two-dimensional proper motions located in the north-east-segment of the PMD. The histogram was fitted with a Gaussian function. The respective $2\,\sigma$ values of the Gaussian fit are indicated as the dash-dotted lines in all three panels (red: $K_s < 19.0$ mag; green: $K_s < 17.5$ mag).

colour selection (cf. Sect. 3.5, Fig. 3.8). Field stars scatter even well into the north-east segment (see also Fig. 4.12), which was for Field 1 considered to be almost devoid of field stars. In the right panel of Fig. 4.14 the proper motion distribution of stars located in the north-east segment in the PMD of Field 2 is fitted by a Gaussian curve for both magnitude selections. Even if only stars with $K_s < 17.5$ mag are used, the retrieved width $\sigma = 1.53$ mas/yr of the Gaussian fit is considerably larger than for Field 1 ($\sigma = 1.13$ mas/yr), where the maximum included magnitude was $K_s < 19.0$ mag. As can be seen in Fig. 4.14 (left panel), the application of a fixed $2\,\sigma$-selection in the PMD for proper motion members would include a large fraction of field stars in the cluster sample.

A magnitude limit of $K_s < 17.5$ mag as for Field 2 to select only stars with comparatively small proper motion uncertainties, i.e. before the step rise towards fainter magnitudes, is also valid for Fields 3, 4 and 5 (see Fig. 4.13). The median value of the scatter of proper motion uncertainties for $K_s < 17.5$ mag is 0.40, 0.66 and 0.41 mas/yr for Field 3, 4 and 5, respectively. The PMDs for these fields in Fig. 4.12 only contain stars brighter than $K_s = 17.5$ mag. In contrast to the other fields, the PMD of Field 5 shows a very distinct clustering at its centre, indicating that either the mapping of both epochs is very accurate or the number of cluster stars is increased compared to the other outer fields. As for Fields 3 and 4 a considerable number of presumable field stars is located in the north-east segment, a Gaussian fit to the distribution of proper motions in that segment will be similarly biased as it is for Field 2.

In order to derive a more reliable membership criterion than a fixed $1\,\sigma$- or $2\,\sigma$-selection in the PMD, the selection of proper motion members for the outer Quintuplet fields was based instead on the membership probability of each star. The method for the determination of the membership probabilities and its application to the PMDs of Fields 2, 3, 4, and 5 are detailed in the next sections.

4.2.2 Determination of membership probabilities

As has been shown in the previous section and as expected for the outer parts of the cluster, the field star population dominates the PMDs of the outer fields even if only stars brighter than $K_s = 17.5$ mag are considered. Due to the larger fraction of field stars even the north-east segment of the PMD is

strongly contaminated (at least for Fields 2, 3, and 4), which biases the Gaussian fit to the histogram of proper motions in this segment. This prevents the derivation of a single σ value as membership criterion as applied in the centre of the Quintuplet cluster (see Chapter 3). The proper motion membership sample in the outer parts of the cluster was hence established differently by determining the membership probability of each star based on its location in the PMD and a fit to the distribution of proper motions of the field and the cluster population. This approach has several advantages compared to selecting all stars within a certain radius from the origin in the PMD, i.e. using a fixed σ-selection criterion: 1.) The membership probability is determined for each star individually. 2.) Individual proper motion errors can be accounted for. 3.) The cluster surface density profile and the position of each star in the observed area can be considered, such that field stars can be identified even if they share the proper motion of the cluster population.

The method to determine the membership probabilities, its application to synthetic datasets in order to assess the method, and finally to the measured PMDs, are detailed in the following sections.

4.2.2.1 Method

The assignment of cluster membership probabilities based on the position of the stars in the PMD was introduced by Vasilevskis et al. (1958). The method was later enhanced to account for the spatial density distribution of cluster stars (Jones & Walker 1988) and the individual measurement errors of the proper motions (Kozhurina-Platais et al. 1995).

The distribution of cluster and field stars in the PMD is described by two bivariate normal distributions (cf. Eq. (16.1.4) in Press et al. 2007):

$$\Phi\left(\boldsymbol{\mu}\,|\,\overline{\boldsymbol{\mu}},\,\boldsymbol{\Sigma}\right) = \frac{1}{2\pi\,|\boldsymbol{\Sigma}|^{1/2}}\,\exp\left(-\frac{1}{2}\,(\boldsymbol{\mu}-\overline{\boldsymbol{\mu}})\cdot\boldsymbol{\Sigma}^{-1}\cdot(\boldsymbol{\mu}-\overline{\boldsymbol{\mu}})\right), \tag{4.5}$$

where $\boldsymbol{\mu} = \binom{\mu_x}{\mu_y}$ is the two-dimensional proper motion of each star, $\overline{\boldsymbol{\mu}}$ the centroid of the (cluster or field) distribution and $\boldsymbol{\Sigma}$ its covariance matrix. If it is for simplicity assumed that the spatial density distributions of cluster and field are both uniform, the probability of a given star n with a proper motion $\boldsymbol{\mu}_n$ to be a cluster member ($p_{n,c}$) is given by

$$p_{n,c} = \frac{\pi_c\,\Phi_c\left(\boldsymbol{\mu}_n\,|\,\overline{\boldsymbol{\mu}}_c,\,\boldsymbol{\Sigma}_c\right)}{\pi_c\,\Phi_c\left(\boldsymbol{\mu}_n\,|\,\overline{\boldsymbol{\mu}}_c,\,\boldsymbol{\Sigma}_c\right) + \pi_f\,\Phi_f\left(\boldsymbol{\mu}_n\,|\,\overline{\boldsymbol{\mu}}_f,\,\boldsymbol{\Sigma}_f\right)}, \tag{4.6}$$

where π_c and π_f are the fractions of stars belonging to the cluster and the field, respectively (cf. Eq. (16.1.5) in Press et al. 2007).

The assumption of a uniform spatial distribution of the cluster stars is in general not valid, except if the observed area on the sky is restricted to the flat core of the surface density profile of the cluster (see e.g. Clarkson et al. 2012) or at large radial cluster distances, where the cluster density profile flattens out and the cluster merges into the field distribution. In most other cases this assumption will result in underestimated membership probabilities for stars located near the cluster centre[17], but overestimated membership probabilities for stars at larger distances (Jones & Walker 1988). To account for a non-uniform spatial distribution of the cluster stars, their fraction π_c in Eqn. (4.6) has to be multiplied by the cluster density profile $\rho_{c,\mathrm{norm}}(x,y)$, which is normalized such that its integral over the observed area A is equal to unity, i.e. $\rho_{c,\mathrm{norm}}(x,y) = \frac{\rho_c(x,y)}{\iint_A \rho_c(x,y)\mathrm{d}x\mathrm{d}y}$. The spatial density distribution of the field stars is

[17] The terms cluster centre and cluster density profile refer in the context of membership probabilities to the centre of the spatial distribution of cluster stars and their spatial number density profile (or surface density profile) and not to the centre of the mass density and the mass density profile, respectively.

assumed to be constant, but has to be normalized in the same way, such that $\rho_{f,\mathrm{norm}} = 1/A$. Throughout this thesis it is assumed, that the cluster is radially symmetric, i.e. $\rho_{c,\mathrm{norm}}(x,y) = \rho_{c,\mathrm{norm}}(r)$. The cluster membership probability of a star with a proper motion of $\boldsymbol{\mu}_n$ and located at a distance r_n from the cluster centre is then given by

$$p_{n,c} = \frac{\pi_c \, \rho_{c,\mathrm{norm}}(r_n) \, \Phi_c \left(\boldsymbol{\mu}_n \,|\, \overline{\boldsymbol{\mu}}_c,\, \boldsymbol{\Sigma}_c\right)}{\pi_c \, \rho_{c,\mathrm{norm}}(r_n) \, \Phi_c \left(\boldsymbol{\mu}_n \,|\, \overline{\boldsymbol{\mu}}_c,\, \boldsymbol{\Sigma}_c\right) + \pi_f \, \frac{1}{A} \, \Phi_f \left(\boldsymbol{\mu}_n \,|\, \overline{\boldsymbol{\mu}}_f,\, \boldsymbol{\Sigma}_f\right)}\,, \tag{4.7}$$

while the probability of the same star belonging to the field population is

$$p_{n,f} = \frac{\pi_f \, \frac{1}{A} \, \Phi_f \left(\boldsymbol{\mu}_n \,|\, \overline{\boldsymbol{\mu}}_f,\, \boldsymbol{\Sigma}_f\right)}{\pi_c \, \rho_{c,\mathrm{norm}}(r_n) \, \Phi_c \left(\boldsymbol{\mu}_n \,|\, \overline{\boldsymbol{\mu}}_c,\, \boldsymbol{\Sigma}_c\right) + \pi_f \, \frac{1}{A} \, \Phi_f \left(\boldsymbol{\mu}_n \,|\, \overline{\boldsymbol{\mu}}_f,\, \boldsymbol{\Sigma}_f\right)}\,. \tag{4.8}$$

In order to determine the kinematic parameters $(\overline{\boldsymbol{\mu}}_c, \boldsymbol{\Sigma}_c, \overline{\boldsymbol{\mu}}_f, \boldsymbol{\Sigma}_f)$ of the bivariate normal distributions of the cluster and field stars and their respective fractions (π_c, π_f), as well as the membership probability $p_{n,c}$ of each star, the expectation-maximisation (EM) algorithm as described in detail in Sect. 16.1 in Press et al. (2007) was used. The algorithm was slightly adopted to support a non-uniform cluster density profile. The cluster density profile itself is not determined by the algorithm, but is assumed to be known. Starting from an initial guess for the centroids of the cluster and the field star distribution in the PMD, the EM algorithm determines the kinematic parameters and fractions iteratively by maximising the likelihood $\mathscr{L}$ (cf. Eqns. (16.1.2) and (16.1.3) in Press et al. 2007):

$$\mathscr{L} = \prod_n P(\boldsymbol{\mu}_n, r_n) \tag{4.9}$$

$$P(\boldsymbol{\mu}_n, r_n) = \pi_c \, \rho_{c,\mathrm{norm}}(r_n) \, \Phi_c \left(\boldsymbol{\mu}_n \,|\, \overline{\boldsymbol{\mu}}_c,\, \boldsymbol{\Sigma}_c\right) + \pi_f \, \frac{1}{A} \, \Phi_f \left(\boldsymbol{\mu}_n \,|\, \overline{\boldsymbol{\mu}}_f,\, \boldsymbol{\Sigma}_f\right), \tag{4.10}$$

where $P(\boldsymbol{\mu}_n, r_n)$ is the probability of finding a star with the measured proper motion $\boldsymbol{\mu}_n$ which is located at a distance r_n from the cluster centre given the kinematic parameters $(\overline{\boldsymbol{\mu}}_c, \boldsymbol{\Sigma}_c, \overline{\boldsymbol{\mu}}_f, \boldsymbol{\Sigma}_f)$ and the fraction of cluster and fields stars (π_c, π_f). Maximising the likelihood $\mathscr{L}$ hence results in obtaining those parameters for the two bivariate Gaussian distributions which can best explain the distribution of stars in the observed PMD, i.e for which the probability of each star to belong to either of the two distributions is maximised for all stars.

The EM algorithm proceeds in two steps, the expectation step and the maximisation step (for a more detailed explanation see Press et al. 2007). In the expectation step the probabilities $p_{n,c}$ and $p_{n,f}$ and the likelihood $\mathscr{L}$ are calculated from the data with Eqs. (4.7), (4.8), and (4.9), respectively, using the estimators of the kinematic parameters $(\overline{\boldsymbol{\mu}}_c, \boldsymbol{\Sigma}_c, \overline{\boldsymbol{\mu}}_f, \boldsymbol{\Sigma}_f)$ and of the fractions of cluster and field stars (π_c, π_f). In the maximisation step these estimators are re-estimated (see Eqns. (16.1.6) and (16.1.7) in Press et al. 2007), using the probabilities $p_{n,c}$ and $p_{n,f}$ calculated in the previous expectation step. Both steps are iterated until the change of the likelihood between two iterations is smaller than a given threshold.

The individual proper motion errors do not enter the computation of the kinematic parameters and the cluster and field fractions with the EM algorithm. Instead the method of Kozhurina-Platais et al. (1995) is applied, where the membership probabilities are re-calculated in a second step using the individual proper motion errors and the kinematic parameters and fractions, as derived above (see also Clarkson et al. 2012). For each star, its membership probability is integrated over the proper motion

Table 4.6: Inserted and retrieved parameters of the synthetic dataset shown in Fig. 4.15.

	$\pi_c{}^c$	$\overline{\mu}_{c,x}$	$\overline{\mu}_{c,y}$	$\overline{\mu}_{f,x}$	$\overline{\mu}_{f,y}$	d^d	$\sigma_{c,x}{}^e$	$\sigma_{c,y}{}^e$	$\rho_c{}^e$	$\sigma_{f,x}{}^e$	$\sigma_{f,y}{}^e$	$\rho_f{}^e$
Input	0.50	0.00	0.00	3.00	-4.32	5.26	0.70	0.70	0.00	1.50	1.87	-0.60
Fit (case 1)^a	0.51	0.03	-0.01	3.04	-4.36	5.29	0.68	0.75	-0.03	1.47	1.80	-0.58
Fit (case 2)^b	0.50	0.01	0.01	3.01	-4.31	5.25	0.68	0.74	0.00	1.48	1.83	-0.59

Notes. $^{(a)}$ Fit of the kinematic components ignoring the spatial positions of the stars. $^{(b)}$ Fit of the kinematic components accounting for the surface density profile of the cluster. $^{(c)}$ $\pi_c = \sum_n^N p_{n,c}/N$, with N being the number of datapoints. $^{(d)}$ Separation of the centroids of the cluster and field distribution. $^{(e)}$ Elements of the covariance matrices of the cluster and the field (Σ_c and Σ_f, cf. Eq. (4.13)). σ_x and σ_y are the standard deviations in the x- and y-direction and ρ is the correlation between proper motions in the x- and y-direction.

error ellipse (see Eq. (6) in Kozhurina-Platais et al. 1995[18]):

$$p_{n,c,err} = \int_{-\infty}^{\infty} \frac{\pi_c \, \rho_{c,\mathrm{norm}}(r_n) \, \Phi_c\left(\boldsymbol{\mu} \,|\, \overline{\boldsymbol{\mu}}_c, \, \boldsymbol{\Sigma}_c\right)}{\pi_c \, \rho_{c,\mathrm{norm}}(r_n) \, \Phi_c\left(\boldsymbol{\mu} \,|\, \overline{\boldsymbol{\mu}}_c, \, \boldsymbol{\Sigma}_c\right) + \pi_f \, \frac{1}{A} \, \Phi_f\left(\boldsymbol{\mu} \,|\, \overline{\boldsymbol{\mu}}_f, \, \boldsymbol{\Sigma}_f\right)} \cdot \frac{1}{2\pi \left|\boldsymbol{S}_n\right|^{1/2}} \exp\left(-\frac{1}{2}\left(\boldsymbol{\mu} - \boldsymbol{\mu}_n\right) \cdot \boldsymbol{S}_n^{-1} \cdot \left(\boldsymbol{\mu} - \boldsymbol{\mu}_n\right)\right) d\boldsymbol{\mu} \tag{4.11}$$

where $\boldsymbol{S}_n$ is the proper motion error matrix of the star n. Equation (4.11) yields the final cluster membership probability of each star.

4.2.2.2 Application to synthetic datasets

The adaption of the C++ code stated in Press et al. (2007) to IDL, the implementation of the cluster density profile in the EM algorithm and the re-estimation of the cluster membership probabilities using the individual proper motion errors were assessed and studied using synthetic datasets. A synthetic dataset encompasses the spatial positions, the proper motions and the proper motion errors of a set of datapoints. The datapoints are divided into two components, with the first component roughly resembling the positional and kinematic features of a stellar cluster, while the second component emulates the properties of stars from the stellar field[19]. The positions of stars, intended to belong to the field component, were uniformly distributed within given boundaries, while the positions of intended cluster stars were for simplicity (but cf. Sect. 4.2.2.3) drawn from a spatial bivariate normal distribution with equal semi-axes. The proper motions of field and cluster stars were drawn from two bivariate normal distributions in the proper motion plane, where the semi-axes of the cluster component were chosen equal and its centroid to be at the origin of the PMD ($\overline{\boldsymbol{\mu}}_c = \mathbf{0}$).

Figure 4.15 shows an example of such a synthetic model with the spatial distribution of stars belonging to the cluster (black dots) or field component (red dots) in the top left panel and the associated PMD in the top right panel, respectively. The parameters of the model are provided in Table 4.6. The cluster and the field components contain both 500 datapoints and their distribution of proper motions were chosen to have a slight overlap.

[18] In the two-dimensional case the denominator of Eq. (6) in Kozhurina-Platais et al. (1995) $\sqrt{2\pi}$ has to be replaced by $2\pi^{m/2} = 2\pi$ (with $m = 2$ being the number of dimensions of the normal distribution).

[19] Datapoints belonging to the cluster or field component of the synthetic model are for simplicity referred to as cluster and field stars, respectively.

Effect of the cluster density profile on the membership probabilities The kinematic parameters and the cluster membership probabilities $p_{n,c}$ were first derived from the PMD without taking into account the spatial positions of the datapoints (i.e. using Eq. (4.6)). They are compared in Table 4.6 and Fig. 4.15 (bottom panels) to the respective properties retrieved if the values of the surface density profile $\rho_{c,\mathrm{norm}}(r_n)$ – calculated at the spatial position of each datapoint – enters the derivation of the kinematic parameters and of the $p_{n,c}$ (Eq. (4.7)). If the spatial positions of the stars remain unaccounted for, the input parameters of the two proper motion distributions are well retrieved by the EM algorithm. This is important as the kinematic parameters directly influence the derived membership probabilities. However, as the value of the membership probability $p_{n,c}$ does only depend on the kinematic parameters and the location of the respective star in the PMD (see Eq. (4.6)), cluster or field stars scattering well into the area of the other distribution can not be attributed to their original distribution anymore. In this example, mostly field stars were misidentified as cluster stars, which is expected from the specific set-up of the model. Due to the relative sharpness of the cluster distribution and the equal number of cluster and field stars distributed across the PMD, all stars located within the $2\,\sigma$-ellipse of the kinematic fit to the cluster distribution have a membership probability of $p_{n,c} > 0.75$ (see Fig. 4.15, bottom left panel). Only a very small number of cluster stars (14) would be misidentified as field stars if $p_{n,c} > 0.75$ would be applied as selection criterion of cluster members. In the overlap region of both distributions outside of the $2\,\sigma$-ellipse of the cluster distribution a few stars with intermediate cluster membership probabilities ($0.25 < p_{n,c} < 0.75$ are found which depending on the chosen selection criterion might be classified as cluster or as field stars. The loss of inserted field stars is reflected in the slightly shorter semi-major axis of the fitted field star distribution compared to the kinematic parameters of the inserted distribution.

The usage of the spatial positions in the derivation of the kinematic parameters and the membership probabilities allows for the identification of field stars located even close to the centroid of the cluster distribution in the PMD if they are located at large distances from the spatial density centre of the cluster (see top left panel of Fig. 4.16). Again, the fitted kinematic parameters of both distributions are very close to the input parameters (see Table 4.6). To establish a proper motion cluster sample a membership criterion has to be selected which maximises the number of recovered cluster stars while minimising the number of residual field contaminants. In the context of membership probabilities the membership criterion p_{crit} is the minimum membership probability of a star to be classified as a proper motion cluster member. To quantify the effect of not accounting (case 1) or accounting for the spatial distribution of the datapoints (case 2), the fractions of stars identified as cluster ($p_{n,c} > p_{crit}$) or field stars ($p_{n,c} \leq p_{crit}$) relative to the number of inserted cluster and field stars was determined in dependence of the membership criterion p_{crit} for both cases. Fig. 4.16 (top right panel) shows the respective fractions of cluster and field stars for case 1 (solid lines) and case 2 (dash-dotted lines) as a function of the chosen membership criterion p_{crit}. In addition to the fraction of stars assigned to the cluster (black) or the field (red), the fractions of inserted cluster and field stars, which were correctly attributed to their parent distribution, are drawn as well (blue and orange lines, respectively). For example, if case 1 and a membership criterion of $p_{crit} = 0.50$ are considered, the fraction of cluster stars relative to the total number of inserted cluster stars (black solid line) is 1.05, hence an additional 5% of the field stars must be misidentified as cluster members at least. As for this synthetic dataset the number of inserted field stars was chosen to be equal to the number of inserted cluster stars, the fraction of field stars (red solid line) is therefore 0.95. The fraction of inserted cluster stars satisfying $p_{n,c} > p_{crit}$ (blue solid line), i.e. the fraction of inserted cluster stars which are correctly identified, is 0.99, while 1% of the inserted cluster stars are misidentified as field stars. As the fraction of recovered cluster stars at $p_{crit} = 0.50$ is 1.05, 6% of the detected cluster stars are in fact field stars contaminating the cluster sample. For case 1 more than 95% of the inserted cluster stars are

retrieved even at $p_{crit} = 0.85$. For smaller values of p_{crit}, the fraction of field stars attributed to the cluster increases to the still moderate value of about 10% at $p_{crit} = 0.05$. It should be noted that this small number of contaminating field stars is also due to the set-up of the model, i.e. the slight overlap of the two proper motion distributions and the large number of cluster stars. For case 2, i.e. with consideration of the cluster density profile, the retrieval of more than 95% of the inserted cluster stars is achieved even at $p_{crit} = 0.90$. Compared to case 1, field stars are more reliably identified with a fraction of contaminating field stars in the cluster sample of less than 3% at $p_{crit} = 0.05$.

In summary the usage of the surface density profile of the cluster for the derivation of the cluster membership probabilities leads to a cleaner cluster sample and will be of greater importance in the case of a significant kinematic overlap of the cluster and field distributions in the PMD in order to avoid a large fraction of contaminating field stars in the proper motion membership sample. The appropriate membership criterion p_{crit} which minimises the number of misidentified cluster and field stars at the same time is expected to depend on the respective overlap of the cluster and field star distributions in the PMD, the relative numbers of cluster and field stars and the shape of the cluster surface density profile. In order to select the optimum value of p_{crit} for a given dataset, it is necessary to determine the dependence of the number of misidentified cluster and field stars as a function of p_{crit} in the same way as illustrated in Fig. 4.16 (right panels) for a synthetic dataset designed to reflect the properties of the respective measured dataset (see Sect. 4.2.2.3).

Effect of individual proper motion uncertainties on the membership probabilities As mentioned above, one advantage of a membership sample based on membership probabilities instead of a fixed σ selection criterion in the PMD as performed for the central part of Field 1 (Chapter 3), is that the individual proper motion errors are reflected in the derived $p_{n,c,err}$. For example, a star located directly at the centre of the cluster distribution in the PMD but with a large proper motion error will loose membership probability compared to a star at the same location but with a small proper motion error.

To study the influence of the individual proper motion errors on the membership probabilities, errors of the proper motion in the x- and y-directions were randomly drawn from a Gaussian distribution with a mean value of 0.6 and a standard deviation of 0.1 and assigned to the datapoints. The membership probabilities were re-calculated with Eq. (4.11), applying the kinematic parameters derived from case 2, i.e. considering the surface density profile (see Table 4.6). The change of the membership probability before and after accounting for the individual proper motion errors is shown in Fig. 4.16 (bottom left panel). For stars located in the area covered by the cluster distribution the probability of belonging to the cluster decreases after the application of the error, i.e. $p_{n,c,err} < p_{n,c}$, with the largest changes in the overlap area of the cluster and the field distribution. Some stars located in the wing of the field distribution towards the overlap area and which are spatially close to the cluster core gain some probability of belonging to the cluster[20].

To understand this behaviour one has to consider the shape of the membership probability distribution in the proper motion plane, the location of the respective star and the two-dimensional Gaussian function representing its individual proper motion error. Fig. 4.17 shows the membership probability distribution for stars located in the outer region of the spatial distribution of the cluster, i.e. for stars with a value of the surface density profile of $\rho_{c,\mathrm{norm}}(r_n) = 0.2 \cdot \rho_{c,\mathrm{norm}}(0)$. The value of $\rho_{c,\mathrm{norm}}(r_n)$ mostly acts as a scaling factor, i.e. for larger $\rho_{c,\mathrm{norm}}(r_n)$ the membership probability distribution expands, while it shrinks for smaller $\rho_{c,\mathrm{norm}}(r_n)$ (cf. Eq. (4.11)). Additionally drawn are the Gaussian

[20]The gain of membership probability for a few stars around the centre of the field star distribution (bottom left panel of Fig. 4.16) is less than 1% and is therefore negligible. These stars are hence not considered in the following.

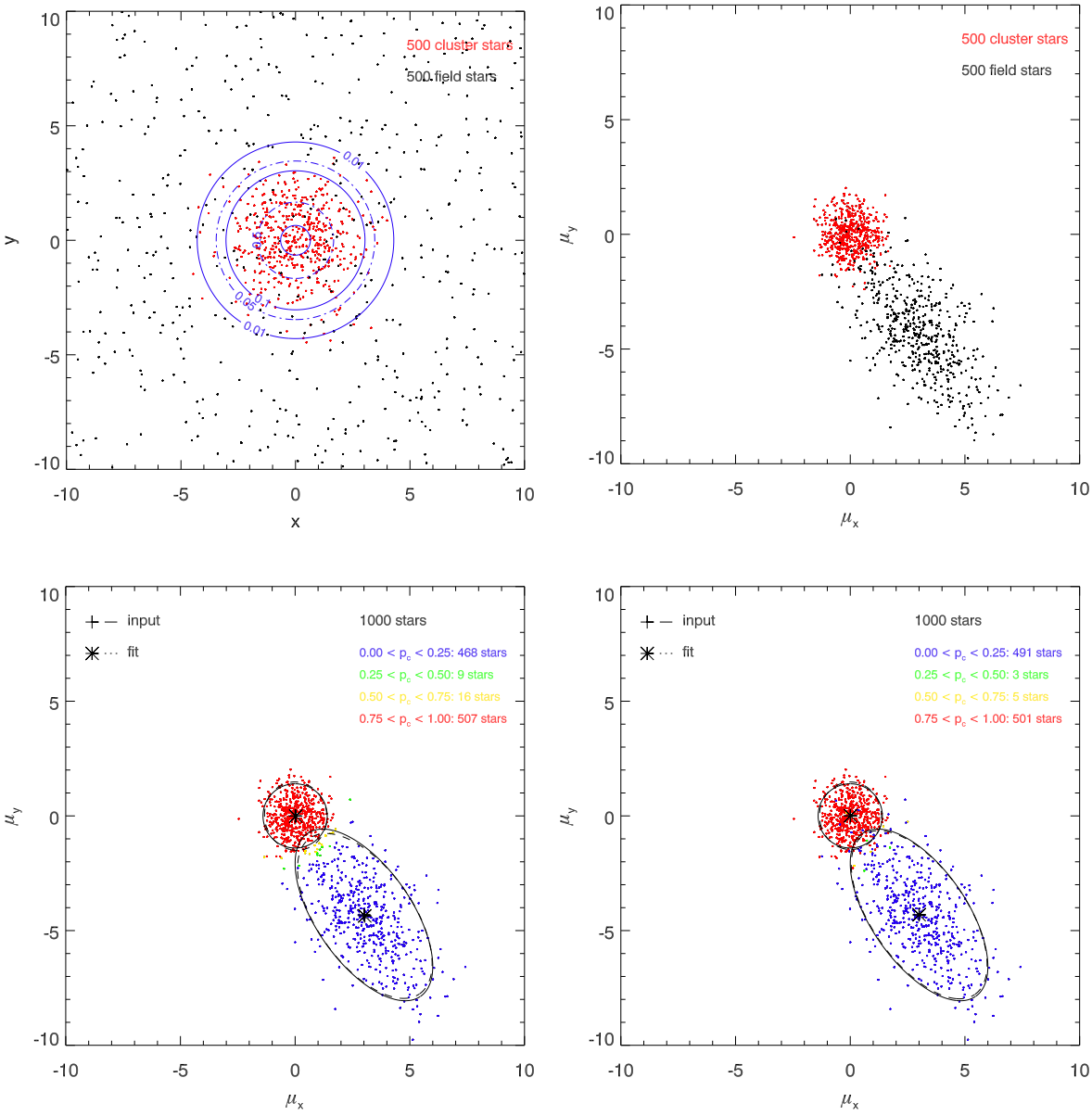

Figure 4.15: *Top left*: Spatial distribution of synthetic datapoints representing either cluster (red) or field stars (black). Field stars are uniformly distributed, cluster stars follow a bivariate normal distribution with equal semi-axes (σ_{pos} = 1.4 for this synthetic dataset). The contours (blue) indicate the radii at which the surface density of cluster stars drops beneath 0.9, 0.5, 0.1, 0.05 and 0.01 of its peak value, respectively. *Top right*: PMD of the synthetic dataset (for the kinematic parameters see Table 4.6). *Bottom left*: PMD with the cluster membership probabilities $p_{n,c}$ as calculated using Eq. (4.6) indicated by the colours. The $2\,\sigma$-contours of the inserted (solid) and fitted cluster and field distributions (dashed) are also shown. Both the kinematic parameters and the $p_{n,c}$ were derived without accounting for the spatial distribution of the stars. *Bottom right*: Same as left, but the kinematic parameters and $p_{n,c}$ were now derived accounting for the surface density profile of the synthetic cluster. The spatial coordinates or proper motions of this synthetic dataset are in arbitrary units.

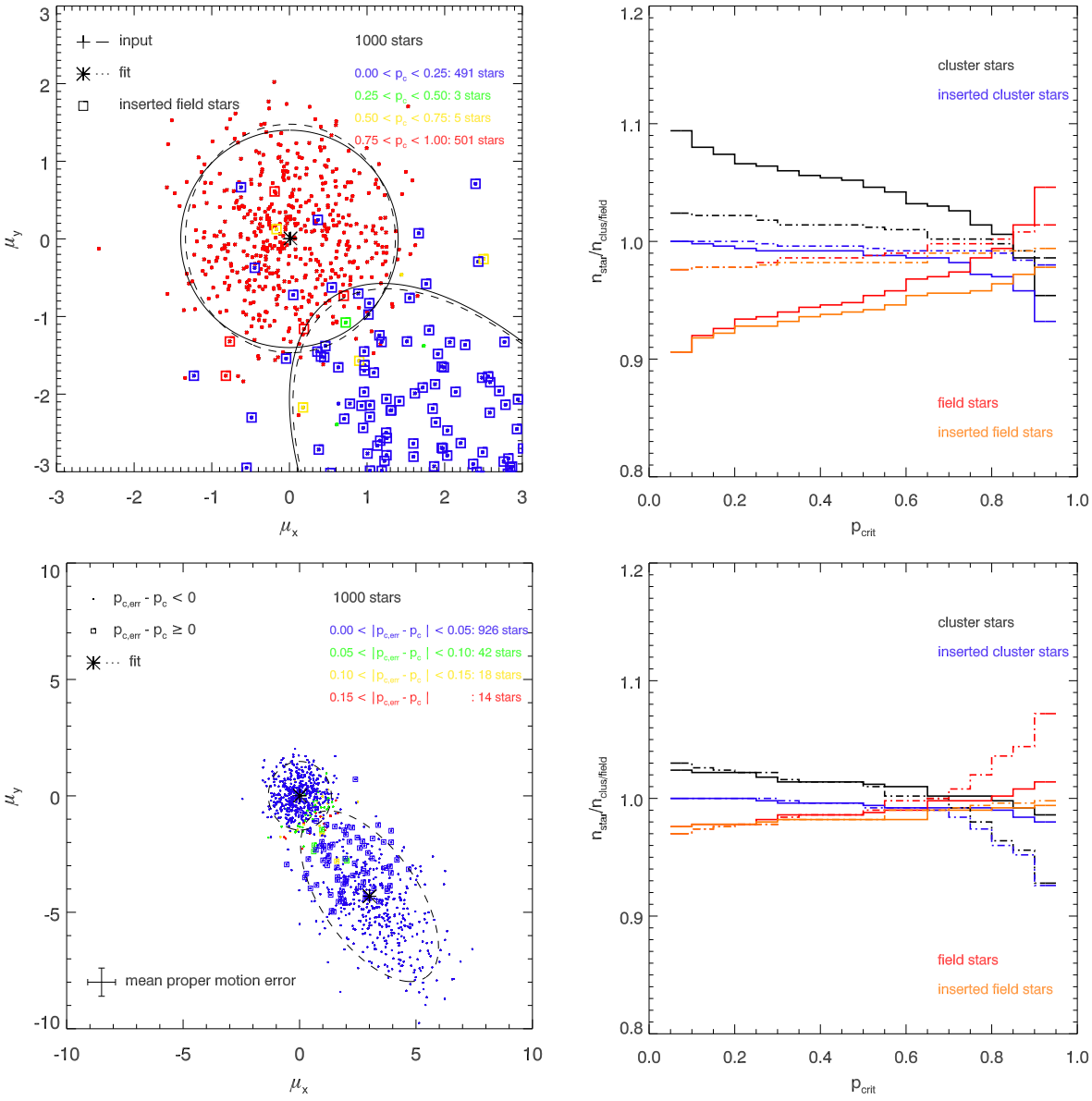

Figure 4.16: *Top left*: Zoom onto the cluster population in Fig. 4.15 (bottom right), i.e. the kinematic parameters and $p_{n,c}$ are derived accounting for the surface density profile. Inserted field stars are indicated by a box. *Top right*: Fraction of datapoints (relative to the total number of inserted cluster or field stars) attributed to the cluster ($p_{n,c} > p_{crit}$) or the field distribution ($p_{n,c} \leq p_{crit}$) as a function of p_{crit} for the synthetic dataset shown in Fig. 4.15. For the solid lines the $p_{n,c}$ values were derived without accounting for the spatial distribution of the stars, whereas the dash-dotted lines show the respective fractions if the spatial distribution was considered (cf. bottom left and bottom right panel in Fig. 4.15). The fraction of misidentified stars either among the cluster or the field stars is significantly lower when the spatial distribution of stars is taken into account. *Bottom left*: Change of the membership probabilities compared to Fig. 4.15 (bottom right) after the membership probabilities have been recalculated with Eq. (4.11) to account for the individual proper motion errors. Datapoints with increased membership probabilities ($p_{n,c,err} - p_{n,c} \geq 0$) are additionally marked with a box point. *Bottom right*: Fraction of datapoints attributed to the cluster or the field distribution as a function of p_{crit}. For the solid lines the membership probabilities were calculated considering the cluster density profile (same as the dash-dotted lines in the *top right panel*), while for the dash dotted lines additionally the individual proper motion errors were accounted for in the derivation of membership probabilities $p_{n,c,err}$.

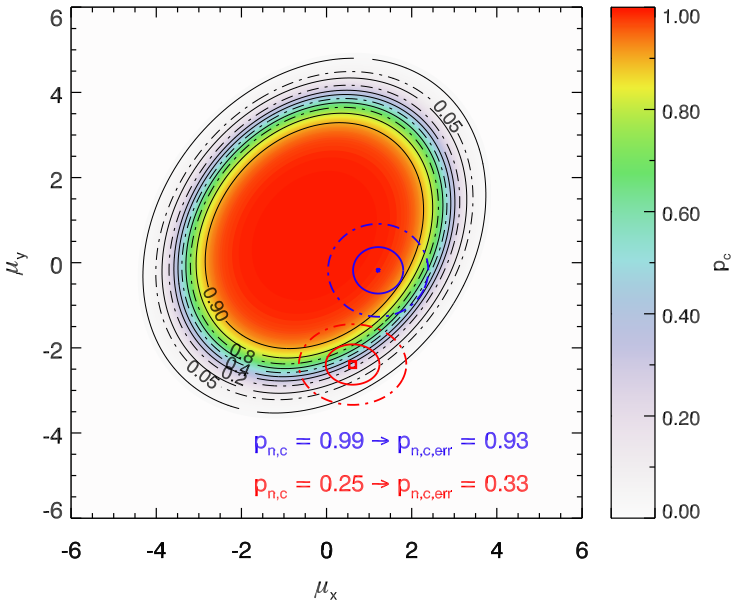

Figure 4.17: Contour plot of the cluster membership probability p_c as determined with the parameters retrieved from the kinematic fit to the synthetic dataset shown in Fig. 4.15 (bottom right panel, cf. Table 4.6, case 2). The contours are drawn for a star located in the outer parts of the spatial distribution of the cluster (see Fig. 4.15, top left panel) with a value of the surface density profile of $\rho_{c,\mathrm{norm}}(r_n) = 0.2 \cdot \rho_{c,\mathrm{norm}}(0)$. The locations and the $1\,\sigma$ and $2\,\sigma$ error ellipses of two stars, one with decreasing ($p_{n,c,err} < p_{n,c}$, blue) and the other with increasing membership probability after the application of the respective proper motion errors ($p_{n,c,err} > p_{n,c}$, red), are shown as well. For the star (blue) close to the most probable region for cluster members in the PMD (red/yellow area), the membership probability decreases as areas with lower values p_c of the membership probability distribution contribute more to the integral in Eq. (4.11) than areas with larger p_c. For a star in the transition region between the cluster and field star distribution the opposite behaviour applies, resulting in $p_{n,c,err} > p_{n,c}$ (red).

error ellipses of two stars from the synthetic model, one with a decreasing membership probability after application of Eq. (4.11) (blue), and a second with an increasing membership probability, $p_{n,c,err} > p_{n,c}$ (red). The distribution of the cluster membership probability p_c features a pronounced plateau with $p_c > 0.90$, which drops off rapidly at larger distances to its centre. The integral in Eq. (4.11) can in principle be considered as the average of the membership probability distribution, weighted with the two-dimensional Gaussian function of the individual proper motion error of the respective star for which the integration is performed. For stars located in the PMD close to or within the plateau of the membership probability distribution, areas with smaller values of the membership probability than at the position of the stars contribute most to the integral of Eq. (4.11), resulting in $p_{n,c,err}$ being smaller than $p_{n,c}$ (e.g. for the star marked in blue in Fig. 4.17). For stars in the transition region between the cluster and field distribution in the PMD the opposite case does apply, where the contributions of areas closer to or within the steeply rising flanks overcome the contributions from the flat tail of the membership probability distribution (red example in Fig. 4.17). As mentioned above, the membership probability after application of the individual proper motion errors does not increase for all stars in the transition region if the surface density profile is accounted for (see Fig. 4.16, bottom left). This is caused by the different extents of the plateau of the membership probability distribution, which depends on the spatial position of the individual stars, i.e its value of $\rho_{c,\mathrm{norm}}(r_n)$. If the surface density profile is not accounted for, only one membership probability distribution applies for all stars and consequently the membership probability of all stars in the transition region does increase after

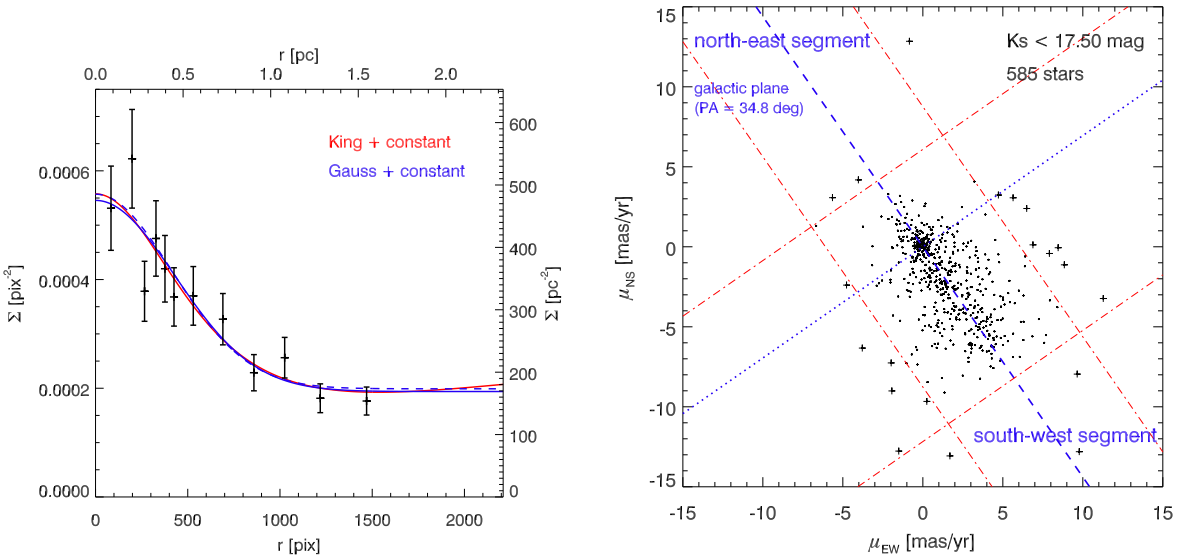

Figure 4.18: *Left panel*: Surface density profile of the Quintuplet cluster derived using cluster members and member candidates located in Field 1 and Field 2, respectively (for details see text). The profile was fitted by a King profile (red) and a Gaussian profile (blue) both with an additive constant term. The profile which was used for the set-up of the synthetic models and the calculation of the membership probabilities is drawn as a blue dashed line. *Right panel*: PMD of Field 2 derived from NACO data obtained in 2008 and 2011. Only stars brighter than $K_s < 17.5$ mag are shown. The red, dash-dotted lines indicate the applied cuts parallel and vertical to the Galactic plane to remove outliers (black crosses), which bias the fit to the distributions of cluster and field stars. Only stars with $|\mu_{\rm VGP}| \leq 5$ mas/yr, $\mu_{\rm PGP,NE} \leq 5$ mas/yr and $\mu_{\rm PGP,SW} \geq -10$ mas/yr are used for the fit.

application of Eq. (4.11).

In Figure 4.16 (bottom right panel), the fractions of cluster and field stars before and after re-calculating the membership probabilities with Eq. (4.11) are compared. Accounting for the individual proper motion error leads to a decrease of the fraction of retrieved cluster stars which for this specific synthetic model is only significant for $p_{crit} > 0.7$.

4.2.2.3 Application to synthetic models of Field 2

To be able to derive a valid cluster membership criterion based on the membership probabilities for the observed PMDs of the outer fields and to quantify the potential losses of cluster stars and the contamination by field stars, a set of synthetic models were designed to represent the spatial density distribution and the PMD of Field 2. This field served as template as its second epoch was available almost a year earlier than the second epoch data of the other fields.

The cluster density profile for the Quintuplet cluster was derived assuming radial symmetry and using the stellar positions of cluster members in Field 1 from the final cluster sample (see Sects. 3.4.3 and 3.5) and of a preliminary selection of cluster candidates in Field 2. The selection of cluster candidates for Field 2 was based on the PMD with a limiting magnitude of $K_s = 17.5$ mag as the proper motion errors increase very steeply towards fainter magnitudes (see Fig. 4.13). As the ratio of field to cluster stars is strongly increased compared to Field 1 (cf. Figs. 3.7 and 4.14), the fit to the histogram of proper motions located in the north-east segment of the PMD is affected by field stars scattering well beyond the origin into the north-east segment as discussed in Sect. 4.2.1.2. The width of the fitted Gaussian (see right panel of Fig. 4.14) is hence too large for an effective distinction

between cluster and field stars. Instead, the same proper motion membership criterion as for Field 1 was applied to Field 2, and all stars within a radius of 2.26 mas/yr from the origin of the PMD were selected as preliminary cluster member candidates. The positions of cluster members with magnitudes brighter than $K_s = 17.5$ mag found in Field 1 and Field 2 were transformed to a common coordinate system using the positions of common stars in the overlap region to determine the relative offsets of both fields. The cluster centre was derived from the final cluster sample in Field 1 using Eqns. (II.3) and (II.6) in Casertano & Hut (1985, number of nearest neighbours $j = 6$) and is located about 1″ to the south-west of the Quintuplet star Q12 (see Fig. 1.1). The radial distance to this centre was derived for the cluster members and member candidates with $K_s < 17.5$ mag in Field 1 (central part, 315 stars) and Field 2 (250 stars), respectively, and the stars were assigned to equal-number annuli. Each annulus was scaled by its area, i.e. the number of stars within each annulus was divided by the number of image pixels located within the respective annulus, where only pixels within the used detector areas, and for Field 1 only pixels located within the central parts ($r < 500$ pixel, see Sect. 3.4.2), were counted.

Figure 4.18 (left panel) shows the cluster density profile, where the spatial density was determined within 12 annuli containing 47 or 48 stars each. A King profile (red line, see Eq. (14) in King 1962) as well as a Gaussian function (blue line), both with an additive constant term, were used to fit the observed surface density profile. As both profiles agree well, for the sake of simplicity the Gaussian profile was adopted which yielded consistent fits to the surface density profiles derived using 8, 10, 12, 14, 16, 18, and 20 annuli. The retrieved parameters of the Gaussian fits were averaged and adopted as the values to set up the synthetic models for Field 2:

$$f_c(r) = 0.00036\, e^{-\frac{1}{2}\left(\frac{r[\mathrm{pixel}]}{416}\right)^2} + 0.00020\,. \tag{4.12}$$

It should be noted that for the set-up of the synthetic models and the determination of the membership probabilities not the absolute values of the peak and the additive constant are relevant, but only their ratio, as the surface density profile has yet to be normalized to serve as input for Eq. (4.7).

The presence of the constant term is not expected and indicates either that the selection of member candidates for Field 2 contains still a number of field stars or that the cluster extends beyond the radius covered by the NACO observations. The derived surface density profile (Eq. (4.12)) can therefore only be regarded as preliminary and has to be revised once a clean, complete membership sample is established for Field 2. Nevertheless, the derived profile is sufficient to set up the positions of the synthetic models of Field 2, and to determine the membership probabilities. As all stars within Field 2 have a distance to the cluster centre of more than 525 pixel and are hence mostly located in the tail of the cluster density profile (see left panel in Fig. 4.18), only 13% of the model datapoints which represent the cluster stars (and are called such for simplicity for the remainder of this section) were distributed following the Gaussian profile (without the constant term). The expected effect of the surface density profile on the membership probabilities of stars located in this field is therefore small or even negligible. The positions of the remaining 87% of the cluster stars and of course of all field stars were uniformly distributed within the range in the x- and y-position defined by the extent of the combined image of Field 2.

As mentioned above, the proper motion errors and their scatter heavily increase towards fainter magnitudes (see Fig. 4.13), which is expected to bias the kinematic parameters derived from a fit to the measured PMD (see Appendix D in Clarkson et al. 2012). To avoid this kind of bias the derivation of a clean cluster sample based on membership probabilities for Field 2 is restricted to stars brighter than $K_s = 17.5$ mag. Of the remaining 585 stars in the PMD, 20 stars with proper motions strongly deviating from both the distributions of field and cluster stars were excluded as outliers (see right panel

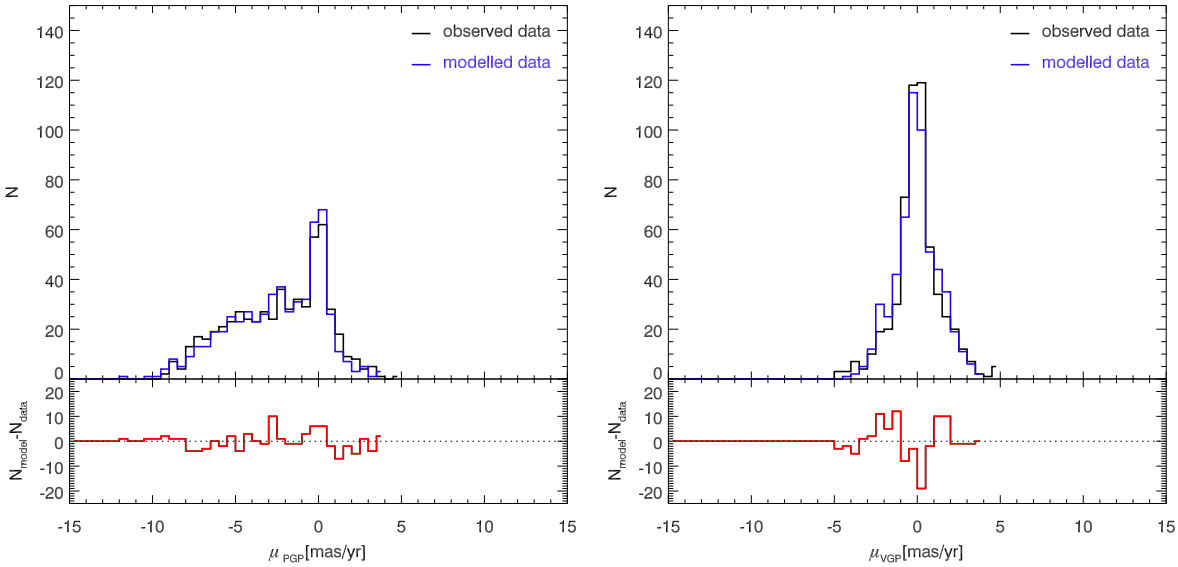

Figure 4.19: Histograms of the proper motions parallel (*left panel*) and vertical to the Galactic plane (*right panel*). The histograms in black represent the measured proper motions in Field 2 (NACO 2008 - NACO 2011) for stars with $K_s < 17.5$ mag. The histograms in blue show the modelled proper motions of one of the ten models designed to match the observed distribution of the proper motions (see text and Fig. 4.20). The residua between the observed data and the model are drawn in red.

in Fig. 4.18). As only two components are assumed in the kinematic fit to the distribution of stars in the PMD, the inclusion of these outliers would introduce a strong bias of the retrieved kinematic parameters. Most of these removed stars have close neighbours on the image, which are partly not detected in the less-well resolved K_s-band dataset from 2011, but which do affect in this dataset the fitted centroids of the detected stars, such that their proper motions are not reliable. The synthetic models are consequently designed to resemble the measured PMD after exclusion of these outliers.

To generate a set of synthetic models, a total of 12 parameters which determine the distribution of cluster and field stars in the PMD can be varied:

$$\begin{gathered} n\,,\ \pi_c\,,\ \overline{\boldsymbol{\mu}}_c = \begin{pmatrix} \overline{\mu}_{x,c} \\ \overline{\mu}_{y,c} \end{pmatrix},\ \overline{\boldsymbol{\mu}}_f = \begin{pmatrix} \overline{\mu}_{x,f} \\ \overline{\mu}_{y,f} \end{pmatrix}, \\ \boldsymbol{\Sigma}_c = \begin{pmatrix} \sigma^2_{x,c} & \rho_c\,\sigma_{x,c}\,\sigma_{y,c} \\ \rho_c\,\sigma_{x,c}\,\sigma_{y,c} & \sigma^2_{y,c} \end{pmatrix},\ \boldsymbol{\Sigma}_f = \begin{pmatrix} \sigma^2_{x,f} & \rho_f\,\sigma_{x,f}\,\sigma_{y,f} \\ \rho_f\,\sigma_{x,f}\,\sigma_{y,f} & \sigma^2_{y,f} \end{pmatrix} \end{gathered} \tag{4.13}$$

where n is the total number of stars, π_c the fraction of cluster stars, $\overline{\boldsymbol{\mu}}_c$ and $\overline{\boldsymbol{\mu}}_f$ denote the centroids of the cluster and field star distributions, $\boldsymbol{\Sigma}_c$ and $\boldsymbol{\Sigma}_f$ are the respective covariance matrices with the standard deviations σ_x and σ_y in the x- and y-direction and the correlation ρ between the proper motions in the x- and y-direction.

As the synthetic models are to resemble the measured PMD, the number of parameters can be reduced. The number of simulated stars is set to 565, i.e. the number of stars in the measured PMD. The distribution of cluster stars is centred at the origin ($\overline{\mu}_{x,c} = \overline{\mu}_{y,c} = 0$) and assumed to be circular ($\sigma_{x,c} = \sigma_{y,c}$, $\rho_c = 0$), which is expected if the proper motion errors in the x- and y-direction are of comparable size. As the semi-major axis of the field star distribution runs approximately parallel to the Galactic plane (P.A. = 34.8°), $\overline{\mu}_{y,f}$ is determined by the choice of $\overline{\mu}_{x,f}$, and $\sigma_{y,f}$ has to be chosen

Table 4.7: Inserted and retrieved properties of the two bivariate normal distributions representing the cluster and the field stars in the PMD of the 10 synthetic datasets (cf. top right panel in Fig. 4.20).

	d^b mas/yr	${\theta_c}^c$ °	${\theta_f}^c$ °	${a_c}^d$ mas/yr	${b_c}^e$ mas/yr	${a_f}^d$ mas/yr	${b_f}^e$ mas/yr
Input	3.07	0.0	34.7	0.40	0.40	2.73	1.53
Fit[a]	3.06 ± 0.12	66.7 ± 38.7	35.0 ± 1.7	0.42 ± 0.03	0.36 ± 0.01	2.79 ± 0.08	1.50 ± 0.06

Notes. [(a)] Mean values and standard deviations from the kinematic fitting of the 10 synthetic models. [(b)] Separation of the centroids of the bivariate normal distributions representing the cluster and the field stars. [(c)] Position angle (east of north) of the semi-major axis of the cluster or the field star distribution. [(d)] Semi-major axis of the $1\,\sigma$ ellipse. [(e)] Semi-minor axis of the $1\,\sigma$ ellipse.

as a function of $\sigma_{x,f}$ and ρ_f. The remaining five free parameters were varied in an appropriate range of values: $\pi_c = [0.10, 0.40]$ (step size = 0.05), $\overline{\mu}_{x,f} = [1.5, 2.5]$ (step size = 0.25), $\sigma_{x,c} = [0.10, 1.00]$ (step size = 0.10), $\sigma_{x,f} = [1.5, 2.5]$ (step size = 0.25), and $\rho_f = [-0.8, -0.4]$ (step size = 0.1)[21]. For every generated model the proper motion histograms parallel (PGP) and vertical to the Galactic plane (VGP) were subtracted from the respective measured proper motion histograms of Field 2 (see Fig. 4.19) and the sum of the absolute values of the residua $R = N_{\rm model} - N_{\rm data}$ (see inserts in Fig. 4.19) in all bins was determined ($R_{\rm total,PGP}$ and $R_{\rm total,VGP}$). The mean of the added residua of the histograms in both directions $\overline{R}_{\rm total} = (R_{\rm total,PGP} + R_{\rm total,VGP})/2$ was used to assess the agreement between the modelled and measured PMD. For each set of parameters 100 models were generated and the mean, the minimum and the maximum values of $\overline{R}_{\rm total}$ were determined to judge the agreement with the measured proper motion data. Due to the large number of combinations of parameter values which yield satisfyingly small values of $\overline{R}_{\rm total}$, the ranges of the different parameters could only be slightly reduced. Furthermore, the retrieved $\overline{R}_{\rm total}$ of different realisations generated with the same set of parameter values scatter significantly. It is hence not possible to decide unambiguously on a set of parameters. Therefore, the PMDs of 10 parameter sets which yielded the smallest minimum values of $\overline{R}_{\rm total}$ (ranging from 86 to 91) were compared visually with the measured PMD and the model with the best agreement was selected: $\pi_c = 0.20$, $\overline{\mu}_{x,f} = 1.75$, $\sigma_{x,c} = 0.40$, $\sigma_{x,f} = 2.0$, $\rho_f = -0.50$. For the selected best-fit model, 10 synthetic PMDs with values of $\overline{R}_{\rm total}$ not exceeding the previously retrieved minimum value of $\overline{R}_{\rm total} = 90$ for this parameter set by more than two (i.e. $\overline{R}_{\rm total} \leq 92$) were generated (see Fig. 4.19 and top left panel in Fig. 4.20). It should be noted that the purpose of the modelling was not to determine the kinematic parameters of the real cluster and field populations, but to generate synthetic datasets closely resembling the measured PMD (and the cluster density profile) for Field 2, which are then to be used to derive a valid cluster membership criterion p_{crit} based on the membership probabilities.

For each of the 10 generated models the kinematic parameters and the membership probabilities according to Eq. (4.7) were determined with the EM algorithm (see top right panel in Fig. 4.20). The position angles θ of the semi-major axis (east of north in the PMD) and the lengths of the semi-major and semi-minor axis of the $1\,\sigma$-ellipses of the cluster and field star distribution were derived from the eigenvectors and eigenvalues of the respective covariance matrices $\mathbf{\Sigma}_c$ and $\mathbf{\Sigma}_f$. Their mean values and the mean values of the centroids of the field and cluster distribution are compared in Table 4.7 with the respective input values common to all 10 models. The centroids of the cluster and the field

[21] Ranges and step sizes of $\overline{\mu}_{x,f}$, $\sigma_{x,c}$, $\sigma_{x,f}$ are in units of mas/yr.

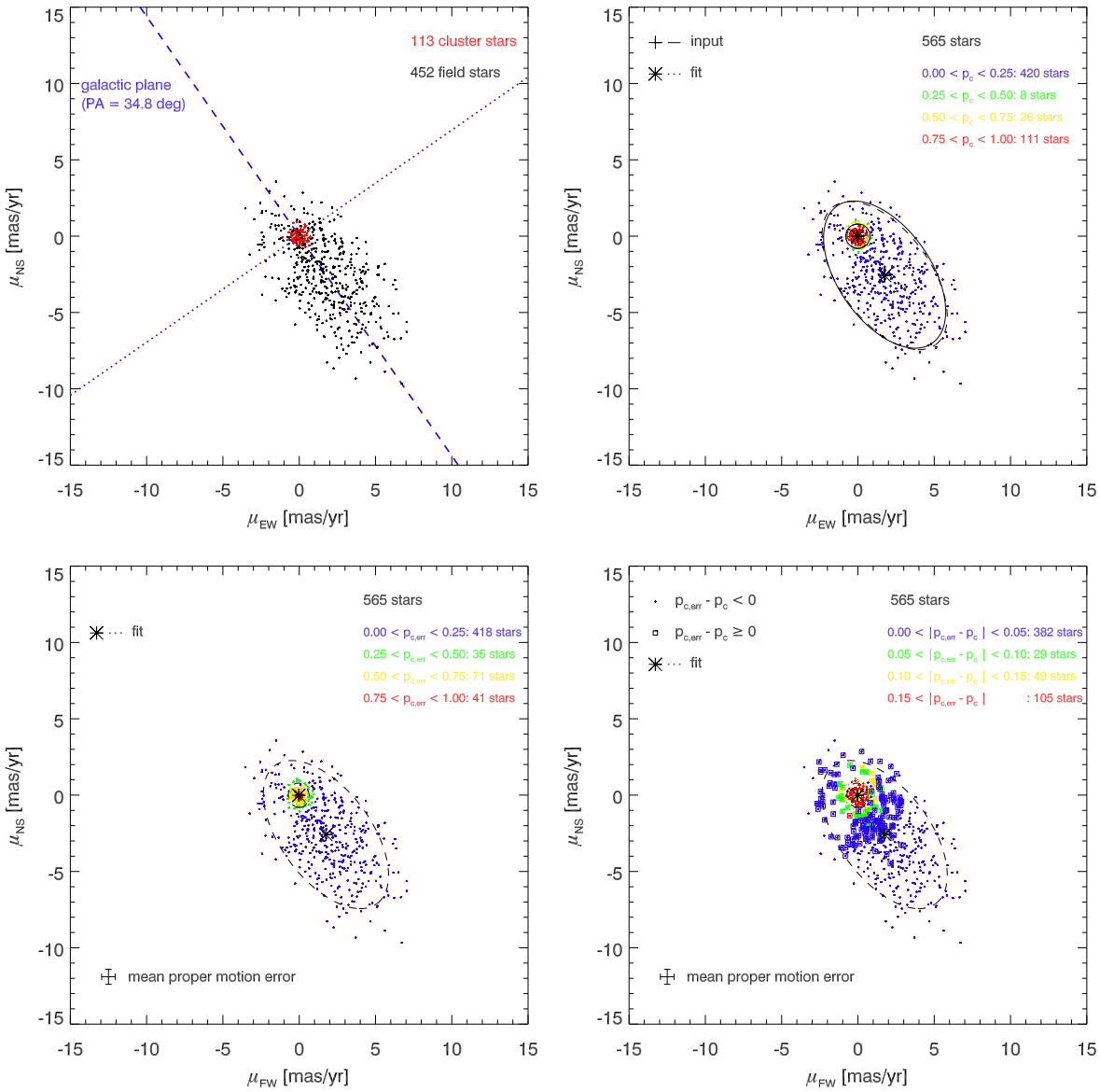

Figure 4.20: *Top left*: PMD of the synthetic cluster model (cf. Fig. 4.19), the red dots mark the inserted cluster members. *Top right*: PMD with the cluster membership probabilities of the individual stars $p_{n,c}$ as calculated with Eq. (4.7) indicated by the colours and the $2\,\sigma$-contours of the inserted (solid) and fitted cluster and field distributions (dashed). *Bottom left*: Cluster membership probabilities re-calculated with Eq. 4.11 to account for the individual proper motion errors ($p_{n,c,err}$). *Bottom right*: Difference of the cluster membership probabilities shown in the *top right* and *bottom left panel*. Datapoints with larger membership probabilities after application of the individual proper motion errors ($p_{n,c,err} - p_{n,c} \geq 0$) are additionally marked with a box point.

distribution, their separation and the semi-major and semi-minor axis of the field distribution agree remarkably well with the respective input values of the model. The slight elongation of the cluster distribution is not surprising given the significant overlap of the two distributions.

The comparison of the top panels in Fig. 4.20 shows that the membership probabilities of a datapoint only reflects its distance from the centroid of the cluster distribution irrespective of it being inserted as a cluster or a field star. The influence of the x-, y-position of a star on its membership probability is

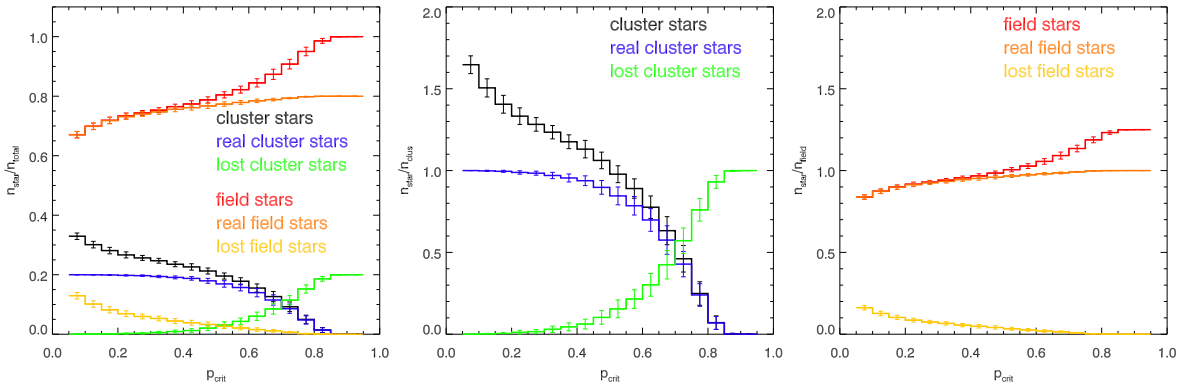

Figure 4.21: Mean fraction of datapoints attributed to the cluster or the field distribution determined from the 10 synthetic cluster models for Field 2 (see text). Datapoints with $p_{n,c,err} > p_{crit}$ are regarded as cluster stars, otherwise as field stars. The error bars represent the respective standard deviations. *Left panel*: Fraction of cluster and field stars relative to the total number of inserted stars. The fractions of inserted cluster and field stars are $\pi_c = 0.2$ and $\pi_f = 0.8$, respectively. *Middle and right panel*: Fraction of cluster/field stars relative to the total number of inserted cluster (*middle panel*) or field stars (*right panel*).

therefore negligible for Field 2 due to the flatness of the cluster density profile at these large distances from the spatial density centre, which is reflected in the constant term (cf. left panel in Fig. 4.18). Field stars located close to the centroid of the cluster distribution in the PMD can therefore not be identified and removed based on their membership probability.

In order to use the same error statistics as for the real data, the measured proper motion errors of the 565 stars were randomly assigned to the datapoints of each of the 10 modelled datasets. The membership probabilities were re-calculated with Eq. (4.11) using the assigned proper motion errors and the already derived kinematic parameters of each model. The bottom panels of Fig. 4.20 show the revised membership probabilities $p_{n,c,err}$ as well as the difference $p_{n,c,err} - p_{n,c}$ for one of the 10 models. The general results are similar to the findings in Sect. 4.2.2.2, i.e. the membership probabilities of stars located within or near the $2\,\sigma$-ellipse of the cluster star distribution drop, while for stars located farther out the probability of belonging to the cluster increases when proper motion errors are accounted for. However, the effects are more pronounced as the mean proper motion error relative to the size of the fitted cluster distribution is larger than for the synthetic model in Sect. 4.2.2.2 (cf. bottom left panels in Figs. 4.16 and 4.20). The decrease of the membership probability of stars residing at the centre of the cluster distribution in the PMD is less pronounced than for stars slightly farther out which reflects that mostly the plateau of the distribution of the cluster membership probability (cf. Fig. 4.17) contributes to the integral in Eq. 4.11 for these stars. As the influence of the spatial density function of the cluster is almost negligible for Field 2, the membership probability increases for all stars located in the proper motion tail of the cluster distribution (cf. the previous section and Fig. 4.17), for which the contributions to the integral in Eq. (4.11) of areas closer to its peak overcome the contributions from the areas farther out, where the change of the membership probability is comparatively small.

In order to derive a valid membership criterion for the measured PMD of Field 2 based on the value of $p_{n,c,err}$, the number of cluster stars ($p_{n,c,err} \geq p_{crit}$), the number of field stars ($p_{n,c,err} < p_{crit}$), and the numbers of inserted and correctly identified cluster and field stars were determined as a function of p_{crit} for each model. The respective mean values of the ten models are plotted vs. p_{crit} in Fig. 4.21 and are summarized in Table 4.8.

The number of inserted cluster stars with $p_{n,c,err} \geq p_{crit}$ steeply increases for values smaller than

Table 4.8: Number of cluster stars, contaminating field stars and unidentified (lost) cluster stars for the synthetic models of Field 2 as a function of the membership criterion p_{crit}. The synthetic PMDs of Field 2 contain 113 cluster stars ($\pi_c = 0.2$) and 452 field stars ($\pi_f = 0.8$). For Field 2 and the other outer fields a membership criterion of $p_{crit} = 0.40$ was adopted (Sect. 4.2.3).

p_{crit}	$n_{c,m}{}^a$	$n_{cont,m}{}^b$	$n_{lost,m}{}^c$	$n_{cont,m}/n_{c,m}$	$n_{lost,m}/n_{c,m}$
0.05	186.1 ± 6.1	73.1 ± 6.1	0.0 ± 0.0	0.39 ± 0.04	0.00 ± 0.00
0.10	170.1 ± 6.3	57.3 ± 6.2	0.2 ± 0.4	0.34 ± 0.04	0.00 ± 0.00
0.15	158.8 ± 6.1	46.3 ± 5.9	0.5 ± 0.7	0.29 ± 0.04	0.00 ± 0.00
0.20	150.6 ± 5.7	38.9 ± 5.4	1.3 ± 1.2	0.26 ± 0.04	0.01 ± 0.01
0.25	144.9 ± 4.7	33.7 ± 4.6	1.8 ± 1.4	0.23 ± 0.03	0.01 ± 0.01
0.30	139.5 ± 4.6	29.9 ± 4.6	3.4 ± 2.2	0.21 ± 0.03	0.02 ± 0.02
0.35	132.9 ± 4.8	25.0 ± 4.5	5.1 ± 2.8	0.19 ± 0.03	0.04 ± 0.02
0.40	127.8 ± 6.1	21.8 ± 4.7	7.0 ± 3.4	0.17 ± 0.04	0.05 ± 0.03
0.45	120.0 ± 5.7	18.6 ± 4.7	11.6 ± 4.7	0.16 ± 0.04	0.10 ± 0.04
0.50	110.5 ± 5.8	15.0 ± 4.2	17.5 ± 6.2	0.14 ± 0.04	0.16 ± 0.06
0.55	100.6 ± 6.7	11.9 ± 3.6	24.3 ± 6.4	0.12 ± 0.04	0.24 ± 0.07
0.60	87.7 ± 7.8	8.8 ± 3.3	34.1 ± 7.9	0.10 ± 0.04	0.39 ± 0.10
0.65	71.5 ± 9.7	6.5 ± 2.6	48.0 ± 9.9	0.09 ± 0.04	0.67 ± 0.17
0.70	52.1 ± 9.2	3.7 ± 1.3	64.6 ± 8.8	0.07 ± 0.03	1.24 ± 0.28
0.75	28.1 ± 8.1	1.0 ± 0.8	85.9 ± 7.8	0.04 ± 0.03	3.06 ± 0.93
0.80	8.0 ± 4.7	0.2 ± 0.4	105.2 ± 4.5	0.03 ± 0.05	13.15 ± 7.69
0.85	0.2 ± 0.4	0.0 ± 0.0	112.8 ± 0.4	–	–
0.90	0.0 ± 0.0	0.0 ± 0.0	113.0 ± 0.0	–	–

Notes. [(a)] Mean number of cluster stars ($p_{n,c,err} > p_{crit}$) as derived from the 10 synthetic models of Field 2. The stated errors are the respective standard deviations. [(b)] Number of contaminating field stars within $n_{c,m}$. [(c)] Number of inserted cluster stars not contained in $n_{c,m}$.

$p_{crit} = 0.75$ and converges to the total number of inserted cluster stars at about $p_{crit} = 0.25$ (blue line in the middle panel of Fig. 4.21). This implies that for Field 2, according to this simulation, all cluster members would only be recovered if the selection criterion is $p_{crit} \leq 0.25$. The number of stars with $p_{n,c,err} \geq p_{crit}$, i.e. of stars attributed to the cluster (black line), naturally increases for decreasing values of p_{crit} and deviates more and more from the number of inserted cluster stars with $p_{n,c,err} \geq p_{crit}$ (blue line). This indicates an increasing percentage of contaminating field stars in the member sample for decreasing values of p_{crit}. For example, the percentage of contaminants amounts to about 35% of the inserted cluster stars for a membership criterion of $p_{crit} = 0.20$ (see middle panel in Fig. 4.21). Due to the overlap of the cluster and field star distributions in the PMD, a residual contamination of the proper motion membership sample by field stars is unavoidable unless it is accepted that a large fraction of cluster stars are lost. A membership criterion $p_{crit} = 0.40$ serves as a compromise in order to retrieve a large fraction of the inserted cluster stars (95%), while expecting only a moderate percentage of contaminating field stars (17% relative to the number of stars in the membership sample). As the photometric colours of the observed stars in the outer fields are known by combining the NACO K_s-band and the WFC3 $F153M$ and $F127M$ datasets, some of the contaminating field stars can be removed on the basis of their colours (see Sect. 4.3.1).

4.2.3 Proper motion membership samples based on membership probabilities

4.2.3.1 Field 2

The EM algorithm was finally applied to the measured proper motion data of Field 2, as derived from the two NACO K_s-band datasets from 2008 and 2011. As explained in the last section, only stars with $K_s < 17.5$ mag were used and outliers in terms of their proper motion were excluded (see the PMD in Fig. 4.18). The top left panel in Fig. 4.22 shows the PMD with the $p_{n,c,err}$ and the $2\,\sigma$-ellipses of the cluster and field stars. The determined properties from fitting the distributions of cluster and field stars in the PMD are summarised and compared to the respective values of the synthetic models of Field 2 in Table 4.9. While the measured separation of the two distributions and the properties of the field stars distribution agree with the modelled kinematic properties within $2\,\sigma$, the fitted cluster distribution in Field 2 is somewhat more elongated than expected from the models. The large standard deviation of the position angle θ_c of the modelled cluster distribution indicates that the orientation of the circular-shaped cluster distribution can not be well constrained and is very sensitive to small variations of the determined values of $\sigma_{x,c}$, $\sigma_{y,c}$ and ρ_c. An obvious difference between the properties derived for the model and the measured data is the elongation of the measured cluster distribution. The deviation from the circular shape for the measured cluster distribution is not an intrinsic feature of the kinematic properties of the cluster, as we do not resolve internal motions, but caused by the impact of the field distribution on the kinematic fit to the cluster distribution (and vice versa). As the elongation is more pronounced than in any of the 10 models, this might indicate that some features of the measured PMD cannot be fully reproduced by a purely two-component Gaussian mixture model. Especially for the Galactic field the description by a single normal bivariate distribution might be too simplified. For example, stars located at larger distances to the origin in the north-east segment of the measured PMD appear to be more concentrated along the direction of the Galactic plane than it can be produced by a two-component model which otherwise shows a good correspondence of the other observed features. These additional stars compared to the model are very likely the reason for the more pronounced elongation of the kinematic fit to the measured cluster distribution.

The fractions of detected field and cluster stars relative to the total number of stars are shown as a function of p_{crit} in the top left panel of Fig. 4.23 and compared to the respective mean values of the synthetic model. The agreement between the model and the measured data is better than two times the standard deviation σ of the model for most values of p_{crit}. In the range from $p_{crit} = 0.35$ to 0.50 the retrieved fraction of cluster stars is below the values expected from the model with a maximum deviation of $2.6\,\sigma$ at $p_{crit} = 0.45$. Although the membership sample might be slightly less complete than expected, the results of the best-fit model, i.e. the membership criterion $p_{crit} = 0.40$, is applied to the measured data. Applying this membership criterion, the proper motion membership sample for Field 2 is expected to contain a fraction of 0.17 ± 0.04 unidentified field stars, while $5 \pm 3\%$ of all real cluster stars are expected to be lost (see Table 4.8). The number of contaminants will be decreased once an appropriate colour selection is applied to the proper motion membership sample in Sect. 4.3.

4.2.3.2 Fields 3, 4 and 5

The general results of the synthetic models of Field 2 are expected to be applicable to Fields 3, 4 and 5 as the effect of the cluster density profile is negligible for all outer fields and the intrinsic separation of the cluster and field distribution, i.e. the movement of the cluster relative to the field population, are the same. Slight differences may be introduced by a possible variation of the fraction of cluster stars between the outer fields or the different astrometric quality of the datasets and hence the derived geometric transformations. As for Field 2, the EM algorithm was applied to the PMDs of Fields 3, 4

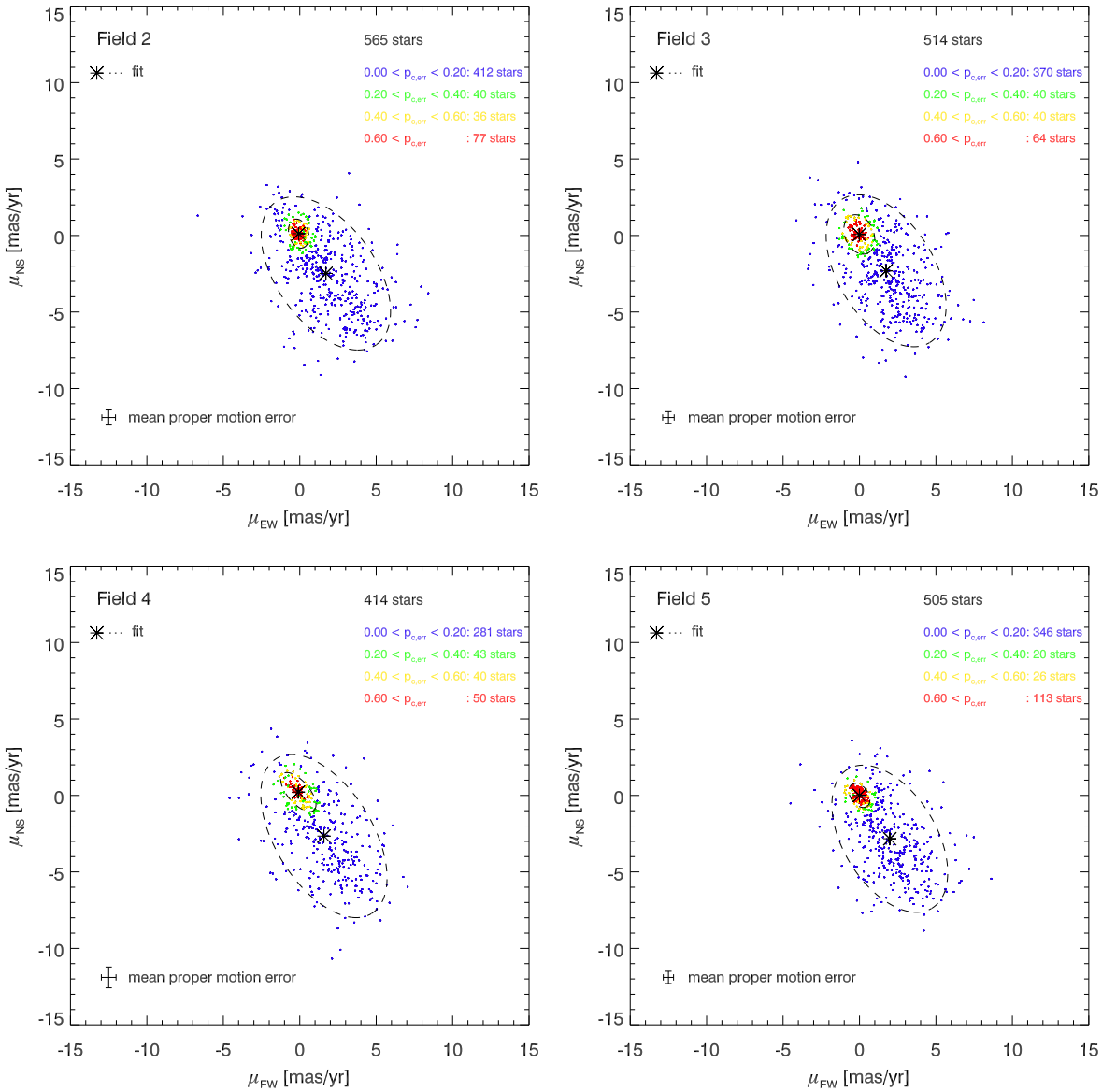

Figure 4.22: PMDs of the Quintuplet outer fields ($K_s < 17.5$ mag, outliers are excluded as shown in the right panel of Fig. 4.18) with the cluster membership probabilities of the individual stars $p_{n,c,err}$ indicated by the colour coding and the $2\,\sigma$-contours of the fitted cluster and field distributions (dashed) shown as dashed ellipses. Note the different concentration of the presumed cluster candidate distributions.

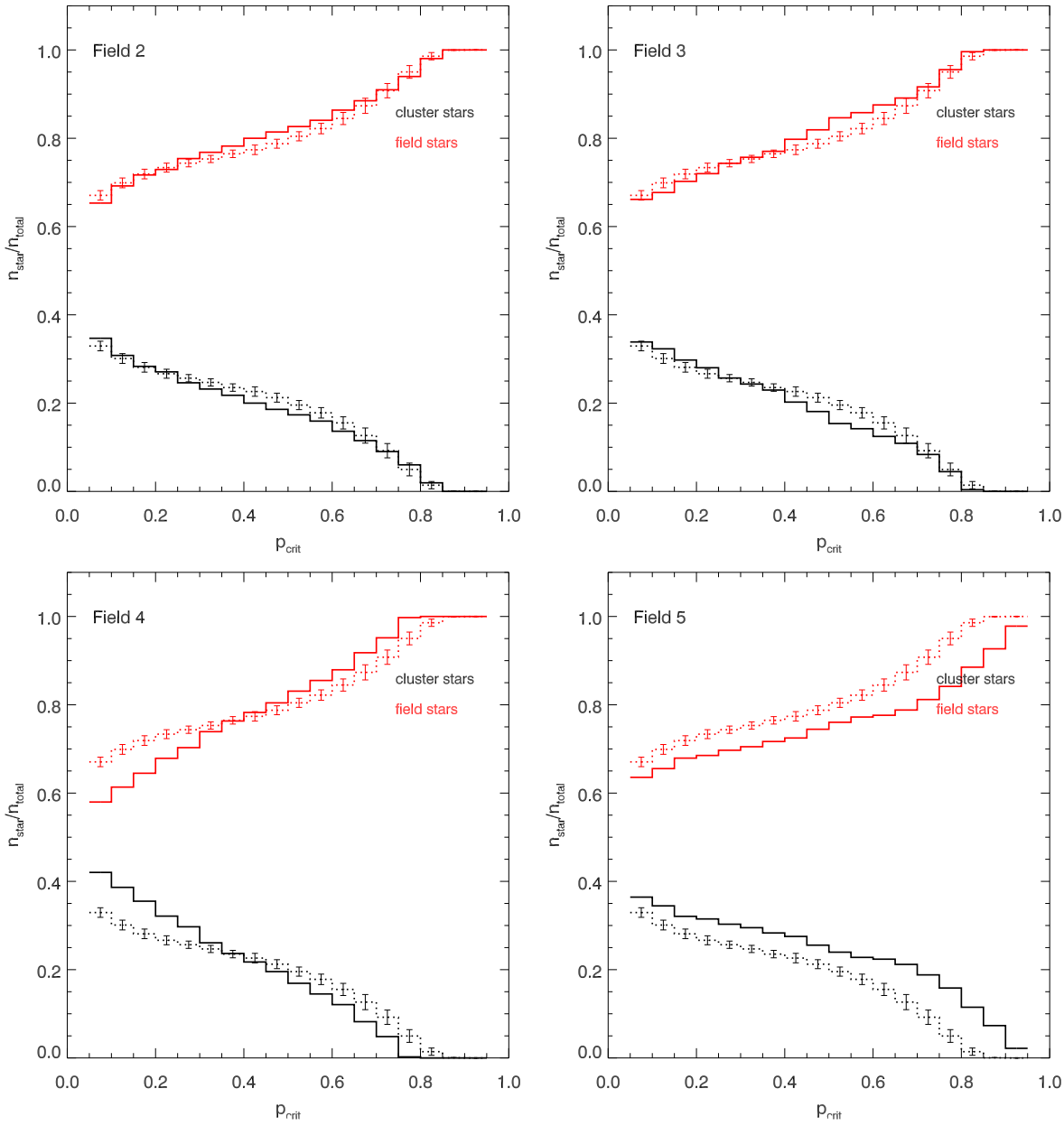

Figure 4.23: Fraction of cluster and field stars relative to the total number of observed stars in the PMD (excluding outliers, see text) for all Quintuplet outer fields. The dotted lines show the respective mean fractions and their standard deviation as error bars of the 10 synthetic datasets adapted to the proper motion distribution of Field 2 (cf. Fig. 4.21 for comparison).

Table 4.9: Properties of the cluster and field star distribution in the PMD of the outer fields (cf. bottom left panel in Fig. 4.20 and Fig. 4.22) and of Field 1 (central parts).

	d mas/yr	θ_c °	θ_f °	a_c mas/yr	b_c mas/yr	a_f mas/yr	b_f mas/yr
Model[a]	3.06 ± 0.12	66.7 ± 38.7	35.0 ± 1.7	0.42 ± 0.03	0.36 ± 0.01	2.79 ± 0.08	1.50 ± 0.06
Field 2	3.15	15.9	35.5	0.49	0.32	2.86	1.61
Field 3	2.96	22.9	31.3	0.67	0.47	2.75	1.58
Field 4	3.33	40.5	31.6	0.78	0.36	2.97	1.59
Field 5	3.46	34.4	31.2	0.44	0.29	2.66	1.52
Field 1	3.78	17.7	37.6	0.51	0.40	2.86	1.63

Notes. [(a)] Values from the fit to the synthetic models of Field 2 (see Table 4.7).

and 5 using only stars with $K_s < 17.5$ mag and after the removal of outliers which might bias the kinematic fit. For the three fields the same rejection criterion as for Field 2 was applied, i.e. only stars with $|\mu_{\rm VGP}| \leq 5$ mas/yr, $\mu_{\rm PGP,NE} \leq 5$ mas/yr and $\mu_{\rm PGP,SW} \geq -10$ mas/yr were used (cf. right panel in Fig. 4.18). The PMDs of all outer fields with the $p_{n,c,err}$ indicated by the colour coding are shown in Fig. 4.22. The properties of the kinematic fits are summarised in Table 4.9.

The agreement of the fitted kinematic parameters of the cluster and field populations for Fields 3, 4 and 5 with the synthetic models of Field 2 is naturally less good than for Field 2. The orientations as well as the elongations of the fitted cluster distributions vary considerably between the outer fields (cf. previous section), which is expected considering the variation of the apparent concentration at the origin of the respective PMD. For example the PMD of Field 3 is much less concentrated than the PMDs of Fields 2 or 5, and consequently the values of a_c and b_c are larger for this field. The fit to the cluster distribution in Field 4 is strongly elongated. Its orientation is roughly aligned with the field distribution, indicating that the field stars bias the kinematic fit of the cluster distribution. Hence the number of contaminating field stars is expected to be largest for the proper motion sample of this field. The position angle of the field population θ_f for Field 4 agrees within $2\,\sigma$ with the models, while the deviation for Fields 3 and 5 is only slightly larger ($2.2\,\sigma$). The ratios of the semi-minor to the semi-major axis of the field populations of all outer fields agree with values between 0.54 and 0.57 remarkably well, which indicates that the differences in the absolute sizes of a_f and b_f reflect the different size of the proper motion uncertainties. The size of the minor and major axis of the field population is for Fields 3 and 5 in agreement with the model. For Field 4, the major axis of the field population is slightly larger ($2.3\,\sigma$) than expected from the models. The number of stars in the PMD of this field is about 25% smaller than the number of datapoints used for the models such that the tolerated $2\,\sigma$ ranges derived from the model are probably too strict for Field 4. The clearest difference between the models of Field 2 and the measured PMDs of the outer fields occurs in the separation d between the cluster and the field distribution for Fields 4 and 5 which is by 2.3 and $3.3\,\sigma$ larger than expected from the models. Field 5 shows a very strong concentration around the origin and a comparatively small fraction of stars scattering far into the north-east segment, which may cause that the centroid of the field distribution is less shifted towards the origin as compared to the model. Figure 4.23 shows the ratio of cluster and field stars relative to the total number of stars as a function of the membership criterion p_{crit} for all outer fields and compares it with the ratios expected from the models of Field 2. For Field 3 the retrieved fraction of cluster stars is below the fraction expected from the model by more than $2\,\sigma$ for values of p_{crit} between 0.35 and 0.6. The largest deviation ($4.2\,\sigma$)

occurs at $p_{crit} = 0.5$, while for $p_{crit} = 0.4$ and $p_{crit} = 0.6$ the deviation is with $2.2\,\sigma$ still in reasonable agreement with the models. As can be expected from the significant elongation of the fitted cluster distribution, the fraction of the cluster stars as a function of p_{crit} of Field 4 deviates strongly from the model with a decreased fraction of cluster stars with high membership probabilities ($p_{n,c,err} > 0.5$) and an increased fraction with lower membership probabilities ($p_{n,c,err} < 0.3$)[22]. For Field 5, the fraction of cluster stars is increased for all p_{crit} compared to the model of Field 2 which is not surprising given the pronounced concentration of stars at the origin of the PMD for this field. The difference of the fraction of cluster stars between the observed PMD and the model is for all values of $p_{crit} < 0.6$ rather constant with about 0.05.

Ideally, a customized model for each of the four outer fields would be required to determine an appropriate membership criterion for each field individually. Unfortunately this was not possible due to time constraints. As the decrease of the fraction of cluster stars relative to the total number of stars with increasing p_{crit} is for Field 3 and 5 in agreement with the model of Field 2 for values of $p_{crit} \leq 0.4$ (see black curve in Fig. 4.23), the cluster membership criterion applied for Field 2 ($p_{crit} = 0.40$) was also used for these two fields and for consistency also for Field 4 to establish the respective proper motion membership samples.

From the cluster density profile, the number density and hence the fraction of cluster stars in the proper motion sample is expected to decrease systematically with distance from the cluster centre assuming that the cluster is spherically symmetric. The fraction of cluster stars is hence expected to be almost equal in Field 2 ($d_{\rm cent} = 28''$) and Field 5 ($29''$), slightly smaller in Field 4 ($35''$) and smallest in Field 3 ($46''$). However, this trend is not observed and the fractions of cluster stars at $p_{crit} = 0.40$ in Fields 3, 4 and 5 is larger than anticipated, i.e. equal to (Fields 3 and 4) or larger (Fields 5) than in Field 2 (see Fig. 4.23). It is hence unlikely that the applied membership criterion is too strict for Fields 3, 4 and 5. Because a certain extent of contamination by fields stars is unavoidable and is largely reduced by the subsequent colour selection, the main concern for the application of the membership criterion $p_{crit} = 0.40$ as derived for Field 2 is that the membership sample contains about the same fraction of the total number of cluster stars in every field.

4.2.3.3 Bulk motion

The separation between the cluster and the field star distributions corresponds to the bulk proper motion of the Quintuplet cluster with respect to the Galactic field along the line of sight to the cluster. As the central part of Field 1 contains the most cluster stars, the kinematic fitting routine was also applied to the PMD of this field using only stars with $K_s < 17.5$ mag and applying the same rejection criterion for outliers as for Field 2. The retrieved parameters of the kinematic fit are added to Table 4.9. The motion of the cluster with respect to the field is not well constrained by the kinematic fits to the PMDs of Fields 1 to 5 and ranges between 3.0 and 3.8 mas/yr which corresponds at a presumed distance of 8 kpc to a bulk motion of 114 - 144 km/s for the Quintuplet cluster. As noted by Clarkson et al. (2012), a simple interpretation of the bulk motion is hampered among other things by the fact that the contributions of field stars at different Galactocentric radii and hence with different average proper motions to the field star distribution in the PMD are unknown. The measured bulk motion can thus not be referenced to an absolute zero point of the proper motion such as e.g. the proper motion of the Galactic centre. Assuming that the properties of the Galactic field are similar along the lines of sight to the Arches and the Quintuplet cluster, the bulk motion of the Quintuplet cluster is somewhat smaller than the value for the Arches cluster of 172 ± 15 kms/s ($K_s < 18$ mag) recently derived by

[22] In the end, Field 4 was disregarded for the derivation of the PDMF of the Quintuplet cluster (see Sect. 4.3.1.2).

Clarkson et al. (2012).

If it is nevertheless assumed that the centroid of the field star distribution in the PMD corresponds to zero motion with respect to the Galactic centre, the measured bulk motion of the Quintuplet cluster represents its absolute bulk proper motion in the Galaxy and can be combined with its radial velocity to derive the three-dimensional space motion of the cluster. The radial velocity of the cluster was determined as the mean radial velocity of the early-type stars from the LHO catalogue where stars with uncertain values (marked with ':' in the catalogue) were excluded. The found mean radial velocity of 103 ± 2 km/s (standard deviation: 14 km/s) is somewhat lower than the value of 113 ± 4 km/s (standard deviation: 17 km/s) which was used by Liermann et al. (2009) to establish cluster membership and which is the mean radial velocity of the 15 Q-stars from Glass et al. (1990). This difference is understandable as most of the Q-stars are WR stars which have a higher mean radial velocity (114 km/s) than the more numerous OB stars (101 km/s). By combining the mean bulk proper motion of 128 ± 17 km/s, where the adopted measurement uncertainty is the maximum deviation of the bulk motions measured in Fields 1 to 5 from the mean bulk motion, with the mean radial velocity of the cluster (103 ± 2 km/s), the three-dimensional space motion of the cluster is found to be 164 ± 17 km/s. This value is significantly lower than the value of the space motion of the Arches cluster of 232 ± 30 km/s derived by Stolte et al. (2008) or of 196 ± 17 km/s if the bulk motion of Clarkson et al. (2012) is applied. Whether this excludes that both clusters might have a similar origin or not requires a study of the cluster orbit in the Galactic potential comparable to the one performed by Stolte et al. (2008) for the Arches cluster, which is beyond the scope of this study.

4.3 Colour-magnitude diagrams and mass assignment

4.3.1 Colour-magnitude diagrams of the Quintuplet outer fields

The CMDs of the four Quintuplet outer fields are shown in Fig. 4.24. All stars contributing to the CMD have measured proper motions, i.e. they are detected in both epochs of the K_s-band data, and are contained in the J_s- and H-band catalogues (see end of Sect. 4.1.2.3). The K_s-band magnitude is used as ordinate as the photometric uncertainties are smallest for the NACO data. Because the separation in colour between the cluster and the field population is more distinct in $J_s - K_s$ than in $H - K_s$ and the photometric uncertainties in the J_s-band are smaller than in the H-band (see Fig. 4.6, bottom panels), the K_s-band magnitudes are plotted vs. $J_s - K_s$ in the CMDs. In that way both the number of residual field stars in the final cluster sample after the colour selection as well as the uncertainty of the mass assignment are minimised. The saturated cores of the three brightest stars in Field 3 (see Fig. 1.1, left half of Field 3) could not be repaired and these stars are therefore missing from the CMD of Field 3. A fourth very bright star at the left image margin is outside the used image area (see Fig. 4.11) and hence does not appear in the CMD, too. As the flux of Q7 exceeds the non-linearity limit in both K_s-band datasets and the H-band dataset considerably and its measured magnitude and colour strongly deviate from the values stated in Figer et al. (1999b, designated as qF192 in their Table 2), this star is not shown in the CMD of Field 5.

As explained in Sect. 4.2.1.2, the proper motion membership sample was established only for stars brighter than $K_s = 17.5$ mag due to the steeply increasing uncertainty of the measured proper motions. The residual contaminants in the proper motion membership samples were excluded from the final cluster sample by two colour cuts at $J_s - K_s = 3.5$ and 4.5 mag (vertical short-dashed lines in Fig. 4.24). The position of the red boundary was selected to be the approximate blue boundary of the distribution of red clump stars in the CMD (cf. Fig. 4.24).

The combined source catalogue of each field was compared to the LHO K-band spectral catalogue

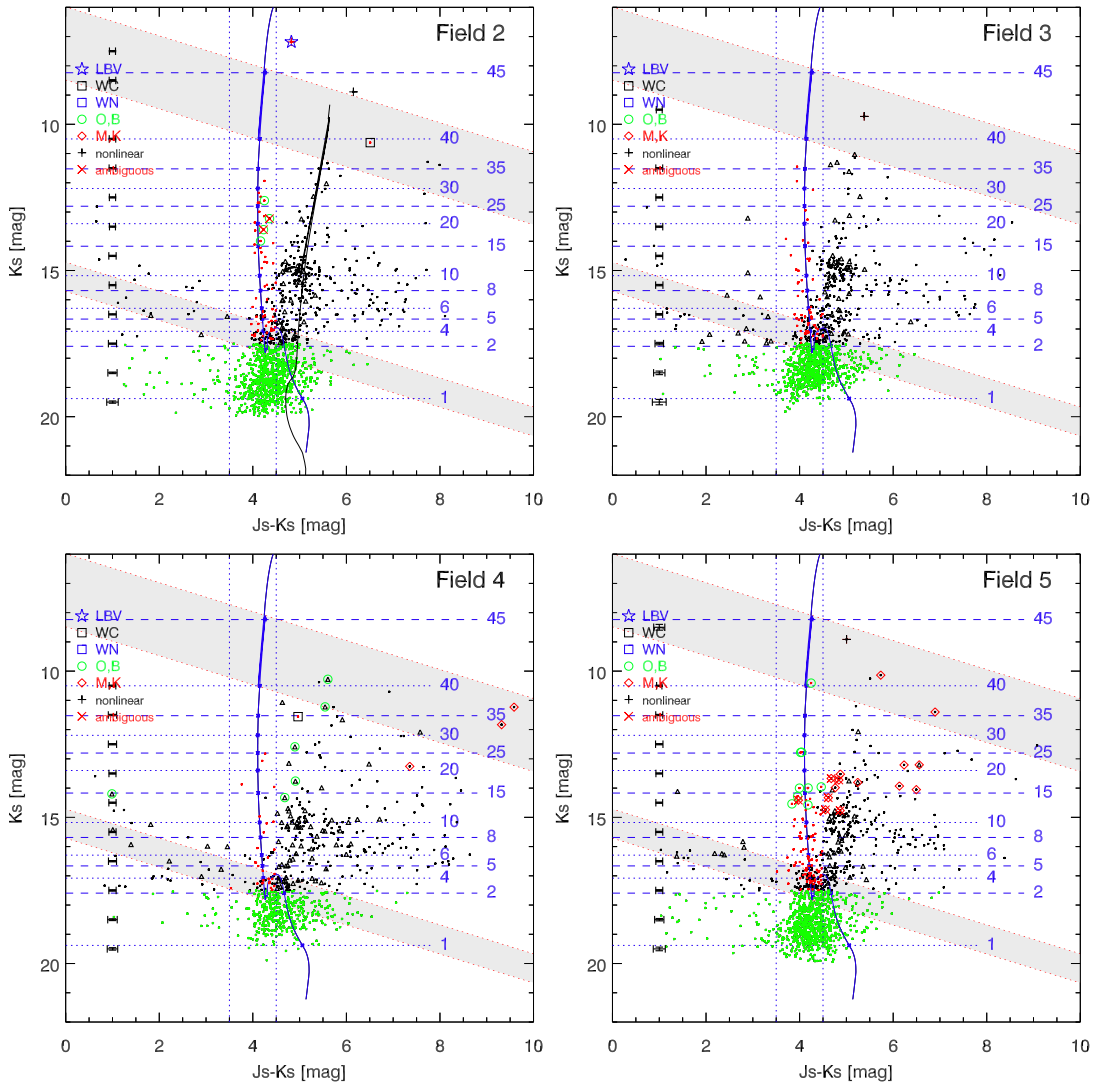

Figure 4.24: CMDs of the four Quintuplet outer fields. A 4 Myr isochrone (MS: Padova isochrone, PMS: Pisa-FRANEC isochrone) shifted to a distance of 8 kpc and a foreground extinction of $A_{K_s} = 2.15$ mag is shown for reference. Initial stellar masses are marked along the isochrone (blue horizontal lines). To indicate the approximate locus of the old population in the Galactic bulge, an additional 10 Gyr Padova isochrone is shown in the CMD of Field 2 (*upper left panel*). The error bars to the left of the CMD show the mean uncertainties in colour and magnitude, respectively. The applied colour selection ($3.5 < J_s - K_s < 4.5$ mag) to remove field stars from the proper motion membership sample is indicated by the vertical short-dashed lines. For stars fainter than 17.5 mag the proper motion membership was not assessed (green dots). For $K_s < 17.5$ mag, stars belonging to the Galactic field according to their proper motions or colours are drawn as black dots and black triangles, respectively, while designated cluster stars are drawn in red. Crosses mark stars whose fluxes exceed the linearity limit of the NACO detector. Stars with counterparts either in the LHO catalogue or in Figer et al. (1999b) are flagged according to their spectral type (blue star: LBV, black box: WC star, green circle: OB star, red diamond: M,K (super-)giant). Stars which are ambiguous counterparts of the sources in the less well-resolved spectral catalogues are indicated by a red X-cross. As in Fig. 3.9, the grey shaded areas mark the regions in the CMD within which the isochrone has multiple intersections with the line of reddening using the extinction law by Nishiyama et al. (2009).

and the spectral classifications in Figer et al. (1999b, Table 3). Due to the superior spectral resolution of the LHO catalogue of $R \approx 4000$ compared to $R \approx 525$ for the K-band spectra in Figer et al. (1999b), the spectral classification in the LHO catalogue was given preference for stars appearing in both catalogues. The uppermost parts of Field 2, the right, lower corner of Field 4 and the upper part of the right edge of Field 5 are covered by the LHO spectral catalogue. Six additional stars at larger distances from Field 1 are listed in Table 3 in Figer et al. (1999b). As for the central part of the Quintuplet cluster (see Sect. 3.5), several entries in the LHO catalogue have two potential counterparts in the combined source catalogues of the outer fields (indicated by an X-cross in Fig. 4.24). For Fields 2 and 5, the spectral classifications confirm the proper motion members within the colour selection and the choice of the red boundary. The single late-type spectral identification within the member sample (Field 5) is ambiguous and most probably belongs to the second counterpart outside the colour selection which is brighter in K_s by 1.1 mag. For Field 4, all spectroscopically identified early-type stars are outside the colour selection. Possible explanations for this peculiar behaviour are discussed in Sect. 4.3.1.2.

A 4 Myr isochrone, combined from a Padova MS isochrone and a Pisa-FRANEC PMS isochrone (see Sect. 3.6 for details), is shown in all CMDs. As for Field 1, solar metallicity and a distance of 8 kpc was assumed. The isochrone was shifted to a foreground extinction of $A_{K_s} = 2.15$ mag to match the observed MS of the cluster stars (cf. Sect 4.3.1.1). To the right of the cluster MS a second, slanted sequence is visible which is presumably composed of stars belonging to the Galactic bulge. The bulge is dominated by an old population ($\sim$ 10 Gyr) and the broad distribution of metallicities peaks roughly at solar metallicities (Brown et al. 2010). A 10 Gyr Padova isochrone with solar metallicity shifted to the Galactic centre distance of 8 kpc and the foreground extinction of the cluster is hence shown for reference in the CMD of Field 2. The applied distance and foreground extinction are rough approximations as the Galactic bulge is composed of stars with a large spread of distances and extinction values. As the bulge sequence is broadened and converges with the cluster sequence at about $K_s = 17$ mag, a few residual field stars within the proper motion member sample for $K_s > 16$ mag may not be removed by the applied colour selection.

4.3.1.1 Comparison with Field 1

For a comparison with the CMDs of the outer fields the source catalogue of Field 1 was matched with the J_s-band source catalogue of the extracted WFC3 field (Fig. 4.4). The resulting CMD is shown in Fig. 4.25 (left panel). Compared to the CMDs of the outer fields, the cluster MS in Field 1 appears to be shifted by about $J_s - K_s = 0.4$ mag towards redder colours (cf. the blue and black isochrone in the left panel of Fig. 4.25). This discrepancy can be caused either by a systematically larger extinction in the central 0.5 pc of the cluster or by a zeropoint offset in the K_s-band of -0.4 mag in Field 1 relative to the outer fields. A similar zeropoint offset in J_s as explanation for the discrepancy can be excluded as the used J_s-band source catalogue covers all observed fields.

In order to decide between the two explanations, a calibration field overlapping all fields except Field 4 and obtained in the K_s-band during the same night as the second epoch data of Field 3 (2012-06-14) was calibrated with respect to Fields 1, 2, 3, and 5. As the overlap of the calibration field with Field 1 is small, stars outside of the innermost 0.5 pc of Field 1 were used as calibrators, as well. The derived zeropoints of the calibration field are summarised in Table 4.10. The zeropoint of the calibration field derived with respect to Field 1 is with 22.26 mag about 0.2 mag smaller than the zeropoints of the three outer fields, $\langle zp_{\mathrm{F2,F3,F5}} \rangle = 22.49^{+0.06}_{-0.04}$ mag. The difference of the zeropoints between Fields 3 and 5 is, albeit larger than the formal zeropoint errors, still in the expected range of systematic zeropoint variations across the NACO FOV due to anisoplanatism effects. To assess whether local zeropoint variations are present, the calibration field was subsequently calibrated with

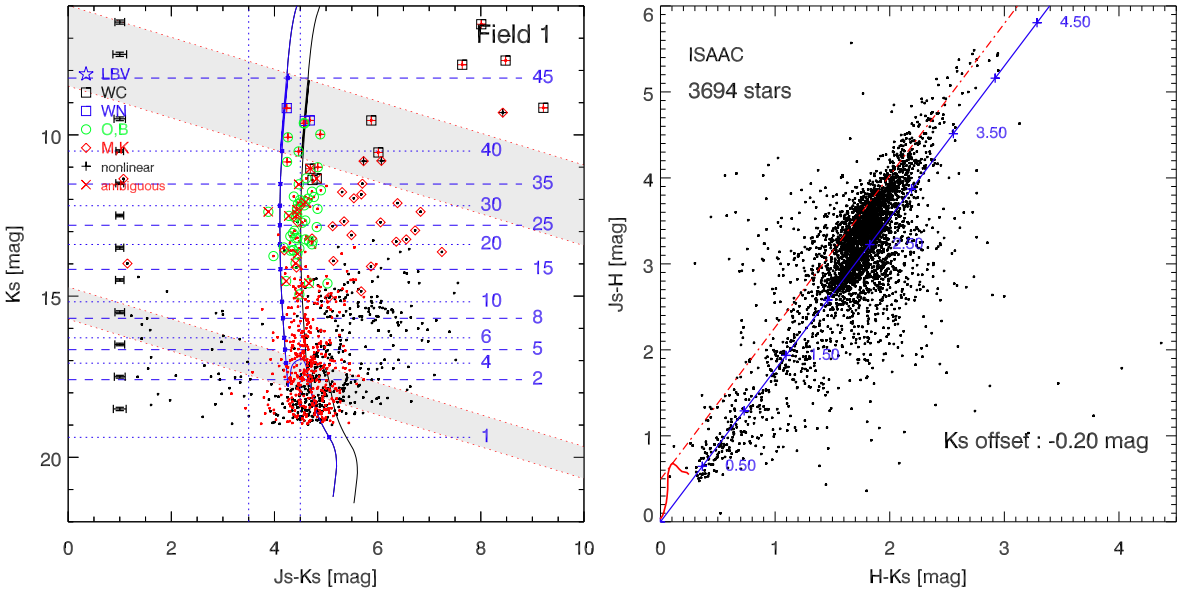

Figure 4.25: *Left panel*: CMD of Field 1 (K_s vs. $J_s - K_s$). The 4 Myr isochrone drawn in black is shifted to a distance of 8 kpc and a foreground extinction of $A_{K_s} = 2.35$ mag to match the upper cluster MS (see Sect. 3.6). The second isochrone (blue) is shifted to a foreground extinction of $A_{K_s} = 2.15$ mag which was found to be appropriate for the Quintuplet outer fields. *Right panel*: CCD of the ISAAC data of the Quintuplet cluster. The line of reddening for MS stars adopting the extinction law by Nishiyama et al. (2009) is drawn as blue line and the respective foreground extinction A_{K_s} is indicated. In order for the MS population to match the line of reddening an additive zeropoint offset in K_s of −0.20 mag was applied. The intrinsic colours and the enframing line of reddening of giants with spectral types from G0 to M5 (Currie et al. 2010) are drawn as solid and dashed dotted curves, respectively.

respect to the wide-field ISAAC K_s-band data. The derived zeropoint is compared in Table 4.11 to the mean zeropoints of the calibrators within the overlap areas of the calibration field with Fields 1, 2, 3, and 5. The derived zeropoint of 22.49 mag and the mean zeropoints in the overlap regions with Fields 2, 3, and 5 agree within the errors and are consistent with the respective zeropoints in Table 4.10. The zeropoint in the overlap region with Field 1 is in contrast to this by about 0.1 mag smaller. Combined with the previous findings (cf. Table 4.10), this indicates that a zeropoint offset of the order of −0.1 to −0.2 mag between the photometry of Field 1 and the outer fields is likely present.

The found zeropoint offset may be caused by the different reference catalogue used for the respective calibration of Field 1 and the outer fields. The K_s-band data of Field 1 were calibrated with respect to the UKIDSS catalogue. Due to the low number of usable calibrators in the UKIDSS catalogue for each individual outer field, the zeropoints of the outer fields were determined using the calibrated ISAAC data. The calibration of the ISAAC K_s-band data itself was performed using the UKIDSS catalogue (see Sect. 4.1.1.2). If Field 1 is re-calibrated with respect to the calibrated ISAAC data, the zeropoint of this field is 0.1 mag larger than the zeropoint of the original calibration and the discrepancy between the K_s-band magnitudes of Field 1 and the outer fields is hence reduced. As additional check, the $J_s - H$, $H - K_s$ colour-colour diagram (CCD) of the ISAAC data of the Quintuplet cluster was created and it was found that the distribution of MS stars from the cluster and the foreground population was offset from the line of reddening of MS stars (see right panel in Fig. 4.25). Assuming that no zeropoint offset in J_s (see above) and H is present, the additive zeropoint offset in K_s required to shift the MS population onto the line of reddening was found to be −0.20 mag. The consistency

Table 4.10: Zeropoints of the calibration field determined with respect to Fields 1, 2, 3 and 5.

Reference field	n_{cal}[a]	zp (mag)	σ_{zp}[b] (mag)
Field 1	60	22.26	0.03
Field 2	181	22.48	0.02
Field 3	145	22.45	0.03
Field 5	100	22.55	0.03

Notes. [(a)] Number of selected calibration stars. [(b)] The zeropoint error includes the zeropoint error of the respective reference field used for the calibration.

Table 4.11: Zeropoint of the calibration field determined with respect to the ISAAC K_s-band data using the complete calibration field or only the overlap regions with Field 1, 2, 3, or 5, respectively.

Image part	n_{cal}[a]	zp (mag)	σ_{zp}[b] (mag)
Complete image	190	22.49	0.01
Overlap with Field 1	31	22.37	0.03
Overlap with Field 2	94	22.46	0.02
Overlap with Field 3	75	22.50	0.02
Overlap with Field 5	39	22.46	0.02

Notes. [(a)] Number of selected calibration stars. [(b)] The zeropoint error includes the zeropoint error of the respective reference field for the calibration.

of this zeropoint offset with the previous results indicates that the observed zeropoint offset in K_s between Field 1 and the outer fields originates from the calibration of the ISAAC data and that the direct calibration of Field 1 vs. the UKIDSS catalogue is more accurate. As the exact size of the zeropoint offset in K_s is not known, but only the range between -0.1 to -0.2 mag, and the expected systematic uncertainty of the zeropoint across the NACO FOV due to anisoplanatism effects of the order of ~ 0.1 mag , the K_s-band magnitudes of the outer fields were not corrected.

In summary, there appears to be a zeropoint offset of -0.1 to -0.2 mag between the K_s-band photometry of Field 1 and the outer fields which originates from the calibration with respect to the UKIDSS catalogue or the calibrated ISAAC data, respectively. This offset is on the same order as the expectable absolute zeropoint uncertainty and is not expected to affect the derivation of the individual masses and the inferred mass function slopes substantially. As the found zeropoint offset in K_s is not sufficient to explain the observed difference of the MS colour ($J_s - K_s$) between Field 1 and the outer fields of 0.4 mag an additional trend in extinction of the order of $\Delta(A_{J_s} - A_{K_s}) = 0.2$ mag between Field 1 and the outer fields may be present. Adopting the extinction law by Nishiyama et al. (2009) this corresponds to an additional foreground extinction of $\Delta A_{K_s} = 0.1$ mag for Field 1 compared to the outer fields.

4.3.1.2 Colour-magnitude diagram of Field 4

The CMD of Field 4 (Fig. 4.24, bottom left panel) shows some peculiar characteristics which distinguish it from the CMDs of the other outer fields. The scatter of the measured K_s-band magnitudes is increased which can be seen best at the dispersed appearance of the red clump. The MS is least

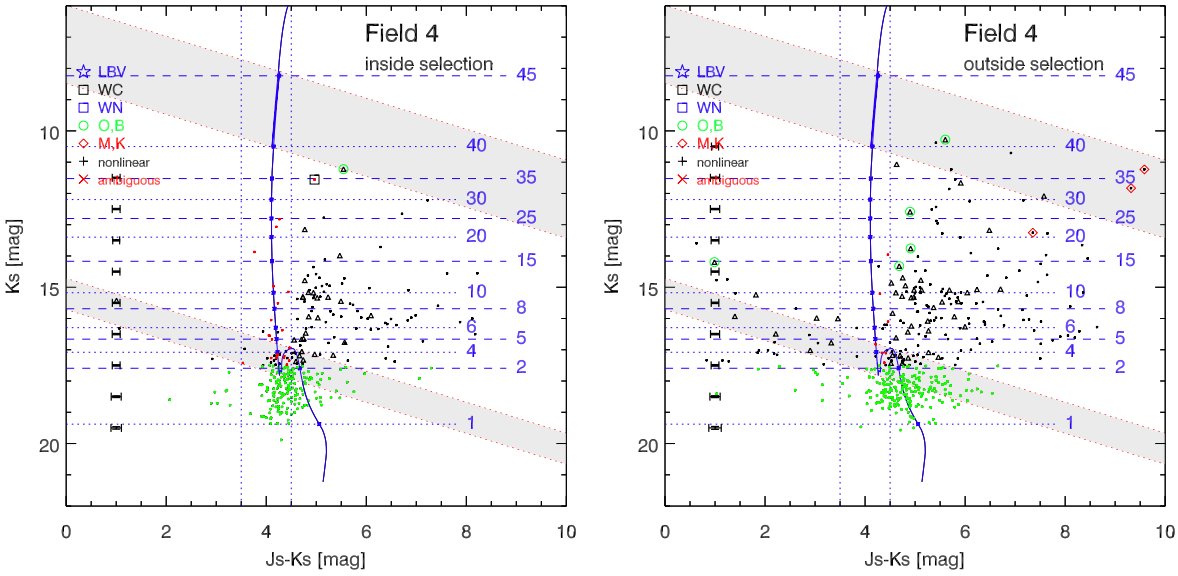

Figure 4.26: *Left panel*: CMD of Field 4 showing all stars within the rectangular selection of the central image part (see text and Fig. 4.11). *Right panel*: CMD of Field 4 showing all stars outside the rectangular selection. The increased scatter is apparent to the right of the PMS and above the red clump.

populated of all the outer fields and all spectroscopically identified early-type stars are outside of the applied colour selection for cluster stars. One OB star (green circles in Fig. Fig. 4.24) is obviously a foreground star and correctly removed from the cluster sample by the blue colour-boundary. All the other OB stars are redder than $J_s - K_s = 4.5$ mag and hence outside the red colour-boundary. Assuming that these OB stars are part of the cluster, their red colours may either be explained by serious problems with the accuracy of the K_s-band photometry or by an increased and very patchy extinction in this field.

As the guide star is located in the top left image corner, this field is affected by pronounced anisoplanatism with strongly elongated stars at larger guide star distances. The combined image after subtraction of the fitted PSFs of detected sources shows large stellar residua mostly located along the edges of the field which indicates that in these areas the spatially varying PSF as generated with *daophot* is not a good representation of the local PSF. To check whether this is the cause for the peculiarities in the CMD, a rectangular area in the image centre with the least residua was selected (red dashed rectangle in Fig. 4.11). The CMDs of stars located inside and outside of this selection are shown in the left and right panel of Fig. 4.26, respectively. Inside the selection area, the scatter towards very red colours appears to be decreased compared to stars outside of the selection, which is best seen to the right of the PMS and above the distribution of red clump stars (see left panel of Fig. 4.26). The few remaining stars on the MS appear to be equally distributed to the left and right of the MS. For the CMD of Field 4, using only stars outside of the rectangular selection (right panel of Fig. 4.26), stars on the MS appear to be predominantly located to the right of the isochrone . Strangely, the number of stars rejected by the blue colour boundary is also larger, so that both selections differ not only in a shift in colour.

To check whether a locally increased extinction in Field 4 is responsible for or contributes to the observed scatter and the shift to redder colours, the J_s- and K_s magnitudes of two OB stars (qF344, qF358) and the WC star (qF309) were compared to the respective J- and K-band magnitudes of Figer

et al. (1999b). They are found to agree within 0.2 mag which is the estimated error of their J- and K-band photometry. Seven stars contained in the LHO catalogue yielded on average 0.2 mag larger K_s-band magnitudes than derived from the NACO data. Yet even if the K_s-band magnitudes from the LHO catalogue or the colours of Figer et al. (1999b) would be applied, four of the five OB stars (ignoring the blue foreground OB star) would not reside within the colour selection. This indicates that Field 4 is particularly affected by strong, patchy extinction most pronounced in the regions outside the performed rectangular selection. In the three-colour image of the cluster in Fig. 4.4 a darkish arc located above Field 1 and stretching into the left part of Field 4 can be faintly seen. All of the spectroscopically identified OB stars reside within or close to this arc. The OB stars from the LHO catalogue are located in the bottom right corner of Field 4 close to its apparent edge and qF344 and qF358 are in the top left image corner, where the darkened arc bends into Field 4. Even in the centre, there appear to be less and fainter stars compared to e.g. Field 5 which is also suggestive of an increased and patchy extinction in Field 4. The contribution of possible systematic photometric errors due to pronounced anisoplanatism in Field 4 to the shift towards redder colours cannot be distinguished from effects of varying extinction. In the presence of strong local extinction variations, a colour selection valid for all stars in Field 4 cannot be defined reliably. Even if only stars within the rectangular selection are used and the same colour selection as for the other fields is applied, the corresponding field star PMD, i.e. the PMD containing only field stars based on their proper motion or colour with $K_s < 17.5$ mag, still shows some central clusterings indicative of cluster stars outside the colour selection. As it is hence not possible to establish a reliable cluster sample, Field 4 is disregarded in its entirety for the derivation of the PDMF.

4.3.1.3 Area selection for Field 2

For Fields 3 and 5, proper motion members inside and outside the colour selection are approximately evenly distributed across the respective field. In contrast, all proper motion members located in the lower right image corner of Field 2 are rejected by the red colour-boundary at $J_s - K_s = 4.5$ mag which is indicative for a larger local extinction. As it is not possible to shift the colour-boundary to redder colours without introducing presumable red-clump stars or stars from the old Galactic bulge population into the cluster sample, the affected area was covered by a rectangular mask. Within another small area close to the centre of the left image margin proper motion members are completely lacking (cf. red dashed line in Field 2 in Fig. 4.11). This area is disregarded for the mass function derivation as well. These two area selections do not exclude any cluster members shown in the CMD of Field 2, but reduce only the area regarded as covered by the observations which acts as a weighting factor for the derivation of the mass function within different annuli (see Sect. 4.4).

4.3.2 Comparison with the predictions of the synthetic models of Field 2

The proper motion membership criterion $p_{crit} = 0.40$, i.e. the minimum membership probability of a star to be included in the membership sample, was established based on the synthetic models of Field 2 (see Sect. 4.2.2.3). It was chosen such that the expected fraction of field stars in the sample and the fraction of lost cluster stars are at the same time as low as possible, and it was applied to all outer fields. Based on the models, the fraction of contaminating field stars within the proper motion member sample is expected to be 0.17 ± 0.04 (Table 4.8). The fractions of proper motion members which were removed from the member sample by the colour selection are 0.30, 0.46 and 0.30 for Fields 2, 3 and 5, respectively.

Even for Field 2, the fraction of proper motion members removed by the colour selection is larger

than predicted by the model designed to resemble the PMD of this field. This could indicate that the applied colour selection is too strict and rejects stars which actually belong to the cluster. While proper motion members to the left of the blue colour-boundary are clearly separated from the cluster MS and can safely be classified as foreground stars, the distinction between cluster and field at redder colours is less clear due to the scatter of the red clump and the convergence of the second sequence from the old bulge population with the cluster population (see Fig. 4.24). Hence, some of the proper motion members redder than $J_s - K_s = 4.5$ mag, which is the approximate onset of the red clump distribution in the CMDs, could be actually reddened cluster members. Otherwise, shifting the red colour-boundary towards redder colours might introduce a severe contamination by bulge stars.

Another possible explanation for the discrepancy between the predicted fraction of the contaminants and the fraction of rejected cluster members could be that modelling the distribution of field stars in the PMD by a single bivariate normal distribution is an oversimplification. Field stars along the line of sight sample a large variety of rotation velocities due to their different Galactocentric distances and in addition originate from different constituents of the Milky Way such as the Galactic disc, the Galactic bulge and possibly the nuclear stellar disc (Launhardt et al. 2002; Clarkson et al. 2012). The preferential loss of stars at larger distances due to extinction may further introduce a bias to the observed field distribution. Sumi et al. (2003) found that red clump stars at the near side of the Galactic bulge have a proper motion of 1.5 ± 0.1 mas/yr ($\hat{=} 57 \pm 4$ km/s at $d = 8$ kpc) relative to red clump stars at the far side, which is consistent with a rotation of the bulge in the same direction as the Sun. Hence, as the bulge stars follow the Galactic rotation, their proper motions are distributed around the line indicating the Galactic plane in the PMD and, because the cluster was used as reference frame, reside in the south-west segment (cf. Fig. 4.12). Furthermore, stars from the near side of the Galactic bulge are on average closer to the origin of the PMD which is defined by the cluster rest frame, while bulge stars from the far side are expected to reside at larger distances. Such a connection between the colour of a field star and its location in the PMD was actually found by Stolte et al. (2008) for the Arches cluster and can thus be expected for the Quintuplet cluster. The preferential loss of bulge stars at the far side of the bulge due to extinction might lead to a non-symmetric field star distribution biased towards proper motions with smaller offsets from the origin towards the south-west of the PMD. In that case modelling the field star distribution with a bivariate normal distribution would underestimate the presence of field stars close to the origin and attribute a number of field stars to the cluster distribution. The model would hence predict a too low fraction of contaminants within the proper motion cluster sample.

In summary, the discrepancy between the fraction of field stars in the proper motion member sample $n_{cont,m}$ as predicted by the models of Field 2 (see Sect. 4.2.2.3) and the fraction of proper motion members removed by the colour selection might indicate that the red colour-boundary at $J_s - K_s = 4.5$ mag excludes some reddened cluster members. Alternatively, caused by an extinction-induced asymmetry of the observed field star distribution, $n_{cont,m}$ could be underestimated as the field star distribution in synthetic PMD was modelled by a single bivariate normal distribution.

The fractions of the finally selected cluster stars relative to the total number of stars are 0.17, 0.12, and 0.20 for Fields 2, 3, and 5, respectively[23]. For Fields 2 and 5 the percentage of cluster members are close to the inserted fraction of cluster stars for the models ($\pi_c = 0.20$) and the two fields show the same fraction of proper motion members removed by the colour selection (30%). The relative similarity of these two fields is expected due to their comparable distance from the cluster centre[24]

[23] The stated values refer to stars located within the areas used to derive the mass function (green line in Fig. 4.11) and with assigned membership probabilities, i.e. stars with measured proper motions brighter than $K_s = 17.5$ mag.

[24] The distance is measured from the centre of the respective field to the cluster centre.

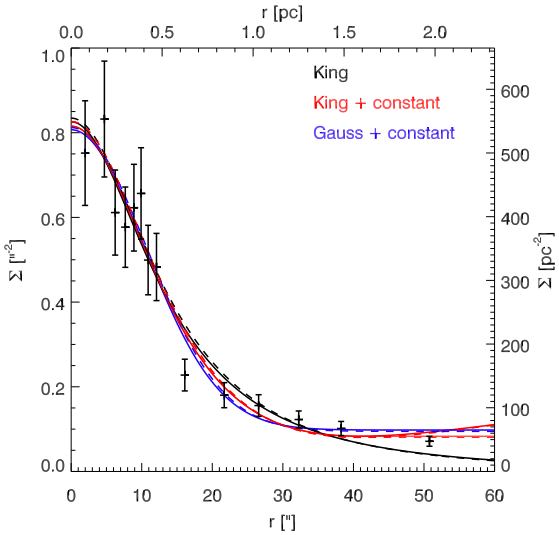

Figure 4.27: Surface density profile of the Quintuplet cluster derived from the cluster members in Fields 1, 2, 3, and 5 ($K_s < 17.5$ mag) located within the areas finally used to derive the MF (green line in Fig. 4.11). The surface density within 14 equal-number annuli was fitted by a King profile (black, King 1962), a King profile with a constant term (red), and Gaussian profile with a constant term (blue). The dashed lines indicate the respective profiles adopting the averaged fit parameters determined for using 8, 10, 12, 14, 16, 18, and 20 equal-number annuli. The thin red lines (solid and dashed) show the value of the additive constant beyond the tidal radius for the King profile with constant term. The error bars show the Poissonian errors divided by the area of each annuli.

(28″ and 29″). The increased fraction of contaminating fields stars and the lower percentage of cluster stars after the colour selection found for Field 3 can be explained at least qualitatively by the larger distance of the centre of Field 3 from the cluster centre which is about 46″. As the cluster density and hence the ratio of cluster to fields stars drops with larger distance to the cluster centre, the fraction of contaminating field stars in the cluster sample, i.e. of field stars with proper motions indistinguishable from the cluster population, does increase. Furthermore, the cluster distribution fitted to the PMD and its extent compared to the field distribution are both larger for Field 3 than for Fields 2 and 5 (see Table 4.9) which increases the number of stars attributed to the cluster distribution for this field. All in all, the relative similarities and differences between the three outer fields regarding the fraction of contaminating field stars in the proper motion member sample and the fraction of cluster stars after the colour selection are at least qualitatively consistent with the decrease of the number density of cluster stars with distance from the cluster centre (see Fig. 4.27).

The fraction of stars classified as field stars solely because of their proper motion or solely because of their colour[25] relative to the total number of field stars ranges between 0.15 (Field 2) to 0.22 (Fields 3 and 5) and 0.09 (Field 2) to 0.12 (Field 3), respectively. This small scatter is expectable if the field star population is homogeneous across the outer fields and suggests that the distinction between cluster and field is of similar quality for Fields 2, 3, and 5 and that the colour selection does not remove a disproportionally large number of proper motion members for Field 3.

[25]Most field stars differ in proper motion *and* colour from the cluster population and are hence removed from the proper motion sample *and* reside outside the colour selection.

Table 4.12: Averaged parameters of the profile fitting to the surface density determined within 8, 10, 12, 14, 16, 18, and 20 annuli (cf. Fig. 4.27). The error bounds indicate the difference of the maximum/minimum retrieved fit parameter from the respective average.

Profile	Peak		r_c		r_t		Constant term	
	($''^{-2}$)	(10^2 pc^{-2})	($''$)	(pc)	(10^2 $''$)	(pc)	($''^{-2}$)	(10^2 pc^{-2})
King	$0.83^{+0.03}_{-0.03}$	$5.5^{+0.2}_{-0.2}$	$14.6^{+0.4}_{-0.5}$	$0.57^{+0.01}_{-0.02}$	$1.9^{+0.6}_{-0.3}$	7^{+2}_{-1}		
King + bg[a]	$0.74^{+0.02}_{-0.02}$	$4.9^{+0.1}_{-0.1}$	$18.6^{+1.0}_{-0.5}$	$0.72^{+0.04}_{-0.02}$	$0.41^{+0.01}_{-0.01}$	$1.59^{+0.05}_{-0.05}$	$0.081^{+0.003}_{-0.001}$	$0.53^{+0.02}_{-0.01}$
Profile	Peak		σ				Constant term	
	($''^{-2}$)	(10^2 pc^{-2})	($''$)	(pc)			($''^{-2}$)	(10^2 pc^{-2})
Gauss + bg	$0.72^{+0.03}_{-0.03}$	$4.8^{+0.2}_{-0.2}$	$10.7^{+0.4}_{-0.3}$	$0.41^{+0.02}_{-0.01}$			$0.095^{+0.003}_{-0.002}$	$0.63^{+0.02}_{-0.01}$

Notes. [a] The fit of the surface density profile with a the King profile with constant term did not converge for using 8 annuli. The stated parameters are therefore the average of the respective parameters of fitting the surface density determined within 10, 12, 14, 16, 18, and 20 annuli.

4.3.3 Surface density profile

The surface density profile of the Quintuplet cluster was determined using all cluster members with $K_s < 17.5$ mag located within the areas of Fields 1, 2, 3, and 5 which were actually used to derive the mass function (enframed in green in Fig. 4.11). An estimation of the cluster centre using all observed cluster members would be biased as the outer fields do only cover the areas to the south and east of the central parts of the cluster. Hence, the cluster centre derived from the final cluster sample in Field 1 (see Sect. 4.2.2.3) was applied again. To determine the surface density, the stars were distributed among equal-number annuli, where the number of stars within each annulus was divided by the area flagged as good in the bad area mask (Fig. 4.11) within the respective annulus. The surface density within 8, 10, 12, 14, 16, 18, and 20 equal-number annuli was fitted by King profiles with and without a constant term and a Gaussian profile with a constant term (see Fig. 4.27). The King profile is defined as (see Eq. (14) in King 1962)

$$\Sigma(r) = k\left(\frac{1}{\left(1+\left(\frac{r}{r_c}\right)^2\right)^{\frac{1}{2}}} - \frac{1}{\left(1+\left(\frac{r_t}{r_c}\right)^2\right)^{\frac{1}{2}}}\right)^2 , \tag{4.14}$$

with the parameters r_c and r_t being termed as core and tidal radius, respectively. The averaged fit parameters are summarized in Table 4.12.

The measured surface density at $r = 0.6$ pc is below all fitted profiles. This may be caused by the fact that the respective annulus contains the gap between Field 1 and the outer fields, such that the surface density determined for this annulus and the radius to which this value is assigned are probably not accurate. Disregarding this datapoint, all three profiles inside of $r \lesssim 1.5$ pc are a good representation of the measured surface density, while further out the King profile without additive constant term declines too fast and the value of the constant determined for the Gaussian profile appears to be slightly overestimated. Considering that the PDMF slope in the range of $1.2 < r < 1.8$ pc is still slightly flattened (see Table 4.15), the tidal radius of the King profile with constant term, $r_t = 1.59^{+0.05}_{-0.05}$ pc, seems to be too small especially as the tidal radius of the cluster is expected to be

larger than 1.7 pc (see Sect. 4.4.3). On the other hand, the tidal radius of the King profile without a constant component is by a factor of two larger than expected when assuming that the cluster resides within 200 pc from the Galactic centre. As the value of r_t is hence highly dependent on the actual value of the additive constant, the tidal radius of the Quintuplet cluster cannot be well constrained by means of fitting a King profile to the observed surface density. To a lesser extent this applies also to r_c as the maximum of the King profile depends not only on k and the constant term, but also on the ratio of r_t/r_c.

Compared to the preliminary surface density profile which was determined using the final cluster sample in Field 1 and member candidates in Field 2 (see Sect. 4.2.2.3), the value of the additive constant drops to about a third of its preliminary value. This indicates that the usage of membership probabilities to establish the proper motion sample of cluster stars instead of a fixed σ value and the subsequent application of the colour selection significantly improved the cluster sample. Although there still might be some contaminating field stars within the final cluster sample, the constant offset cannot simply be regarded as the surface density of the field population, as certainly not all cluster stars in the outermost radial bin (see Fig. 4.27) are misclassified field stars.

4.3.4 Mass assignment

The masses of cluster members located in the Fields 2, 3, and 5 were derived using the same isochrones as for the central part of the cluster (Field 1), i.e. from three isochrones with ages of 3, 4, and 5 Myr which were combined from a Padova MS and Pisa-FRANEC PMS isochrone of the respective age, and from a single 4 Myr Geneva MS isochrone (see Sect. 3.6 for details). The initial and present-day masses of each cluster member are determined from the intersection of the line of reddening through the respective star with the isochrone in the K_s, $J_s - K_s$ CMD using the extinction law of Nishiyama et al. (2009, $A_J : A_{K_s} = 3.02 : 1$) and assuming a distance to the cluster of 8 kpc.

The uncertainty of the masses as inferred from the isochrones was assessed by determining the minimum and maximum mass achievable within the range spanned in brightness and colour by the photometric uncertainties of the respective star. The mass uncertainty of each star was estimated as the maximum absolute difference between its best-guess mass and its minimum and maximum mass. For the outer fields, the average percental mass uncertainty is about 5% of the best-guess initial or present-day mass for stars with $4 < m_{\rm init} < 6\,{\rm M}_\odot$ and decreases towards larger masses. For the masses inferred for Field 1 (see Sect. 3.6), the average percental mass uncertainty in the same mass range is 9% and less for higher masses. Although the quality of the photometry in Field 1 is not inferior compared to the outer fields, the mass uncertainty is in general increased due to the steeper slope of the line of reddening in the respective CMD which is $A_H/(A_H - A_{K_s}) = 2.37$ compared to $A_{K_s}/(A_{J_s} - A_{K_s}) = 0.495$ in the outer fields.

4.4 Mass function

4.4.1 Present-day mass function of the Quintuplet cluster

The PDMF in the outer parts of the Quintuplet cluster as covered by Fields 2, 3, and 5 was determined within two annuli with origins at the presumed cluster centre (see Sect. 4.2.2.3). The radial ranges spanned by the two annuli are $0.6 < r < 1.2$ pc and $1.2 < r < 1.8$ pc. By chance, the brightest cluster members with $r > 1.2$ pc reside outside of $r = 1.8$ pc. Therefore, the PDMF within the outer annulus was also derived for setting its outer boundary to $r = 2.1$ pc. As the observed Quintuplet fields do not cover the full area within $r = 1.8$ or 2.1 pc, the area fractions within $r < 0.6$ pc and the two annuli

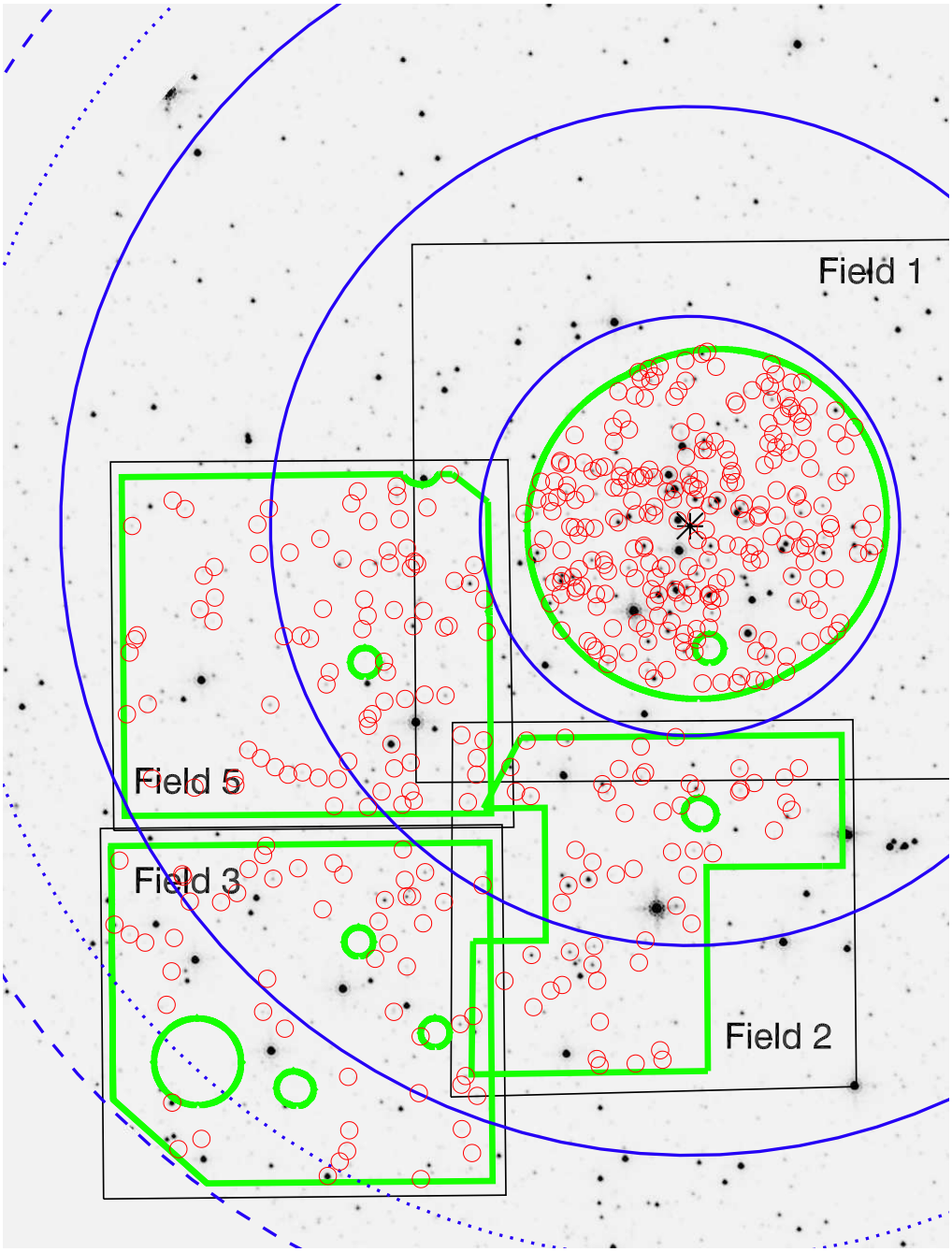

Figure 4.28: Sources and annuli used for the derivation of the PDMFs. Circles with radii of 0.6, 1.2, and 1.8 pc (blue solid lines) and 2.1 and 2.35 pc (blue dotted and dashed lines) assuming a distance of 8 kpc are overlaid on the selected area of the WFC3 $F127M$ combined image. The presumed cluster centre is indicated by the black asterisk. The areas which were actually used to derive the MF are enframed in green, the positions of cluster members ($K_s < 17.5$ mag) are marked with red circle points.

Table 4.13: Comparison of the PDMF slope for the central part of the Quintuplet cluster ($r < 0.6$ pc, see Fig. 4.28).

Isochrone name	n [a]	n_{J_s} [b]	$m_{\rm min}$ [c] ($M_\odot$)	$m_{\rm max,init}$ [d] ($M_\odot$)	$m_{\rm max,act}$ [d] ($M_\odot$)	$\alpha_{\rm m_{init}}$ [e]	$\alpha_{\rm m_{init},J_s}$ [f]	$\alpha_{\rm m_{act}}$ [g]
3 Myr Padova	220	187	5.5	65.8	44.5	−1.72	−1.75	−1.52
4 Myr Padova	261	217	4.6	46.7	34.2	−1.68	−1.69	−1.43
5 Myr Padova	289	237	4.0	34.5	29.0	−1.55	−1.56	−1.36
4 Myr Geneva	261	217	4.5	47.3	35.1	−1.77	−1.78	−1.58

Notes. [(a)] Number of stars in the initial mass range $m_{\rm min} < m < m_{\rm max,init}$ used to determine the PDMF slope $\alpha_{\rm m_{init}}$ (see Table 3.5) and $\alpha_{\rm m_{act}}$. [(b)] Number of stars in the initial mass range $m_{\rm min} < m < m_{\rm max,init}$ used to determine the PDMF slope $\alpha_{\rm m_{init},J_s}$. [(c)] Minimum mass of a star above the PMS/MS transition, i.e. above the lower grey shaded area in Fig. 3.11 for the 3, 4, and 5 Myr Padova isochrones. For the 4 Myr Geneva isochrone the minimum mass was chosen such that the same stars as for the 4 Myr Padova isochrone are included (see Sect. 3.6 and Table 3.5). [(d)] Maximum mass, i.e. uppermost bin boundary of the PDMF as determined with Eq. (3.4), excluding identified WR stars. [(e)] PDMF slope derived using initial stellar masses (see Table 3.5). [(f)] PDMF slope derived using initial stellar masses but only stars with counterparts in the WFC3 source catalogue and $J_s - K_s < 5.05$ mag. [(g)] PDMF slope derived using actual (present-day) stellar masses and the same sample of stars as for $\alpha_{\rm m_{init}}$.

covered by the observations and used for the derivation of the mass function were determined (see Fig. 4.28). The central part of Field 1 which was selected to derive the PDMF in the cluster core (see Sect. 3.4.2) covers the area within $r < 0.6$ pc for the most part (71%). The area fractions of the inner and outer annuli are 28% and 21%, respectively. If the outer boundary of the second annulus is shifted to $r = 2.1$ pc the observed area fraction of this annulus is reduced to 17%. The annuli, the used areas and the cluster members are indicated in Fig. 4.28.

The slope of the PDMF in the outer parts of the cluster was determined using both initial and present-day masses to ensure the comparability with MF slopes stated in the literature. The PDMF slopes for the central part of the cluster as stated in Table 3.5 were derived using initial stellar masses. As addendum the slope of the PDMF determined from the present-day masses and distributing the datapoints among 12 bins is listed for all four isochrones in Table 4.13. The average of these four slopes is $\alpha_{\rm m_{act}} = 1.47^{+0.12}_{-0.10}$ compared to $\alpha_{\rm m_{init}} = 1.68^{+0.13}_{-0.09}$ (see Sect. 3.7), where the maximum difference between the average slope and the individual slopes of the PDMF derived from each isochrone was adopted as the lower and upper bounds in both cases.

The flattening of the slope $\alpha_{\rm m_{act}}$ by about 0.2 dex compared to $\alpha_{\rm m_{init}}$ is caused by the contraction of the mass range due to the mass loss by stellar winds predicted by the stellar models for stars with $m_{\rm init} \gtrsim 12 M_\odot$. As mentioned in Sect. 3.7, a residual contamination by red clump stars mostly from the south-west segment of the PMD could not be removed from the cluster sample of Field 1 by the colour selection in $H - K_s$. The distinction between cluster members and field stars in the K_s, $J_s - K_s$ CMD (Fig. 4.25) is more pronounced due to the wider colour baseline, such that field stars from the red clump and the older population of the Galactic bulge can be effectively removed by an additional colour selection at $J_s - K_s = 5.05$ mag. The colour selection was chosen such that all previously designated cluster members in Field 1 with $K_s < 13$ mag are kept, as almost all of these stars are identified in the LHO catalogue as OB stars. Due to the lower resolution of the WFC3 data, 105 members from the source catalogue of Field 1 are lost, but only 17 of these stars are brighter than 17.5 mag. The colour selection removes further 35 or 62 stars brighter than $K_s = 17.5$ mag or 19.0 mag, respectively. From this refined sample the PDMF slope using initial masses was determined in exactly the same way as for the original sample. The derived slope $\alpha_{\rm m_{init},J_s}$ is compared to the

original values $\alpha_{\mathrm{m_{init}}}$ in Table 4.13. The original and the new values of the PDMF slope are in excellent agreement given that the formal fitting uncertainty is 0.09 dex. This indicates that neither the lower resolution of the WFC3 data nor the residual contamination of the original cluster sample by field stars introduces a systematic bias of the PDMF.

As for the central parts of the cluster, the equal-number binning scheme of Maíz Apellániz & Úbeda (2005) was applied for the derivation of the mass function and its slope in the outer parts of the cluster in order to avoid potential biases due to large differences of the number of stars per bin (see Sect. 3.7 for details). For the central part of the cluster, masses were inferred by determining the intersection of the line of reddening with the respective isochrone in the H, $H - K_s$ CMD (see Sect. 3.6). The same procedure was applied also for the outer fields, but in the K_s, $J_s - K_s$ CMDs (Sect. 4.3.4). The minimum mass of stars above the PMS, i.e. with a unique mass assignment, which was applied as lowermost bin boundary for the PDMFs, is hence slightly different between Field 1 and the outer fields (cf. Tables 3.5 and 4.14). The maximum mass, i.e. the uppermost bin boundary of the PDMF, is again derived from the data with Eq. (3.4) after exclusion of one WR star and the Pistol star in Field 2 (cf. Sect. 3.7). As mentioned in the previous section, three very bright stars in Field 3 do not appear in the CMD as they are strongly nonlinear. If belonging to the cluster, these stars are most probable WR stars and would have been excluded from the PDMF in any event. The number of used bins had to be decreased compared to the PDMFs of Field 1 due to the smaller number of cluster stars within the two annuli. Stars were distributed among 6, 8 or 10 bins each containing approximately the same number of stars. The bins to contain one additional star from the potential remainder of the division of the number of stars by the number of bins are selected randomly (see Sect. 3.7), which introduces a slight variation of the slope for the different realisations of the PDMF (cf. $\Delta\alpha_{\mathrm{binning}}$ in Table 3.5). Due to the comparatively small number of cluster stars in the outer parts of the Quintuplet cluster, the difference between the flattest and steepest slope of these different realisations of the PDMF can be as large as 0.16 dex, depending on the choice of the isochrone and the applied number of mass bins. The considered slope for a particular annulus, isochrone and number of bins is the mean value of all possible realisations of the respective PDMF. As the derived mass function slopes using 6, 8 or 10 bins can differ by up to 0.16 dex, the values stated in Table 4.14 are the mean values of the respective three slopes for the different numbers of bins. For the determination of the global PDMF slope within $r < 1.8$ pc (or $r < 2.1$ pc), the refined cluster sample of Field 1 was combined with the cluster stars from Fields 2, 3, and 5. To account for the cluster area which was not covered by the observations or was disregarded for the derivation of the PDMF (see Fig. 4.28), each star was weighted by the inverse of the covered area fraction of the circle or annulus it resides in (see above).

Within the inner annulus ($0.6 < r < 1.2$ pc), the PDMF slope is found to be steeper compared to the central part of the cluster ($r < 0.5$ pc) by about 0.2 to 0.3 dex, but is still slightly flatter than the canonical IMF slope ($\alpha = -2.3 \pm 0.36$, Kroupa et al. 2013). For example, in the case of the 4 Myr Padova isochrone and using initial masses, the slope of the PDMF in the inner annulus is -2.0 ± 0.2 (see Table 4.14) compared to $\alpha_{\mathrm{m_{init}}} = -1.68 \pm 0.09$ in the cluster centre (Table 3.5). For the outer annulus, the results depend strongly on the chosen outer boundary. Using only stars within $1.2 < r < 1.8$ pc, the slope steepens only moderately by 0.1 or 0.3 dex (5 Myr Padova isochrone) and amounts to $\alpha_{\mathrm{m_{init}}} = -2.1 \pm 0.3$ for the 4 Myr Padova isochrone. In contrast, if the outer boundary of this annulus is shifted to $r = 2.1$ pc, the derived slopes are steeper by up to 0.5 dex with respect to the inner annulus. For the 4 Myr Padova isochrone the PDMF slope in the extended outer annulus is $\alpha_{\mathrm{m_{init}}} = -2.4 \pm 0.3$. The large impact of the chosen outer radius can be partly explained by the lack of stars more massive than 25 $M_\odot$ within $1.2 < r < 1.8$ pc. By chance, all three cluster members with

Table 4.14: Overview of the derived slopes of the mass function within two annuli and the overall mass function slope of the Quintuplet cluster. The outer boundary of the outer annulus was set to 1.8 or 2.1 pc.

Isochrone name	Radial range (pc)	n^a	$m_{\rm min}{}^b$ ($M_\odot$)	$m_{\rm max,init}{}^c$ ($M_\odot$)	$m_{\rm max,act}{}^c$ ($M_\odot$)	$\alpha_{\rm m_{init}}{}^d$	$\Delta\alpha_{\rm m_{init}}{}^e$	$\alpha_{\rm m_{act}}{}^d$	$\Delta\alpha_{\rm m_{act}}{}^e$
3 Myr Padova	0.6 – 1.2	54	5.5	77.9	47.3	−1.9	0.2	−1.8	0.2
4 Myr Padova	0.6 – 1.2	69	4.7	52.3	34.0	−2.0	0.2	−1.8	0.2
5 Myr Padova	0.6 – 1.2	79	4.1	35.0	29.9	−1.9	0.2	−1.8	0.2
4 Myr Geneva	0.6 – 1.2	69	4.7	47.1	37.3	−2.0	0.2	−1.9	0.2
3 Myr Padova	1.2 – 1.8	42	5.5	26.0	25.5	−2.0	0.3	−2.0	0.3
4 Myr Padova	1.2 – 1.8	52	4.7	24.1	23.6	−2.1	0.3	−2.0	0.3
5 Myr Padova	1.2 – 1.8	65	4.1	21.9	21.4	−2.2	0.3	−2.1	0.3
4 Myr Geneva	1.2 – 1.8	52	4.7	23.1	22.4	−2.1	0.3	−2.1	0.3
3 Myr Padova	< 1.8	283	5.5	65.8	44.5	−2.0	0.1	−1.8	0.1
4 Myr Padova	< 1.8	338	4.7	46.7	34.2	−2.00	0.09	−1.83	0.09
5 Myr Padova	< 1.8	381	4.1	34.5	29.0	−1.92	0.09	−1.79	0.09
4 Myr Geneva	< 1.8	338	4.5^f	47.3	35.1	−2.00	0.09	−1.88	0.09
3 Myr Padova	1.2 – 2.1	49	5.5	38.7	36.2	−2.4	0.3	−2.4	0.3
4 Myr Padova	1.2 – 2.1	63	4.7	33.7	31.6	−2.4	0.3	−2.4	0.3
5 Myr Padova	1.2 – 2.1	76	4.1	28.7	26.9	−2.4	0.2	−2.3	0.2
4 Myr Geneva	1.2 – 2.1	63	4.7	33.4	31.2	−2.5	0.3	−2.5	0.3
3 Myr Padova	< 2.1	290	5.5	65.8	44.5	−2.1	0.1	−1.9	0.1
4 Myr Padova	< 2.1	349	4.7	46.7	34.2	−2.07	0.09	−1.92	0.09
5 Myr Padova	< 2.1	392	4.1	34.5	29.0	−2.00	0.09	−1.88	0.09
4 Myr Geneva	< 2.1	349	4.5^f	47.3	35.1	−2.08	0.09	−1.97	0.09

Notes. $^{(a)}$ Number of stars in the initial mass range $m_{\rm min} < m < m_{\rm max,init}$ used to determine the PDMF slope. $^{(b)}$ Minimum mass of a star above the PMS/MS transition, i.e. above the lower grey shaded area in Fig. 3.11 for the 3, 4, and 5 Myr Padova isochrones. For the 4 Myr Geneva isochrone the minimum mass was chosen such that the same stars as for the 4 Myr Padova isochrone are included (cf. Sect. 3.6). $^{(c)}$ Maximum mass as calculated with Eq. (3.4). $^{(d)}$ Average of the PDMF slopes binning the initial or actual (present-day) masses into 6, 8 and 10 bins. $^{(e)}$ Average of the uncertainty of the PDMF slopes using 6, 8, and 10 bins. The uncertainty of the PDMF slope accounts for the formal uncertainty of the linear fit, the uncertainty introduced by the random distribution of surplus stars, and the deviation of the slope derived for the respective number of bins from the average PDMF slope. $^{(f)}$ For the overall mass function ($r < 1.8$ pc or $r < 2.1$ pc), $m_{\rm min}$ had to be slightly adapted for the 4 Myr Geneva isochrone in order to include the same stars in the PDMF as for the 4 Myr Padova isochrone.

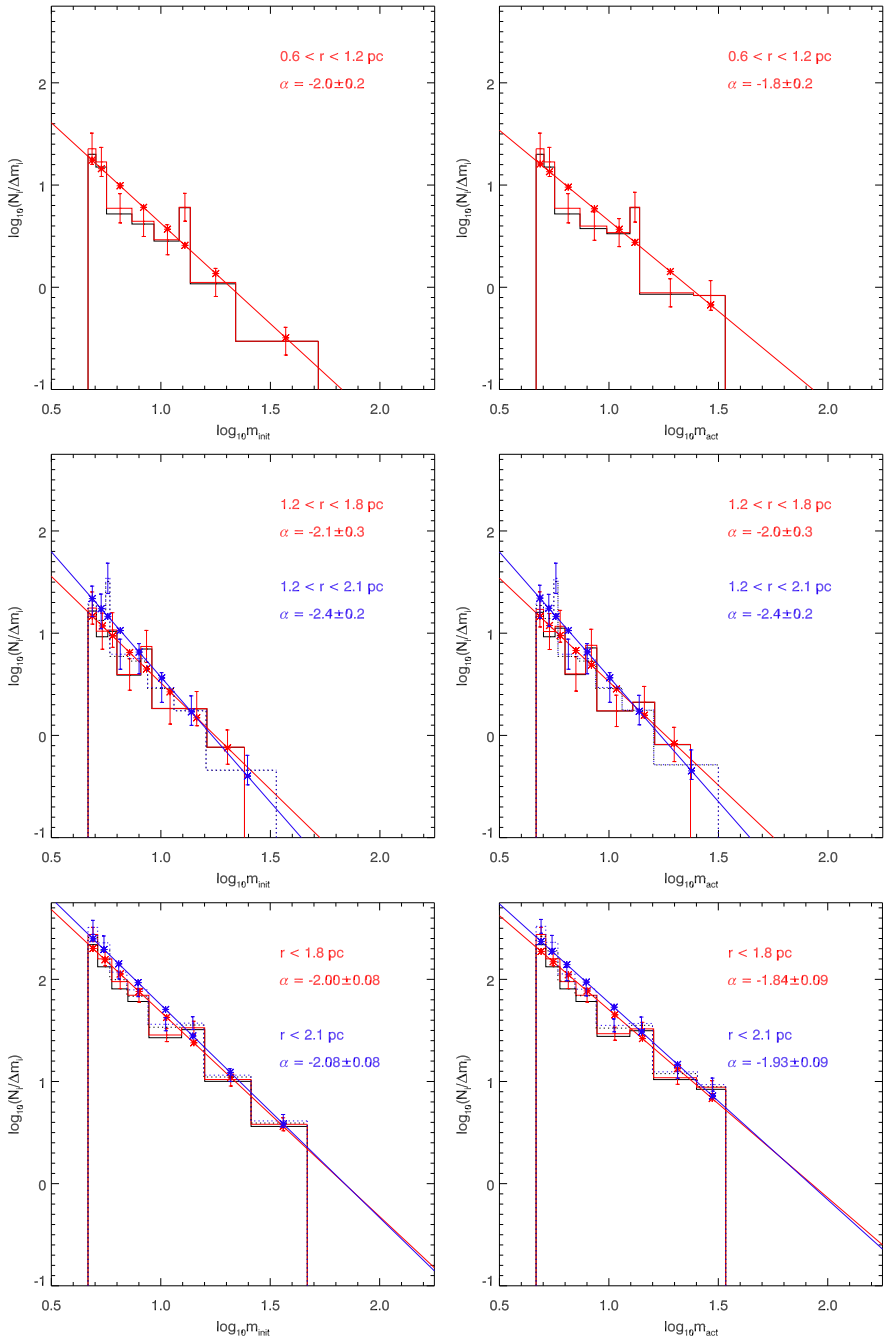

Figure 4.29: Present-day mass function of stars located within two annuli covering the outer parts of the Quintuplet cluster (*top panel* and *middle panel*) and the overall PDMF including the central part of the cluster and the two annuli (*bottom panels*). Initial (*left panels*) and present-day (actual) masses (*right panels*) were inferred from the 4 Myr Padova isochrone and distributed among 8 bins such that each bin contains approximately the same number of stars. The inner annuli covers the radial range of $0.6 < r < 1.2$ pc, while the outer annuli contains stars within $1.2 < r < 1.8$ pc (solid lines) or $1.2 < r < 2.1$ pc (dotted lines). For the overall mass function ($r < 1.8$ pc or $r < 2.1$ pc), the number of stars was scaled with the covered area fraction of the annulus the respective star resides in. The mass functions without and with completeness correction are drawn in black and in colour (red or blue), respectively. The linear fits to the completeness corrected mass functions are shown as well.

Table 4.15: Final values of the PDMF slope estimated as the average PDMF slope of all considered isochrones (cf. Tables 4.13 and 4.14).

Radial range (pc)	$\alpha_{\mathrm{m_{init}}}{}^{a}$	$\alpha_{\mathrm{m_{act}}}{}^{a}$
< 0.5	$-1.68^{+0.13}_{-0.09}$	$-1.5^{+0.1}_{-0.1}$
$0.6 - 1.2$	$-1.9^{+0.2}_{-0.2}$	$-1.8^{+0.2}_{-0.2}$
$1.2 - 1.8$	$-2.1^{+0.3}_{-0.3}$	$-2.1^{+0.3}_{-0.3}$
$< 1.8^{b}$	$-1.97^{+0.09}_{-0.09}$	$-1.83^{+0.09}_{-0.09}$
$1.2 - 2.1$	$-2.4^{+0.3}_{-0.3}$	$-2.4^{+0.3}_{-0.3}$
$< 2.1^{b}$	$-2.05^{+0.09}_{-0.09}$	$-1.92^{+0.09}_{-0.09}$

Notes. [(a)] The stated error bounds are either the maximum differences between the respective average slope and the four averaged slopes (one for each isochrone) or the mean slope uncertainty of the averaged slopes, depending on what error range is larger. [(b)] The stated error bounds of the overall PDMF slopes do not include the uncertainty of the area fractions which were applied to correct for the cluster areas not covered by the observations and are hence lower limits to the true uncertainty of the slope.

$m_{\mathrm{Pad,4Myr}} > 30\,M_{\odot}$ are located outside of $r = 1.8\,\mathrm{pc}$[26]. If $r = 2.1\,\mathrm{pc}$ is used as the outer boundary, one of these three stars is included in the PDMF and the maximum mass is increased (see Table 4.14) which lowers the normalized number of stars in the last mass bin (middle panels in Fig. 4.29). To quantify the effect of the larger maximum mass alone, the PDMF of the outer annulus was derived using only stars within $1.2 < r < 1.8\,\mathrm{pc}$, but with the uppermost bin boundary set to $33.7\,M_{\odot}$, i.e. m_{max} for the 4 Myr Padova isochrone in the radial range $1.2 < r < 2.1\,\mathrm{pc}$. The larger maximum mass causes a systematic steepening of the slope by 0.1 to 0.3 dex compared to the values stated in Table 4.14. The remaining difference of the slopes for the two choices of the outer boundary can be explained by the increased number of low mass stars ($4.5 < m < 6\,M_{\odot}$) in the radial range of $1.8 < r < 2.1\,\mathrm{pc}$. It should be noted that a further increase of the outer boundary to $r = 2.35\,\mathrm{pc}$ to include all observed cluster stars (see Fig. 4.28) including the further two massive stars with $m_{\mathrm{Pad,4Myr}} > 30\,M_{\odot}$ (see above) has no significant effects on the derived slopes. The overall slope ($r < 1.8\,\mathrm{pc}$ or $r < 2.1\,\mathrm{pc}$) is marginally flatter than the canonical slope. For the two annuli, the slopes derived using present-day masses $\alpha_{\mathrm{m_{act}}}$ are not significantly flattened compared to the corresponding values of $\alpha_{\mathrm{m_{init}}}$. As the mass loss by stellar winds strongly increases with mass and the fraction of very massive stars is lower compared to Field 1, the difference between the usage of present-day and initial masses has less impact on the mass function (cf. $\alpha_{\mathrm{m_{init}}}$ and $\alpha_{\mathrm{m_{act}}}$ in Tables 4.13 and 4.14).

The slope values for the outer annulus and hence the overall slopes should be taken with care. For $r = 1.8\,\mathrm{pc}$ as the outer boundary of the outer annulus, the main concern is the accidental absence of higher mass stars in the areas covered by observations within this annulus and the pronounced effect of such stars on the PDMF slope. Due to the large number of high mass stars in the central parts of the cluster the expected effect of few additional high mass stars in the outer annulus on the overall slope ($r < 1.8\,\mathrm{pc}$) is expected to be small. If $r = 2.1\,\mathrm{pc}$ is used as the outer boundary, a further concern arises from the fact that the radial range $1.8 < r < 2.1\,\mathrm{pc}$ is only probed by a small part of Field 3 (see Fig. 4.28). The reported slopes are hence likely biased by stars located closer to the inner radius of

[26] Presumable WR stars are disregarded for the derivation of the PDMF (see above and cf. Sect. 3.7).

Table 4.16: Total initial/present-day mass of all detected cluster members ($m > 4.7\,M_\odot$) for the 4 Myr Padova isochrone excluding WR stars or LBVs.

Radial range (pc)	$M_{\rm cl,init}$ [a] ($10^3\,M_\odot$)	$M_{\rm cl,init,compl}$ [b] ($10^3\,M_\odot$)	$M_{\rm cl,init,compl,area}$ [c] ($10^3\,M_\odot$)	$M_{\rm cl,act}$ [a] ($10^3\,M_\odot$)	$M_{\rm cl,act,compl}$ [b] ($10^3\,M_\odot$)	$M_{\rm cl,act,compl,area}$ [c] ($10^3\,M_\odot$)
< 0.6	3.1	3.5	4.9	3.0	3.3	4.7
0.6 – 1.2	0.8	0.9	3.0	0.8	0.8	3.0
1.2 – 1.8	0.5	0.5	2.5	0.5	0.5	2.5
< 1.8	4.4	4.9	10.4	4.3	4.7	10.1
1.2 – 2.1	0.6	0.6	3.8	0.6	0.6	3.8
< 2.1	4.5	5.0	11.8	4.4	4.8	11.4

Notes. [(a)] Total mass of all stars included for the determination of the PDMF. [(b)] Total mass after correcting for completeness of the detected stars. [(c)] Total mass after correcting for completeness of the detected stars and for the area not covered by the observations (cf. Fig. 4.28).

the annulus. For the overall slope ($r < 1.8$ pc or $r < 2.1$ pc), a further slight bias might be introduced by the small gap between the inner radius of the annulus at $r = 0.6$ pc and the area of Field 1 used to derive the PDMF (Fig. 4.28). As each star is weighted by the inverse of the covered area (see above), the impact of the central part of the cluster on the overall PDMF might be artificially increased.

As the slopes within each annulus derived from the four different isochrones agree within the uncertainties, the average of these slopes is provided as the final value of the PDMF slope for each radial range in Table 4.15. The upper and lower error bounds were assessed in the following way. First the maximum differences between the final value of the slope and the four individual slopes – given in Tables 4.15 and 4.14, respectively – were determined providing preliminary upper and lower bounds for each radial range. These error bounds were then compared to the mean slope uncertainty of the four individual slopes for each radial range ($\Delta\alpha_{\rm m_{init}}$ and $\Delta\alpha_{\rm m_{act}}$ in Table 4.14). For a conservative estimate of the uncertainty the larger of these two error ranges was applied as the error bounds of the respective final value of the PDMF slope.

Liermann et al. (2012) determined the PDMF slope of the Quintuplet cluster ($m_{\rm init} > 10\,M_\odot$) based on a sample of likely cluster stars from the LHO catalogue. Adopting the line of sight velocity $v_{\rm los}$ as selection criterion, their member sample includes all stars brighter than the completeness limit at $K = 13$ mag and with line of sight velocities within $\sigma = \pm 17$ km/s from the line of sight velocity of the cluster (113 km/s). Masses were inferred from the K-band magnitudes of the stars and a mass-luminosity relation derived from a 4 Myr Geneva isochrone. Using all stars in the member sample (including WR stars), they determined a mass function slope of $\alpha_{\rm m_{init}} = -1.23 \pm 0.51$. If only OB stars were selected, the retrieved PDMF slope was $\alpha_{\rm m_{init}} = -1.66 \pm 0.51$. This value is within the errors in good agreement with the mass function slopes derived from the proper motion member sample within $r = 1.2$ pc which is the approximate area covered by the LHO catalogue (cf. Table 4.15).

4.4.2 Total mass

The total measured mass above the PMS/MS transition region (i.e. $m_{\rm min}$ in Table 4.14) as the sum of the individual derived stellar masses was determined separately for each of the four applied isochrones and for using the initial and the present-day stellar masses. As for the derivation of the overall mass function, the refined cluster sample of the central part of the cluster ($r < 0.6$ pc, see previous section) was combined with the catalogue of cluster members in Fields 2, 3, and 5. To account for detection

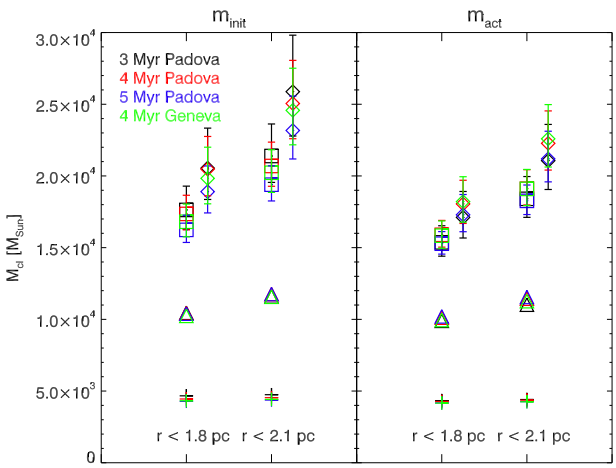

Figure 4.30: Total mass of the Quintuplet cluster within $r < 1.8$ pc or $r < 2.1$ pc using initial (left half) or present-day (actual) stellar masses (right half). The contribution of the known WR stars and LBVs in the Quintuplet cluster to the total mass are not accounted for in this plot. The total masses including all stars above the PMS/MS transition region (see $m_{\rm min}$ in Table 4.14) which are detected within the areas covered by the observations (cf. Fig. 4.28) are drawn as crosses for all used isochrones. The total masses above $m_{\rm min}$ corrected for the incompleteness and areas not covered by the observations are shown as triangles. The diamond and box points (for clarity drawn with a slight horizontal offset) show the total masses extrapolated down to 0.5 and 1 $M_\odot$, respectively, using the appropriate PDMF slopes (see Table 4.14). The error bars reflect the minimum and maximum extrapolated masses accounting for the uncertainty of the PDMF slope.

losses due to crowding, the mass of each star was divided by its individual completeness value. As not all the area within an annulus was actually covered by the observations or was used for the analysis (see Fig. 4.28), the total measured mass was scaled to the full area by dividing it by the respective area fraction (see Sect. 4.4.1). The area correction contributes more than 60% to the such determined total mass above $m_{\rm min}$ and is afflicted with some uncertainties. For the area correction spherical symmetry was assumed, which has not necessarily to be the case as for example Westerlund 1 with a similar age as the Quintuplet cluster shows a pronounced elongation with an axis ratio of about 3:2 (Gennaro et al. 2011). As the area fractions especially of the two annuli are small, the impact of a potential asymmetry of the cluster and of statistical variations in the distribution of high mass stars may be pronounced. The corrected total masses have therefore to be considered with care. Table 4.16 summarises the measured total mass before and after completeness correction and correction for the areal coverage for the 4 Myr Padova isochrone and all radial ranges. The average of the measured total mass for all isochrones within $r = 2.1$ pc, corrected for the incompleteness and the covered area fraction and using initial masses, amounts to $1.17^{+0.01}_{-0.01} \times 10^4\ M_\odot$. The stated upper and lower bounds enclose the maximum and minimum measured total mass derived from the individual isochrones. As the uncertainties of the area fraction are not known and can hence not be accounted for, the error bounds are lower limits.

The corrected total mass (within $r < 1.8$ pc or $r < 2.1$ pc) was extrapolated to 0.5 and 1 $M_\odot$ adopting the appropriate PDMF slope for each isochrone and for using initial and present-day masses. Fig. 4.30 shows the measured total mass, the total mass after completeness and area correction, and the extrapolated total masses for all isochrones. The best guess value of the total mass is estimated as the average of the extrapolated total masses for all isochrones (see Table 4.17) and is $2.5^{+0.5}_{-0.3} \times 10^4\ M_\odot$ ($r < 2.1$ pc) for using initial masses and extrapolating down to 0.5 $M_\odot$. The lower and upper bounds enframe the

Table 4.17: Cluster mass extrapolated down to a minimum mass of 0.5 and 1 $M_\odot$. The masses of the LBVs and WR stars in the Quintuplet cluster are not included.

	$m_{\rm min} = 0.5\,M_\odot$		$m_{\rm min} = 1\,M_\odot$	
Radial range (pc)	$M_{\rm cl,init}{}^a$ ($10^4\,M_\odot$)	$M_{\rm cl,act}{}^a$ ($10^4\,M_\odot$)	$M_{\rm cl,init}{}^a$ ($10^4\,M_\odot$)	$M_{\rm cl,act}{}^a$ ($10^4\,M_\odot$)
< 1.8	$2.0^{+0.3}_{-0.3}$	$1.8^{+0.2}_{-0.2}$	$1.7^{+0.2}_{-0.2}$	$1.6^{+0.1}_{-0.1}$
< 2.1	$2.5^{+0.5}_{-0.3}$	$2.2^{+0.3}_{-0.3}$	$2.0^{+0.3}_{-0.2}$	$1.9^{+0.2}_{-0.2}$

Notes. $^{(a)}$ $M_{\rm cl}$ denotes the average value of the extrapolated total masses for all isochrones. The error bounds enframe the maximum and the minimum achieved total masses, i.e. the total range spanned by the errors bars in Fig. 4.30.

maximum and the minimum derived total masses, i.e. the total range spanned by the errors bars in Fig. 4.30. The values of the cluster mass within $r = 2.1$ pc should be considered with special caution as the radial range $1.8 < r < 2.1$ pc is only probed by a small portion of Field 3 (see Sect. 4.4.1). The results of the mass extrapolation in general can only provide a rough estimate of the cluster mass as it was presumed that the measured PDMF slopes are valid down to 0.5 or 1 $M_\odot$. Due to mass segregation, the mass function slope for higher mass stars is likely flattened compared to the value of the overall IMF, but the transition between the flattened and the still unaffected mass range of the PDMF is unknown and depends also on the considered radial range. Hence, the extrapolated total mass using the PDMF slope determined in the mass range $m \gtrsim 4.5\,M_\odot$ most probably constitutes a lower limit to the present-day mass contained within the probed area of the cluster.

So far, the contribution of the known WR stars in the Quintuplet cluster to the cluster mass was not accounted for. Within $r < 1.8$ pc or $r < 2.1$ pc reside in total 19 or 20 WR stars, respectively. These WR stars include the 14 WR stars listed in the LHO spectral catalogue[27], the re-identified WN-star LHO 110 (Liermann et al. 2010), four additional WR stars from Table 3 in Figer et al. (1999b) (qF76, qF151, qF274, qF309), one WR star from Mauerhan et al. (2010c) (Table 5, GXOGC J174617.7-285007[28]), and with the largest distance from the cluster centre WR 102ca (Homeier et al. 2003). If the mass ranges of the WR stars are inferred from the respective stellar models (cf. Sect. 3.6), a WR star at an age of 4 Myr has an initial mass of about 55 $M_\odot$ and an actual mass of roughly 20 $M_\odot$ and the contribution of the WR stars to the cluster mass amounts to 1045 - 1100 $M_\odot$ (initial masses) or 360 - 400 $M_\odot$ (present-day masses). Sander, A. et al. (2012) derived the luminosities and the stellar temperatures of Galactic WC stars by comparing the observed spectra with a grid of non-blanketed models of stellar atmospheres. Based on the position of these stars in the HRD, they inferred an initial mass range for WC stars at solar metallicity of about $25 - 40\,M_\odot$. Of the total of 19 (20) WR stars within $r < 1.8$ pc (2.1 pc), 13 (14) are WC stars, while the remaining six are WN stars. Liermann et al. (2010) derived for two of these WN stars initial masses above $150\,M_\odot$, and for three other WN stars initial masses in the range between $60 - 120\,M_\odot$. Adopting for the WC stars and the one remaining WN star without mass estimate an average mass of $30\,M_\odot$, and for the five WN stars the lower mass estimates from Liermann et al. (2010), the contribution of the WR stars to the initial mass is slightly reduced to $870 - 900\,M_\odot$. All of these mass estimates assume that the WR stars are single stars. At least for the five eponymous Quintuplet stars (Q1 – Q4, Q9), this assumption does not hold as

[27] For cross-references to the WR stars already contained in Table 3 of Figer et al. (1999b) see Table 2 in Liermann et al. (2009).

[28] The identifier is slightly misspelled. The correct identifier for this source is GXOGC J174617.8-285007 (see Table 1 in Wang et al. 2006).

these objects were identified as colliding-wind binaries (Tuthill et al. 2006). As close binary evolution decreases the required minimum initial mass for a star to enter the WR phase (Eldridge et al. 2008), the estimated contribution of known WR stars to the total mass of the Quintuplet cluster are supposedly upper limits. The masses of the two LBVs in the Quintuplet cluster are highly uncertain. Figer et al. (1998) estimated the mass of the Pistol star (qF134) to be initially about 200 – 250 $M_\odot$, while Najarro et al. (2009) derived an initial mass of only 100 $M_\odot$. In any case, the contribution of these two stars to the total cluster mass is negligible given the large uncertainties of the extrapolated cluster mass. In summary, including a contribution of $\sim 1.0 \pm 0.1 \times 10^3\ M_\odot$ from the population of WR stars to the total cluster mass, the Quintuplet cluster is expected to have a total stellar mass of $2.6^{+0.5}_{-0.3} \times 10^4\ M_\odot$ within $r < 2.1$ pc using initial masses and extrapolated down to 0.5 $M_\odot$.

4.4.3 Discussion

A direct inference of the cluster's IMF from its PDMF is complicated even for young massive clusters by the effects of the stellar and dynamical evolution. Due to dynamical friction stars more massive than the average stellar mass tend to sink towards the centre, while less massive stars drift towards the outer parts. As the timescale of this migration is inversely proportional to the stellar mass (see Eq. (20) in Portegies Zwart et al. 2010), the massive stars concentrate faster in the cluster core than the intermediate mass stars which results in an inward flattening of the mass function. Such a flattening of the MF slope towards the centre is a common finding among young massive clusters. In Table 4.18 and Fig. 4.31, the final values of the PDMF slope derived for the Quintuplet cluster are compared to the PDMF slopes at different radii of the Galactic young massive clusters Arches, NGC 3603 and Westerlund 1. For all four clusters, the PDMF in their innermost annulus is significantly flattened compared to the canonical IMF slope of $\alpha = -2.3$ ($m > 0.5\,M_\odot$, Kroupa 2001). Between the inner- and the outermost observed radius, the PDMF slope steepens considerably by 0.6 to 1.6 dex and approaches (NGC 3603) or even exceeds the canonical slope value. Although it is still debated if and to what extent star clusters are born initially mass segregated (see e.g. Bonnell & Davies 1998; Littlefair et al. 2003; Chen et al. 2007; Allison et al. 2009; Sana, H. et al. 2010; Pang et al. 2013), numerical simulations for the Arches cluster show that dynamical mass segregation alone is sufficient to explain the observed flattening of the MF in the cluster core even if the IMF had a Salpeter slope (Portegies Zwart et al. 2007; Harfst et al. 2010). If the cluster is observed out to its tidal radius to cancel the effects of mass segregation, the determined PDMF may still deviate from the overall IMF. The high mass part may be influenced by ejections of massive stars due to dynamical few-body interactions in dense cluster cores (Fujii & Zwart 2011; Banerjee & Kroupa 2012) and in particular by stellar evolution. Especially the occurrence of supernovae might deplete the highest mass bins and thus alter the measured slope even if initial masses are used to generate the PDMF. For Westerlund 1, the presence of an X-ray pulsar shows that at least one supernova has already occurred in the cluster (Muno et al. 2006a), but the total number of supernovae is estimated to be about 10^2 ($m_{\rm init} > 50\,M_\odot$) assuming a cluster age of 4-5 Myr (Muno et al. 2006b; Clark et al. 2008). While the stellar evolution is of minor or no importance for low and intermediate mass stars ($m \lesssim 20\,M_\odot$) given the young age of the considered clusters, the preferential loss of low mass stars from a mass segregated cluster due to evaporation (Baumgardt & Makino 2003) might be speeded up in a strong tidal field as experienced by the Arches and Quintuplet clusters near the Galactic centre and deplete the low mass parts of the PDMF. The same effects which hamper the inference of the IMF from the PDMF also complicate the comparison of MF slopes of young massive clusters as their impact depends on the age and the initial conditions of the respective cluster. Hence, to deduce the initial conditions of a cluster, to infer its IMF and to allow for a detailed comparison with other clusters, numerical simulations customised to

Table 4.18: Comparison of PDMF slopes of Galactic young massive clusters.

Quintuplet		Arches[a,b]		NGC 3603[a,c]		Westerlund 1[a,d]	
r (pc)	$\alpha_{\mathrm{m_{init}}}$	r (pc)	$\alpha_{\mathrm{m_{init}}}$	r (pc)	$\alpha_{\mathrm{m_{init}}}$	r (pc)	$\alpha_{\mathrm{m_{init}}}$
		< 0.2	-1.6	< 0.2	-1.3		
				0.2 – 0.3	-1.6		
< 0.5	$-1.68^{+0.13}_{-0.09}$	0.2 – 0.4	-2.3	0.3 – 0.5	-1.8		
				0.5 – 0.7	-1.8	< 0.75	-1.6
0.6 – 1.2	$-1.9^{+0.2}_{-0.2}$	0.4 – 1.5	-3.2	0.7 – 1.3	-1.9	0.75 – 1.5	-2.3
1.2 – 1.8	$-2.1^{+0.3}_{-0.3}$			1.3 – 2.0	-1.9	1.5 – 2.1	-2.6
< 1.8	$-1.97^{+0.09}_{-0.09}$	< 1.5	-2.6				
1.2 – 2.1	$-2.4^{+0.3}_{-0.3}$			1.3 – 2.0	-1.9	1.5 – 2.1	-2.6
< 2.1	$-2.05^{+0.09}_{-0.09}$						
						2.1 – 3.3	-2.7

Notes. [(a)] PDMF slopes are rounded to their significant digits. The typical size of the slope errors is about 0.2 – 0.3dex. For the precise values the reader is referred to the respective references (see below). [(b)] PDMF slopes ($m_{\mathrm{min}} = 12.5\,M_{\odot}$ ($r < 0.2$ pc) or $9.7\,M_{\odot}$) taken from Habibi et al. (2013) assuming the extinction law of Nishiyama et al. (2009), a cluster age of 2.5 Myr, and a distance to the cluster of 8 kpc. The values of $\alpha_{\mathrm{m_{init}}}$ within $r = 0.4$ pc are in full agreement with Espinoza et al. (2009). [(c)] PDMF slopes ($1 < m < 100\,M_{\odot}$) from Pang et al. (2013) adopting a cluster age of 1 Myr and a distance of 6.9 ± 0.6 kpc. [(d)] PDMF slopes ($3.4 < m < 27\,M_{\odot}$) from Brandner et al. (2008) adopting a cluster age of 3.9 Myr and a distance to the cluster of 3.55 ± 0.17 kpc.

the observed properties of the respective cluster are required.

In the following, the PDMFs of the Quintuplet and the Arches cluster are compared in detail as both clusters are located in the Galactic centre region and have probably formed in the same environment and evolved in the strong tidal field of the Galactic centre. Furthermore, at present times the masses of the two clusters are of comparable size, albeit both clusters and especially the older Quintuplet cluster may already have lost a significant fraction of their original mass due to tidally induced evaporation (Kim et al. 2000; Portegies Zwart et al. 2002). To determine the total mass within $r < 0.4$ pc, Espinoza et al. (2009) extrapolated the PDMF of the Arches cluster down to $1\,M_{\odot}$ (using initial masses) and found a total mass of $2.0 \pm 0.6 \times 10^4\,M_{\odot}$. In a similar way, Habibi et al. (2013) determined a cluster mass of $1.9^{+0.3}_{-0.3} \times 10^4\,M_{\odot}$ for $r < 1.5$ pc using present-day masses and a minimum mass of $0.5\,M_{\odot}$. Clarkson et al. (2012) estimated the total cluster mass within $r = 1$ pc from the measured velocity dispersion in the cluster centre to be $1.5^{+0.74}_{-0.60} \times 10^4\,M_{\odot}$. The total extrapolated masses of the Quintuplet cluster are of similar size ranging between 1.6 - $2.2 \times 10^4\,M_{\odot}$ (present-day masses) depending on the applied radial range and the minimum mass for the extrapolation (see Table 4.17).

The comparison of the PDMF of the Quintuplet and the Arches cluster is carried out with the PDMF slopes $\alpha_{\mathrm{m_{init}}}$ (see Table 4.18) derived using initial stellar masses to minimise effects of the stellar evolution. The PDMF of the Quintuplet cluster in its central parts ($r < 0.5$ pc) is found to be flat ($\alpha_{\mathrm{m_{init}}} = -1.68^{+0.13}_{-0.09}$). The PDMF slope steepens moderately in the intermediate annulus ($0.6 < r < 1.2$ pc) to $\alpha_{\mathrm{m_{init}}} = -1.9^{+0.2}_{-0.2}$, and approaches the canonical slope in the outer annulus: $\alpha_{\mathrm{m_{init}}} = -2.1^{+0.3}_{-0.3}$ ($1.2 < r < 1.8$ pc) or $\alpha_{\mathrm{m_{init}}} = -2.4^{+0.3}_{-0.3}$ ($1.2 < r < 1.8$ pc, see Table 4.15). Although the pronounced

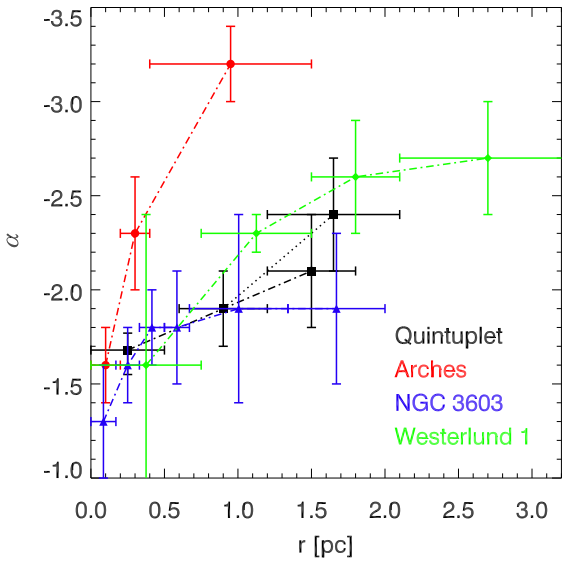

Figure 4.31: PDMF slopes of Galactic young massive clusters vs. radius (cf. Table 4.18). The PDMF slopes are derived using initial masses. The radial extent of the respective annulus is indicated by the error bars.

steepening of the PDMF observed when extending the limit of the outer annulus from 1.8 to 2.1 pc is mostly due to the difference in the upper mass limit (see Table 4.14), the also observed increase of the number of low mass stars (see Sect. 4.4.1) indicates that the PDMF slope steepens further towards larger radii. The approximate Galactocentric distance of the cluster ranges from the projected distance of the cluster to the Galactic centre of 30 pc to about the Galactocentric distance of the Central Molecular Zone along the line of sight, which the cluster is thought to reside in (Figer et al. 1999b). This distance is assumed here to be roughly 200 pc (Morris & Serabyn 1996). Adopting the values of the enclosed mass in the inner part of the Milky Way from Fig. 14 in Launhardt et al. (2002)[29], the resulting tidal radius of the Quintuplet cluster is in the range of 1.7 - 3.6 pc. Hence, depending on the actual Galactocentric distance, the observations within $r < 1.8$ pc (2.1 pc) may either cover the whole tidally bound population of the Quintuplet cluster or reach only out to about half of the tidal radius.

In the core of the Arches cluster ($r < 0.2$ pc) and the first annulus ($0.2 < r < 0.4$ pc) the values of the PDMF slope are $\alpha_{\mathrm{m_{init}}} = -1.6 \pm 0.2$ and -2.3 ± 0.3, respectively (Habibi et al. 2013), compared to $-1.68^{+0.13}_{-0.09}$ for the inner 0.5 pc of the Quintuplet cluster. In the outer parts of the Arches cluster ($0.4 < r < 1.5$ pc) the PDMF slope of -3.2 ± 0.2 is significantly steeper than the canonical IMF and also steeper by 1.3 dex or 0.8 dex than the PDMF slope of the Quintuplet cluster in the first ($0.6 < r < 1.2$ pc) or second annulus ($1.2 < r < 2.1$ pc), respectively. While the overall slope of the Arches cluster $\alpha_{\mathrm{m_{init}}} = -2.6 \pm 0.2$ ($r < 1.5$ pc) is slightly steeper than the canonical IMF slope, the overall PDMF slope of the Quintuplet cluster[30] is within $r = 2.1$ pc still slightly flattened: $\alpha_{\mathrm{m_{init}}} = -2.05^{+0.09}_{-0.09}$. It is striking that in all compared radial ranges the Quintuplet PDMF is flatter than the PDMF of the Arches cluster. The Quintuplet cluster at an approximate age of 4 Myr does therefore not only show a much more dispersed configuration than the Arches cluster, but the radial extent in which the PDMF is flattened compared to the canonical IMF slope is also inflated.

Whether these findings confute the possibility that both clusters were born under similar initial

[29] Data table kindly provided by R. Launhardt, private communication.

[30] As the uncertainty of the applied area fraction is not included, the stated upper and lower limits are lower bounds of the true error of the overall PDMF slopes of the Quintuplet cluster.

conditions and with similar initial properties and whether the flat PDMF of the Quintuplet cluster is reconcilable with a canonical IMF can only be judged using numerical simulations adapted to the respective cluster. Up to now numerical models of the young massive clusters close to the Galactic centre concentrate on the Arches cluster (Kim et al. 2000; Portegies Zwart et al. 2002, 2007; Harfst et al. 2010), mostly because this cluster has been studied in more detail. The Arches cluster is much more compact than the Quintuplet cluster such that at least in its centre proper motions are not necessarily required to establish a meaningful sample of cluster stars. Harfst et al. (2010) constrained the initial conditions of the Arches cluster by comparing a set of N-body simulations with the cumulative mass profile, the total mass and the mass function as determined from the observations by Stolte et al. (2005). So far, their simulations do not account for the movement of the cluster in the Galactic tidal field. Their best-fitting models include models starting with a Salpeter and a flat IMF ($\alpha = -1.9$). For both cases, the PDMF is flattened in the cluster core and steepens towards larger radii. The PDMF slope of the models starting with a flat IMF remain flatter at all times than the PDMF slopes of the models adopting the Salpeter IMF. Although within $r < 0.4$ pc both assumed IMFs are reconcilable with the data, the models using the standard IMF are in better agreement with the observations if evolved to the presumed cluster age of 2.5 Myr. The recently derived PDMF slope of the Arches cluster between $0.4 < r < 1.5$ pc by Habibi et al. (2013) is in very good agreement with the predicted PDMF slopes of these dynamical simulations for this radial range and supports the notion that an initial top-heaviness of the Arches MF is not required to explain its presently observed flattened MF slope in the cluster core. If the Quintuplet cluster shared similar initial properties with the Arches cluster and can be considered as its older version, the cluster would have had to undergo a very strong expansion between 2.5 and 4 Myr to evolve from the very compact state of the Arches to its dispersed configuration observed today. Olczak et al. (2012) adopted the favoured initial conditions of Harfst et al. (2010) for the Arches cluster and compared the evolution of the model with and without accounting for the orbital motion of the cluster in the Galactic tidal field. In both cases the expansion of the half-mass radius between 2.5 and 4 Myr is very moderate with an increase of roughly 0.1 pc (see their Fig. 2). This expansion appears to be too small to inflate the areas with a flattened PDMF in the Arches cluster to the large radial range with a top-heavy PDMF in the Quintuplet cluster. Assuming that the perigalacticon of the Quintuplet cluster is not much smaller than that of the orbit adopted by Olczak et al. (2012) for the Arches cluster, it is likely that the Quintuplet cluster was already initially less concentrated.

It should be noted that the Arches model placed in the Galactic tidal field is initially not in dynamical equilibrium (Olczak et al. 2012). This leads to an in initial expansion of the cluster and a core density decreased by a factor of two compared to the model without tidal field during the further evolution of the cluster (see Fig. 2 in Olczak et al. 2012). It is therefore probable that the initial conditions of the Arches cluster were slightly different than originally inferred by Harfst et al. (2010), i.e. that the initial density was higher than determined with neglect of the Galactic centre tidal field. Whether this influences also the fiducial value of the IMF slope is currently not clear. At least qualitatively and with care some implications for the Quintuplet cluster might be drawn from the orbiting model of the Arches cluster. At an age of 5 Myr, the losses due to the Galactic tidal field are still quite moderate with only $\sim$ 5% of the stellar population residing in the tidal arms (C. Olczak, private communication). As a result, the PDMF of the model does not deviate from the applied IMF for $m \lesssim 5\,M_{\odot}$ at all radial ranges (see Fig. 4.32). This implies, that the observed Quintuplet PDMF ($m \gtrsim 4\,M_{\odot}$) could be unaffected from the loss of low mass stars in the Galactic tidal field, unless the perturbations of the cluster are much more violent than for the presumed orbit of the Arches cluster.

The PDMF of the Quintuplet cluster shows an pronounced radial trend and is found to be top-heavy

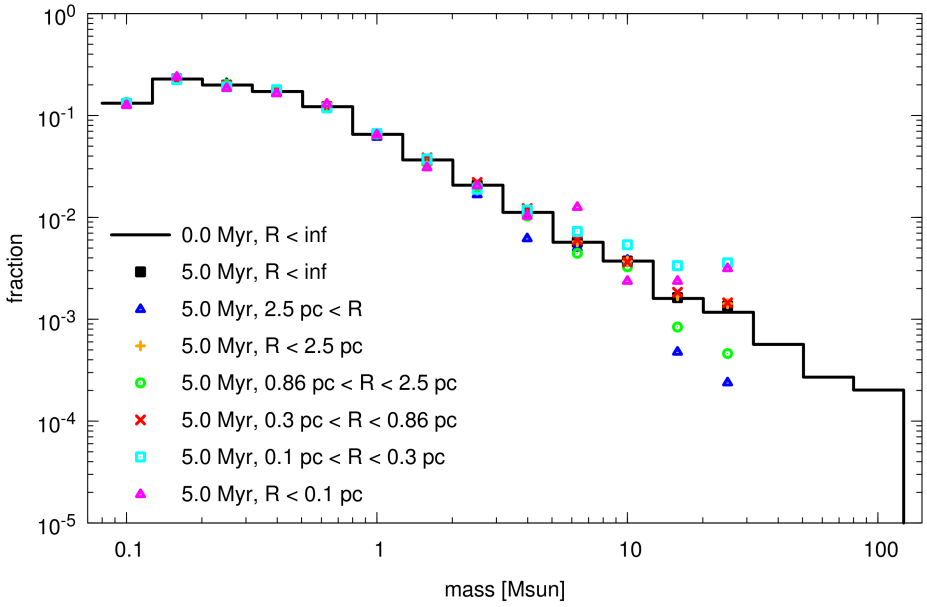

Figure 4.32: PDMF of the dynamical model of the Arches cluster orbiting in the Galactic tidal field (see Olczak et al. 2012) at a cluster age of 5 Myr (Christoph Olczak, private communication). The canonical IMF (Kroupa 2001) is drawn as the solid, black line, while the PDMF in different radial annuli is indicated by different symbols (see legend). For intermediate and high mass stars ($m \gtrsim 5\,M_{\odot}$) within the cluster core ($r_{\rm core} = 0.3$ pc), the PDMF is flattened compared to the canonical IMF, while for stars between the half-mass and the tidal radius ($r_{\rm halfmass} = 0.86$ pc, $r_{\rm tidal} = 2.5$ pc) and outside of $r_{\rm tidal}$ the PDMF is steepened. For lower mass stars the PDMF at all radial ranges is essentially unaffected by the internal and external dynamical evolution. Stars within the three uppermost mass bins of the IMF already have become supernova.

in the cluster centre ($\alpha_{\rm m_{init}} = -1.68^{+0.13}_{-0.09}$, $r < 0.5$ pc), while in the outer parts of the cluster the PDMF slope is consistent with the canonical IMF slope ($\alpha_{\rm m_{init}} = -2.4^{+0.3}_{-0.3}$, $1.2 < r < 2.1$ pc). The outward steepening of the PDMF is a typical result for a young massive cluster and indicative of mass segregation. Compared to the Arches cluster, the PDMF of the Quintuplet cluster is flatter in all observed radial ranges. Numerical models of the Arches cluster indicate that the half-mass radius between 2.5 and 4 Myr expands by only 0.1 pc which appears not sufficient for an Arches-like cluster to enlarge its core with the top-heavy PDMF to the extent a flat PDMF is observed in the Quintuplet cluster. Therefore the Quintuplet cluster has likely formed with different properties than the Arches cluster, i.e. less compact. For a thorough understanding of the dynamical evolution of the Quintuplet cluster and to constrain the initial properties of the cluster, an individual set of customised numerical models is required. A similar parameter study as has been performed for the Arches cluster (Harfst et al. 2010) is currently undertaken by Harfst et al. (in prep.).

5 Infrared excess sources in the Quintuplet cluster

Near-infrared imaging surveys of young open clusters revealed that a significant fraction of their stellar content consists of excess sources, i.e. that the $H-K$ or $K-L$ colours of the respective stars are significantly redder than the locus of MS stars in the CCDs (see e.g. Haisch et al. 2000; Lada et al. 2000; Haisch et al. 2001b). Near-infrared excess emission[1] from young stellar sources is an indicator for protoplanetary discs and traces hot dust in their inner parts (Haisch et al. 2001a). For Herbig AeBe stars, the assumption of a hot puffed-up inner rim roughly at the dust sublimation radius enhancing the near-infrared emission of the disc can account for the local bump at about $3\,\mu$m in their SEDs (Natta et al. 2001; Dullemond et al. 2001). As the excess in L-band is more pronounced than in K-band and is hence detectable independently of the disc inclination, surveys including L-band data provide an almost full census of circumstellar discs above the completeness limit in young star forming regions (Haisch et al. 2001a). For the Trapezium cluster, 97% of proplyds seen at optical wavelengths also show an excess in $K-L$ indicating that the detected near-infrared excess is a reliable tracer of protoplanetary discs (Lada et al. 2000).

The fraction of disc-bearing stars is a function of the cluster age and the stellar mass (Haisch et al. 2001a; Hernández et al. 2005; Kennedy & Kenyon 2009). For low mass stars (spectral type F and later) the high disc fractions of > 80% at young ages ($\lesssim 2$ Myr) indicate that initially (almost) all stars are born with a circumstellar disc generated in the star formation process. The fraction of stars with L-band excess decreases strongly with cluster age with an approximate timescale for the dissipation of the inner disc of about 6 Myr for low mass stars (Haisch et al. 2001b). For intermediate and higher mass stars (spectral type A and earlier) the disc dissipation timescale is significantly smaller. In the Trapezium cluster at an age of ~ 1 Myr the fraction of discs around stars of spectral types OBA is with 42% only about half of the overall disc fraction (Lada et al. 2000). Hernández et al. (2005) identified Herbig AeBe stars in nearby OB associations with ages between 3 – 16 Myr based on their Hα emission and near-infrared excess in the $J-H$, $H-K$ CCDs. Equating the fraction of Herbig AeBe stars in these OB associations with the fraction of stars with optically thick inner discs, they found that the disc fraction at an age of 3 Myr is about a factor of 10 smaller compared to the disc frequency around lower mass stars. They concluded that the disc dissipation timescale for the Herbig AeBe stars is only about 3 Myr. The dissipation of gaseous circumstellar discs is caused by photoevaporation of the central star or an external UV field and dynamical encounters and proceeds rapidly (Alonso-Albi et al. 2009, and references therein). From a sample of discs detected at mm wavelengths around Herbig AeBe stars, the authors inferred that the destruction of discs around stars more massive than $3\,M_{\odot}$ occurs within $\lesssim 2$ Myr. As the coupling of the dust grains to the gas depends on the size of the dust grains, compact dust discs comprising of larger grains may survive the dissipation of their gaseous circumstellar discs. The disc dissipation timescale of Hernández et al. (2005) is with 3 Myr slightly longer than the estimate by Alonso-Albi et al. (2009), but their disc fractions relied on excess at near-infrared rather than mm wavelengths and the estimated masses of the Herbig AeBe stars in

[1] In this chapter the term 'near-infrared excess' refers to excess emission at wavelengths between 1 and $4\,\mu$m. Excess emission at wavelengths > $4\,\mu$m is considered as mid-infrared excess.

their sample are comparatively low ($m \leq 3.6\,M_{\odot}$, cf. Tables 2 and 3 in Hernández et al. 2005).

Besides the age and the mass of the host star also the density and the number of high mass stars within the cluster or star forming region have a strong impact on the lifetime of protoplanetary discs (see e.g. Fig. 13 in Stolte et al. 2010). The external heating of gas in the outer disc by the FUV and EUV fields of early B and O stars in the cluster contributes significantly to the dissipation of circumstellar discs also around low mass stars. For example, in the young open cluster NGC 2244 (age: $2-3$ Myr) the disc fraction within projected distances < 0.5 pc from the nearest O star was determined to be only about half the disc frequency at larger projected distances (Balog et al. 2007). Guarcello et al. (2009) estimated the flux incident from the OB stars in NGC 6611 on stars with circumstellar discs and found that the disc fraction decreases with increasing external UV irradiation. The efficiency of tidal encounters in depleting and disrupting circumstellar discs was determined to depend on the stellar density of the cluster (Olczak et al. 2010). Based on size- and density-scaled models of the Orion Nebula Cluster (ONC) they find that within 1.5 Myr the disc fraction in their model of the ONC (central density: $0.5 \times 10^4\,\mathrm{pc}^{-3}$) decreases to about 85%, while at higher central densities of $4.2 \times 10^4\,\mathrm{pc}^{-3}$ the disc fraction drops down to $\sim 72\%$. Surprisingly, at the even higher core densities of the Arches cluster the disc destruction by tidal encounters seems to be less efficient with about 80% of the discs surviving the first 2.5 Myr and still at 6 Myr the disc fraction in their model is larger than 50% (Olczak et al. 2012). According to the authors, this is explained by the fact that in high density environments stellar encounters are dominated by hyperbolic flybys between low and intermediate mass stars with typically only minor impact on the disc mass. In contrast, at lower stellar densities the gravitational focusing of high mass stars becomes important leading to parabolic encounters with enhanced disc mass loss. It should be noted, that all these models do not account for the photoevaporation of the discs by internal or external UV radiation which is expected to be a very important mechanism for the disc destruction in rich clusters.

Due to the intense UV-field of their numerous OB stars and the high stellar densities, young massive clusters provide an especially hostile environment for the survival of protoplanetary discs. The disc fractions of the two young massive clusters NGC 3603 and Pismis 24 (ages: ~ 1 Myr) are with 27%[2] ($m > 1.2\,\mathrm{M}_{\odot}$) and 30% ($m > 0.5\,\mathrm{M}_{\odot}$) significantly reduced compared to disc frequencies of about 80% in less dense and less massive star forming environments such as the Trapezium cluster at the same age (Stolte et al. 2004; Fang et al. 2012). As observed in lower mass open clusters, the disc fraction of young massive clusters shows a similar dependence on the distance to the cluster centre. For Pismis 24 the disc frequency within a radial distance of less than 0.6 pc from the most massive stellar system Pismis 24-1 is with 19% only half the value outside of this radius. A similar trend is observed for NGC 3603 where again the disc fraction within $r = 0.6$ pc is only half as large (20%) as for $0.6 < r < 1.0$ pc. The overall disc fraction of the 2.5 Myr old Arches cluster of only $6 \pm 2\%$ for B-type stars ($2 < m < 20\,\mathrm{M}_{\odot}$, Stolte et al. 2010) indicates that the timescale of disc dissipation in young massive clusters is shortened compared to less extreme star forming environments. As expected the highest disc frequency of $9.7 \pm 3.7\%$ is observed in the outermost radial bin ($0.3 < r < 0.8$ pc). The finding of surviving circumstellar discs around B stars in the Arches cluster is surprising given the fast dissipation of the gaseous disc around a B-type host star by its own UV radiation (Alonso-Albi et al. 2009; Gorti et al. 2009) and the low disc fractions of Herbig AeBe stars (<6%) at an age of ~ 3 Myr even in OB associations (Hernández et al. 2005). Stolte et al. (2010) hence suggested that the remaining discs were massive, initially.

[2]This value is probably a lower limit as the results from higher resolved JHK_sL'-observations of NGC 3603 by Harayama et al. (2008) revealed a higher disc fraction of MS stars of $22 \pm 10\%$ within $r < 0.4$ pc compared to 12% from Stolte et al. (2004) for a similar mass and radial range.

Table 5.1: Overview of the VLT/NACO L'-band datasets.

Field	Date	Filter	Frames[a]	DIT (s)	NDIT	$t_{\rm int}$[b] (s)	Airmass	Seeing ($''$)	FWHM[d] ($''$)	Strehl ratio[d]
1	2009-06-17	L'	36	0.175	170	1071	1.04 – 1.08	0.57 – 0.71	0.110	0.21
2	2011-09-10	L'	21	0.175	170	625	1.06 – 1.10	1.19 – 2.14	0.115	0.20
3	2011-09-11	L'	15	0.175	170	446	1.02 – 1.05	0.98 – 1.45	0.111	0.23
5	2012-06-13	L'	38	0.200	100	760	1.01 – 1.04	0.71 – 1.18	0.115	0.18

Notes. [(a)] Number of dithered frames used to generate the final combined image. [(b)] Total integration time of the central part of the image with maximum overlap. [d] Determined from the extracted PSF of the combined image.

At the age of the Quintuplet cluster (4 Myr), the fraction of surviving circumstellar discs around intermediate and higher mass stars is expected to have further decreased and to be very low or even zero. To address the question whether the inner parts of circumstellar discs might survive the harsh conditions in a young massive cluster up to this age, NACO L'-data of the central and the outer parts of the Quintuplet cluster were obtained and near-infrared excess sources were identified based on their location in the $J_s - K_s$, $K_s - L'$ CCD. The L'-band datasets, their reduction and photometric calibration are detailed in Sect. 5.1. The CCDs and the selection of near-infrared excess sources as candidates for stars hosting surviving circumstellar discs are described in Sect. 5.2. The completeness of the L'-band data is assessed in Sect. 5.3 and in Sect. 5.4 the fraction of excess sources is derived. A discussion of the results concludes this chapter (Sect. 5.5).

5.1 Datasets and data reduction

5.1.1 VLT/NACO L'-band data

All of the five Quintuplet fields which were observed in the K_s-band (cf. Fig. 1.1) were also covered in the L'-band ($\lambda_c = 3.80\,\mu$m) to search for infrared excess sources among the cluster members. The datasets were obtained during several observation periods in 2009 (Field 1, PI: A. Stolte, Program ID 083.D-0513(B)), 2011 (Fields 2 and 3, PI: C. Olczak, Program ID: 087.D-0720(B)), and 2012 (Fields 4 and 5, PI: A. Stolte, Program ID: 089.D-0121(A)). The Fields 1 to 3 were observed in service mode, while the data of Fields 4 and 5 were obtained during the first of the two observing runs in 2012 in visitor mode (cf. Sect. 4.1.1.1). Field 4 turned out to be too shallow and was disregarded, also because no reliable member selection could be established for this field (see Sect. 4.3.1.2).

All fields were observed with the L27 camera having a pixel scale of $0.02719''\text{pixel}^{-1}$ and a FOV of $27.8'' \times 27.8''$. The natural guide stars for the infrared wavefront sensor were the same as for the K_s-band data with the exception of Q3 which was used as guide star for Field 5 instead of Q7 (see Fig. 1.1). The datasets were obtained with a DIT of 0.175 s and NDIT of 170 except for Field 5, where the DIT and NDIT were 0.2 s and 100, respectively (see Table 5.1). The short DITs compared to the DIT of the K_s-band data are required due to the high thermal background in the L'-band which quickly exceeds the saturation limit of the detector. For Field 1, in total 15 sky frames were obtained in three blocks before, in between and after the two blocks of science frames which each contained 18 frames. For Fields 2 and 3, the sky and science frames were recorded alternating in pairs of two, while no sky frames are available for Field 5.

For Field 1, the complete data reduction was performed with the custom-made data reduction

pipeline. As for Fields 2, 3 and 5 a more complicated estimation of the sky was required, the sky derivation and basic data reduction of these datasets were carried out manually[3]. Although Field 5 was obtained in cube mode the data reduction for this field was not performed with the single layers (DITs) of the data cube (cf. Sect. 4.1.1.1), but all NDIT layers of a cube were averaged into a single layer frame prior to the reduction. This helped to speed up the data reduction as no frame selection was required due to the constant performance for this dataset (see below). Due to the fast change of the thermal background in the L'-band, the method of the sky derivation from the sky or science frames had to be adjusted to each dataset individually. For Field 1, three skies were derived from the three blocks of sky frames and subtracted from the respective nine science frames with the shortest time delay to the respective sky. As the sky frames for Fields 2 and 3 contained particularly strong circular patterns probably caused by the thermal radiation of defocused dust grains on the tip tilt mirror, they were not used for the generation of the skies. Instead for each science frame an individual sky was determined from the four science frames with the shortest time lag to the respective science frame. The same procedure was applied for Field 5 albeit using the eight closest science frames. Of all L'-band datasets only Field 5 required a correction of the 50 Hz noise.

As the quality of the reduced science frames of a dataset judged by the FWHM of a reference source in the individual frames did not vary significantly, no selection of frames was performed based on that criterion. However, seven of 22 frames obtained of Field 3 were rejected due to strong, not removed sky patterns. For Field 5, the relative offsets of six science frames could not be determined reliably, hence only 38 of 44 obtained frames were combined with the *drizzle* algorithm. The area covered by the combined L'-images was for Fields 1 to 3 the same or slightly larger than that of the respective K_s-band observations (see Fig. 1.1). The L'-band data of Field 5 are shifted by about 5.7″ to the west and 2.8″ to the south with respect to the K_s-band observations. Hence in Field 5, only for about 85% of the area covered in K_s-band complementary L'-band data are available.

5.1.2 Source detection and photometric calibration

The source detection and PSF fitting was performed with the *daophot* package (cf. Sect. 4.1.1.2). For Fields 1 and 5 a quadratically varying analytical PSF was used, while the best source subtraction for Fields 2 and 3 was obtained with a constant PSF. The photometric uncertainties of the L'-datasets were estimated in the same manner as for the K_s-band data of the outer fields (for details see Sect. 4.1.1.3).

The photometric calibration was done with respect to the Galactic Legacy Infrared Mid-Plane Survey Extraordinaire (GLIMPSE) which uses the Infrared Array Camera (IRAC) onboard the Spitzer Space Telescope (Benjamin et al. 2003; Churchwell et al. 2009). To fulfil the requirement for the GLIMPSE catalogue to be $\geq$ 99.5% reliable, all sources within the wings of saturated stars are rejected to prevent the detection of false sources (see Sect. 3.2 and Appendix B in the GLIMPSE Data Release v2.0 document[4]). The wings of saturated stars are thereby assumed to affect a region with a radius of about 14.4″ around the respective star which in combination with the numerous WR stars in the cluster results in the GLIMPSE catalogue being devoid of usable calibrators within the area covered by the Quintuplet fields. Hence a 225″ $\times$ 225″ GLIMPSE image in the IRAC band 1 (central wavelength $\sim 3.6\,\mu$m) centred at the cluster was retrieved from the NASA/IPAC Infrared Science Archive[5]. The *daophot* package was used to detect stellar sources in the image and the respective cat-

[3] Dr. Andrea Stolte performed the data reduction and image combination of the L'-band data of Fields 2, 3 and 5. Further, the source detection with the *daophot* package for the Fields 2 and 3 was also carried out by Dr. Andrea Stolte.

[4] The GLIMPSE Data Release v2.0 document is available online at `http://www.astro.wisc.edu/glimpse/glimpse2_dataprod_v2.1.pdf`.

[5] `http://irsa.ipac.caltech.edu/data/SPITZER/GLIMPSE/`.

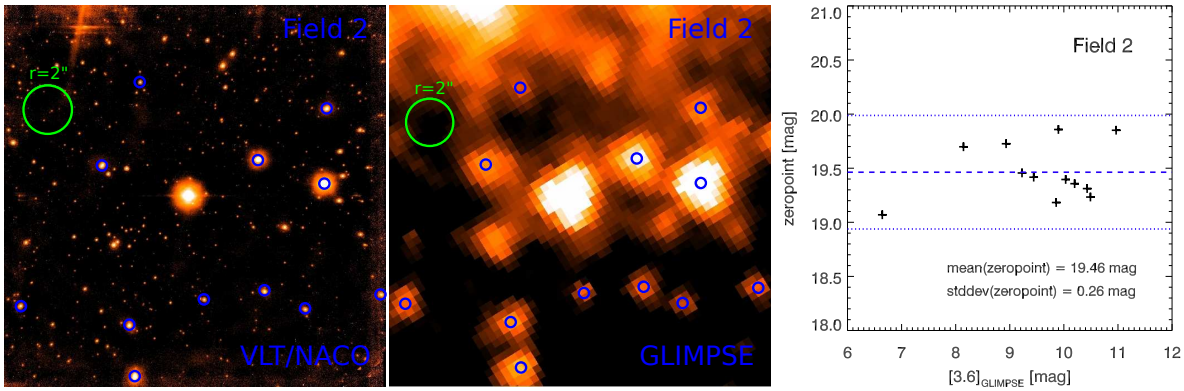

Figure 5.1: Calibration of the NACO L'-data of Field 2 with respect to the GLIMPSE source catalogue. The 12 used calibrators are indicated in the NACO L'-image of Field 2 (*left panel*) and the respective extract from the GLIMPSE data (IRAC band 1, $\lambda_c = 3.6\,\mu$m, *middle panel*). The *right panel* shows the zeropoint of each calibrator ($zp = m_{[3.6]} + 2.5 \log F_{\mathrm{NACO}}$) as a function of the magnitude of the calibrated GLIMPSE source catalogue ($m_{[3.6]}$). The PSF flux within $r = 2.0''$ (green circles) from the respective calibrator in the NACO data was summed up (F_{NACO}) and compared to the magnitude $m_{[3.6]}$ of the respective calibrator (see text). The dashed, blue line shows the mean zeropoint applied for the calibration of the L'-data of Field 2 and the blue, dotted lines are drawn at $\pm 2\,\sigma$ from the mean zeropoint.

alogue was calibrated with respect to 141 selected stars in the GLIMPSE catalogue yielding a standard deviation of the derived zeropoint of 0.12 mag. This calibrated source catalogue was in turn used for the calibration of the NACO L'-band data of the Quintuplet cluster[6].

The NACO observations are naturally far better resolved than the GLIMPSE data for which the analytical *daophot* PSF has a FWHM of 2.0″. Hence several stars resolved in the NACO data contribute to each source in the calibrated GLIMPSE source catalogue. The most consistent calibration was achieved by comparing the summed up PSF flux within a radius of 2.0″ in the NACO L'-band observations with the flux of the respective source in the GLIMPSE data. The calibration of the L'-band data of Field 2 with respect to 12 calibrators from the GLIMPSE source catalogue yielded a standard error of the zeropoint of 0.08 mag. The zeropoints of the L'-data of the Quintuplet Fields 1, 3, and 5 were then determined using common stars in the respective overlap areas with the calibrated source catalogue of Field 2. The zeropoint error for these fields includes the zeropoint error of the calibration of Field 2 vs. the GLIMPSE source catalogue and the uncertainty of the subsequent calibration of Fields 1, 3, and 5 vs. Field 2, but due to the comparatively large number of common stars this second contribution to the error is negligible.

It should be noted that the central wavelength as well as the width of the NACO L'-filter ($\lambda_c = 3.80\,\mu$m, $\Delta\lambda = 0.62\,\mu$m) differ from the values of the IRAC band 1: $\lambda_c = 3.6\,\mu$m, $\Delta\lambda = 0.7\,\mu$m[7]. The existence of a colour term between the two filters is hence likely, but difficult to assess reliably because of the large difference in the spatial resolution of the NACO and the GLIMPSE data and the very small number of usable stars. As the aim of this study is to identify near-infrared excess sources as candidates for circumstellar discs to be later confirmed by spectroscopic means, the additional uncertainty of the L'-magnitudes introduced by the potential colour term between the NACO and

[6]The calibrated source catalogue for the Quintuplet cluster from the GLIMPSE catalogue as described in the text was created by Dr. Andrea Stolte.

[7]The width $\Delta\lambda$ was determined from the cut-on and cut-off wavelengths inferred from the transmission curve of the IRAC band 1 available online at `http://irsa.ipac.caltech.edu/data/SPITZER/docs/irac/calibrationfiles/spectralresponse/080924ch1trans_full.txt`.

the GLIMPSE data is of less importance. Furthermore, as the distribution of stars in the colour-colour-diagram (see next section) is well-fitted by the reddening path adopting the extinction law from Nishiyama et al. (2009), the colour terms can not be very pronounced.

5.2 Colour-colour diagrams

The L'-source catalogues of the Fields 1, 2, 3 and 5 were matched with the respective source catalogues containing all stars with measured proper motions detected in the J_s-, H-, and K_s-band. Again, only stars located within the areas used to derive the mass function were considered (see Fig. 4.11). Stars in Field 2 residing within the areas which were disregarded due to a supposed increased local extinction (see Sect. 4.3.1.3) were re-included as they are expected to follow the reddening path in the CCDs unless they are excess sources. In order to exclude spurious detections or stars with inaccurate photometry in L', an additional selection of sources was applied based on the magnitude errors estimated during the PSF fitting with *daophot*. Although these errors are not a reliable estimate of the photometric errors, they provide a relative scale of the goodness of the PSF fitting. Figure 5.2 shows the formal magnitude error as a function of L' for the Fields 1, 2, 3 and 5 and the applied selection. Sources with large photometric uncertainties at brighter magnitudes ($L' < 13.5$ mag) which are typically located within the halo of the brightest stars or are wrongly fitted by multiple components were removed as well as all detections with formal photometric uncertainties larger than 0.09 mag. The fixed error cut was set to the lower boundary of a horizontal cumulation of spurious detections (best seen in the left panels of Fig. 5.2), albeit most of these misdetections are removed by the matching of the L'-band catalogue with the J_sHK_s catalogue.

The $J_s - K_s$, $K_s - L'$ CCDs containing proper motion members (red) and non-members (black) of all four fields are shown in Fig. 5.3. As the photometric uncertainties of the J_s-band and K_s-band data are much smaller than for the WFC3 H-band data (see Sect. 4.1.2.3), the $J_s - K_s$ colour instead of the usual $J_s - H$ colour was adopted as the ordinate. The location of non-extincted MS stars in the CCD is very close to its origin. Stars affected by foreground extinction only scatter around the reddening path through the origin due to their photometric uncertainties. For the reddening path which is drawn as a blue solid line in Fig. 5.3 the extinction law by Nishiyama et al. (2009) is adopted.

Originally, the distributions of stars in the CCDs showed an offset relative to the reddening path. Due to the pronounced, rapidly varying thermal background in the L'-band which is difficult to completely remove by the sky subtraction and the comparatively low resolution of the GLIMPSE data used to calibrate Field 2, the photometric calibration of the L'-data is probably less accurate than for the J_s- and K_s-band data. Further, Fields 1, 3 and 5 were calibrated with respect to Field 2 using common stars in the overlap areas which are naturally located close to the edges of the respective fields. In contrast, the J_s-band data covers all four fields and the calibration of the K_s-band data of Fields 2, 3, and 5 were found to be consistent (see Sect. 4.1.1.2) which suggests that the offset in the CCDs of these fields should be uniform if they originated from the J_s- or K_s-band photometry. As the offsets have different sizes, it is assumed that they originate from the calibration of the L'-band data. The L'-band offsets were determined as the median horizontal distance of the distribution of stars from the reddening path excluding highly reddened and very blue stars. The applied offsets added to the magnitudes in L' were -0.27, 0.02, 0.01 and -0.04 mag for Fields 1, 2, 3, and 5, respectively. The large offset in L' required for Field 1 is not fully understood. In the $J_s - H$, $H - K_s$ CCD of Field 1 using the NACO H-band photometry, the distribution of cluster stars does not show any displacement from the line of reddening, so that an additional offset in the J_s- or K_s-band can be excluded. As Field 1 is the largest of all fields, areas close to the edges of this field are covered with less than a third of the

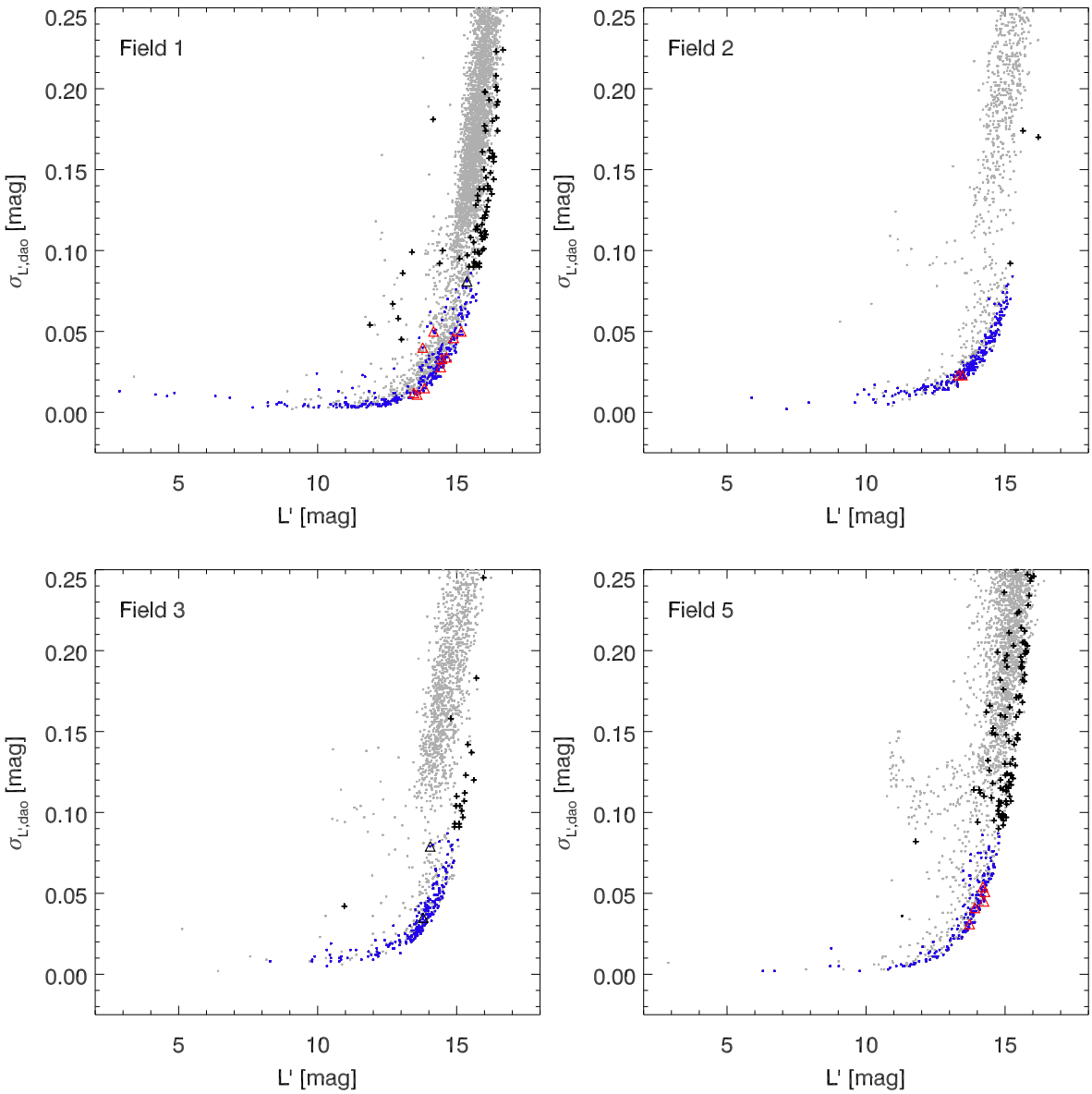

Figure 5.2: Formal photometric uncertainties of the NACO L'-band datasets as estimated during the PSF fitting with *daophot* plotted vs. the L'-band magnitude (light grey). Stars also detected in J_sHK_s and with measured proper motions are drawn as blue dots or black crosses. Blue dots indicate stars used for the CCDs (Fig. 5.3), while datapoints drawn as black crosses were rejected. Near-infrared excess candidates are drawn as triangles (red: proper motion members, black: proper motion non-member). The shown magnitudes have been corrected for the respective L'-offsets required to shift the distribution of non-excess sources onto the line of reddening in the CCDs (see text for details).

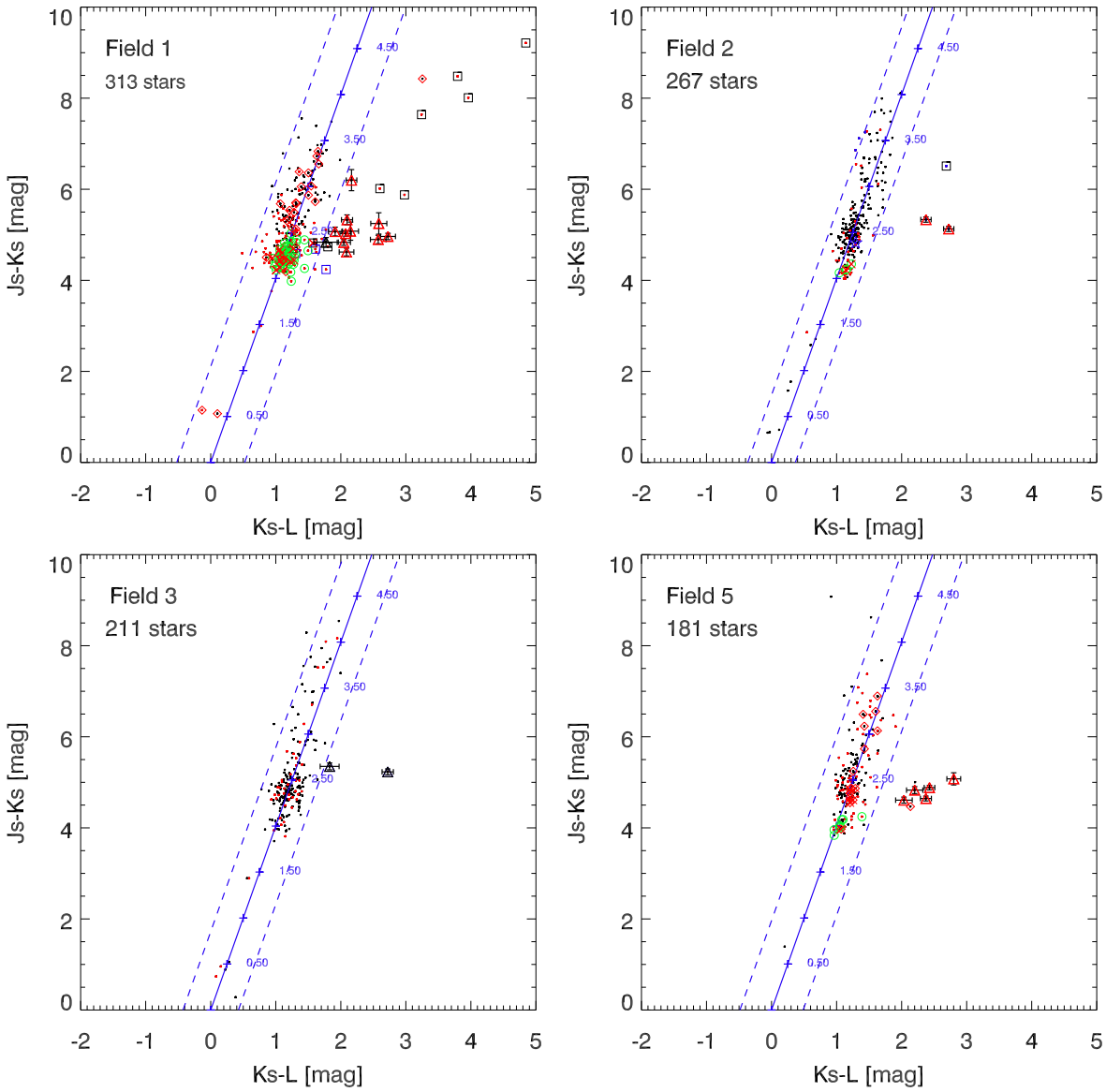

Figure 5.3: CCDs of proper motion members (red dots) and non-members (black dots) for all four Quintuplet fields. Stars with known spectral type are marked by the same symbols as in Fig. 4.24. The foreground extinction A_{K_s} is indicated along the line of reddening (solid line) for which the extinction law by Nishiyama et al. (2009) was adopted. The standard deviation σ of the distribution of stars around the line of reddening is determined excluding spectroscopically identified WR stars and a preliminary selection of excess candidates (see text for details). The dashed lines drawn at perpendicular distances of $\pm 3\,\sigma$ from the line of reddening enframe the region of stars without (significant) near-infrared excess in the CCD. Stars redward of this region are classified as excess candidates if they are fainter than $K_s = 14$ mag in order to exclude WR stars and RSGs (indicated by box and diamonds symbols, respectively). Excess candidates are indicated by red (proper motion member) or black triangles (proper motion non-member).

number of frames contributing to the central part of the combined image of Field 1. All calibrators are located near the lower edge of Field 1 and hence in an area with an increased background noise compared to the location of the stars appearing in the CMD (cf. Fig. 4.11). The zeropoint derived in the overlap area with Field 2 might therefore not be correct for the central part of the image, which might explain the large required L'-band offset of Field 1.

The identification of L'-excess candidates in the Quintuplet cluster follows the approach by Stolte et al. (2010). The standard deviation σ of the distribution of cluster and field stars without excess perpendicular to the reddening path was determined for all fields in an iterative way. First a preliminary value of the standard deviation was derived from all stars excluding only identified WR stars as these stars are intrinsically reddened (indicated as box symbols in Fig. 5.3). The final standard deviation σ was determined using only stars with a perpendicular distance from the line of reddening of less than two times the preliminary standard deviation, again excluding identified WR stars. Excess candidates are required to be outside and to the right of the $3\,\sigma$ envelope (blue dashed lines in Fig. 5.3) and to be fainter than $K_s = 14$ mag in order to exclude unidentified WR stars and RSGs which are not contained in the spectral catalogues of Liermann et al. (2009) or Figer et al. (1999b). Table 5.2 lists all detected excess candidates in the Quintuplet cluster and includes proper motion members and non-members. All proper motion non-members showing traces of near-infrared excess are definite field stars based on their location in the PMD. In order to check whether the photometry of an excess candidate might be influenced by close neighbours, halos of bright stars or background noise, the excess candidates were visually inspected in all bands. Affected stars are indicated by $f_{\rm phot} = -2$ or, if the source definitely possesses an excess in $K_s - L'$, by $f_{\rm phot} = -1$. One excess candidate (No. 14) in Field 3 was disregarded ($f_{\rm phot} = 0$), as it is located in a bright background stripe in the L'-data. Of the six excess candidates with $f_{\rm phot} = -1$ or -2, only for one of these stars the NACO K_s-band photometry may be affected significantly by a close neighbour, while for most of these stars the supposed impairment of their photometry arises from the less well resolved WFC3 data in the J_s- and H-band. Excess candidates with photometric errors intersecting with the $3\,\sigma$ envelope are flagged by $f_{\rm err} = -1$ in Table 5.2. Two excess candidates, No. 11 in Field 1 and No. 15 in Field 3, are proper motion non-members. While No. 15 appears to be a definite excess source in the field, excess candidate No. 11 is just outside the $3\,\sigma$ envelope and its large error in $K_s - L'$ makes it consistent with being a non-excess source. In total 15 reliable and 2 less reliable ($f_{\rm err} = -1$ or $f_{\rm phot} = -2$) near-infrared excess sources among the proper motion members are detected in the used areas of the four Quintuplet fields.

Assuming that the J_s-band magnitudes are least affected by the emission of the potential circumstellar discs, the mass of each excess source was inferred by comparing its J_s-band brightness after correcting for the assumed distance to the cluster (8 kpc) and the mean extinction of MS cluster stars in the respective field with the combined 4 Myr Padova isochrone. Depending on its size, the J_s-band magnitude of an excess source may correspond to a stellar mass along the MS and, due to the local maximum of the PMS, to two masses on the PMS. In Table 5.2, the masses along the MS and/or the rising branch of the PMS are hence listed individually and are thus upper and lower bounds to the mass of the respective star. The uncertainties of the stated stellar masses are inferred from the photometric uncertainties of the respective star in the J_s-band. For two stars only the faint limit of the measured magnitude has an intersection with the rising PMS branch so that only this mass is stated as lower mass limit. The masses covered by the excess sources which are also proper motion members range from ~ 2 to $10\,M_\odot$. Hence, the excess sources in the Quintuplet cluster are likely mid A- to early B-type stars.

Table 5.2: Catalogue of excess candidates in the Quintuplet cluster.

No.	Field	ΔR.A.[a] (″)	ΔDecl.[a] (″)	J_s (mag)	σ_{J_s} (mag)	K_s (mag)	σ_{K_s} (mag)	L'[b] (mag)	$\sigma_{L'}$ (mag)	$f_{\rm pm}$	$f_{\rm err}$[c]	$f_{\rm phot}$[d]	$m_{\rm MS}$ ($M_\odot$)	$m_{\rm PMS}$ ($M_\odot$)	Comment
1	1	10.18	11.70	20.07	0.04	15.24	0.05	13.19	0.09	y	1	1	$9.90^{+0.20}_{-0.20}$	–	
2	1	1.11	-6.12	20.98	0.06	16.09	0.07	13.51	0.10	y	1	-1	$6.70^{+0.15}_{-0.20}$	–	
3	1	-0.40	10.51	20.68	0.05	15.65	0.03	13.58	0.08	y	1	1	$7.65^{+0.20}_{-0.15}$	–	
4	1	5.97	17.93	20.91	0.08	16.29	0.04	14.20	0.11	y	1	-2	$6.90^{+0.25}_{-0.25}$	–	
5	1	-8.37	9.05	21.59	0.06	16.62	0.03	13.90	0.11	y	1	-1	$5.00^{+0.20}_{-0.15}$	–	
6	1	1.57	13.19	21.99	0.23	16.74	0.03	14.16	0.12	y	1	-1	$4.10^{+0.50}_{-0.45}$	2.20	
7	1	-6.76	13.81	21.59	0.20	16.51	0.04	14.37	0.12	y	1	1	$5.00^{+0.50}_{-0.45}$	–	
8	1	1.13	12.28	21.88	0.09	16.81	0.03	14.89	0.10	y	1	1	$4.35^{+0.20}_{-0.20}$	–	
9	1	-2.49	-2.73	22.05	0.10	16.72	0.03	14.62	0.08	y	1	1	$3.97^{+0.23}_{-0.19}$	2.27	
10	1	6.08	7.15	21.67	0.23	15.47	0.03	13.31	0.08	y	-1	-2	$4.80^{+0.60}_{-0.50}$	–	
11	1	-3.96	-3.45	21.71	0.07	16.87	0.07	15.10	0.18	n	-1	1	$4.70^{+0.20}_{-0.15}$	–	field excess source?
12	2	-1.56	-20.30	21.18	0.05	15.84	0.02	13.47	0.08	y	1	-1	$4.35^{+0.15}_{-0.10}$	–	
13	2	4.09	-12.77	21.17	0.05	16.04	0.02	13.32	0.08	y	1	1	$4.35^{+0.15}_{-0.10}$	–	
14	3	22.86	-26.35	21.23	0.07	15.88	0.03	14.05	0.14	n	-1	0	–	–	disregarded
15	3	22.05	-18.88	21.75	0.05	16.52	0.03	13.79	0.08	n	1	1	–	–	field excess source
16	5	32.17	4.95	20.94	0.07	16.11	0.02	13.91	0.12	y	1	1	$4.55^{+0.15}_{-0.20}$	–	
17	5	35.45	-0.38	21.04	0.05	16.15	0.02	13.72	0.08	y	1	1	$4.30^{+0.10}_{-0.10}$	–	
18	5	20.69	-12.71	20.85	0.06	16.24	0.02	14.20	0.13	y	1	1	$4.75^{+0.15}_{-0.15}$	–	
19	5	24.05	4.56	21.29	0.05	16.65	0.02	14.28	0.08	y	1	1	$3.79^{+0.08}_{-0.09}$	$2.27^{+0.00}_{-0.05}$	
20	5	23.26	-2.70	22.12	0.13	17.04	0.02	14.24	0.10	y	1	1	–	$2.00^{+0.03}_{-0.03}$	

Notes. [(a)] Positional offset in right ascension and declination relative to the AO guide star Q2 (R.A. = 17:46:14.690, Dec. = -28:49:40.71 [J2000]). [(b)] L'-magnitudes are corrected for the L'-band zeropoint offsets found in the CCDs. [(c)] Excess candidates with error bars reaching into the $3\,\sigma$-envelope in the CCD (see Fig. 5.3) are indicated by $f_{\rm err} = -1$. [(d)] Flag indicating whether the photometry of the respective excess candidate might be affected by close neighbours, PSF halos or background noise. Excess candidates whose photometry is most likely not biased by these effects are indicate by $f_{\rm phot} = 1$. Sources where such an influence can not be excluded are flagged by a value of -2 or, if they feature a definite L'-band-excess, by $f_{\rm phot} = -1$. One source is disregarded as excess candidate ($f_{\rm phot} = 0$) as its photometry in J_sL' is considered unreliable.

5.3 Completeness

In order to estimate the L'-band completeness of the excess candidates in the Quintuplet cluster, artificial star experiments have been performed for all four L'-datasets. Artificial stars were inserted at the same position as for the completeness determination of the K_s-band data and with artificial colours of $K_s - L' = 1.2$ mag which are appropriate for the cluster MS. This ensures that the spatial sampling of the recovery fraction for the L'-data is equally well as in the K_s-band (cf. Sects. 3.3 and 4.1.3) Artificial stars in the magnitude range $8.8 < L' < 19.3$ mag (Field 1) or $8.8 < L' < 20.8$ mag (Fields 2, 3, 5) were inserted using the IRAF *addstar* routine. In total 50400 artificial stars were inserted into the L'-images of Fields 2 and 3, where each generated star field contained 100 artificial stars. For the largest of the four Quintuplet fields, Field 1, the total number of artificial stars was 77300, while for Field 5 which was spatially offset in L' relative to the K_s-band data of this field (see Sect. 5.1.1) the total number of artificial stars was 37000. The source detection was performed with the *daophot* package applying the same parameter settings and the same PSF as for the original source extraction of the respective field.

For consistency with the performed data selection based on the formal photometric errors provided by *daophot* (see Sect. 5.2), all recovered artificial stars with formal photometric errors larger than 0.09 mag were treated as not recovered. As for the completeness determination in the other bands (see Sect. 4.1.3.1), an additional selection based on the difference between the inserted and recovered magnitudes of the artificial stars was applied (see Fig. 5.4). The selection criterion to reject stars with recovered magnitudes strongly deviating from their inserted magnitudes was again chosen to be magnitude dependent, such that the maximum allowed absolute magnitude difference was 0.25 mag at the bright end and 0.5 mag at the faint end. A fit to the standard deviation of the magnitude difference times 2.5 was used to interpolate between this lower and upper boundary. Due to the previous selection based on the formal photometric errors the impact of this second selection is rather small with a maximum decrease of the recovery fraction of 3% for Fields 2, 3 and 5. Due to the increased scatter of the magnitude differences for Field 1, which is probably caused by the larger number of cluster stars in this field, the maximum decrease of the recovery fraction due the imposed selection is 8% ($14.75 < L' < 15.25$ mag), but less than 4% for brighter magnitudes. The average completeness within magnitude bins of 0.25 mag is shown in Fig. 5.5. The magnitude dependence of the completeness is very similar for Fields 1, 2, and 3 within the magnitude range occupied by the excess candidates while only Field 5 seems to be slightly less complete.

The set-up of the artificial star experiments allowed to determine the combined completeness in K_sL' for stars on the cluster MS. As only excess candidates which are proper motion members are used to determine the fraction of excess candidates in the cluster, the artificial star catalogues for the four L'-band datasets were matched with the respective combined artificial K_s-band catalogues (cf. Sect. 4.1.3.1). Only those artificial stars recovered in the artificial star experiments for the L'- and both epochs of K_s-band data were considered as re-detected and marked accordingly in the combined K_sL' artificial star catalogue. It turned out that the combined completeness in K_sL' is limited by the depth of the L'-data and the applied error selection. Within the magnitude range of the excess sources ($13.10 < L' < 14.99$ mag) the maximum difference found in all fields between the mean completeness in L' and the mean combined completeness in K_sL' is only 3%. As the colour $K_s - L' = 1.2$ mag of the artificial stars inserted into the L'-band images of the four Quintuplet fields corresponds to the colour of the MS cluster population, it is bluer than the colour of the near-infrared excess candidates. By applying the combined completeness in K_sL' to the excess candidates their completeness is hence slightly underestimated, but as the combined completeness is almost completely dominated by the

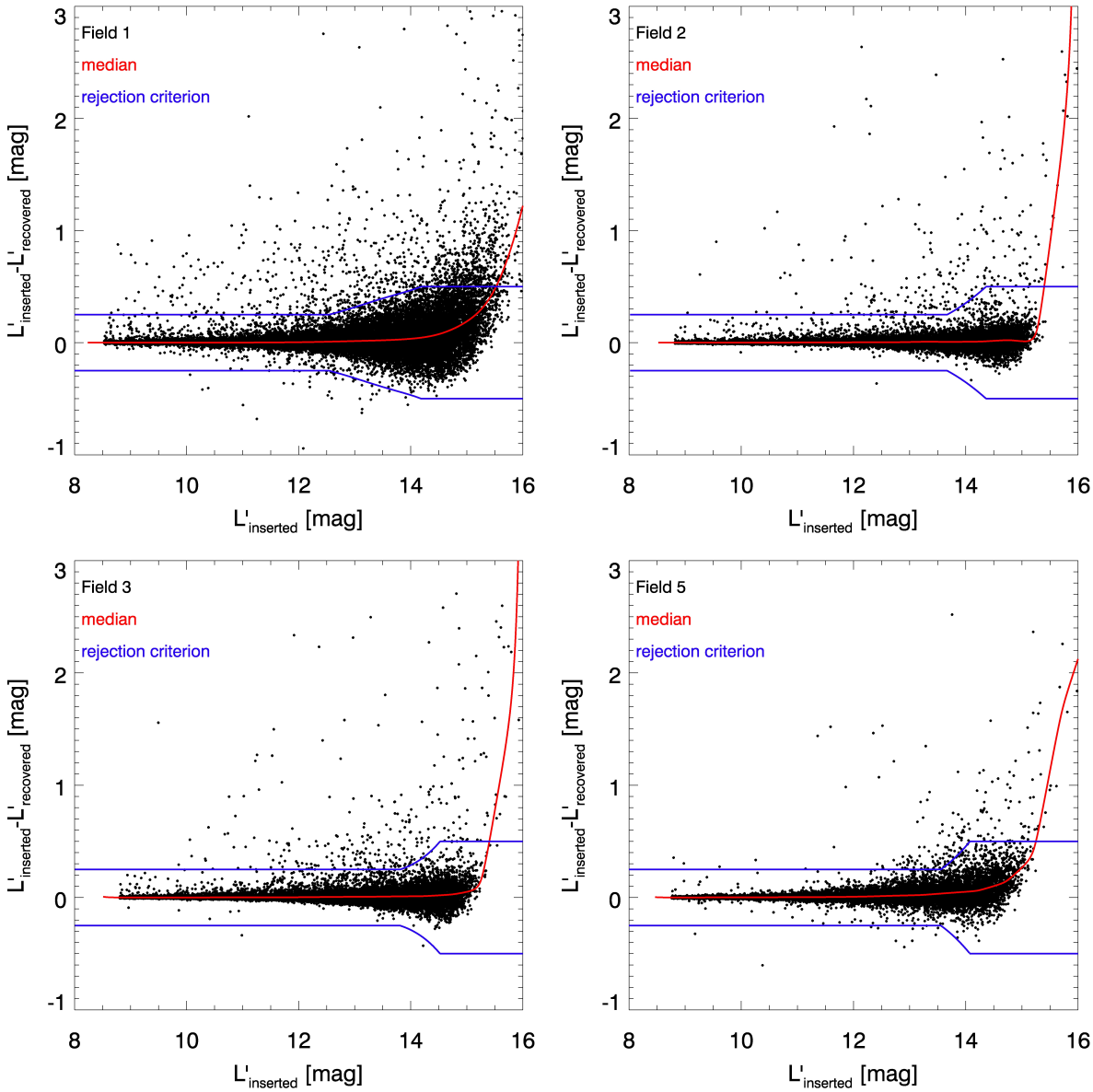

Figure 5.4: Magnitude difference of the inserted and recovered artificial stars with formal photometric errors < 0.09 mag plotted vs. the L'-band magnitude for all observed fields. The L'-offsets required to shift the distribution of non-excess sources onto the line of reddening in the CCDs was applied. A spline interpolation of the median of the magnitude difference (red line) and the criterion to reject recovered stars based on the magnitude difference (blue line) are shown as well.

completeness in L' this bias is negligible[8].

[8]The artificial star experiments had been performed before L'-offsets were found in the CCDs (see Sect. 5.2). While due to the small zeropoint offset in L' the colours of the inserted artificial stars for Fields 2, 3 and 5 still resemble the colour of a MS star, the colour of an artificial star inserted into the combined image of Field 1 is actually by 0.27 mag redder than the MS and corresponds to a weak excess source. Hence, accidentally the combined K_sL' completeness for Field 1 resembles the completeness of an excess source more closely than for the other fields, but the actual impact of this is negligible as the completeness in L' and the combined K_sL'-completeness are almost identical.

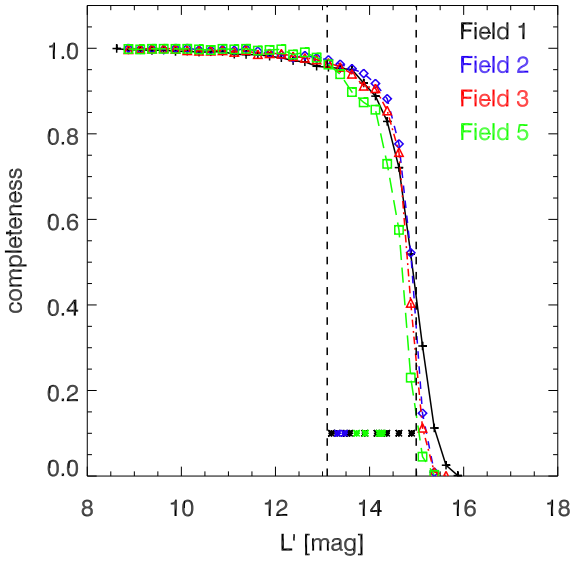

Figure 5.5: Average completeness of artificial stars vs. the respective L'-band magnitude: Field 1 (black crosses), Field 2 (blue diamonds), Field 3 (red triangles), Field 5 (green boxes). The dashed vertical lines enframe the magnitude range of excess candidates (see Sect. 5.4), while the star symbols drawn in the colour of the respective field indicate the magnitudes of the individual excess candidate.

5.4 Excess source fraction

All 17 stellar sources providing evidence in the CCD for near-infrared excess among the Quintuplet proper motion members are regarded as excess candidates. Fifteen excess candidates are considered and referred to as excess sources in the following as their errors do not reach into the $3\,\sigma$-envelope ($f_{\rm err} = -1$ in Table 5.2) and their photometry is either considered reliable in all bands or they show an unambiguous excess in $K_s - L'$ ($f_{\rm phot} = 1$ or -1).

The 90% L'-band completeness limit of Field 1, the most complete L'-dataset, at $L' = 14.0$ mag corresponds to a stellar mass on the cluster MS of about 11 $M_\odot$ which is above the upper end of the masses estimated for the excess candidates. At the faint limit of the excess candidates in the L'-band the reference sample of cluster stars is hence highly incomplete and determining the excess fraction using the sample of cluster stars detected in all bands ($J_s HK_s L'$) would overestimate the percentage of excess candidates (cf. Sect. 3.3 in Stolte et al. 2010). Instead, for a star to be included in the reference sample it is only required that it is detected in $J_s HK_s$. The reference samples for Fields 1, 2, 3, and 5 consist of MS stars and evolved stars from the respective cluster member samples established in Chapters 3 and 4. A few excess candidates are contained in the cluster samples as their colours in $H-K_s$ (Field 1) or J_s-K_s (Fields 2, 3, 5) are within the applied colour selections for cluster members. These excess candidates are excluded from the respective reference sample. Although the CCD of Field 2 contains also stars within the area with supposed increased local extinction (see Sect. 5.2), a reliable member sample only exists outside of this area (cf. Sect. 4.3.1.3 and Fig. 4.11). Fortunately, the two excess sources in this field are located outside or just inside the excluded area, such that the member sample of Field 2 as established in Sect. 4.3.1 can be applied. Due to the magnitude limit of the proper motion member samples of the outer fields at $K_s = 17.5$ mag, the reference sample of cluster stars for Fields 2, 3, and 5 is incomplete for $J_s \gtrsim 21.5$ mag. In contrast, for Field 1 due to the fainter limit of the proper motion membership sample at $K_s = 19.0$ mag, the reference sample covers

Table 5.3: Average completeness values of the sample of cluster stars and of the excess candidates.

	Cluster sample	Excess candidates		
Field	J_sHK_s compl.[a]	J_sH compl.[b]	K_sL' compl.[c]	J_sHK_sL' compl.[d]
1	0.88	0.84	0.92	0.78
2	0.92	0.90	0.93	0.83
3	0.87	0.90	0.90	0.81
5	0.94	0.90	0.87	0.78
1 (all)	0.84	0.82	0.84	0.69

Notes. [(a)] The stated completeness value of the reference sample of cluster stars is the average of the individual completeness values of stars with $J_s < 21.5$ mag (Field 1, 2, 3, 5) or $J_s < 22.25$ mag (Field 1 (all)). [(b)] Average completeness as derived from the combined artificial star catalogue in J_sH in the appropriate magnitude range of excess candidates (cf. footnote 9). The applied magnitude ranges are $20.02 < J_s < 21.50$ mag for Fields 1, 2, 3, 5 and $20.02 < J_s < 22.25$ mag for Field 1 (all). [(c)] Average completeness as derived from the combined artificial star catalogue in K_sL' in the appropriate magnitude range of excess candidates (cf. footnote 9). The applied magnitude ranges are $13.10 < L' < 14.36$ mag for Fields 1, 2, 3, 5 and $13.10 < L' < 14.99$ mag for Field 1 (all). [(c)] Average completeness of the excess candidates in J_sHK_sL' determined as the product of the average completeness in J_sH and the average completeness in K_sL'.

the full magnitude range of the excess candidates down to $J_s = 22.25$ mag, which corresponds to the faintest J_s-band magnitude (including the photometric error σ_{J_s}) and hence the minimum mass of all excess candidates. To determine the overall excess fraction in the cluster the strict J_s-band limit at 21.5 mag had to be applied to the cluster sample and the sample of excess candidates for all fields including Field 1. This limit excludes 5 excess sources and 1 excess candidate from the 10 excess candidates in Field 1 and another excess source in Field 5. It should be stressed here, that the lack of excess candidates in the outer fields with $21.5 < J_s < 22.25$ mag is not introduced by the K_s-band limit of the proper motion member samples in the outer fields, as those excess sources would have been detected albeit without any membership information based on their proper motion. The fraction of excess candidates ($f_{\rm ec}$) and of excess sources ($f_{\rm es}$) is determined relative to the sum of the number of stars in the cluster reference sample and the number of excess candidates, i.e. $f_{\rm ec} = n_{\rm ec}/(n_{\rm clus} + n_{\rm ec})$ and $f_{\rm es} = n_{\rm es}/(n_{\rm clus} + n_{\rm ec})$.

In order to correct for the incompleteness of the sample of cluster stars within each field, their number was divided by the average value of the individual completeness values in J_sHK_s of cluster stars brighter than $J_s = 21.5$ mag (all fields) or $J_s = 22.25$ mag (additionally for Field 1). Similarly, the number of excess candidates/sources in each field was divided by the product of the mean completeness in J_sH and the mean completeness in K_sL' within the appropriate magnitude ranges of excess candidates in J_s and L'[9]. The applied completeness values for the sample of MS stars and excess candidates[10] are summarised in Table 5.3.

The completeness corrected overall fraction of excess candidates and excess sources within the selected area of the Quintuplet cluster are $f_{\rm ec} = 2.8 \pm 0.9\%$ and $f_{\rm es} = 2.5 \pm 0.8\%$, respectively. The values of $f_{\rm ec}$ and $f_{\rm es}$ for the individual fields are listed in Table 5.4. The fractions of excess sources in

[9] Except for the lower J_s-band limit which was set to 21.5 mag (see above), the applied magnitude ranges are defined by the minimum and maximum magnitudes of the excess candidates in J_s and L' including the respective photometric uncertainties σ_{J_s} and $\sigma_{L'}$ (Table 5.2). The magnitude ranges used for all fields were hence $20.02 < J_s < 21.50$ mag and $13.10 < L' < 14.36$ mag, respectively. To include all excess sources in Field 1 the completeness was also determined in the magnitude ranges of $20.02 < J_s < 22.25$ mag and $13.10 < L' < 14.99$ mag, where the faint magnitude limit in J_s was also set by the faintest excess candidate in that band again accounting for σ_{J_s}.

[10] Excess candidates and sources occupy the same magnitude range in J_s. Hence the average completeness values to correct the number of the excess candidates and excess sources are the same.

Table 5.4: Completeness corrected fraction of excess candidates (f_{ec}) and excess sources (f_{es}) in the Quintuplet cluster.

Field[a]	n_{clus}[b]	n_{ec}[b]	n_{es}[b]	f_{ec} (%)	f_{es} (%)
All	397	10	9	2.8 ± 0.9	2.5 ± 0.8
1	224	4	3	2.0 ± 1.0	1.5 ± 0.9
2	52	2	2	4.1 ± 2.8	4.1 ± 2.8
3	49	0	0	0.0	0.0
5	72	4	4	6.3 ± 3.0	6.3 ± 3.0
1 (all)	298	10	8	3.9 ± 1.2	3.2 ± 1.1

Notes. [(a)] The stated values are determined considering stars in the cluster sample and excess candidates/sources with $J_s < 21.5$ mag (Fields 1, 2, 3, 5) or $J_s < 22.25$ mag (Field 1 (all)). The limiting magnitude at $J_s = 21.5$ mag is set by the magnitude limit of the proper motion cluster membership sample at $K_s = 17.5$ mag for Fields 2, 3, and 5, while for Field 1 (all) the magnitude limit at $J_s = 22.25$ mag is defined by the minimum brightness in J_s of all excess candidates. [(b)] The stated number of stars in the cluster sample n_{clus} and the number of excess candidates/sources (n_{ec} and n_{es}) are not corrected for the incompleteness in JHK_s or JHK_sL', respectively.

Fields 2 and 5 appear to be larger than in the central parts of the cluster, although the excess source fractions for Fields 1 and 2 are consistent within the large error ranges. In contrast to this, excess sources are completely lacking in Field 3, but due to the low number statistics of excess sources in the outer fields it is not possible to decide whether this lack is of significance or not. Further it has to be considered that 7 of 17 excess candidates had to be excluded from the determination of the excess fraction, due to the incompleteness of the cluster reference sample for $J_s > 21.5$ mag. As for Field 1 the proper motion membership was established even below the faint J_s-band limit of the excess sources, the excess fraction of all excess sources and candidates in this field could be determined and was found with $f_{ec} = 3.9 \pm 1.2\%$ to be about twice as large as for the brighter J_s-band limit at 21.5 mag required for the outer fields ($f_{ec} = 2.0 \pm 1.0\%$, see Table 5.4). As with exception of Field 5, the outer fields do not contain further excess sources at fainter J_s-band magnitudes than 21.5 mag, shifting the faint limit of the cluster reference sample down to $J_s = 22.25$ mag for the outer fields would hence decrease their respective values of f_{ec} and f_{es}. The trend for larger excess fractions in the Fields 2 and 5 is therefore less pronounced than could be supposed from the listed values in Table 5.3. A radial increase of the excess fraction would be expected if the near-infrared excess would originate from circumstellar discs due to the increased disc destruction in the vicinity of massive O and B stars. Unfortunately, at this point it is not possible to draw a definite conclusion whether the distribution of excess sources in the Quintuplet cluster shows such a trend or not. In the following section the disc fraction in the Quintuplet cluster is hence discussed referring to the overall fraction of excess candidates and sources in the cluster (first row in Table 5.4).

5.5 Discussion

5.5.1 Comparison with other young stellar populations

Under the assumption that the L-band excess of the excess sources in the Quintuplet cluster is indicative of circumstellar discs (but see Sect. 5.5.2), the value of f_{es} can be compared with the disc frequency found in other young clusters. In their Fig. 13, Stolte et al. (2010) have compiled from the

literature the fraction of L-band excess sources for clusters of different ages (see Fig 5.6). As the disc fraction is a function of the stellar mass (Kennedy & Kenyon 2009), the value of $f_{\rm es}$ of the Quintuplet cluster which was determined for stars with $m > 2\,{\rm M}_{\odot}$ has to be compared to the disc fraction around intermediate and high mass stars of spectral types OBA (black circles in Fig 5.6). The fraction of excess sources in the Quintuplet cluster of $2.5 \pm 0.8\%$ at an age of 4 ± 1 Myr is somewhat smaller than the disc frequency in the Arches cluster ($6 \pm 2\%$ at 2.5 Myr) and similar to the one of σ Ori of $4 \pm 4\%$ at 3 Myr (Stolte et al. 2010; Hernández et al. 2007). Compared with the fraction of Herbig AeBe stars in the sample of nearby OB associations from Hernández et al. (2005), the value of $f_{\rm es} = 2.5 \pm 0.8\%$ in the Quintuplet cluster seems to be consistent with the Herbig AeBe fraction in two of three OB associations in the relevant age range, Ori OB1bc ($3.8 \pm 2.2\%$, age: 3.5 ± 3 Myr) and Upper Scorpius ($3.3 \pm 1.3\%$, age: 5 ± 1 Myr), while in Per OB2 (age: 4-8 Myr) no Herbig AeBe stars were found. In summary, although the survival of primordial circumstellar discs around intermediate mass stars up to the age of the Quintuplet cluster is rather unexpected, this possibility can not be disregarded based on the comparison of the excess source fraction with other young stellar populations.

A few more comparisons between the excess sources in the Arches and the Quintuplet cluster should be made here as their fraction were derived in a consistent way and they both constitute young massive clusters in the GC region. The mass range of the excess sources in the Quintuplet cluster ($2 < m < 10\,{\rm M}_{\odot}$) is somewhat smaller than in the younger Arches cluster ($2 < m < 20\,{\rm M}_{\odot}$) and is hence at least qualitatively consistent with the expectation that higher mass stars disperse their discs more rapidly. Excess sources in the Quintuplet cluster are on average by 0.40 ± 0.07 mag redder in $H-K_s$ than the reference sample of cluster stars. This value is slightly smaller than the mean excess in $H-K'$ of 0.52 ± 0.06 mag in the Arches cluster[11], although the values are consistent within the errors. Stolte et al. (2010) compared the positions of the Arches excess sources and of disc-bearing Herbig Be stars (ages <1 Myr) from Hillenbrand et al. (1992) in the H, $H-K'$ CMD and concluded that the decreased excess in $H-K'$ of the discs in Arches compared to the Herbig Be stars might indicate a more evolved state, i.e. an increased depletion of their hot inner rim. The same interpretation might be valid for the Quintuplet excess sources, too. Also, the mean excess of the excess sources in the Quintuplet cluster in $K_s - L'$ of 1.20 ± 0.07 mag is somewhat smaller than the respective value for the Arches cluster (1.31 mag). Supposing the excess sources in the Quintuplet cluster (age: 4 ± 1 Myr) are discs, these findings indicate that the depletion of gas and dust in their inner parts has only moderately proceeded compared to the Arches cluster (age: 2.5 Myr) which is a rather surprising finding given the age difference between the two clusters in the range of about 0.5 to 2.5 Myr.

5.5.2 Alternative sources of the L'-excess

Although L-band excess from stars within young clusters is generally interpreted as originating from hot dust grains in the innermost parts of protoplanetary discs, the straightforward interpretation of the excess sources in the Quintuplet cluster as stars with surviving primordial discs is problematic. The masses of the Quintuplet excess sources as inferred from their J_s-band magnitudes in the range from 2 to $10\,{\rm M}_{\odot}$ (see Table 5.2) correspond to spectral types A5 to B2 on the zero age main sequence (ZAMS)[12]. At ages of 5 Myr, primordial discs around stars more massive than about $1.2\,{\rm M}_{\odot}$ are apparently missing in young open clusters and OB associations, although excess emission at mid-infrared wavelengths consistent with originating from debris discs can be detected (Williams & Cieza 2011,

[11] The mean excess of the Arches cluster in $H-K'$ was derived from the Arches source catalogue available online at `http://vizier.cfa.harvard.edu/viz-bin/VizieR?-source=J/ApJ/718/810` using the designated excess sources and establishing the MS sample as described in Sect. 3.3.1 in Stolte et al. (2010).

[12] At an age of 4 Myr and solar metallicity only stars with $m \gtrsim 3\,{\rm M}_{\odot}$ have already reached the ZAMS.

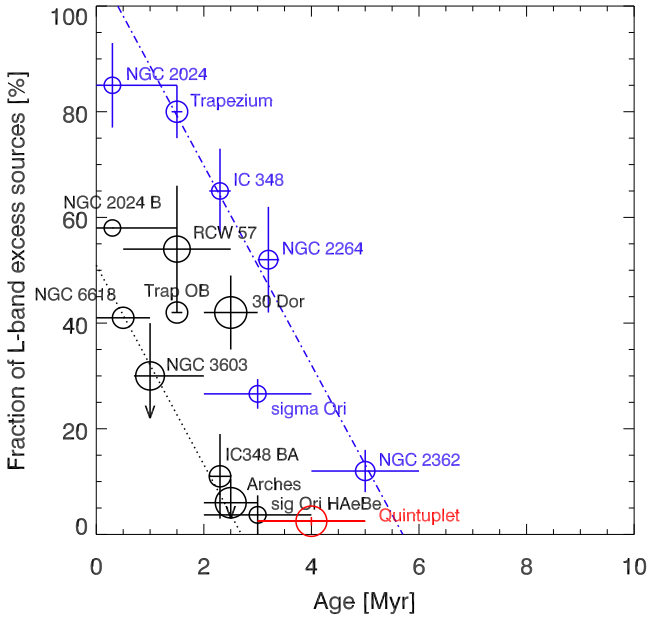

Figure 5.6: Disc fraction vs. cluster age adopted from Fig. 13 in Stolte et al. (2010). The symbols are scaled to the logarithm of the cluster mass. Black circles show the disc fraction around high mass stars (spectral types OBA), while the disc fractions drawn in blue are dominated by low mass stars (see caption in Fig. 13 in Stolte et al. 2010 for further details). The overall fraction of the excess sources in the Quintuplet cluster (2.5 ± 0.8%) is drawn in red, assuming a total mass of $2 \times 10^4\,M_\odot$ (Sect. 4.4.2) and an age of 4 ± 1 Myr (Figer et al. 1999b).

and references therein). Due to the comparatively high density and the large number of luminous OB stars, the dispersal of primordial circumstellar discs around intermediate mass stars in the 4 Myr old Quintuplet cluster is expected to proceed more rapidly than in the more moderate environments provided by young open clusters. In fact, even for the younger Arches cluster (age: 2.5 Myr) the finding of surviving circumstellar discs around B-type stars was surprising due to the expected fast disc dissipation for Herbig Be stars within 2 Myr ($m > 3\,M_\odot$, Alonso-Albi et al. 2009) and the intense external UV field produced by the numerous OB stars.

The presence of near-infrared excess from B-type stars is not an unambiguous tracer for primordial circumstellar discs and may be of different origin, though. For example, stars showing the B[e] phenomenon which constitute a variety of very different objects are distinguished besides the presence of strong hydrogen and forbidden emission lines of [Fe II] and [O I] also by a strong near-infrared excess (Lamers et al. 1998). According to Lamers et al. (1998), B[e] stars may be divided into five classes: B[e] supergiants, PMS B[e] stars, compact planetary nebulae B[e] type stars (cPNB[e]), symbiotic B[e]-type stars, and unclassified B[e] stars. Unclassified B[e] stars do not clearly fit into any of the other classifications and an assessment whether they might be an explanation for the excess candidates in the Quintuplet cluster is not possible. As the excess candidates in the Quintuplet cluster are all proper motion members, objects of type cPNB[e] and symbiotic B[e] stars which are interacting binaries including a cool giant can be disregarded as they are much older than the Quintuplet cluster. All excess candidates are with $K_s > 15$ mag by at least 4 to 5 mag fainter considering the distance and the mean extinction of the Quintuplet cluster than expected for a B[e] supergiants (see Fig. 1 in Bik et al. 2006), such that these kind of sources can be excluded, as well. The PMS B[e] stars are thought to be related to Herbig AeBe stars where the near-infrared excess is expected to originate either from a circumstellar disc and/or a dusty envelope (Lamers et al. 1998), but for these stars a similarly rapid

disruption of the discs as for 'normal' Herbig AeBe stars would be expected. Therefore, stars showing the B[e] phenomenon offer no alternative explanation in place of the survival of circumstellar discs for the excess sources in the Quintuplet cluster.

Also classical Be stars show near-infrared excess from free-free or free-bound emission originating from ionised circumstellar gas which is thought to be distributed in a thin disc around the star (Porter & Rivinius 2003). Based on a sample of 144 Be stars the excess in $K-L$ was determined by Dougherty et al. (1994) to be in the colour range of $0.0 < K - L < 0.6$ mag. As the only exception 51 Oph has a particularly high excess in $K - L$ of 1.13 mag (see their Table 1[13]) which is dominated by emission from hot dust rather than free-free emission (Waters et al. 1988). This and the finding of CO bandhead emission challenges the identification of 51 Oph as a classical Be star (van den Ancker et al. 2001; Thi et al. 2005; Tatulli et al. 2008). The typical excess of classical Be stars is significantly smaller than the mean excess of the excess sources in the Quintuplet cluster which are on average by 1.20 ± 0.07 mag redder in $K_s - L'$ than the MS reference sample of cluster stars. This large near-infrared excess of the Quintuplet excess sources makes it rather unlikely that they are actually classical Be stars.

While primordial circumstellar discs are thought to be destroyed within 2 to 7 Myr depending on the mass of the host star and the environment, mid-infrared surveys indicate that optically-thin debris discs around intermediate mass stars seem to be present already at ages $\gtrsim 3$ Myr (Hernández et al. 2009). By comparing the disc fraction including primordial, transition and debris discs of five star-forming regions in the age range from ~ 3 to 10 Myr, the authors find that for ages > 5 Myr the disc fraction of intermediate mass stars (spectral types B8 to F0) is larger than the fraction of low mass stars (K0.5 to M0.5) and increases with time from ~ 20 to 50% which they ascribe to the formation of debris discs. In general, debris disc are differing from primordial discs by a lack of near-infrared excess, while showing excess emission at mid- and far-infrared wavelengths from cold, second generation dust produced by collisions between planetesimals. Although a near-infrared excess from three debris discs around intermediate stars in NGC 1960 (age: ~ 16 Myr) was reported by Smith & Jeffries (2012), the excess in $K_s - L$ between 0.3 and 0.5 mag is small compared to the pronounced excess of the Quintuplet excess sources. Hence, assuming that the Quintuplet excess sources host circumstellar discs, they constitute rather peculiar objects whether they are considered to be primordial or evolved discs. On the assumption that the excess sources are coeval with the rest of the cluster population and were not formed in a second or prolonged star formation event, no primordial discs are expected to have survived around intermediate mass stars up to the age of the Quintuplet cluster. But then, their excess in $K_s - L'$ is pronounced and significantly larger than for the debris discs with near-infrared excess in NGC 1960.

In order to constrain and clarify the nature of the Quintuplet excess sources further observations are required. Especially K-band spectra of the excess sources are suited to either support or disprove the possibility that they are primordial discs based on the presence or absence of CO bandhead emission. The emission of the first overtone bands of CO requires high densities ($>10^{10}$ cm^{-3}, Carr 1989) and temperatures, conditions which are fulfilled in the inner regions (0.1 – 5AU) of circumstellar discs around young stars (Bik & Thi 2004). The CO bandhead emission profiles of a number of intermediate and high mass YSOs could be very well fitted by models of circumstellar disc with Keplerian rotation (see e.g. Chandler et al. 1995; Bik & Thi 2004; Blum et al. 2004; Ilee et al. 2013). For three excess sources in the Arches cluster, K'-band spectra were obtained by Stolte et al. (2010) and all featured strong CO bandhead emission which supports their identification as dense circumstellar discs. While for primordial discs around intermediate mass stars it is expected to see first overtone CO bandhead emission in the K-band spectra, this is not the case for debris discs, as these discs are basically gas

[13] Available online at `http://vizier.cfa.harvard.edu/viz-bin/Cat?J/A%2bA/290/609`.

free, as well as transition discs. Although CO bandhead emission in the *M*-band ($\lambda_c \sim 4.7\,\mu$m) is detected from transition discs around Herbig AeBe stars, the origin of this emission is outside of 10 AU (Brittain et al. 2009; Salyk et al. 2009). For transition discs around intermediate mass stars it can hence be expected that they lack first overtone CO bandhead emission such that primordial and transition discs might be discernible based on their *K*-band spectra. As the discs of classical Be stars are ionised, no CO bandhead emission is present in their *K*-band spectra which would provide an additional criterion to judge their plausibility as explanation for the excess sources in the Quintuplet cluster.

With imaging data obtained at longer wavelengths it would be possible to construct and study the SEDs of the excess sources. Based on the SED slope in the mid-infrared it is for example possible to discern between primordial and more evolved circumstellar discs (Lada et al. 2006; Hernández et al. 2008) and to constrain the disc properties by fitting a disc model to the SED. While due to the infrared atmospheric window ground-based observations in the mid-infrared are possible in the *M*- and *N*-band ($\lambda_c = 4.7$ and $10\,\mu$m, respectively), e.g. with VLT/NACO, data at longer mid-infrared wavelengths can only be acquired with space telescopes. Due to the high stellar density in the Quintuplet fields the spatial resolution of the longer wavelength data is required to be high and comparable to the resolution of the WFC3 J_sH-band data ($\mathrm{FWHM_{PSF}} \sim 0.2''$), which prevents the use of existing mid-infrared surveys such as GLIMPSE ($\mathrm{FWHM_{PSF}} \sim 2''$, see Sect 5.1.2). The Mid-Infrared Instrument (MIRI) on board the James Webb Space Telescope (JWST, projected launch in 2018) will be able to cover the wavelength range from 5 to $28\,\mu$m with an expected spatial resolution between about $0.2''$ and $0.9''$ depending on the wavelength[14]. At least for wavelengths $\lesssim 10\,\mu$m the improved resolution of MIRI will suffice to avoid blending of the Quintuplet excess sources with close neighbours such that they can be unambiguously matched with their counterparts in the existing shorter wavelength data. Also the next generation, ground-based, extremely large telescopes (ELTs) which will be equipped with high-order AO systems and mid-infrared imaging cameras such as METIS (Brandl et al. 2010) for the European Extremely Large Telescope (E-ELT) will be well suited to clarify the nature of the Quintuplet excess sources and to study the survival of circumstellar discs in young massive clusters.

[14]The spatial resolution at different wavelengths was estimated as the FWHM of the modelled PSF for JWST/MIRI available online from `http://www-int.stsci.edu/~mperrin/software/psf_library/`.

6 Summary and outlook

The study of the stellar population of the Quintuplet cluster, a young massive star cluster with an age of 4 ± 1 Myr located at a projected distance of 30 pc from the Galactic centre, is observationally challenging. Because of its large distance of ~ 8 kpc, high resolution imaging data are required to resolve the cluster population beyond its brightest members. For ground-based observations a sufficient resolution can only be achieved by large telescopes (mirror diameter: ~ 8 m) equipped with an adaptive optics system. As the Galactic centre is obscured at optical wavelengths by molecular clouds and dust along the line of sight ($A_V \sim 30$ mag), data at near- or mid-infrared wavelengths have to be obtained. A further complication arises from the rich field population which, as it is comprised mostly of stars from the Galactic bulge with a comparable distance as the cluster, has a similar colour in the near-infrared as the cluster population. Cluster and field stars can hence not be discerned by their colours alone. As the Quintuplet cluster is less concentrated as e.g. the Arches cluster also located in the Galactic centre environment, the study of its stellar content above a few solar masses requires an additional effective mean to establish a clean member sample. The primary criterion to discern cluster and field stars applied in the presented work is based on the common bulk motion of the cluster stars with respect to the Galactic field. From the established unbiased member sample the present-day mass function of the Quintuplet cluster and the circumstellar disc fraction could be derived.

Cluster sample: The thorough analysis of near-infrared observations of the Quintuplet cluster obtained at the Very Large Telescope with the NAOS-CONICA instrument providing adaptive optics corrected data with a resolution close to the diffraction limit[1] and high astrometric accuracy constitutes the basis of this thesis. The central part of the cluster was covered and the outer parts probed out to distance of 2.1 pc from the cluster centre by four connected fields, as it was the goal of the presented study to measure the mass function slope within a large radial range, ideally out to the tidal radius of the cluster. Each field was observed twice in the K_s-band with a timebase of 3.2 yr (outer parts) or 5.0 yr (cluster centre) between the respective two epochs allowing to determine the individual stellar proper motions. Due to the lack of an absolute frame of reference, the proper motions were measured in the cluster rest frame. It should be noted here that the uncertainties of the derived proper motions are higher than the expected internal velocity dispersion ($6 - 8$ km/s) of the cluster and therefore internal motions are so far not resolved. The proper motion membership of each star was established based on its position in the proper motion diagram. Although stars as faint as $K_s > 19$ mag ($\hat{\approx} 1.4\, M_\odot$) can be readily detected, the proper motion member samples are restricted to $K_s < 19$ mag (central parts) and $K_s < 17.5$ mag (outer parts) due to the strong increase of the proper motion uncertainties towards fainter magnitudes. As for the field covering the cluster centre the proper motion uncertainties increase strongly towards larger radii, only stars in the area within $r < 0.5$ pc from the centre of this field are used to derive the properties of the central part of the cluster. For the central part of the cluster, all stars within $2\,\sigma$ from the origin of the proper motion diagram, i.e. the cluster rest frame, were selected for the proper motion membership sample. In the outer parts of the cluster the selection of a valid radius as membership criterion was complicated due to the overlap of the cluster and field

[1] The diffraction limit for an 8 m telescope in the K_s-band is about 0.07″. The full width at half maximum of the point spread function was $\leq 0.1''$ for all NAOS-CONICA datasets in the K_s-band (see Tables 3.1 and 4.1).

star distributions and the decline of the fraction of cluster stars towards larger cluster radii. Therefore, even close to the origin of the proper motion diagram the contribution of the field stars was found to be significant. In the three outer fields, a kinematic fit to the cluster and the field star distributions in the proper motion diagram by two bi-variate Gaussian distributions was determined with the expectation-maximisation algorithm, and the probability of a star to be part of the cluster distribution was calculated. The advantage of this procedure is that the spatial position of a star relative to the cluster centre as well as its individual proper motion uncertainty can be accounted for and influence its membership probability. As additional benefit, the performed kinematic fit allows to estimate the bulk proper motion of the cluster with respect to the Galactic field. From the distance between the peak positions of the fitted cluster and field star distributions, the bulk proper motion was found to be 128 ± 17 km/s which combined with its radial velocity yields a three-dimensional space motion of the cluster of 164 ± 17km/s. The membership criterion, i.e. the minimum value of the membership probability for a star to be considered as a cluster star, was chosen based on a synthetic proper motion diagram designed to resemble the measured proper motion diagram of one of the outer fields (Field 2). This membership criterion minimises the fraction of misidentified (lost) cluster stars and the number of contaminating field stars in the member sample at the same time.

However, due to the overlap of the field and cluster distributions in the proper motion diagram, a residual contamination of the proper motion member sample by field stars is unavoidable. Especially for the outer parts of the cluster, an additional refinement of the cluster sample by a colour selection was required. In combination with the K_s-band data, the necessary colour information was either provided by H-band data obtained with NAOS-CONICA or in the case of the outer fields by HST/WFC3 data in the J_s-band which allowed to construct the colour-magnitude diagrams of the individual fields. The presence of blue foreground stars, presumably main sequence stars from the Galactic disc, as well as red clumps stars and red giants in the colour-magnitude diagrams of proper motion members showed that some field stars cannot be distinguished from the cluster stars based on their proper motion alone. Because of their blue or red colours these residual field stars in the proper motion member sample could be effectively distinguished from cluster main sequence stars. The clean membership sample contained in total 603 cluster stars[2] of which 349 stars with $m > 4.7\,M_{\odot}$ (excluding WR stars) entered the derivation of the present-day mass function within $r < 2.1$ pc.

Present-day mass function: Initial and present-day stellar masses were inferred from the intersection of the line of reddening through the position of the respective star in the colour-magnitude diagram with an isochrone shifted to the Galactic centre distance of 8 kpc. By this approach, the individual extinction of each cluster star could be accounted for. To study the impact of different cluster ages and different sets of stellar models on the mass function slope, masses were derived from three Padova isochrones with ages of 3, 4, and 5 Myr (Marigo et al. 2008) and a 4 Myr Geneva isochrone (Lejeune & Schaerer 2001). The effect of using isochrones of different ages and different underlying stellar models on the mass function slope was found to be rather small, i.e. within about ±0.1dex from the average slope value derived from the four isochrones[3]. In order to avoid biases introduced by mass bins containing a low number of stars, an equal-number binning scheme as proposed by Maíz Apellániz & Úbeda (2005) was applied for generating the mass function, such that each mass bin contains the same number of stars. The mass function was determined in three radial ranges, i.e. within the central part ($r < 0.5$ pc) of the cluster and two annuli from $0.6 - 1.2$ pc and $1.2 - 1.8$ pc, respectively. It was

[2]This number contains all cluster members located in the outer fields ($K_s < 17.5$ mag) and the cluster members from the central part of the cluster ($K_s < 19.0$ mag) after application of the colour selection in $J_s - K_s$ (see Sect. 4.4.1 for details).
[3]In the following only these average values (see Table 4.15) are discussed.

also derived within an enlarged outermost annulus with $1.2 < r < 2.1$ pc to include another bright cluster member. As the outer fields cover only a part of the two annuli and due to the gap between the central part of the cluster and the inner annulus, a correction for the not covered areas had to be applied in order to determine the overall mass function of the cluster within $r < 1.8$ pc or $r < 2.1$ pc.

The present-day mass function of the Quintuplet cluster in the approximate mass range from 4 to 40 $M_\odot$ is found to be top-heavy in its central parts with a slope[4] of $\alpha_{\mathrm{m_{init}}} = -1.7 \pm 0.1$, compared to the canonical initial mass function slope of −2.3. Towards larger radii, the present-day mass function steepens moderately in the first annulus with a slope of -1.9 ± 0.2 and approaches with $\alpha_{\mathrm{m_{init}}} = -2.1 \pm 0.3$ the canonical slope value in the second annulus ($1.2 < r < 1.8$ pc). If the outer radius of the second annulus is increased to 2.1 pc, the derived slope is steeper with $\alpha_{\mathrm{m_{init}}} = -2.4 \pm 0.3$. The overall value of the present-day mass function slope is -2.0 ± 0.2 within $r < 1.8$ pc and -2.1 ± 0.2 within $r < 2.1$ pc, respectively. Such a radial trend which is indicative of mass segregation is commonly observed in young massive clusters. The present-day mass function slope of the Quintuplet cluster was compared in detail to the present-day mass function slope of the younger Arches cluster (age: 2.5 Myr) which is located in the same region. The Quintuplet cluster is not only significantly less dense than the Arches cluster, but also its radial extent with a flattened present-day mass function is much larger. For example, the slope of the Arches cluster is consistent with the canonical slope already in the radial range $0.2 < r < 0.4$ pc, and for larger radii ($0.4 < r < 1.5$ pc) with $\alpha_{\mathrm{m_{init}}} = -3.2 \pm 0.2$ significantly steeper than the slope of the Quintuplet cluster even in the outermost annulus ($1.2 < r < 2.1$ pc). As numerical models from the literature customised to the Arches cluster indicate that the expected expansion of its half-mass radius between its current age of 2.5 Myr and the age of the Quintuplet cluster of 4 Myr is only about 0.1 pc, it appears unlikely that both clusters were born with similar initial properties, but instead that the Quintuplet cluster formed already less concentrated.

If the measured mass of the Quintuplet cluster within $r < 2.1$ pc is corrected for completeness and the areas not covered by observations, and extrapolated down to 0.5 $M_\odot$, its total present-day mass[5] amounts to $2.2 \pm 0.3 \times 10^4$ $M_\odot$ which is on the same order as the total mass estimates of the Arches cluster and NGC 3603. As the Galactocentric radius r_{GC} of the cluster is not well constrained, its tidal radius is also uncertain and ranges between 1.7 to 3.6 pc for $r_{\mathrm{GC}} = 30 - 200$ pc. Whether the mass function probes the whole bound population of the cluster or not is therefore not clear.

Near-infrared excess sources: The combination of the $J_s K_s$ photometry of the membership sample with NAOS-CONICA L'-band data obtained for all Quintuplet fields, enabled the search for near-infrared excess sources among the proper motion members to assess the presence of surviving circumstellar discs in the cluster. Excess candidates were identified based on their position in the $J_s - K_s$, $K_s - L'$ colour-colour diagrams and were required to deviate by more than 3σ from the line of reddening of MS stars, where σ is the standard deviation of the distribution of stars without excess. After excluding evolved stars, the fraction of near-infrared excess sources for $K_s < 17.5$ mag was found to be 2.5 ± 0.8%. The estimated masses of the excess sources are between 2 and 10 $M_\odot$, i.e. the excess sources constitute mid A- to early B-type stars. The excess source fraction was compared to the disc fractions of stars of spectral types OBA in other young clusters as well as associations and found to be generally consistent. As the survival of primordial circumstellar discs around intermediate mass stars up to the age of the Quintuplet cluster is unexpected, especially if the intense UV-field in the cluster due to the large number of luminous OB stars is considered, possible alternative explanations for the

[4]The subscript $\mathrm{m_{init}}$ indicates that the stated slopes were determined by fitting the present-day mass function constructed from initial stellar masses.

[5]Due to their uncertain present-day masses WR stars and LBVs are not included in this mass estimate.

detected near-infrared excess such as Be stars, stars showing the B[e] phenomenon or evolved stellar discs were discussed.

Outlook: The next steps following the presented study towards a more complete understanding of the Quintuplet cluster include the inference of its possible formation locus, constraining its initial properties and future evolution and follow-up observations to clarify the nature of the detected excess sources. Using the estimated three-dimensional space motion of the cluster, its orbit in the gravitational potential of the inner Galaxy can be determined in dependence of the present-day Galactocentric distance of the cluster in a similar way as was already done for the Arches cluster. By tracing the orbit back in time, the location of the Quintuplet cluster in the Galaxy at the time of its birth can be estimated which might help to constrain possible formation scenarios. The orbit of the cluster extrapolated into the future may also help to determine how long the cluster will survive in the Galactic centre potential. The clean membership sample of the cluster and its measured present-day mass function can be used as input for customised numerical models of the Quintuplet cluster set out to constrain its initial properties including its initial mass function. Such a study was already performed for the Arches cluster (Harfst et al. 2010) and is currently conducted by the same group for the Quintuplet cluster. Future observational studies of the cluster might also go for a more complete coverage of the cluster reaching out to larger distances from the cluster centre, allowing for a determination of its extent and shape. However, especially the later point might not be possible to achieve with adaptive optics systems using a single guide star such as NAOS-CONICA. Although the high resolution offered by this instrument is indispensable in order to derive proper motions with a sufficient accuracy, the strong dependence of the adaptive optics performance from the guide star distance imposes limitations to the area covered by a single field. In order to measure proper motions in the reference frame of the cluster to establish a proper motion sample requires a sufficiently large number of cluster stars within the observed field and hence an instrument with a large field of view which simultaneously covers the cluster centre and the outskirts. Instruments which fulfil these requirements are the WFC3 camera onboard the Hubble Space Telescope and supposedly next generation multi-conjugate adaptive optics systems providing adaptive optics correction over a large area. To shed light on the origin of the near-infrared excess produced by some intermediate mass members of the Quintuplet cluster additional observations are required. Especially the detection of first overtone CO bandhead emission in K-spectra which could be obtained with SINFONI at the Very Large Telescope would support the disc origin of the excess. Observing the excess sources also at mid-infrared wavelengths would allow to construct the spectral energy distributions and distinguish between primordial and evolved circumstellar discs. However, no instrument capable of observing at wavelengths $> 10\,\mu$m with the necessary spatial resolution is currently available.

In summary, the present-day mass function of the Quintuplet cluster is top-heavy in its inner parts and steepens towards larger radii as expected for a dynamically evolved cluster. It is very probable that the steepening of the mass function with radius continues beyond $r = 2.1$ pc, but this has to be verified by future studies. Although a final conclusion depends on customised numerical models of the cluster, it is likely with regards to the results for the Arches cluster that also the Quintuplet cluster was formed with a standard initial mass function. If this is confirmed, the implications are that even under the extreme conditions experienced in the Galactic centre environment star formation proceeds in a surprisingly normal fashion contrary to expectations.

The presence of near-infrared excess sources albeit constituting only a minor fraction of the intermediate mass cluster stars deserves closer attention and follow-up observations set-out to confirm or disprove their nature as disc-bearing stars. Providing that the excess is indeed caused by circumstel-

lar material, it would be exciting to determine whether the excess sources house primordial, evolved or even secondary discs. The knowledge of the evolutionary stage of the discs could help to assess timescales for primordial disc destruction in young massive clusters.

A Proper motion uncertainty (appendix for Chapter 3)

Appendix A is a reproduction of Appendix B of the following publication:[1]
The present-day mass function of the Quintuplet cluster based on proper motion membership; Hußmann, B., Stolte, A., Brandner, W., Gennaro, M., & Liermann, A. 2012, A&A, 540, A57, reproduced with permission ©ESO.

The uncertainty of the proper motion in the east-west ($\sigma_{\mu_{\alpha\cos(\delta)}}$) or north-south direction (σ_{μ_δ}) are computed as

$$\sigma_{\mu_{\alpha\cos(\delta)}} = \sigma_{\mu_\mathrm{x}} = \frac{1}{\Delta t}\sqrt{\sigma^2_{\mathrm{x},2003} + \sigma^2_{\mathrm{x},2008} + \sigma^2_{\mathrm{trans,x}}} \tag{A.1}$$

and

$$\sigma_{\mu_\delta} = \sigma_{\mu_\mathrm{y}} = \frac{1}{\Delta t}\sqrt{\sigma^2_{\mathrm{y},2003} + \sigma^2_{\mathrm{y},2008} + \sigma^2_{\mathrm{trans,y}}}\,. \tag{A.2}$$

The uncertainties of the position in the x- (east-west) and y-direction (north-south) in the proper motion plane (see Fig. 3.6) are denoted as $\sigma_{\mathrm{x,year}}$ and $\sigma_{\mathrm{y,year}}$, respectively, and are the standard errors of the three independent measurements of the position of each star in the three auxiliary images (see Sect. 3.2.4). The residual rms deviations in the x- and y-direction of the geometric transformation, which is used to map the positions of the 2003 epoch onto the correct positions of the 2008 epoch, are $\sigma_{\mathrm{trans,x}}$ and $\sigma_{\mathrm{trans,y}}$.

The proper motion membership criterion is derived from the total proper motion $\mu = \sqrt{\mu^2_{\alpha\cos(\delta)} + \mu^2_\delta}$ (see Sect. 3.4.3). The uncertainty of the combined proper motion σ_μ is therefore

$$\sigma_\mu = \frac{1}{\Delta t}\sqrt{\sigma^2_{\mathrm{pos},2003} + \sigma^2_{\mathrm{pos},2008} + \sigma^2_{\mathrm{trans,x}} + \sigma^2_{\mathrm{trans,y}}}\,, \tag{A.3}$$

where the astrometric uncertainty $\sigma_{\mathrm{pos,year}}$ is the average of the positional uncertainties in the x- and y-direction,

$$\sigma_{\mathrm{pos,year}} = \frac{\sigma_{\mathrm{x,year}} + \sigma_{\mathrm{y,year}}}{2}\,, \tag{A.4}$$

(see Sect. 3.2.4).

[1] Equations A.1, A.2, and A.3 were corrected by adding the missing factor of $1/\Delta t$ (Δt: timebase).

B Assessment of the remaining contaminants in the cluster sample (appendix for Chapter 3)

Appendix B is a reproduction of Appendix C of the following publication:
The present-day mass function of the Quintuplet cluster based on proper motion membership; Hußmann, B., Stolte, A., Brandner, W., Gennaro, M., & Liermann, A. 2012, A&A, 540, A57, reproduced with permission ©ESO.

After the proper motion member selection and the additional colour-cut had been applied (see Sect. 3.5), 6 M,K supergiants remained in the cluster sample and could only be removed because their spectral type is known from the LHO catalogue. In order to study the influence of hidden field stars in the final cluster sample on the MF slope, their number was estimated in the mass range from $4.6 \leq m_{\mathrm{Pad,4Myr}} \leq 40.0\,M_{\odot}$. The minimum mass of $4.6\,M_{\odot}$ corresponds to the minimum mass entering the mass function for the 4 Myr Padova isochrone, while the upper mass boundary at $m_{\mathrm{Pad,4Myr}} = 40.0\,M_{\odot}$ is chosen such that for all stars with higher masses the spectral type is known and the final cluster sample can be considered clean. This mass range was splitted in six mass bins with equal spacing in H-band (see left panel in Fig. B.1, tilted lines). About 70% of all cluster members residing within the three uppermost bins (bins 4 to 6 in Table B.1, $m_{\mathrm{Pad,4Myr}} \geq 18.0\,M_{\odot}$) have a unique counterpart in the LHO spectral catalogue (see Fig. 3.9). The estimation of the number of contaminating field stars n_{cont} among stars without a spectral classification within bin 4 to 6 can therefore be based on the known number of M,K giants in each bin (Appendix B.1). Due to the lack of spectral identifications in the mass range $m_{\mathrm{Pad,4Myr}} < 18.0\,M_{\odot}$ this is not possible for the bins 1 to 3. The assessment of n_{cont} within these bins relies on the ratio of the number of field stars which are removed due to their red colour to the number of field stars identified by their proper motions in the same colour-range (see Appendix B.2). The MF slope is then re-determined after randomly selecting and removing the estimated number of contaminants within each mass bin from the final cluster sample (Appendix B.3).

B.1 Estimation of n_{cont} for $m_{\mathrm{Pad,4\,Myr}} \geq 18.0\,M_{\odot}$

50 stars out of a total of 568 stars in the final cluster sample have a unique counterpart of spectral type O or B in the LHO catalogue. Further 13 stars can not be assigned unambiguously to early type sources in the spectral catalogue. The ambiguous assignments for these stars are caused by the higher resolution of the NACO datasets such that several stars in the final catalogue are the potential counterparts of one source in the LHO catalogue (these stars are marked by an X-cross in Fig. 3.9). For the bulk of cluster members within the high mass bins (4 to 6) the spectral types are known. The 6 M,K supergiants, which were excluded from the final cluster sample, are located in the same region of the CMD. Therefore, the estimation of the number of contaminants among the stars without known spectral type can be based on the ratio of the number of known M,K supergiants $n_{\mathrm{M,K}}$ to the number of spectroscopically classified early type stars n_{ST} (ST stands for spectral type) in the respective bin.

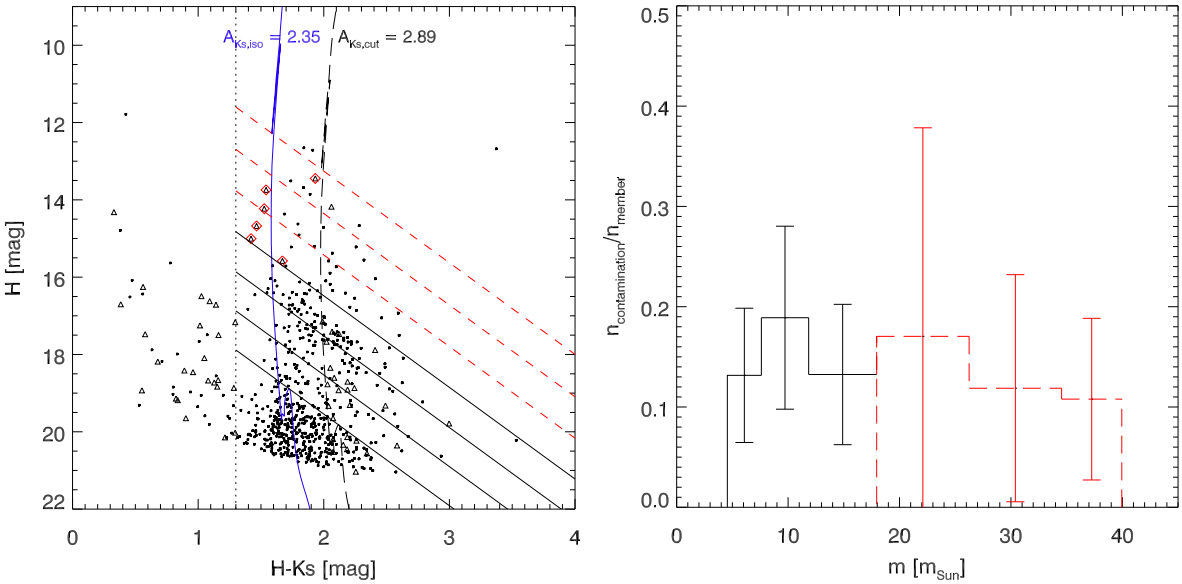

Figure B.1: Left panel: Colour-magnitude diagram of stars classified as belonging to the field according to their proper motion (dots) and of stars removed from the member sample based on their colour or known spectral type (triangles). Field stars which could only be discerned due to the knowledge of their spectral type are additionally drawn as diamonds. The vertical, short-dashed line and the second isochrone ($A_{K_s,cut} = 2.89$ mag, long-dashed line) indicate the position of the blue and the red colour-cut (see Sect. 3.5). The tilted lines, equally spaced in *H*-band, are lines of reddening according to the extinction law of Nishiyama et al. (2009) and are the boundaries of the bins used to estimate the residual contamination of the member sample. The estimation was performed in two different ways for bins 1 to 3 (counted from bottom to top, solid lines) and for bins 4 to 6 (dashed lines). Right panel: Ratio of the number of expected contaminating field stars in the member sample after proper motion selection and colour-cut to the number of cluster members for the respective mass bin (see right panel) plotted vs. the initial mass as determined from the 4 Myr Padova isochrone. The number of contaminating field stars for the first three bins (solid) and for the bins 4 to 6 (dashed) are estimated according to Appendix B.2 and Appendix B.1, respectively.

For each of the bins 4 to 6 the numbers of stars in the final cluster sample with a unique ($n_{\rm ST}$), an ambiguous ($n_{\rm ambST}$) and without assignment ($n_{\rm noST}$) to a source in the LHO catalogue are determined. The number of stars with an ambiguous assignment within each bin is distributed among $n_{\rm ST}$ and $n_{\rm noST}$. For example two stars in bin 6 are potential counterparts for the WR-star with number 47 in the LHO catalogue. As only one of the two stars is the true counterpart, $n_{\rm ST}$ and $n_{\rm noST}$ are both increased by one. If the two stars would reside in two different bins, $n_{\rm ST}$ and $n_{\rm noST}$ would be each increased by 0.5 in both bins.

The number of hidden M,K supergiants ($n_{\rm cont,MK}$) among the stars of the final cluster sample without or with ambiguous spectral identification within the bins 4 to 6 is the ratio of the number of identified M,K giants ($n_{\rm M,K}$) in the respective bin (see left panel in Fig. B.1) to $n_{\rm ST}$ times $n_{\rm noST}$:

$$n_{\rm cont,MK} = n_{\rm cont} = \frac{n_{\rm M,K}}{n_{\rm ST}} n_{\rm no,ST} \,. \tag{B.1}$$

These numbers are stated in Table B.1.

Table B.1: Estimated remaining contaminations in the cluster member sample after proper motion and colour selection.

Bin No.	$m_{\rm min}$ [a] ($M_\odot$)	$m_{\rm max}$ [a] ($M_\odot$)	$n_{\rm f,red,cc}$ [b]	$n_{\rm f,red,pm}$ [c]	$n_{\rm f,within\,cc}$ [d]	$n_{\rm cont}$ [e]	$n_{\rm M,K}$ [f]	$n_{\rm m}$ [g]	$n_{\rm cont}/n_{\rm m}$ [g]
1	4.6	7.6	6	17	41	14.5 ± 7.2		110	0.13 ± 0.07
2	7.6	11.9	7	26	33	8.9 ± 4.1		47	0.19 ± 0.09
3	11.9	18.0	5	35	38	5.4 ± 2.7		41	0.13 ± 0.07
4	18.0	26.3				2.6 ± 1.8	3	33	0.17 ± 0.21 [h]
5	26.3	34.6				1.0 ± 0.8	2	25	0.12 ± 0.11 [h]
6	34.6	40.0				0.3 ± 0.4	1	12	0.11 ± 0.08 [h]

Notes. [a] The initial masses refer to the 4 Myr Padova isochrone (Marigo et al. 2008). [b] Number of field stars removed solely by the red colour-cut (see left panel Fig. B.1). [c] Number of field stars removed based on their proper motion, but redder than the red colour-cut. [d] Number of field stars removed based on their proper motion within the blue and the red colour-cut. [e] Estimated number of contaminating stars. [f] Number of spectroscopically identified M,K supergiants within the proper motion member sample after the colour-cut. [g] Number of proper motion cluster members after the colour-cut. Unlike in the final cluster sample, the spectroscopically identified M,K supergiants are not removed. [h] The number of contaminants includes $n_{\rm cont}$ and $n_{\rm M,K}$ (see text).

B.2 Estimation of $n_{\rm cont}$ for $m_{\rm Pad,4\,Myr} < 18.0\,M_\odot$

For stars fainter than about $H = 15.5$ mag the cluster membership of a star in the final cluster sample could not be confirmed by its spectral identification in the LHO catalogue anymore (see Fig. 3.9) and the number of residual field stars hidden in the final cluster sample can only be estimated. The estimation of $n_{\rm cont}$ for stars with $m_{\rm Pad,4Myr} < 18.0\,M_\odot$ uses the field stars outside the colour-cuts (see Fig. B.1, black triangles), to assess the ratio of the number of field stars, which are removed from the cluster sample solely due to their colour, to the number of field stars, which are already identified because of their proper motions. The field stars removed by the blue and the red colour-cut (see Sect. 3.5) belong to different populations, though.

Stars with colours $H - K_s \leq 1.3$ are likely main sequence foreground stars located in the Galactic spiral arms. As these stars are co-moving with the disc with ~ 200 km/s and hence posses similar proper motions as the cluster, it is not possible to discriminate these stars based on their proper motion alone. However, they are very effectively removed by the blue colour-cut, as their colours due to their smaller distance and, therefore, lower extinction differ from the colour of stars in the inner bulge. In fact, for the mass bins 1 and 2 the number of presumed foreground stars, which are rejected because of their blue colour, is equal to or exceeds the number of blue proper motion non-members by a factor of five. At least for the lowermost mass bin cluster and foreground stars are more effectively discerned based on their colours than on their proper motions, which significantly increases the estimated number of contaminants for the respective mass bins. But because of the distinct colour ranges of stars in the final cluster sample and blue foreground stars from the spiral arms in the mass range used for the PDMF derivation (see Fig. 3.8), a significant contribution of foreground stars to the residual contamination of the final cluster sample is not expected. Therefore stars left of the blue colour-cut are not used to estimate the remaining contamination, as this would overestimate the number of contaminants.

Otherwise, the bulk of stars located in the Galactic bulge experience a similar or larger extinction as the cluster (see right panel in Fig. 3.8). Bulge stars, which due to their large number constitute the dominant source of contaminants for lines of sight towards the Galactic centre, are hence harder to discern from the cluster by their colour, but because of their randomized motion and systematically

lower velocities (see Fig. 3 in Rich et al. 2007) they are more easily removed by the proper motion membership criterion.

To estimate the number of residual contaminants in the cluster sample for bins 1 to 3 we therefore use the red sources in the field star CMD. Within each of the mass bins 1 to 3, the number of field stars removed based on the red colour-cut ($n_{\mathrm{f,red,cc}}$) is divided by the number of field stars in the same colour-range identified by their proper motion ($n_{\mathrm{f,red,pm}}$). This ratio is then multiplied with the number of field stars between the red and blue colour-cut in that mass bin ($n_{\mathrm{f,within\,cc}}$) to retrieve the expected number of contaminating field stars in the cluster sample:

$$n_{\mathrm{cont}} = \frac{n_{\mathrm{f,red,cc}}}{n_{\mathrm{f,red,pm}}} n_{\mathrm{f,within\,cc}} \,. \tag{B.2}$$

The estimated numbers of contaminants n_{cont} within the three mass bins are stated in Table B.1 (bin number 1 to 3).

The ratio of n_{cont} to the number of cluster members n_{m} (including the 6 known M,K supergiants) is drawn in Fig. B.1 (right panel) for all mass bins (solid for bins 1 to 3, dashed for bins 4 to 6). As for bins 1 to 3 n_{cont} refers to the total number of contaminants after proper motion and colour-selection, the number of identified M,K supergiants $n_{\mathrm{M,K}}$ is added to the estimated number of hidden field stars n_{cont} for the bins 4 to 6. The error bars follow from error propagation assuming Poisson errors for the number of identified M,K supergiants and cluster members in each mass bin. The ratios $n_{\mathrm{cont}}/n_{\mathrm{m}}$ are consistent for all mass bins within the uncertainties, with an expected average residual contamination of $\langle n_{\mathrm{cont}}/n_{\mathrm{m}} \rangle = 14 \pm 5\%$.

As explained above we expect to overestimate n_{cont} if stars left of the blue colour-cut are as well taken into account for the derivation of n_{cont}, but we state the retrieved values for completeness. The usage of red *and* blue sources leads to considerably larger values of n_{cont} for the mass bins 1 and 2, yielding 25.1 ± 10.4 and 9.8 ± 4.3 , respectively (see Table B.1 for comparison). The ratio $n_{\mathrm{cont}}/n_{\mathrm{m}}$ for these two bins is raised to 0.23 ± 0.10 (bin 1) and 0.21 ± 0.10 (bin 2), which slightly increases the average residual contamination: $\langle n_{\mathrm{cont}}/n_{\mathrm{m}} \rangle = 16 \pm 5\%$.

B.3 Influence of hidden field stars on the mass function slope

The influence of the contaminants on the mass function slope was studied for the mass function derived for the 4 Myr Padova isochrone. Within each mass bin, n_{cont} stars, with n_{cont} being the estimated number of contaminants in the respective mass bin, were randomly selected and removed from the final cluster sample. For the bins 4 to 6 only stars without spectral identification were selected and removed, whereas at least one star of each LHO number occurring in the full final cluster sample remained in the cluster sample. The mass function was then derived in the same way as for the full sample (see Section 3.7) using equal number bins (Method A).

To account for the error of n_{cont}, the removed number of contaminants in each bin was independently varied between the three values $n_{\mathrm{cont}} - \Delta n_{\mathrm{cont}}$, n_{cont} and $n_{\mathrm{cont}} + \Delta n_{\mathrm{cont}}$. For each combination of the removed number of contaminants per bin the random selection and removal of stars was repeated 100 times. The retrieved mass functions slopes α vary in the range between -1.74 and -1.50. The mean value of all derived slopes is -1.63, which is the same slope as derived using the best value of n_{cont} for all bins. In general the mass function slope flattens for a larger total number of removed stars, as the number of estimated contaminants (and the respective errors) increases towards lower masses. The steepest slopes are naturally derived for combinations where the ratio of the number of stars removed in bins 1 to 3 to the number of stars removed in bin 4 to 6 is largest. The steepest retrieved

slope of -1.74 ± 0.09 is still well contained within the errors of the MF slope for the 4 Myr Padova isochrone derived without accounting for residual field stars ($\alpha = -1.68 \pm 0.09$). On the other hand, the flattest slope -1.50 ± 0.09 is considerably flatter, although the ranges of the formal fitting errors still marginally overlap. The mass function slopes reported in Table 3.5 can therefore (within the uncertainties) be regarded as lower (steep) limits for the true PDMF slope of the Quintuplet cluster.

If stars left of the blue colour-cut are considered during the estimation of $n_{\rm cont}$ (see last paragraph of Appendix B.2), the number of stars to be removed from the two lowest mass bins (bin 1 and 2) is significantly increased. The retrieved PDMF slopes are therefore flatter, ranging from $\alpha = -1.71$ to -1.39 with an average value of $\alpha = -1.55$ (compared to $\alpha_{\rm min} = -1.74$, $\alpha_{\rm max} = -1.50$ and a mean value of $\alpha = -1.63$).

C Acronyms and abbreviations

2MASS	**2 M**icron **A**ll **S**ky **S**urvey
AO	**A**daptive **O**ptics
CCD	**C**olour-**C**olour **D**iagram
CMD	**C**olour-**M**agnitude **D**iagram
CMZ	**C**entral **M**olecular **Z**one
CONICA	**CO**udé **N**ear **I**nfrared **CA**mera
DIT	**D**etector **I**ntegration **T**ime
EM algorithm	**E**xpectation-**M**aximisation algorithm
FOV	**F**ield **O**f **V**iew
FWHM	**F**ull **W**idth at **H**alf **M**aximum
GLIMPSE	**G**alactic **L**egacy **I**nfrared **M**id-**P**lane **S**urvey **E**xtraordinaire
HRD	**H**ertzsprung-**R**ussel **D**iagram
HST	**H**ubble **S**pace **T**elescope
IMF	**I**nitial **M**ass **F**unction
IRAC	**I**nfra**R**ed **A**rray **C**amera
IRACE	**I**nfra**R**ed **A**rray **C**ontrol **E**lectronics
ISAAC	**I**nfrared **S**pectrometer **A**nd **A**rray **C**amera
JWST	**J**ames **W**ebb **S**pace **T**elescope
LBV	**L**uminous **B**lue **V**ariable
MAST	**M**ikulski **A**rchive for **S**pace **T**elescopes
MIRI	**M**id-**I**nfra**R**ed **I**nstrument
MS	**M**ain **S**equence
NACO	**NA**OS-**CO**NICA
NAOS	**N**asmyth **A**daptive **O**ptics **S**ystem
NDIT	**N**umber of **DIT**s
ONC	**O**rion **N**ebula **C**luster

PDMF	**P**resent-**D**ay **M**ass **F**unction
PMD	**P**roper **M**otion **D**iagram
PMS	**P**re-**M**ain **S**equence
PSF	**P**oint **S**pread **F**unction
RSG	**R**ed **S**uper**G**iant
SED	**S**pectral **E**nergy **D**istribution
SMBH	**S**uper**M**assive **B**lack **H**ole
UKIDSS	**UK**IRT **I**nfrared **D**eep **S**ky **S**urvey
VLT	**V**ery **L**arge **T**elescope
WR star	**W**olf-**R**ayet star
WFC3	**W**ide **F**ield **C**amera **3**
YSO	**Y**oung **S**tellar **O**bject
ZAMS	**Z**ero **A**ge **M**ain **S**equence

Bibliography

Ageorges, N., Lidman, C., Kaufer, A., & Hainaut, O. 2007, Very Large Telescope NAOS-CONICA User Manual, 81st edn., ESO, Garching

Alexander, M. J., Kobulnicky, H. A., Clemens, D. P., et al. 2009, AJ, 137, 4824

Allen, D. A., Hyland, A. R., Longmore, A. J., et al. 1977, ApJ, 217, 108

Allison, R. J., Goodwin, S. P., Parker, R. J., et al. 2009, ApJ, 700, L99

Alonso-Albi, T., Fuente, A., Bachiller, R., et al. 2009, A&A, 497, 117

Alves, D. R. 2000, ApJ, 539, 732

Amico, P., Lidman, C., Pompei, E., Dumas, C., & Kaufer, A. 2008, NACO calibration plan, 84th edn., ESO, Garching

An, D., Ramrez, S. V., Sellgren, K., et al. 2011, ApJ, 736, 133

Ao, Y., Henkel, C., Menten, K. M., et al. 2013, A&A, 550, A135

Ascenso, J., Alves, J., Beletsky, Y., & Lago, M. T. V. T. 2007, A&A, 466, 137

Balog, Z., Muzerolle, J., Rieke, G. H., et al. 2007, ApJ, 660, 1532

Banerjee, S. & Kroupa, P. 2012, A&A, 547, A23

Banerjee, S., Kroupa, P., & Oh, S. 2012a, ApJ, 746, 15

Banerjee, S., Kroupa, P., & Oh, S. 2012b, MNRAS, 426, 1416

Bartko, H., Martins, F., Fritz, T. K., et al. 2009, ApJ, 697, 1741

Bartko, H., Martins, F., Trippe, S., et al. 2010, ApJ, 708, 834

Bastian, N., Covey, K. R., & Meyer, M. R. 2010, ARA&A, 48, 339

Baumgardt, H. & Makino, J. 2003, MNRAS, 340, 227

Becklin, E. E. & Neugebauer, G. 1978, PASP, 90, 657

Benjamin, R. A., Churchwell, E., Babler, B. L., et al. 2003, PASP, 115, 953

Bertelli, G., Bressan, A., Chiosi, C., Fagotto, F., & Nasi, E. 1994, A&AS, 106, 275

Bessell, M. S. & Brett, J. M. 1988, PASP, 100, 1134

Beuther, H., Tackenberg, J., Linz, H., et al. 2012, ApJ, 747, 43

Bik, A., Kaper, L., & Waters, L. B. F. M. 2006, A&A, 455, 561

Bik, A. & Thi, W. F. 2004, A&A, 427, L13

Binney, J., Gerhard, O. E., Stark, A. A., Bally, J., & Uchida, K. I. 1991, MNRAS, 252, 210

Blum, R. D., Barbosa, C. L., Damineli, A., Conti, P. S., & Ridgway, S. 2004, ApJ, 617, 1167

Bonnell, I. A. & Bate, M. R. 2006, MNRAS, 370, 488

Bonnell, I. A. & Davies, M. B. 1998, MNRAS, 295, 691

Bonnell, I. A. & Rice, W. K. M. 2008, Sci, 321, 1060

Bonnell, I. A., Vine, S. G., & Bate, M. R. 2004, MNRAS, 349, 735

Borissova, J., Ivanov, V. D., Hanson, M. M., et al. 2008, A&A, 488, 151

Brandl, B., Blommaert, J., Glasse, A., Lenzen, R., & Pantin, E. 2010, The Messenger, 140, 30

Brandner, W., Clark, J. S., Stolte, A., et al. 2008, A&A, 478, 137

Bressan, A., Fagotto, F., Bertelli, G., & Chiosi, C. 1993, A&AS, 100, 647

Brittain, S. D., Najita, J. R., & Carr, J. S. 2009, ApJ, 702, 85

Brown, T. M., Sahu, K., Anderson, J., et al. 2010, ApJ, 725, L19

Carpenter, J. M. 2001, AJ, 121, 2851

Carr, J. S. 1989, ApJ, 345, 522

Carraro, G., Turner, D., Majaess, D., & Baume, G. 2013, A&A, 555, A50

Casertano, S. & Hut, P. 1985, ApJ, 298, 80

Chabrier, G. 2003, PASP, 115, 763

Chandler, C. J., Carlstrom, J. E., & Scoville, N. Z. 1995, ApJ, 446, 793

Chen, L., de Grijs, R., & Zhao, J. L. 2007, AJ, 134, 1368

Churchwell, E., Babler, B. L., Meade, M. R., et al. 2009, PASP, 121, 213

Clark, J., Muno, M. P., Negueruela, I., et al. 2008, A&A, 477, 147

Clark, J. S., Negueruela, I., Crowther, P. A., & Goodwin, S. P. 2005, A&A, 434, 949

Clark, J. S., Negueruela, I., Davies, B., et al. 2009, A&A, 498, 109

Clarkson, W. I., Ghez, A. M., Morris, M. R., et al. 2012, ApJ, 751, 132

Cotera, A. S., Erickson, E. F., Colgan, S. W. J., et al. 1996, ApJ, 461, 750

Crocker, R. M., Jones, D. I., Melia, F., Ott, J., & Protheroe, R. J. 2010, Nat, 463, 65

Crowther, P. A., Schnurr, O., Hirschi, R., et al. 2010, MNRAS, 408, 731

Cunha, K., Sellgren, K., Smith, V. V., et al. 2007, ApJ, 669, 1011

Currie, T., Hernandez, J., Irwin, J., et al. 2010, ApJS, 186, 191

Da Rio, N., Gouliermis, D. A., & Henning, T. 2009, ApJ, 696, 528

Dabringhausen, J., Kroupa, P., Pflamm-Altenburg, J., & Mieske, S. 2012, ApJ, 747, 72

Davies, B., de la Fuente, D., Najarro, F., et al. 2012, MNRAS, 419, 1860

Davies, B., Figer, D. F., Kudritzki, R.-P., et al. 2007, ApJ, 671, 781

Davies, B., Origlia, L., Kudritzki, R.-P., et al. 2009, ApJ, 694, 46

de Wit, W. J., Testi, L., Palla, F., & Zinnecker, H. 2005, A&A, 437, 247

Degl'Innocenti, S., Prada Moroni, P. G., Marconi, M., & Ruoppo, A. 2008, Ap&SS, 316, 25

Devillard, N. 2001, in ASP Conf. Ser., Vol. 238, Astronomical Data Analysis Software and Systems X, ed. F. R. Harnden Jr., F. A. Primini, & H. E. Payne, 525

Diolaiti, E., Bendinelli, O., Bonaccini, D., et al. 2000, A&AS, 147, 335

Do, T., Lu, J. R., Ghez, A. M., et al. 2013, ApJ, 764, 154

Dougherty, S. M., Waters, L. B. F. M., Burki, G., et al. 1994, A&A, 290, 609

Dullemond, C. P., Dominik, C., & Natta, A. 2001, ApJ, 560, 957

Dutra, C. M. & Bica, E. 2001, A&A, 376, 434

Eisenhauer, F., Quirrenbach, A., Zinnecker, H., & Genzel, R. 1998, ApJ, 498, 278

Eldridge, J. J., Izzard, R. G., & Tout, C. A. 2008, MNRAS, 384, 1109

Espinoza, P., Selman, F., J., & Melnick, J. 2009, A&A, 501, 563

Fang, M., van Boekel, R., King, R. R., et al. 2012, A&A, 539, A119

Ferrière, K., Gillard, W., & Jean, P. 2007, A&A, 467, 611

Figer, D. F. 2004, in ASP Conf. Ser., Vol. 322, The Formation and Evolution of Massive Young Star Clusters, ed. H. J. G. L. M. Lamers, L. J. Smith, & A. Nota, 49

Figer, D. F. 2005, Nat, 434, 192

Figer, D. F., Kim, S. S., Morris, M., et al. 1999a, ApJ, 525, 750

Figer, D. F., MacKenty, J. W., Robberto, M., et al. 2006, ApJ, 643, 1166

Figer, D. F., McLean, I. S., & Morris, M. 1995, ApJ, 447, L29

Figer, D. F., McLean, I. S., & Morris, M. 1999b, ApJ, 514, 202

Figer, D. F., Morris, M., Geballe, T. R., et al. 1999, ApJ, 525, 759

Figer, D. F., Morris, M., & McLean, I. S. 1996, in ASP Conf. Ser., Vol. 102, The Galactic Center, ed. R. Gredel, 263

Figer, D. F., Najarro, F., Gilmore, D., et al. 2002, ApJ, 581, 258

Figer, D. F., Najarro, F., Morris, M., et al. 1998, ApJ, 506, 384

Fritz, T., Gillessen, S., Trippe, S., et al. 2010, MNRAS, 401, 1177

Fruchter, A. & Hook, R. 2002, PASP, 114, 144

Fujii, M. S. & Zwart, S. P. 2011, Sci, 334, 1380

Geballe, T. R., Najarro, F., & Figer, D. F. 2000, ApJ, 530, L97

Gennaro, M., Brandner, W., Stolte, A., & Henning, T. 2011, MNRAS, 412, 2469

Genzel, R., Eisenhauer, F., & Gillessen, S. 2010, Rev. Mod. Phys., 82, 3121

Gerhard, O. 2001, ApJ, 546, L39

Ghez, A. M., Salim, S., Weinberg, N. N., et al. 2008, ApJ, 689, 1044

Gillessen, S., Eisenhauer, F., Fritz, T. K., et al. 2009, ApJ, 707, L114

Girard, J., Dumas, C., & Kaufer, A. 2011, Very Large Telescope NACO User Manual, 87th edn., ESO, Garching

Girardi, L., Bertelli, G., Bressan, A., et al. 2002, A&A, 391, 195

Girardi, L., Bressan, A., Bertelli, G., & Chiosi, C. 2000, A&AS, 141, 371

Glass, I. S., Catchpole, R. M., & Whitelock, P. A. 1987, MNRAS, 227, 373

Glass, I. S., Moneti, A., & Moorwood, A. F. M. 1990, MNRAS, 242, 55P

Gorti, U., Dullemond, C. P., & Hollenbach, D. 2009, ApJ, 705, 1237

Guarcello, M. G., Micela, G., Damiani, F., et al. 2009, A&A, 496, 453

Gürkan, M. A. & Rasio, F. A. 2005, ApJ, 628, 236

Gvaramadze, V. V. & Bomans, D. J. 2008, A&A, 490, 1071

Habibi, M., Stolte, A., Brandner, W., Hußmann, B., & Motohara, K. 2013, A&A, 556, A26

Haisch, K. E., Lada, E. A., & Lada, C. J. 2000, AJ, 120, 1396

Haisch, K. E., Lada, E. A., & Lada, C. J. 2001a, ApJ, 553, L153

Haisch, K. E. J., Lada, E. A., & Lada, C. J. 2001b, AJ, 121, 2065

Hambly, N. C., Collins, R. S., Cross, N. J. G., et al. 2008, MNRAS, 384, 637

Harayama, Y., Eisenhauer, F., , & Martins, F. 2008, ApJ, 675, 1319

Harfst, S., Portegies Zwart, S., & Stolte, A. 2010, MNRAS, 409, 628

Hartung, M. 2003, PhD thesis, Ruperto-Carola University of Heidelberg, Germany

Hasegawa, T., Sato, F., Whiteoak, J. B., & Miyawaki, R. 1994, ApJ, 429, L77

Hernández, J., Calvet, N., Hartmann, L., et al. 2009, ApJ, 707, 705

Hernández, J., Calvet, N., Hartmann, L., et al. 2005, AJ, 129, 856

Hernández, J., Hartmann, L., Calvet, N., et al. 2008, ApJ, 686, 1195

Hernández, J., Hartmann, L., Megeath, T., et al. 2007, ApJ, 662, 1067

Hillenbrand, L. A., Strom, S. E., Vrba, F. J., & Keene, J. 1992, ApJ, 397, 613

Hobbs, A. & Nayakshin, S. 2009, MNRAS, 394, 191

Hodgkin, S. T., Irwin, M. J., Hewett, P. C., & Warren, S. J. 2009, MNRAS, 394, 675

Homeier, N. L., Blum, R. D., Pasquali, A., Conti, P. S., & Damineli, A. 2003, A&A, 408, 153

Hußmann, B., Stolte, A., Brandner, W., Gennaro, M., & Liermann, A. 2012, A&A, 540, A57

Ilee, J. D., Wheelwright, H. E., Oudmaijer, R. D., et al. 2013, MNRAS, 429, 2960

Immer, K., Schuller, F., Omont, A., & Menten, K. M. 2012, A&A, 537, A121

Ivanov, V. D., Borissova, J., Pessev, P., Ivanov, G. R., & Kurtev, R. 2002, A&A, 394, L1

Jones, B. F. & Walker, M. F. 1988, AJ, 95, 1755

Kennedy, G. M. & Kenyon, S. J. 2009, ApJ, 695, 1210

Kim, S. S., Figer, D. F., Kudritzki, R. P., & Najarro, F. 2006, ApJ, L113

Kim, S. S., Figer, D. F., Lee, H. M., & Morris, M. 2000, ApJ, 545, 301

Kim, S. S., Figer, D. F., & Morris, M. 2004, ApJ, 607, L123

Kim, S. S. & Morris, M. 2003, ApJ, 312

Kim, S. S., Saitoh, T. R., Jeon, M., et al. 2011, ApJ, 735, L11

King, I. 1962, AJ, 67, 471

Klessen, R. S., Spaans, M., & Jappsen, A.-K. 2007, MNRAS, 374, L29

Kobayashi, Y., Okuda, H., Sato, S., Jugaku, J., & Dyck, H. M. 1983, PASJ, 35, 101

Koekemoer, A. M., Gonzaga, S., Fruchter, A., et al. 2002, HST Dither Handbook, Version 2.0, STScI, Baltimore

Kozhurina-Platais, V., Girard, T. M., Platais, I., et al. 1995, AJ, 109, 672

Krabbe, A., Genzel, R., Drapatz, S., & Rotaciuc, V. 1991, ApJ, 382, L19

Krabbe, A., Genzel, R., Eckart, A., et al. 1995, ApJ, 447, L95

Kroupa, P. 2001, MNRAS, 322, 231

Kroupa, P. 2002, Sci, 295, 82

Kroupa, P., Weidner, C., Pflamm-Altenburg, J., et al. 2013, Planets, Stars and Stellar Systems, Vol. 5, Stellar Systems and Galactic Structure, ed. T. D. Oswalt & G. Gilmore (Dordrecht: Springer), 115

Krumholz, M. R., Dekel, A., & McKee, C. F. 2012, ApJ, 745, 69

Kudryavtseva, N., Brandner, W., Gennaro, M., et al. 2012, ApJ, 750, L44

Lada, C. J., Forbrich, J., Lombardi, M., & Alves, J. F. 2012, ApJ, 745, 190

Lada, C. J., Muench, A. A., Karl E. Haisch, J., et al. 2000, AJ, 120, 3162

Lada, C. J., Muench, A. A., Luhman, K. L., et al. 2006, AJ, 131, 1574

Lamers, H. J. G. L. M., Zickgraf, F.-J., de Winter, D., Houziaux, L., & Zorec, J. 1998, A&A, 340, 117

Landsman, W. B. 1993, in ASP Conf. Ser., Vol. 52, Astronomical Data Analysis Software and Systems II, ed. R. J. Hanisch, R. J. V. Brissenden, & J. Barnes, 246

Lang, C. C., Goss, W. M., & Wood, O. S. 1997, ApJ, 474, 275

Launhardt, R., Zylka, R., & Mezger, P. G. 2002, A&A, 384, 112

Lawrence, A., Warren, S. J., Almaini, O., et al. 2007, MNRAS, 379, 1599

Lee, E. J., Murray, N., & Rahman, M. 2012, ApJ, 752, 146

Lejeune, T. & Schaerer, D. 2001, A&A, 366, 538

Lenzen, R., Hartung, M., Brandner, W., et al. 2003, in SPIE Conf. Ser., Vol. 4841, Instrument Design and Performance for Optical/Infrared Ground-based Telescopes, ed. M. Iye & A. F. M. Moorwood, 944

Liermann, A., Hamann, W.-R., & Oskinova, L. M. 2009, A&A, 494, 1137

Liermann, A., Hamann, W.-R., & Oskinova, L. M. 2012, A&A, 540, A14

Liermann, A., Hamann, W.-R., Oskinova, L. M., Todt, H., & Butler, K. 2010, A&A, 524, A82

Lim, B., Chun, M.-Y., Sung, H., et al. 2013, AJ, 145, 46

Lis, D. C., Serabyn, E., Zylka, R., & Li, Y. 2001, ApJ, 550, 761

Littlefair, S. P., Naylor, T., Jeffries, R. D., Devey, C. R., & Vine, S. 2003, MNRAS, 345, 1205

Longmore, S. N., Bally, J., Testi, L., et al. 2013a, MNRAS, 429, 987

Longmore, S. N., Kruijssen, J. M. D., Bally, J., et al. 2013b, MNRAS, 433, L15

Longmore, S. N., Rathborne, J., Bastian, N., et al. 2012, ApJ, 746, 117

Lu, J. R., Do, T., Ghez, A. M., et al. 2013, ApJ, 764, 155

Lu, J. R., Ghez, A. M., Hornstein, S. D., et al. 2009, ApJ, 690, 1463

Lucas, P. W., Hoare, M. G., Longmore, A., et al. 2008, MNRAS, 391, 136

Lundin, L. K., Ballester, P., & Peron, M. 2007, Very Large Telescope NACO Pipeline User Manual, ESO, Garching

Maíz Apellániz, J. & Úbeda, L. 2005, ApJ, 629, 873

Marco, O., Chauvin, G., Ageorges, N., Hainaut, O., & Kaufer, A. 2007, NACO data reduction cookbook, 81st edn., ESO, Garching

Marigo, P., Girardi, L., Bressan, A., et al. 2008, A&A, 482, 883

Marks, M., Kroupa, P., Dabringhausen, J., & Pawlowski, M. S. 2012, MNRAS, 422, 2246

Martins, F., Hillier, D. J., Paumard, T., et al. 2008, A&A, 478, 219

Martins, F., R. Genzel, R., Hillier, D. J., et al. 2007, A&A, 468, 233

Mason, E., Schmidtobreick, L., Kaufer, A., & Hainaut, O. 2010, Very Large Telescope ISAAC User Manual, 87th edn., ESO, Garching

Mauerhan, J. C., Cotera, A., Dong, H., et al. 2010a, ApJ, 725, 188

Mauerhan, J. C., Morris, M. R., Cotera, A., et al. 2010b, ApJ, 713, L33

Mauerhan, J. C., Muno, M. P., Morris, M. R., Stolovy, S. R., & Cotera, A. 2010c, ApJ, 710, 706

Mercer, E. P., Clemens, D. P., Meade, M. R., et al. 2005, ApJ, 635, 560

Meynet, G., Maeder, A., Schaller, G., Schaerer, D., & Charbonnel, C. 1994, A&AS, 103, 97

Molinari, S., Bally, J., Noriega-Crespo, A., et al. 2011, ApJ, 735, L33

Moneti, A., Glass, I. S., & Moorwood, A. F. M. 1994, MNRAS, 268, 194

Moneti, A., Stolovy, S., Blommaert, J. A. D. L., Figer, D. F., & Najarro, F. 2001, A&A, 366, 106

Morris, M. 1993, ApJ, 408, 496

Morris, M. & Serabyn, E. 1996, ARA&A, 34, 645

Muno, M. P., Clark, J. S., Crowther, P. A., et al. 2006a, ApJ, 636, L41

Muno, M. P., Law, C., Clark, J. S., et al. 2006b, ApJ, 650, 203

Nagata, T., Woodward, C. E., Shure, M., & Kobayashi, N. 1995, AJ, 109, 1676

Nagata, T., Woodward, C. E., Shure, M., Pipher, J. L., & Okuda, H. 1990, ApJ, 351, 83

Najarro, F., Figer, D. F., Hillier, D. J., et al. 2009, ApJ, 691, 1816

Najarro, F., Figer, D. F., Hillier, D. J., & Kudritzki, R. P. 2004, ApJ, 611, L105

Natta, A., Prusti, T., Neri, R., et al. 2001, A&A, 371, 186

Nayakshin, S., Cuadra, J., & Springel, V. 2007, MNRAS, 379, 21

Negueruela, I., González-Fernández, C., Marco, A., Clark, J. S., & Martínez-Núñez, S. 2010, A&A, 513, A74

Nishiyama, S., Nagata, T., Sato, S., et al. 2006, ApJ, 647, 1093

Nishiyama, S., Tamura, M., Hatano, H., et al. 2009, ApJ, 696, 1407

Oey, M. S. & Clarke, C. J. 2005, ApJ, 620, L43

Oka, T., Geballe, T. R., Goto, M., Usuda, T., & McCall, B. J. 2005, ApJ, 632, 882

Okuda, H., Shibai, H., Kobayashi, Y., et al. 1987, in IAU Symposium, Vol. 115, Star Forming Regions, ed. M. Peimbert & J. Jugaku, 556

Okuda, H., Shibai, H., Nakagawa, T., et al. 1990, ApJ, 351, 89

Olczak, C., Kaczmarek, T., Harfst, S., Pfalzner, S., & Zwart, S. P. 2012, ApJ, 756, 123

Olczak, C., Pfalzner, S., & Eckart, A. 2010, A&A, 509, A63

Pang, X., Grebel, E. K., Allison, R. J., et al. 2013, ApJ, 764, 73

Paumard, T., Genzel, R., Martins, F., et al. 2006, Journal of Physics: Conference Series, 54, 199

Pfalzner, S. 2009, A&A, 498, L37

Pflamm-Altenburg, J. & Kroupa, P. 2006, MNRAS, 373, 295

Pflamm-Altenburg, J. & Kroupa, P. 2010, MNRAS, 404, 1564

Portegies Zwart, S., Gaburov, E., Chen, H.-C., & Gürkan, M. A. 2007, MNRAS, 378, L29

Portegies Zwart, S. F., Makino, J., McMillan, S. L. W., & Hut, P. 2002, ApJ, 565, 265

Portegies Zwart, S. F., McMillan, S. L. W., & Gieles, M. 2010, ARA&A, 48, 431

Porter, J. M. & Rivinius, T. 2003, PASP, 115, 1153

Press, W. H., Teukolsky, S. A., Vetterling, W. T., & Flannery, B. 2007, Numerical recipes - the art of scientific computing, 3rd edn. (Cambridge: Cambridge Univ. Press)

Rajan, A. 2010, WFC3 Data Handbook, Version 2.1, STScI, Baltimore

Rich, R. M., Reitzel, D. B., Howard, C. D., & Zhao, H. 2007, ApJ, 658, L29

Rodriguez-Fernandez, N. J., Combes, F., Martin-Pintado, J., Wilson, T. L., & Apponi, A. 2006, A&A, 455, 963

Rousset, G., Lacombe, F., Puget, P., et al. 2003, in SPIE Conf. Ser., Vol. 4839, Adaptive Optical System Technologies II, ed. P. L. Wizinowich & D. Bonaccini, 140

Salpeter, E. E. 1955, ApJ, 121, 161

Salyk, C., Blake, G. A., Boogert, A. C. A., & Brown, J. M. 2009, ApJ, 699, 330

Sana, H., Momany, Y., Gieles, M., et al. 2010, A&A, 515, A26

Sander, A., Hamann, W.-R., & Todt, H. 2012, A&A, 540, A144

Scalo, J. M. 1986, Fun. Cosm. Phys., 11, 1

Schaller, G., Schaerer, D., Meynet, G., & Maeder, A. 1992, A&AS, 96, 269

Schilbach, E. & Röser, S. 2008, A&A, 489, 105

Schneider, F. R. N., Izzard, R. G., de Mink, S. E., et al. 2013, submitted

Schödel, R., Najarro, F., Muzic, K., & Eckart, A. 2010, A&A, 511, A18

Serabyn, E., Shupe, D., & Figer, D. F. 1998, Nat, 394, 448

Shetty, R., Beaumont, C. N., Burton, M. G., Kelly, B. C., & Klessen, R. S. 2012, MNRAS, 425, 720

Skrutskie, M. F., Cutri, R. M., Stiening, R., et al. 2006, AJ, 131, 1163

Smith, R. & Jeffries, R. D. 2012, MNRAS, 420, 2884

Smith, R. J., Longmore, S., & Bonnell, I. 2009, MNRAS, 400, 1775

Stetson, P. B. 1987, PASP, 99, 191

Stetson, P. B. 1992, J. R. Astron. Soc. Can., 86, 71

Stolte, A., Brandner, W., Brandl, B., et al. 2004, AJ, 128, 765

Stolte, A., Brandner, W., Brandl, B., & Zinnecker, H. 2006, AJ, 132, 253

Stolte, A., Brandner, W., Grebel, E. K., et al. 2005, ApJ, 628, L113

Stolte, A., Ghez, A. M., Morris, M., et al. 2008, ApJ, 675, 1278

Stolte, A., Grebel, E. K., Brandner, W., & Figer, D. F. 2002, A&A, 394, 459

Stolte, A., Morris, M. R., Ghez, A. M., et al. 2010, ApJ, 718, 810

Straižys, V. & Laugalys, V. 2008, Baltic Astronomy, 17, 253

Sumi, T., Eyer, L., & Woźniak, P. R. 2003, MNRAS, 340, 1346

Sung, H. & Bessell, M. S. 2004, AJ, 127, 1014

Tatulli, E., Malbet, F., Ménard, F., et al. 2008, A&A, 489, 1151

Thi, W.-F., van Dalen, B., Bik, A., & Waters, L. B. F. M. 2005, A&A, 430, L61

Tody, D. 1986, in SPIE Conf. Ser., Vol. 627, Instrumentation in Astronomy VI, ed. D. L. Crawford, 733

Tody, D. 1993, in ASP Conf. Ser., Vol. 52, Astronomical Data Analysis Software and Systems II, ed. R. J. Hanisch, R. J. V. Brissenden, & J. Barnes, 173

Tokunaga, A. T., Simons, D. A., & Vacca, W. D. 2002, PASP, 114, 180

Trippe, S., Gillessen, S., Gerhard, O. E., et al. 2008, A&A, 492, 419

Tuthill, P., Monnier, J., Tanner, A., et al. 2006, Sci, 313, 935

van den Ancker, M. E., Meeus, G., Cami, J., Waters, L. B. F. M., & Waelkens, C. 2001, A&A, 369, L17

van der Hucht, K. A. 2006, A&A, 458, 453

van der Tak, F. F. S., Belloche, A., Schilke, P., et al. 2006, A&A, 454, L99

Vasilevskis, S., Klemola, A., & Preston, G. 1958, AJ, 63, 387

Wang, Q. D., Dong, H., & Lang, C. 2006, MNRAS, 371, 38

Waters, L. B. F. M., Cote, J., & Geballe, T. R. 1988, A&A, 203, 348

Weidner, C. & Kroupa, P. 2004, MNRAS, 348, 187

Weidner, C. & Kroupa, P. 2006, MNRAS, 365, 1333

Weidner, C., Kroupa, P., & Maschberger, T. 2009, MNRAS, 393, 663

Whitmore, B. C., Chandar, R., Schweizer, F., et al. 2010, AJ, 140, 75

Williams, J. P. & Cieza, L. A. 2011, ARA&A, 49, 67

Yusef-Zadeh, F., Hewitt, J. W., Arendt, R. G., et al. 2009, ApJ, 702, 178

Yusef-Zadeh, F., Hewitt, J. W., Wardle, M., et al. 2013, ApJ, 762, 33

Yusef-Zadeh, F. & Morris, M. 1987, AJ, 94, 1178

Yusef-Zadeh, F., Morris, M., & Chance, D. 1984, Nat, 310, 557

Yusef-Zadeh, F., Wardle, M., & Roy, S. 2007, ApJ, 665, L123

Acknowledgements

This thesis could not have been completed without the support and help of many people and institutions I am indebted to and to whom I would like to address my deep thanks.

First of all I want to thank Dr. Andrea Stolte for allowing me to conduct this study as a PhD student in her Emmy Noether group and for her great support throughout the time of this thesis project. I am very grateful for her committed supervision, her patience and the encouragements when the analysis of the data or other issues posed some unexpected obstacles.

I would like to thank Prof. Dr. Norbert Langer for evaluating this thesis and for his generous support by a four-month doctoral scholarship.

My special thanks go to Dr. Wolfgang Brandner at the MPIA in Heidelberg for his interest in this work, for many useful discussions and suggestions, for patiently answering my various questions, and for his careful proofreading of the manuscript and giving me useful comments.

Thanks to Dr. Mario Gennaro for allowing me to use his set of combined isochrones and his IDL code for deriving the completeness maps and for answering all my associated questions. I thank Dr. Stefan Harfst and Dr. Christoph Olczak for helping me to understand the impact of the dynamical evolution on the shape of the PDMF and for useful discussions. Thanks also to Dr. Adriane Liermann for sharing her spectroscopic insights into the high mass content of the Quintuplet cluster.

As this thesis is based on observations obtained at the ESO VLT, I also want to thank the NAOS-CONICA instrument scientist team, in particular Dr. Julien Girard, for their careful observations and the maintenance of this instrument.

I gratefully acknowledge the funding by the German Science Foundation (DFG) Emmy Noether Programme under grant STO 496/3-1.

The work presented in this thesis was done at two institutes which belong to two different universities. I hence thank for and acknowledge the support provided by the Argelander Institut für Astronomie and the Universität Bonn and the I. Physikalisches Institut and the Universität zu Köln. In especially I would like to thank the computer groups at both institutes without whose support effective work would not have been possible. Likewise I thank the secretaries for their help in all kinds of practical and administrative issues.

A special thanks goes to Maryam Habibi for the good collaboration in our rather ‘exquisite’ three-person working group. I thank my former and present office mates Markus Bremer, Gunther Witzel, Andreas Küpper, Michael Marks, and Xufen Wu for the pleasant working atmosphere and for thesis related or more general discussions. Thanks also to all the people at the AIfA and at the I. Physikalisches Institut who contributed to the enjoyable atmosphere at both institutes. In particular I

thank Andreas Breslau, Thomas Kaczmarek, Christina Korntreff, Andreas Küpper, Marcel Pawlowksi, and Manuel Steinhausen for the nice lunch conversations.

I am very grateful and indebted to my family for their patience, continuous support and encouragement and for being my safe harbour throughout my life. I thank my brother in-law most cordially for his assiduous and thorough proofreading of this thesis. Thanks also to my godmother for being such a good and attentive listener.